UNIVERSITE DE NICE ET SOPHIA ANTIPOLIS - UFR Sciences

Ecole Doctorale Sciences Fondamentales et Appliquées

THESE

Pour obtenir le titre de

Docteur en Sciences

De l'UNIVERSITÉ de Nice-Sophia-Antipolis

Spécialité : ***Physique***

Présentée et soutenue par

Linda MONDIN

Stabilisation de fréquence de laser Nd:YAG pour applications spatiales

Frequency stabilised Nd:YAG lasers for space applications

Thèse dirigée par **Catherine Nary MAN**

JURY :

M. J. Borgnino	Président
M^{me} C.N. Man	Directeur de thèse
M^{me} M. Houssin	Rapporteur
M. F. Marin	Rapporteur
M. J. Berthon	Examinateur
M. A. Brillet	Examinateur

Remerciements

Je tiens tout d'abord à remercier ma directrice de thèse Nary Man et le directeur du groupe expérimental Alain Brillet pour leur enseignement et leur accueil au sein de l'équipe ARTEMIS. Vous m'avez appris beaucoup sur le plan scientifique et humain.
Mes remerciements vont aussi à tous les membres de mon jury de thèse, M. Borgnino, Mme Houssin, M. Marin, M. Berthon et bien sur Alain et Nary.
Merci a tous ceux qui ont rendu possible les travaux expérimentaux : Jean-Pierre Coulon, un vrai magicien de l'électronique, Gilbert Pen, un expert de la mécanique , ainsi que Christian, Serge Bonhomme et Alain Roussel qui ont aidé dans la conception et la réalisation des ensembles mécaniques. Mes remerciements vont aussi aux deux ingénieurs avec qui j'ai collaboré : Alexandre Bes et Cyrille Baudouin.
Merci à tous les membres de l'équipe ARTEMIS, tous prêt à la discussion et à l'échange d'idées. En particulier je tiens à remercier Henrich Heitmann, Fred Cleva, François Bondu, Jean Cachenaut, Eric Chassande-Mottin, pour leur expertise et savoir faire dont mon travail de thèse a beaucoup bénéficié. Merci à Jean-Yves Vinet pour ces enseignements au cours du DEA et ces efforts dans l'explication des phénomènes optiques.
Mes remerciements vont au CNES pour son financement de ce projet de recherche, en particulier à Sylvie Leon et Jacques Berthon qui ont suivi de près nos activités de recherche.
Merci à M. Taubman, qui a collaboré à la mise en place et à la compréhension du verrouillage sur l'Iode, sa disponibilité, compétence et curiosité ont été de première importance dans la réussite de nos recherches.
Je tiens à remercier tous ceux qui m'ont accompagné dans mon expérience de thèse : Françoise, Hervé, Magali, Philip, François, Philippe, Cedric, Rajesh, Alessandro, Sebastien, Archana, Veronique, Mikael et Mickael.
Des remerciements spéciaux vont à Elena Lega, Jean Vernin et son épouse Mérieme Chadid pour leur amitié et conseil, à D.A. Shaddock pour son encouragement et à John Tully, qui m'a souvent montré le bon chemin.
Merci en particulier à M. Jacques Colin de m'avoir accueillie à l'OCA et d'avoir toujours soutenu nos activités.
Et enfin merci également au secrétariat: Marylène, Seyna, Sophie et Cathy, pour avoir créé une ambiance de travail superbe.
Finalement merci à mes parents qui m'ont toujours soutenue et encouragée.

For Grandmother and Grandfather,

Per aspera ad astra

Table Of Contents

List Of Figures and Tables

Plan du rapport - Outline

Les lasers stabilisés à long terme sont utilisés dans de nombreux domaines en métrologie et constituent la base de toute la recherche expérimentale en spectroscopie à très haute résolution. Leur incursion dans les applications spatiales se précise depuis quelques années, que ce soit pour les missions de physique fondamentale ou pour les missions de géodésie.

Ce mémoire décrit mon travail de thèse sur les lasers à Nd:YAG stabilisés en vue d'applications spatiales. Les points de départ de ce travail concernent les exigences requises pour les lasers du projet LISA (détection spatiale des ondes de gravitation, mission prévue dans 10 ans), en matière de stabilité. D'autre part, en vue de cette application spatiale, nous garderons en arrière-pensée que les montages doivent satisfaire dans la mesure du possible, plusieurs critères parmi lesquels il y a la compacité et la stabilité mécanique, ainsi que bien entendu la robustesse et la fiabilité.

Après une brève introduction, je décrirai les références utilisables pour le long terme (référence moléculaire, chapitre 3) et pour le court terme (référence mécanique, chapitre 4), ainsi que leurs limitations principales. L'analyse et le choix de ces références de stabilisation seront plus ou moins couplés avec le choix des techniques de stabilisation (PDH, Tilt-Locking, Modulation Transfer).

Dans les techniques de stabilisation, celle de Pound-Drever-Hall (PDH) est devenue un classique en matière de configuration car elle donne les meilleurs performances connues à ce jour surtout à court terme. En vue de réduire le nombre de composants actifs, nous avons aussi implanté une technique de stabilisation continue dite de Tilt-Locking, que je comparerai avec celle de PDH dans le cas d'une référence Fabry-Perot monolithique.

Dans la première partie, calcule théorique chapitres 3 et 4, pour chaque technique et chaque type de référence, je commencerai par la description des sources de bruit et calculerai les signaux d'erreur attendus à partir des modélisations que j'ai effectuées. Les performances théoriques sur le long terme et les efficacités quantiques seront inter-comparées.

La deuxième partie, chapitres 5 et 6, donnera les schémas de principe des montages expérimentaux et les résultats que j'ai obtenus, de lasers stabilisés sur Fabry-Perot et sur l'Iode moléculaire. Pour calibrer les dérives de fréquence du Fabry-Perot, sa fréquence de résonance sera mesurée par rapport à celle de la molécule, ce qui me permettra de

présenter des solutions obtenues analytiquement et numériquement pour l'asservissement en longueur de cette référence mécanique.

Enfin des suggestions de prolongation de ces travaux sont suggérés en conclusion et le lecteur trouvera en appendices, les détails de dimensionnement des bruits de LISA conduisant aux spécifications des lasers, le rappel théorique des ondes de gravitation ainsi que divers simulations de calculs que j'ai effectués .

Outline

Long term stabilised lasers are used in a multitude of metrological applications and are the basis of experimental research in very high resolution spectroscopy. In the last few years their mention for space applications has been growing, for fundamental physics experiments as well as for geodesy.

This document describes my thesis work on stabilised Nd:YAG lasers in view of space applications. The starting point of this work takes into account the lasers' requirements for the LISA project in term of stability. Moreover, in view of these space applications, we will keep in mind that all experiments must satisfy as much as possible the many criteria of compactness, mechanical stability as well as robustness and reliability.

After a short introduction, I will describe the possible references useful for the long term (molecular reference) and the short term (mechanical reference) time intervals with their principal limitations. The discussion leading to their choice is actually connected to the stabilisation techniques to be adequately implemented (PDH, Tilt-Locking, Modulation transfer).

Among the stabilisation techniques, the Pound-Drever-Hall (PDH) technique is now a classical configuration as it produces the best performances obtained so far in short term. Along with the requested reduction of active components, we have also implemented a DC technique called Tilt-Locking and I will compare it with the PDH in the case of a monolithic Fabry-Perot reference.

In the first part of the manuscript, I will start, for each technique and each reference, with the description of noise sources and the expected error signals coming from the simulations I have achieved. Theoretical performances on the long term and quantum efficiencies will be compared for different techniques.

The second part gives the schematic principles of the experiences and the results I have obtained from stabilised lasers on Fabry-Perot and molecular iodine. To calibrate the Fabry-Perot drifts, its resonance frequency will be measured vs. the molecular transition

and this will allow me to point out analytical and numerical solutions to control the length of this mechanical reference.

Finally suggestions for further work will be approached in the last part of the document; the reader can find in the appendices details about noise order of magnitudes for LISA (leading to lasers specifications), a theoretical overview of gravitational waves as well as different simulations and calculations I have performed to verify their adaptability to our experimental set-up, focusing on a long term stabilised YAG laser.

1 Introduction

The scope of this thesis work is to analyse and test different techniques and references to implement a frequency stabilisation of an Nd:YAG laser source. The YAG lasers have been chosen as source due to their excellent properties of robustness, intrinsic frequency stability (linewidth is 1kHz @ 0.1s typically), Mean Time Between Failures (MTBF) and wavelength (1064nm is weakly absorbed by the interplanetary medium).

A laser frequency stabilisation can be put into place for many a different aim, and can have different requirements depending on the chosen application, but is usually necessary in metrological precision measurements of length or time. Frequency stability can be characterised by three quantities: stability, reproducibility and 'exactitude' or precision. With the term stability we indicate the frequency variations of the laser with respect to itself, with reproducibility we indicate the possibility of obtaining the same frequency measurement at different times, as long as experimental conditions are identical and with 'exactitude' we indicate the knowledge of the absolute frequency value of our laser. It has to be observed that strictly speaking in metrology exactitude is the precision of a Caesium clock with respect to the etalon Caesium clock, we are hereon (mis)using the term to indicate the incertitude of the laser's real frequency.

The accent for our studies has been put on space applications where frequency stabilised lasers are needed. For space mission the most important parameter is usually stability, though depending on the experiment, precision and reproducibility can be required as well. All formation flight missions will maintain their formation (such as is the case for Darwin the proposed extra solar planet searcher) and measure the satellite's position deviations from the ideal constellations thanks to frequency stabilised laser sources. The requests for this kind of mission can vary depending on the required precision in the measurement of the satellite's position which in turn depends from the chosen application.

For geodesy we must detect displacements of the order of the nm over the few km of the distance between the satellites, this requests a frequency stability for the laser of $3Hz/\sqrt{Hz}$. For an explanation of these units please refer to Section 2.2 (page17).

Proposed formation flight missions such as the extra solar terrestrial planet searcher Darwin typically require a measurement precision of the Á over 100m arms, demanding a frequency stability of $0.3Hz/\sqrt{Hz}$. Other terrestrial planet searchers such as the precursor

mission of Terrestrial Planet Finder called TPF-C will also require a frequency stabilisation to better than $300Hz/\sqrt{Hz}$.

Space GW (Gravitational Waves) detectors such as the Laser Interferometric Space Antenna (for greater details on the LISA mission and the detection of Gravitational Waves, please refer to Appendix A) will also require a frequency stabilised laser source to measure displacements of the order of the atomic diameter (Å) over distances of the order of the UA (Astronomical unit the mean distance Sun-Earth: 150 10^6km). This would request a frequency stability of $3 \cdot 10^{-7} Hz/\sqrt{Hz}$ which is several orders of magnitude better than anything ever done or at all doable with nowadays technology, for the measure of the single arm. Let's consider the expected sensitivity of the LISA antenna, the necessary laser specifications to obtain a Signal to Noise Ratio of 5 and a partial noise contribution summary of the detector, for greater detail please refer to Appendix A. In order to set specifications on frequency stability we have to consider the order of the length variations we want to measure which are given, for arm lengths much smaller than the GW wavelengths, by:

$$\frac{\delta L}{L} \approx h \cdot \cos^2\left(\frac{\pi}{3}\right) \qquad (1\text{-}1)$$

with *h* the GW strain and where the cosine term comes from the triangular geometry of the interferometer. LISA requires a sensitivity sufficient for detection at frequencies between 10^{-4} and 1 Hz with an integration time of 1 year. It has to be remembered that the rotation of the antenna will change the detector alignment with respect to the sources. The antenna will therefore seldom be in the configuration where the signal is maximal. This causes a reduction of the SNR by a factor dependent on the orientation of the interferometer with respect to the antenna. This effect is generally approximated with a reduction of $1/\sqrt{5}$ to the antenna RMS sensitivity on the whole sky.[1] Let us now analyse the two principal noise groups. On one hand we have the optical path noises which derive from effects that change or mimic variations of the optical path. On the other hand we have acceleration noises, due to all spurious forces acting on the test masses. Acceleration noise shall be responsible for the low frequency loss of sensitivity (Figure 1–1). The optical path noise shall limit LISA sensitivity for the higher frequencies instead, in particular with its unavoidable shot-noise contribution. The photon noise generated white noise on the gravitational displacements shall be of the order of:

$$\delta L = \sqrt{\frac{\hbar c \lambda}{2\pi P_{eff}}} \qquad (1\text{-}2)$$

and represents a threshold we wish to attain limiting all frequency and amplitude noises. In the above expression P_{eff} indicates the power effectively used to obtain the error signal and depends quite obviously on the power of the laser used. One can show that with suitable signal analysis algorithms (Appendix A) the requirements on frequency stability are:

$\Delta\nu = 10\,Hz/\sqrt{Hz}$

This is not a definitive specification as studies are still underway to relax the requirements on the laser frequency stabilisation. Additionally to this, it is also necessary that the lasers frequency differences on different satellites be no more than 100MHz apart in frequency in order for the regeneration of the return beam to work properly.

The work I present here concerns studies on stabilised lasers aiming for short term and long term performances in view of these specifications, both for LISA and other possible space experiments.

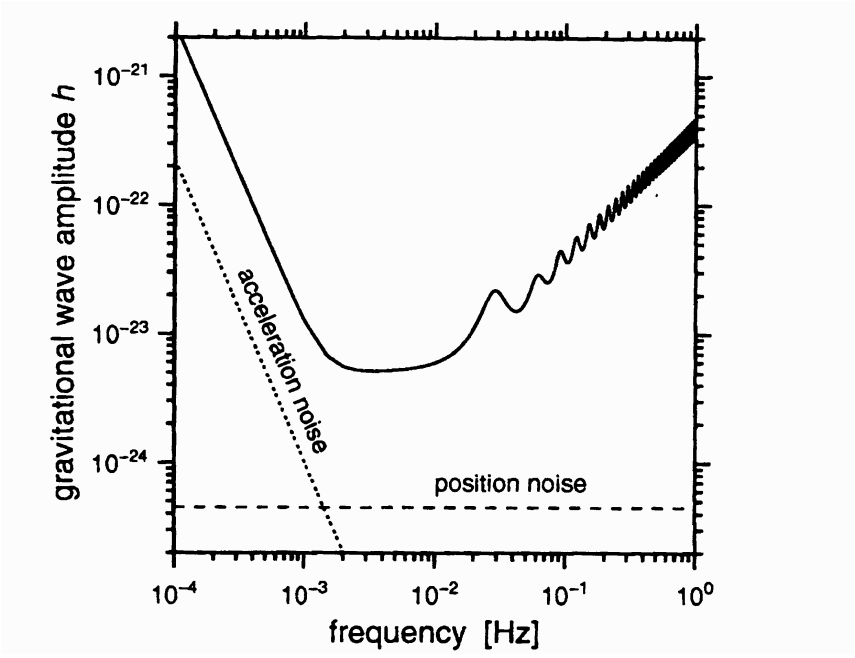

Figure 1–1

2 Frequency Stabilisation principles and characterisation

Before coming to the stabilisation techniques, the first question one can raise is whether for high stability experiments, one must use a laser with special properties, for example massive invar construction. The answer given by Hils and Hall[49] is no, from both theory and experiment, meaning that a commercial laser could be used as well. Actually following the same authors, "what is required, is a laser source with a smoothly evolving phase and a frequency-control access with speed appropriate for the time-scale and level of instability present in the laser". If the laser has a fast-changing optical source, it will influence the choice of the control-loop design and actuator which both must be of significantly greater bandwidth and lower time delay, relative to the intrinsic phase changing process.

We shall now analyse the principles of a stabilisation control, and study the noise influence of the different constituents. Afterwards, I will present the various ways to characterize the stability of a laser and discuss it in terms of signal to noise ratio as well as recalling the definitions of spectral density and Allan variance.

2.1 Locking principles

Let's approach the problem of frequency stabilisation in terms of control theory. Figure 2-1 is a schematic of a frequency control loop and we will use linear spectral densities (recalled in Section 2.2) to describe the noises:

- the laser has a fixed frequency ν, by some noise process it also has $S_{laser}(f)$ which is the linear spectral density of frequency noise in $\mathrm{Hz}/\sqrt{\mathrm{Hz}}$, and is frequency dependent.

- The frequency of the laser is monitored with a discriminator which converts frequency fluctuations into voltage fluctuations with a conversion factor ***D*** in V/Hz, then giving an error signal. $S_{discri}(f)$ is the spectral density of the discriminator noise. Here by discriminator, we comprise the reference with which the laser frequency is compared, and the technique with which one can extract the error signal.

- This error signal is amplified in a servo with a gain ***G(f)*** which is frequency dependant, and fed back to the actuator. In the same way, $S_{servo}(f)$ is the spectral density of the servo noise.

- The actuator, usually a piezoelectric ceramic bonded on the laser cavity, converts the amplified, integrated signal into frequency fluctuations with a coefficient ***A(Hz/V)***. We will assume that the actuator's noise is combined into the laser's noise, as most often they are not easy to distinguish.

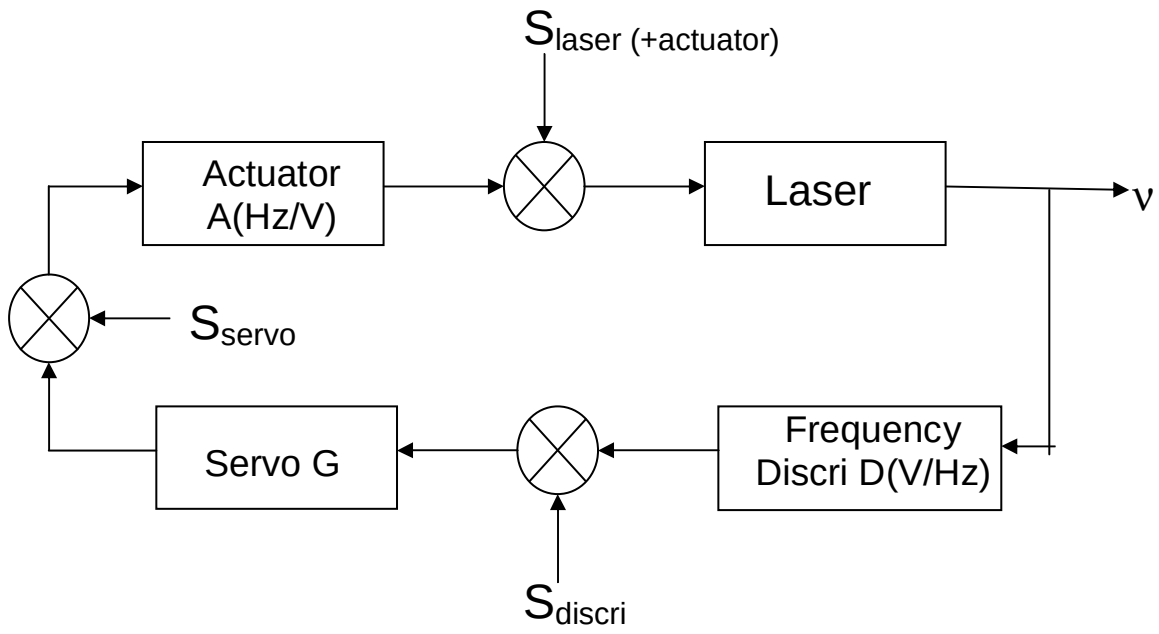

Figure 2–1

In the presence of these noises, one can derived the expression of the closed loop spectral density of frequency noise, which is the quadratic sum of all contributions:

$$S_{closed-loop} = \frac{\sqrt{S^2{}_{laser} + \left|A \cdot S_{servo}\right|^2 + \left|A \cdot G \cdot S_{discri}\right|^2}}{\left|1 + A \cdot G \cdot D\right|} \qquad (2\text{-}1)$$

In the limit of very large servo gain, all the terms drops except the contribution of the third term, and $S_{cl} = \frac{S_{discri}}{D}$ shows the domination of the discriminator noise over the others. The discriminator noise includes contributions from technical noise associated with the noise of the reference, the noise of the amplifiers, etc, as well as the quantum noise associated with detection of the laser frequency. In a properly designed frequency controller, the technical noise should be made very small, then the contribution which remains is due the quantum fluctuations at the discriminator detector. The slope of the

frequency discriminator together with the quantum fluctuations at the detector determine, therefore, the overall performance limit.

The discrimination techniques appropriate for each kind of references are discussed in the following Sections. We recall in the next paragraph how the stability of the laser frequency is characterized depending on the time scale of the measurements.

2.2 Characterisation

We can distinguish between long term and short term stability, the first one measured over times duration larger than 1 s, the latter measured over times smaller than 1 s. Another important parameter to be taken into account is the 'exactitude' or precision as it is requested in formation flight experiments.

The short term frequency stability of a laser is usually estimated thanks to the Signal to Noise Ratio and is usually best obtained with the use of a mechanical reference whose linewidth can be as narrow as 10^2 Hz. In a completely general way to determine the SNR we have to evaluate the error signal slope (χ) as well as the noise (N). χ can be evaluated experimentally or analytically, for a given frequency lock technique, developing in series of small $f=\delta\omega/\gamma$ or $\delta\omega$, where $\delta\omega$ is the detuning of the laser with respect to the reference and γ the linewidth of the latter:

$$\chi(P,f)=\left(\frac{\eta q E_{00}^2}{h\nu Z_{Pd}}\right)\left(ES(0)+\left.\frac{\partial ES}{\partial f}\right|_0 f\right) \tag{2-1}$$

In the above expression $P=E_{00}^2$ is the laser power, Z_{Pd} is the transimpedance of the Photodiode detecting the error signal, q is the electron charge and the term $h\nu$ represent the Energy of the single photon. This parameter measures the slope of the error signal and is given here in units of the photocurrent [A]. For the Noise we can consider the Poissonian shot noise of the photons incident on the photodiode:

$$N(P)=\sqrt{\#_{phot}}\,q=\sqrt{\left.\int_{-\infty}^{\infty}P(x)dx\right|_{DC}}\cdot\sqrt{\frac{\eta}{h\nu Z_{Pd}}}\cdot q \tag{2-2}$$

The Signal to Noise ratio shall therefore have the form:

$$SNR(P,f)=\sqrt{\frac{\eta}{h\nu Z_{Pd}}}\cdot E_{00}\cdot\frac{\left(ES(0)+\left.\frac{\partial ES}{\partial f}\right|_0 f\right)}{\sqrt{\left.\int_{-\infty}^{\infty}\frac{P(x)}{E_{00}^2}dx\right|_{DC}}} \tag{2-3}$$

The frequency stability is preferentially measured, on the short term, using the spectral noise density of the laser. The spectral noise density of a parameter x(t) is given by:

$$S_x(\nu)=\sqrt{\frac{1}{\tau}\left[\int_{-\frac{\tau}{2}}^{\frac{\tau}{2}} x(t)e^{-2i\pi\nu\cdot t}dt\right]^2} \tag{2-4}$$

for a time τ and is measured in the units of the physical variable x divided by $\sqrt{}$Hz. This spectral noise density in our case taken for the power is then converted into a frequency noise spectrum thanks to our knowledge of the error signal's slope:

$$S_\nu(\nu)=S_V(\nu)\cdot\chi\cdot Z_{Pd}\ . \tag{2-5}$$

This measurement yields a frequency stability value in Hz/$\sqrt{}$Hz, for all given frequencies for which we have taken the spectrum.

Another parameter measuring the frequency stability of a laser source is the Allan variance of the phase φ defined for a time τ as:

$$\sigma^2(\tau)=\lim_{n\to\infty}\frac{1}{n}\sum_{k=1}^{n}\frac{1}{2}\left(\varphi_{(k+1)\tau}-\varphi_{k\tau}\right)^2 \tag{2-6}$$

It is also possible to express the Allan variance of the frequency, in place of the phase, this latter parameter having dimension of Hz/$\sqrt{\tau}$ instead of simply 1/$\sqrt{\tau}$.

The Allan variance is linked to the Spectral Noise density by the relation:

$$\sigma^2(\tau)=2\int_0^\infty S(\nu)\frac{\sin^4(\pi\nu\tau)}{(\pi\nu\tau)^2}d\nu \tag{2-7}$$

which can be solved for different spectral noise densities as done by Brillet[3] in his thesis work. The Allan variance is often used for long term frequency variation measurements for practical reasons.

The stability, as shown by Equation (2-5), is closely dependent on the linewidth of the reference, or more precisely on the slope of the error signal. For short term stabilisation we ask only that the slope of the error signal be steep, which implies that the linewidth must be narrow. This is verified for the cavities were the linewidth of the reference (kHz) is narrower than we can obtain with molecules (10^2kHz). For cavities we can also use large laser powers to reduce photon noise. The power usable with molecular references, instead, is limited by the saturation broadening, which for high values of the laser power increases the linewidth of the transition, as will be seen in Section 3.1.1. For equivalent values of the photon noise we shall have much larger linewidths for molecules than obtained with the mechanical references. Resonators are to be preferred for short term stabilisation.

For long term stabilisation, instead, we ask that the frequency of the laser source do not vary significantly over time intervals of over 1000s. These time variations shall mostly

depend on the reference frequency drifts but not on its linewidth. It is, therefore, obvious that for long term frequency stabilisation molecular and atomic transitions are favoured. Molecular linewidth can change significantly (10^4Hz/K) with the pressure (this parameter is in its turn temperature dependent) but the central position of the reference will be independent (10^2Hz/K, 50 Hz/K for I_2 at the temperatures of interest) at first order from the thermodynamic parameters of the gas. On the length of a Fabry-Perot, instead, changes of the order of $\Delta L / L = \alpha \Delta T$ (which shall give, for the frequency, equivalent variations of 1MHz/K) can be expected to intervene, even for an Ultra Low Expansion glass with $\alpha=1.9\cdot10^{-9}(T-T_0)<10^{-8}K^{-1}$.

Reproducibility and exactitude require a molecular or atomic reference, since their long term variations are smaller and their transitions proper frequencies are known. For Fabry-Perot resonators, a detailed explanation is found in Section 4.1, the light is coupled into the reference for all multiples of the Free Spectral Range (FSR) compatible with the laser frequency, i.e. $\nu_{las} = q \cdot FSR$ with q of the order typically of 10^5. So even if the FP proper frequency were measured before the start of a space mission it still would be possible for a laser frequency to be more than one FSR (typically a GHz) away from its chosen frequency. Where an absolute knowledge of the laser's frequency is required a molecular reference must perforce be used. An absolute measure of a frequency can be made thanks to a lambda-meter, or a frequency-meter measuring the beat note with another known frequency standard.

2.3 Noise contributions

There remain different possible noise sources both in the electronics, which we have up to now grouped in the contribution $S_{servo}(f)$ without trying to understand their nature, and in the different references.

The electronics principal noise contributions shall be the photon *shot noise*, which we have discussed above and which is not strictly speaking an electronic noise, the *Johnson* shot *noise* of the control electronics and the *dark current,* coming from the photo-detectors when no beam is incident. Johnson shot noise has a typical noise spectral density given by the well known $\delta\tilde{V} = \sqrt{2k_B TR}$ with k_B is the Boltzman constant, T is the absolute temperature of the resistance in exam, and R is the impedance value. Dark current is measured for each photodiode used in an experiment and typically varies between values close to zero and several μA.

The references' frequency noise sources can vary depending on the chosen type of reference and shall be treated separately in the following chapters.

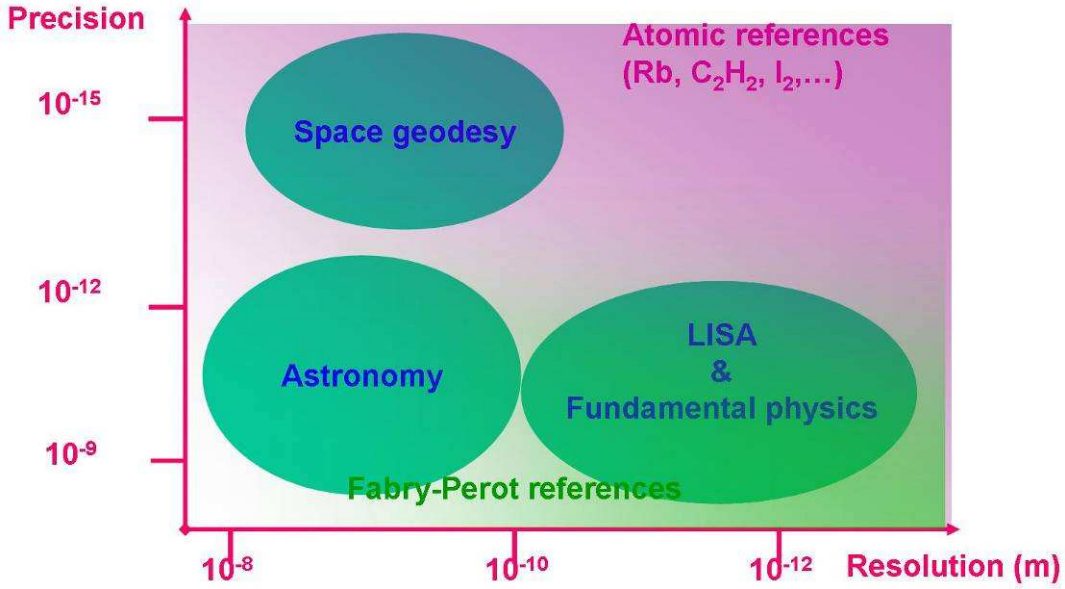

Figure 2–2 Courtesy of A. Brillet CNRS OCA

As is shown by the above schematics, depending on the requested precision and resolution of a lock we have a choice between references to make. We have seen that long term stability favours molecular references, which become necessary where precision is requested, whereas, for short term applications, resonators are to be preferred. Let us now analyse more in detail both these two categories of possible frequency references for Nd:YAG lasers and the accompanying locking techniques.

3 Molecular References

As shown in Section 2.2, to have good frequency stabilities we need transitions with a narrow linewidth. For molecules we shall therefore use the hyperfine transitions of the molecular roto-vibrational spectrum. These narrow (MHz) lines (Figure 3-2B and C) are accessible only after we have reduced Doppler broadening through the use of saturated absorption. In fact the Doppler broadening introduced by the thermal agitation of the molecules can be so important that different transitions in the same band structure are confused for the linear absorption profile, as seen in Figure 3-2A, into a several GHz large molecular band. In order to lock our laser to a molecular transition we have to reduce the Doppler broadening; this is accomplished through the use of Saturated Absorption.

3.1.1 Saturated absorption

Saturated absorption requires two counter-propagating beams: one we shall call pump, which shall saturate the absorption, and the other, the probe, which shall be detected.

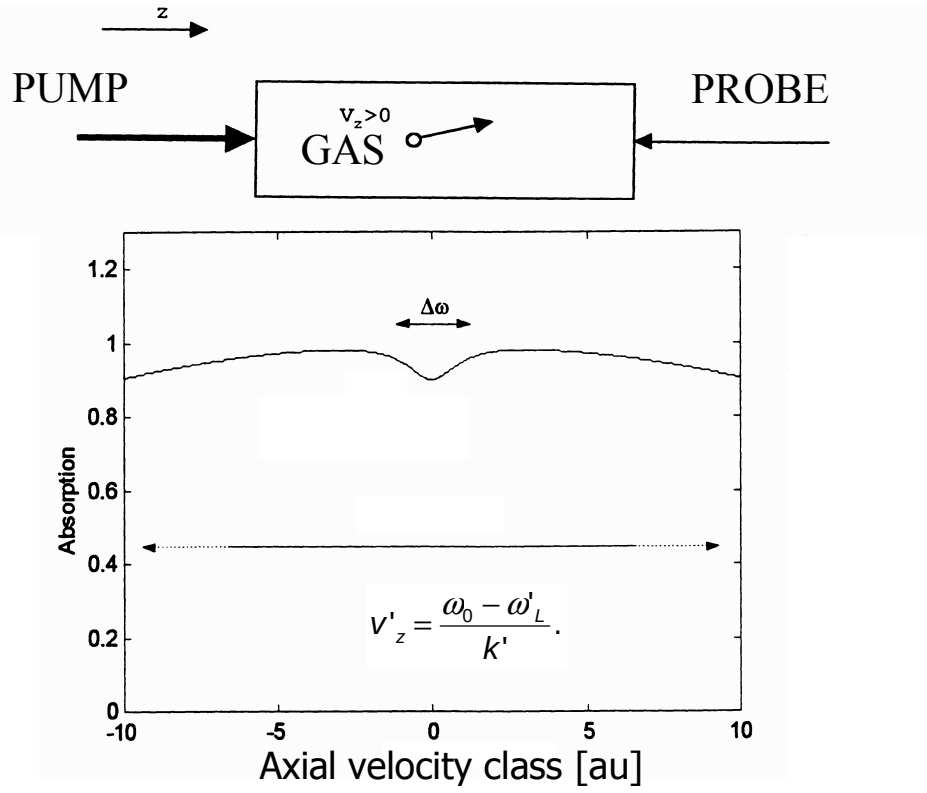

Figure 3–1 Image from Brookman's report[7]

There are two main configurations: the quasi-stationary state, where the two beams have comparable intensities, and the quasi-progressive state in which the probe shall be much weaker than the pump. This technique was studied in detail by Bordé[4][5], Brillet[3] and

Shirley[6], amongst others. Let us analyse in detail the quasi-progressive case. We shall implement it by passing a first intense beam (pump, $I_P > I_{sat}$) through a gas cell with an intensity greater than the medium's saturation and a frequency close to that of the transition we wish to examine. For a two-level atom or molecule its transition shall be at a frequency:

$$\hbar\omega_0 = E_a - E_b \,. \tag{3-1}$$

If the beam is propagating along the z axis we have that the laser shall be resonant with an atom having a velocity $\vec{v}$ for a laser frequency of:

$$\omega_L = \omega_0 + \vec{k}\cdot\vec{v} = \omega_0 + kv_z \tag{3-2}$$

where $\vec{k}$ is the wave-vector. The presence of the pump beam modifies effectively the absorption around the value v_z. If a second counter-propagating beam (probe, $I_{Pr} < I_{sat}$) traverses the cell in the direction $-z$ with a frequency ω_L' close to ω_L it shall interact with atoms having a velocity given by:

$$v_z' = \frac{\omega_0 - \omega_L'}{k'}, \tag{3-3}$$

where k' is this time the probe wave-vector. The absorption of this second beam is proportional to the difference of the atoms populations in the excited and fundamental state in the velocity class space, $N_a(v_z')$-$N_b(v_z')$.

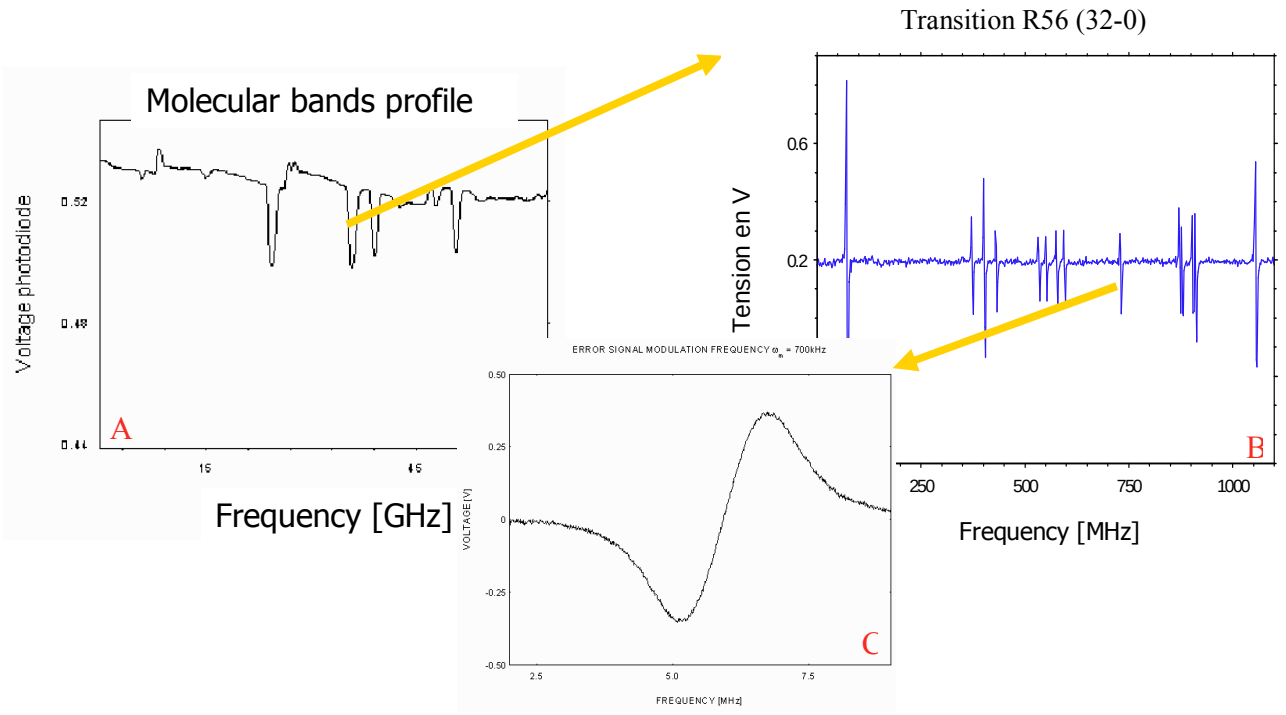

Figure 3–2

Now if the velocities v_z and v'_z are nearly equal and if the frequency difference between the laser beam and the resonance is of the order of the transition linewidth ($\Delta\omega = |\omega_0 - \omega_L| \approx \Gamma$) the absorption in an interval of $\omega_L' = 2\omega_0 - \omega_L$ will be a function of the frequency. We can simply imagine that all molecules having a velocity v_z shall be already in the excited state and that the probe beam won't find any in the fundamental, hence, instead of having its normal peak of absorption at $v_z' \cong v_z$, it shall show a frequency dependent diminution. At the frequency ω_L there will appear a 'Lamb dip' that is to say a resonance with a linewidth close to that of the intrinsic transition for atoms belonging to the v_z velocity class. The case shown in Figure 3–1 is the particular situation where we read the molecules with zero axial velocity. The saturated absorption dip can be created reading any chosen velocity class. We have thus shown that it is possible to use a saturated absorption molecular reference to obtain a narrow resonance for laser locking. We have however to analyse what are the resulting parameters (linewidth, profile) and limits of this reference.

The transition rate γ_{ab} of the molecules is always lower or equal to the decay rate γ of the density matrix of the system. This γ represents the homogenous linewidth, whereas γ_{ab} is the natural linewidth, which is inversely proportional to the lifetime of the transition. The relationship between these two parameters being given by:

$$\gamma = \gamma_{ab} + \gamma_P \tag{3-4}$$

where γ_P is the collision broadening. Saturation is measured thanks to the parameter S which is the ratio between the pump intensity and the saturation intensity:

$$S = \frac{I_P}{I_S} = \frac{\wp^2 E^2}{\hbar \gamma_{ab} \gamma} \tag{3-5}$$

with E being the amplitude of the incident field and $\wp$ the dipole element of the transition from level a to level b.

Saturated absorption has two possible configurations: the quasi-progressive case with weak probe intensity, which we shall examine in detail, and the quasi-stationary case where pump and probe have comparable intensities. In the quasi-progressive case the absorption profile of the pump has approximately the Doppler broadened line-shape divided by a factor $\sqrt{1+S}$. The first of these conditions is always verified for a frequency lock where the laser follows the reference. A saturation translates on the probe beam as a broadening of the parameter γ of the transition that becomes:

$$\gamma_{sat} = \gamma \cdot \sqrt{1+S} \tag{3-6}$$

At the same time it shall create a Lorentzian minimum in the Gaussian shaped linear absorption profile (α_{lin}) of the probe:

$$\alpha_{probe} = \alpha_{lin} e^{-\left(\frac{\omega-\omega_0}{\gamma_{Doppler}}\right)^2} \left[1 - \frac{1}{\sqrt{1+S}} \cdot L\left(\omega - \omega_0, \gamma \frac{1+\sqrt{1+S}}{2}\right)\right] \tag{3-7}$$

where *L* is the Lorentzian function:

$$L(\alpha,\beta) = \frac{\beta^2}{\alpha^2 + \beta^2}.$$

The quasi-stationary case profile is obtained in the same way and is given instead by:

$$\alpha_{probe} = \alpha_{lin} e^{-\left(\frac{\omega-\omega_0}{\gamma_{Doppler}}\right)^2} \frac{1}{\sqrt{1+S}} \left[1 - \left(1 - \frac{\sqrt{1+S}}{\sqrt{1+2S}}\right) \cdot L\left(\omega - \omega_0, \gamma \frac{1+\sqrt{1+S}}{2}\right)\right] \tag{3-8}$$

with the same conventions defined above. As shown by Brillet[3] the determination of the best saturation parameter for the dip linewidth is around unity for the quasi-progressive case, whereas it is closer to 5 for the quasi-stationary conditions.

We have seen that collisions and saturation effects influence the Lamb dip's linewidth; actually, there are other effects to be taken into account in the determination of the linewidth, first of all the time transit broadening. If the beams are narrow the molecule shall traverse them in a time inferior to the decay rate, in this case we shall have broadening of the saturated absorption well. This time transit broadening can be estimated as:

$$\gamma_{TT} = \frac{0.33}{w} \sqrt{\frac{2R_{gas}T}{M}} \tag{3-9}$$

with T temperature of the gas, M the molecular mass in kg of the molecule, and w the beam's waist. Another effect shall be due to residual Doppler broadening linked with the Gaussian beams wavefront curvature, this effect shall engender both a time transit dependent redshift of the absorption signal as well as a further broadening of the transition. A last broadening of the linewidth is present if we introduce a modulation on the beam, this effect shall be expressed by:

$$\gamma_m = \gamma \cdot m \tag{3-10}$$

where m is determined experimentally through measures of the linewidth as a function of the modulation depth. Finally the linewidth of the transition, having taken into account all different broadening contributions, is:

$$\gamma = (\gamma_{ab} + \gamma_P + \gamma_{TT})\sqrt{1+S} \cdot m \tag{3-11}$$

Let us now discuss the simplifications and the residual effects neglected in the above resumed analysis of saturated absorption. The finite extension of the beams shall create a spatial variation of the refraction index, this in turn shall deform the beam Gaussian profile. Relativistic effects concerning the molecule's momentum (the emission or absorption of a photon changes inevitably its momentum hence the velocity is not a null one for the molecules we read) were also left out in the treatment of the saturated absorption. The second order Doppler effect, due to the thermal motion of the molecules not along the beam propagating direction, shall also create a shift of the transition which was neglected. Finally the presence of the laser beam electromagnetic field itself shall influence the energy levels of the molecule and hence the wavelength of the emitted/absorbed light. This effect for two level atoms is of the order of $\delta\nu/\nu \approx 3\ 10^{-23}$ for a laser relative power stability of 10^{-2} and is, indeed, negligible. This is not the case for a three level atom ($\delta\nu/\nu \approx 10^{-15}$) where the pump power shall have to be controlled to avoid significant fluctuations of the frequency.

In the following, we will assume that all other broadenings will be negligible except the ones due to saturation, collision and time transit.

3.2 Molecular references around 1064nm and 532nm

When a stabilised laser is needed as light source I can ask myself which molecular transitions I can use for the stabilisation of a good chosen reliable laser. I have to look for molecules with transition frequencies close to the lasers'. Conversely I can look for a reliable laser in the frequency domain of chosen, narrow, molecular transitions. Actually these searches must be conducted simultaneously leading to couples of good reference usable with good lasers.

A transition between two atomic levels or the excitation of a molecular 'roto-vibrational' spectrum takes place for frequencies equal to $\nu_{ab} = \frac{E_a - E_b}{h}$, for a two-level atom. For an Nd:YAG the laser fundamental frequency is 1064nm which brings the second harmonic in the visible domain (green 532nm). Frequency doubling is a non-linear procedure with a typical single pass efficiency of less than 10%, even for specially constructed doubling crystals, we shall forebear considering molecular transitions requiring higher order harmonics than the second.

With the recent development of high power fibre lasers, the choice of molecular transitions will be enlarged as doubling and tripling laser frequencies will not be the main limitation.

Keeping however in mind the frequency limitation prescribed by the choice of the Nd:YAG laser, today, as the source let us now see which molecules have narrow transitions in their spectra in correspondence to the frequency domains of interest.

3.2.1 Molecular Iodine

Molecular iodine (I_2) has a large number of hyperfine[8][9][10] narrow transitions in the frequency domain around 532nm. As such the use of this reference goes along with frequency doubled YAG lasers, which are now commercialised by several manufacturers with good performances.

Molecular iodine is a strongly absorbing molecule with a linear absorption coefficient of α=0.6 / (m*Pa) which is, therefore, intrinsically adapted for single or multi-pass beams in a cell, no intra-cavity configurations is necessary.

Iodine is an extremely reactive element like all halogens, thus it shall attack all metals but is inert as far as oxides and transition elements are concerned. In particular it doesn't attack glass and is most often sealed in glass cells.

There are several molecular bands with isolated narrow transitions in the 532nm domain. In particular the R(56) 32-0 band. This band a_{10} line is in particular a suggested frequency standard for 532nm by the "Bureau International des Poids et Mesures"[10]. The typical linewidth for Iodine hyperfine transition is around the hundred of kHz. In particular for a_{10} a width of 175kHz has been reported by Hall et al.[11] with a pressure broadening measured to be: 100MHz/Torr @ 300K while the line displacement is around 170 kHz/Torr.[8] The saturation intensity can be expressed as I_{sat} = 300 + 100*P W/m^2. The best results, experimentally obtained, showed Allan variances between 3Hz and 0.3Hz for integration times above 1000s. To sum up, this molecule has excellent properties as far as the linewidths are concerned and is suitable for a doubled YAG laser where it requires a few mW of green power for frequency locking.

3.2.2 Other molecules

C_2H_2

Acetylene is a gas with a very weak absorption in the frequency domain around 1064nm. Its linear absorption coefficient is of the order of 1.9 10^{-7} /(cm Torr).

Acetylene is not reactive at low pressures but is explosive above 760Torr. At this pressure the linear absorption is close to 10^{-4} /cm (absorption of the order of 10mW for a 1m cell from a laser power of 1W). In order to have an acceptable signal to noise ratio an intra-cavity multi-pass technique, such as described in Section 4.4, is required.

The molecular line closest to the 1064nm mark is the R(12) transition at 1064.561 nm, saturation being obtained for the laser intensity of 5 W/cm^2.[12] Its Doppler linewidth is 680MHz. A saturated absorption or dispersion configuration would be necessary to prevent enlarging the laser intrinsic linewidth.

I have found no account in literature of a lock on this transition with an Nd:YAG laser, but excellent locking stabilities have been obtained for the overtone transition P(16) $\nu_1+\nu_3$ @1.5µm Edwards[13] and P(11) $\nu_1+3\nu_3$ @790nm Dubé[14]. In both cases Allan variances were better than 10^{-14} over time stretches of over 5000s. While these results are encouraging and the transition in the R(12) bands looks promising, its feasibility for space experiments has to be considered with special care.

C_2HD

Much like acetylene its mono-deuterated counterpart is a weakly absorbing gas in the neighbourhood of 1064nm.

The P(5) bans has a linear absorption coefficient of $\alpha = 8.8\ 10^{-7}cm^{-1}Torr^{-1}$, again an intra-cavity configuration is necessary to have adequate absorption signals. In the Ma[15] experiment the intra-cavity power necessary to obtain saturation was of the order of 50W for a corresponding gas pressure of the order of the mTorr. The overtone transition of band P(5), $\nu_1 + 3\nu_3$, has already been used by Ye et al.[16] to lock the frequency of a Nd:YAG @ 1064.470 nm. The best Allan variance results were of the order of 3Hz @ 800s. In summary, the acetylene molecules possess intrinsic narrow linewidth, and do not require frequency doubling, but their weak absorption and their high saturation intensity make them less attractive than iodine.

CO_2

Another molecule absorbing in the neighbourhood of 1064nm is carbon dioxide[17], which can be used at room temperature. The pressure necessary for detectable absorption on a 1m optical path in the gas is of 250Torr not advisable in view of pressure broadening and shifting. The closest transition to the Nd:YAG wavelength is the line @ 1064.5050nm identified with the P(6) transition (2 0^0 2) to (2 0^0 3) with intrinsic linewidth of 170Hz and pressure broadening coefficient measured by Inbar et al.[18] of 12.3kHz/Torr.

Cs_2

Another molecule with hyperfine transitions close to 1064nm is molecular Caesium (Cs_2). It is necessary to bring the Caesium to a temperature close to 300℃ [20] to have an absorption of 0.01 /cm as reported by Orlov et al.[19] Molecular Caesium is inert, not so its atomic counterpart which, like all alkali metals, is extremely reactive to all halogens; unlike

Iodine Caesium cannot accommodate glass cells. The transitions in the vibrational $A^1\,\Sigma^+_g \rightarrow A^1\,\Sigma^+_u$ band have frequencies comprised between 880 and 1100nm and include lines around 1064nm. These transitions have linewidths close to 20MHz: the narrowest transition @1064nm reported by Inbar et al.[21] has an intrinsic linewidth of 4.7MHz. On this transition a stability of 3kHz is reported in a single pass. A saturated dispersion intra-cavity experiment is also possible but doesn't better results by more than a factor 2. The large linewidth of the transition is obviously the first limiting factor of this molecule.

3.2.3 Reference choice

The principal characteristics of the above mentioned molecules are summed in Table 3-1 for ease of consultation. With all the above arguments to support our choice we decided to realise a long term stable standard locked on Iodine and to validate its performances on an identical system. This molecule has been extensively studied for many decades; it gives rather narrow linewidths in the region reached by a doubled YAG laser. The request to have a frequency-doubled laser could be a drawback in the space experiments unless monolithic benches can be designed. Furthermore, the Iodine system will allow us to calibrate the frequency drifts of a ULE cavity stored under vacuum for more than 10 years.

Molecular Reference	Linear Absorption [cm^{-1} $Torr^{-1}$]	Intrinsic Linewidth [kHz]	Best Allan variance [Hz] @1000s
C_2H_2	$1.9\ 10^{-7}$	100	3
C_2HD	$8.8\ 10^{-7}$	100	3
CO_2	$7.2\ 10^{-3}$	170	-
Cs_2	0.01 cm^{-1} @300℃	4700	3000
I_2	82	175	0.3

Table 3-1

3.3 Modulation Transfer

The lock on the Iodine molecule is obtained through a homodyne technique called modulation transfer. In this technique we chose the intensities of the pump and probe beam to be in the quasi-progressive state, in our particular configuration the probe beam is the first order beam created by an AOM shifter (more details in the experimental section).

The pump beam is modulated at an RF frequency (typically chosen to be of the order of, or lower, than the intrinsic transition's linewidth). The probe beam acquires the modulation through four-wave mixing in the gas cell, and is then detected on a photodiode. A subsequent homodyne detection yields the error signal. The separation of the pump from the probe is obtained thanks to a polarisation isolation (the pump is polarised along the p direction whereas the probe is in the s state of polarisation) as well as the frequency shift induced by the AOM. This shift, which assures the absence of interference between the two beams on the polariser and detector, leads, as seen in 3.1.1, to selecting molecules which don't belong to the zero velocity class.

Since the probe beam is not directly modulated this technique is insensitive to the linear absorption of the molecular band profile. This is very important because it avoids offsets in the locking point. Much as it is insensitive to linear absorption this technique is also immune (1st order) to amplitude modulation noise, once again thanks to the acquired nature of the probe's modulation, as seen thanks to the simulation.

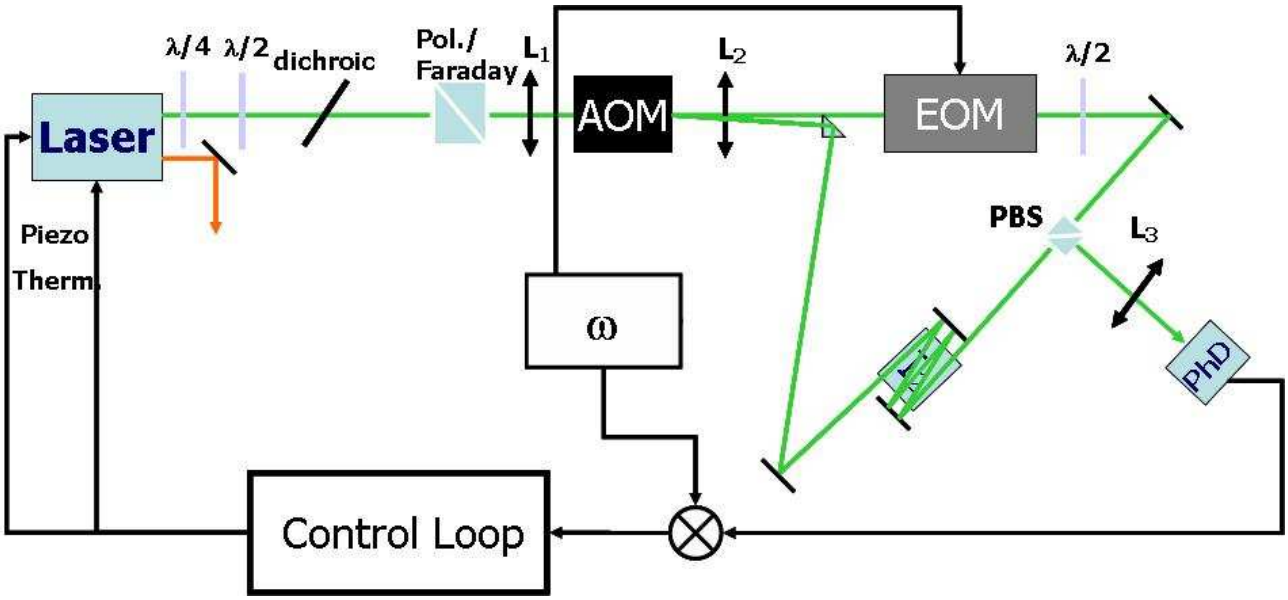

Figure 3–3

Error Signal

To understand how the error signal for the Modulation transfer in our configuration is created let us follow the calculations of Camy et al. [4] and Shirley [6]. The saturating field propagating along the z axis with laser frequency ω, wave number k, phase φ and modulation frequency ω_m can be expressed as:

$$E_S(\omega) = E_{0S} \cdot e^{i\omega t} \cdot e^{iA\sin\omega_m t} \cdot e^{ikz+\varphi} \tag{3-12}$$

which can be also written, if we remember the development of the exponential of the sinus in function of the spherical Bessel functions, as:

$$E_S(\omega) = E_{0S} \cdot e^{i\omega t+ikz+\varphi} \cdot \left(J_0(A) + J_1(A)\left(e^{i\omega_m t} - e^{-i\omega_m t}\right) + \ldots\right) \tag{3-13}$$

higher order harmonics having been neglected. The counter propagating probe beam shall have the expression:

$$E_P(\omega) = E_{0P} \cdot e^{i(\omega+\Delta)t-kz} \tag{3-14}$$

where Δ is the frequency shift given by the AOM. These two beams shall give rise to a macroscopic non-linear polarisation that shall radiate a field having the form:

$$E_R(\omega) \propto e^{i(\omega+\Delta)t-kz}\left(\mathrm{E}_R(0) + \mathrm{E}_R(1)e^{i\omega_m t} + \mathrm{E}_R(-1)e^{-i\omega_m t} + \ldots\right) \tag{3-15}$$

where the amplitudes of each harmonic can have a complex value. In particular following four wave mixing of two arbitrary harmonics of the pump beam and the probe field we shall have, for the radiated field, two emitted fields which interfering shall give a heterodyne beat at the module of the harmonics difference times the modulation frequency, on the photodiode. This shall yield an error signal centred at the frequency ω-ω_0+Δ/2. If we stop at the first order following Shirley's calculations with μ the transition dipole moment, ω_0 the transition's resonance frequency, γ_l the density matrix elements and $S = 4\mu^2 E_S^2/h^2\gamma_1\gamma_2$ the saturation factor. And if we put $Q = \sqrt{1+S}$, the normalised detuning $d_j = (\omega - \omega_0 - j\omega_m)/\gamma_2$ the Lorentzian $L_j = \left(1+d_j{}^2\right)^{-1}$ and $D_j = d_j L_j$, the signal pattern is given by:

$$ES = \frac{1}{2}\mathrm{K}SJ_0(A)J_1(A)\cdot\left[\begin{array}{l}\left(L_1 - L_{1/2} + L_{-1/2} - L_{-1}\right)\cos(\omega_m t+\varphi) + \\ \left(-D_1 + D_{1/2} + D_{-1/2} - D_{-1}\right)\sin(\omega_m t+\varphi)\end{array}\right] \tag{3-16}$$

The exact error signal expression would require the summing of all higher order harmonics as well and is given by the Camy et al.[4] paper.

Simulation

A MATLAB simulation of the error signal obtained by Shirley[6] and expressed in Equation (3-16) was developed with the help of M. Taubman of PNNL.

This routine has allowed us to ascertain the behaviour of the Modulation Transfer for different modulation frequencies, demodulation phase values and modulation depths.

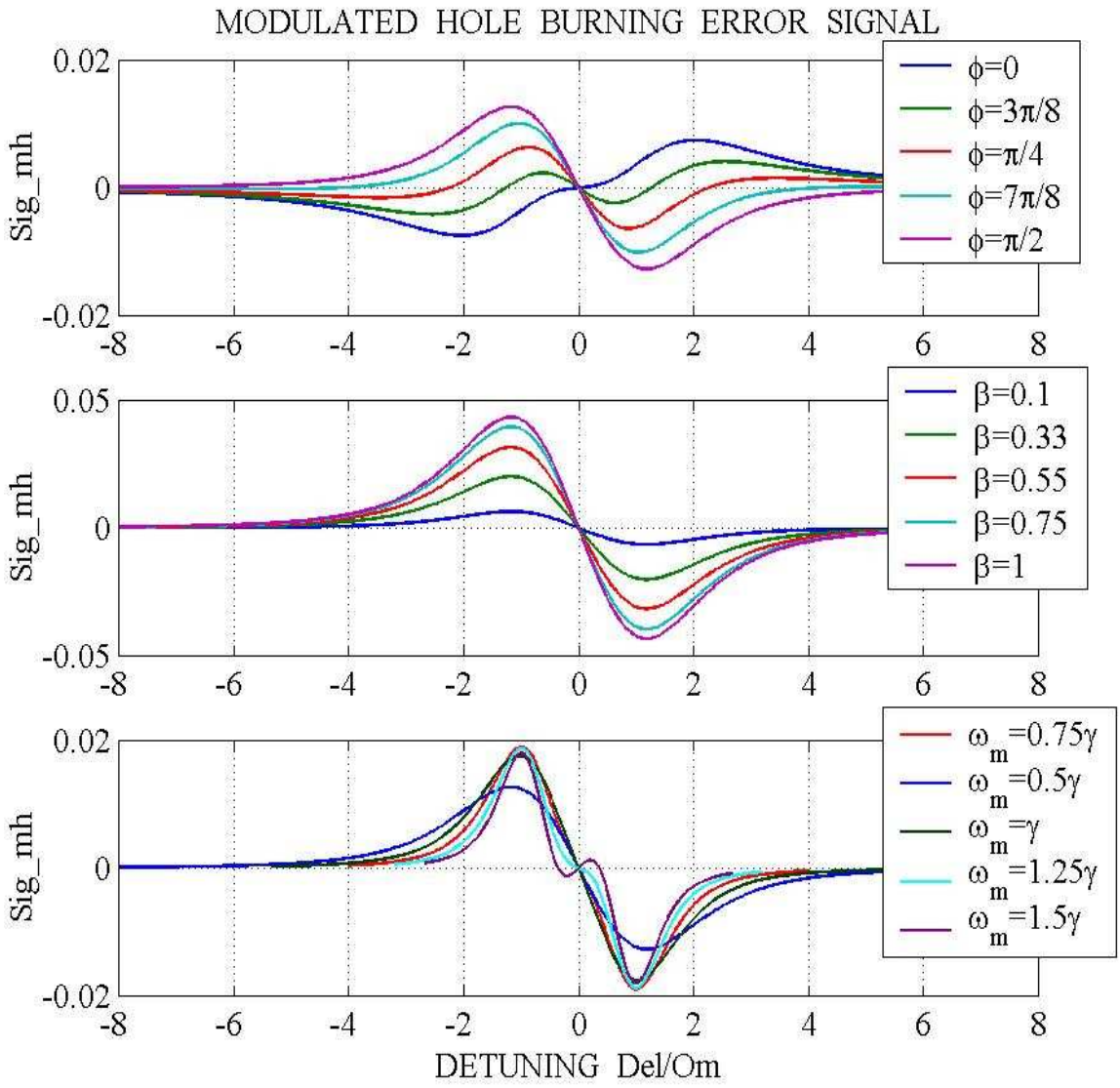

Figure 3–4

In particular we have used this simulation to determine how the amplitude and line-shape of the signal change with regards to the above mentioned parameters to be able to optimise the locking error signal, see Figure 3–4. This program also computes the expected theoretical linewidth for measured experimental conditions (temperature of the cell's cold point etc) and estimated, user introduced, parameters of the saturation and modulation broadening constants.

For the sensitivity of the technique to amplitude modulation we can trace the profile with both the first order and the second order modulation hole burning effect as shown in Figure 3–5. For the figure we can see that the locking point and the slope in the central part of the error signal to not change with the amplitude modulation. We have thus verified that the Modulation transfer technique is effectively amplitude modulation independent at the first order.

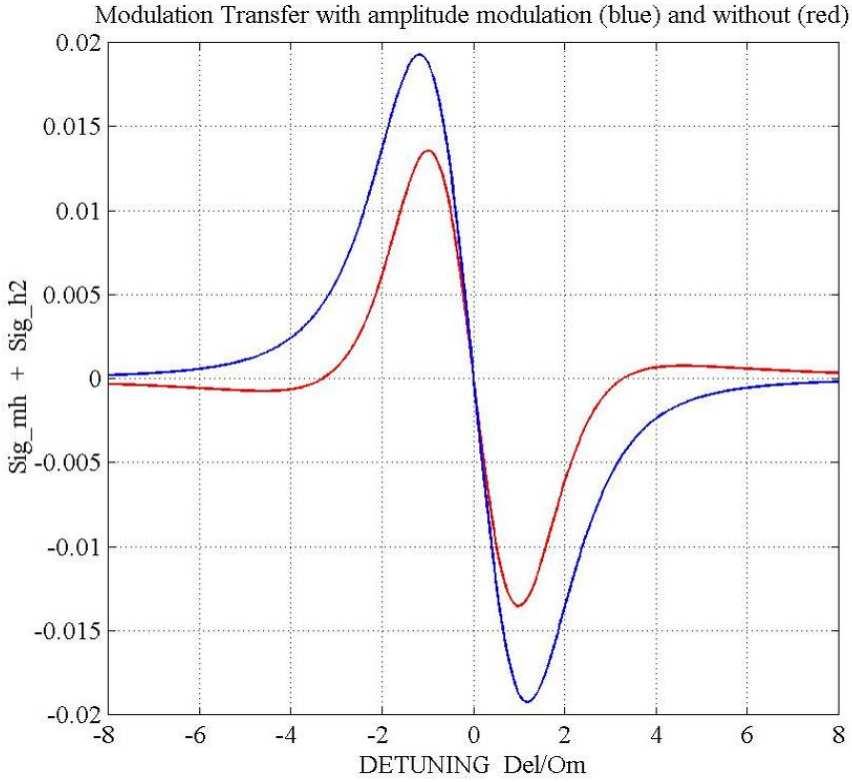

Figure 3–5

4 Mechanical references

After having analysed molecular references we now pass to a few possible techniques to implement cavity locks in space experiments, special attention is given to the correction or shielding of thermal deformations and to the possibility of obtaining 'exactitude' by controlling actively the length of the resonator.

4.1 Fabry-Perot Resonators [48]

A Fabry-Perot resonator is a frequency reference; it has a series of resonance frequencies given by his length. Let us now consider a triangular cavity as the one shown in Figure 4–1. First of all we can define a typical frequency of the cavity, or FSR, as the inverse of the time that light would need to traverse the cavity, or in formulas: $FSR = c/2L$. With c we indicate the speed of light, as customary, and with $2L$ the optical path in the cavity. Actually the light shan't be transmitted after a single pass into the reference but rather after a number of round trips, dependent from the mirror's reflectivities. The cavity itself shall have a proper reflectivity and transmissivity. In particular referring once again to Figure 4–1 we shall have that:

$$E_R = \Re \cdot E_I$$
$$E_T = \Im \cdot E_I$$

The determination of $\Re$ and $\Im$ are fairly immediate but we have to define a convention for mirrors reflectivities and transmissivities. In particular we choose the convention for which we have that all the mirror's reflectivities (r_i) are real and transmissivities (it_i) are complex as seen below. With this conventions the transmitted fields have a $\pi/2$ phase lag with respect to the incident field.

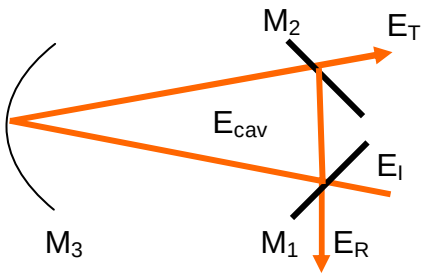

Figure 4–1

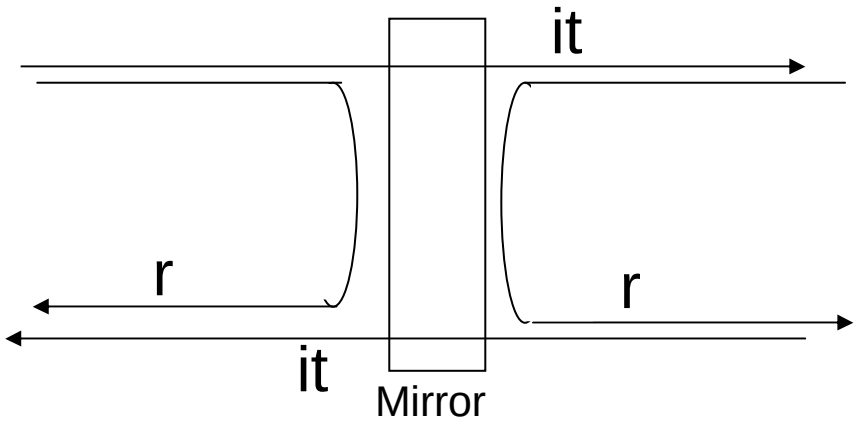

Figure 4–2

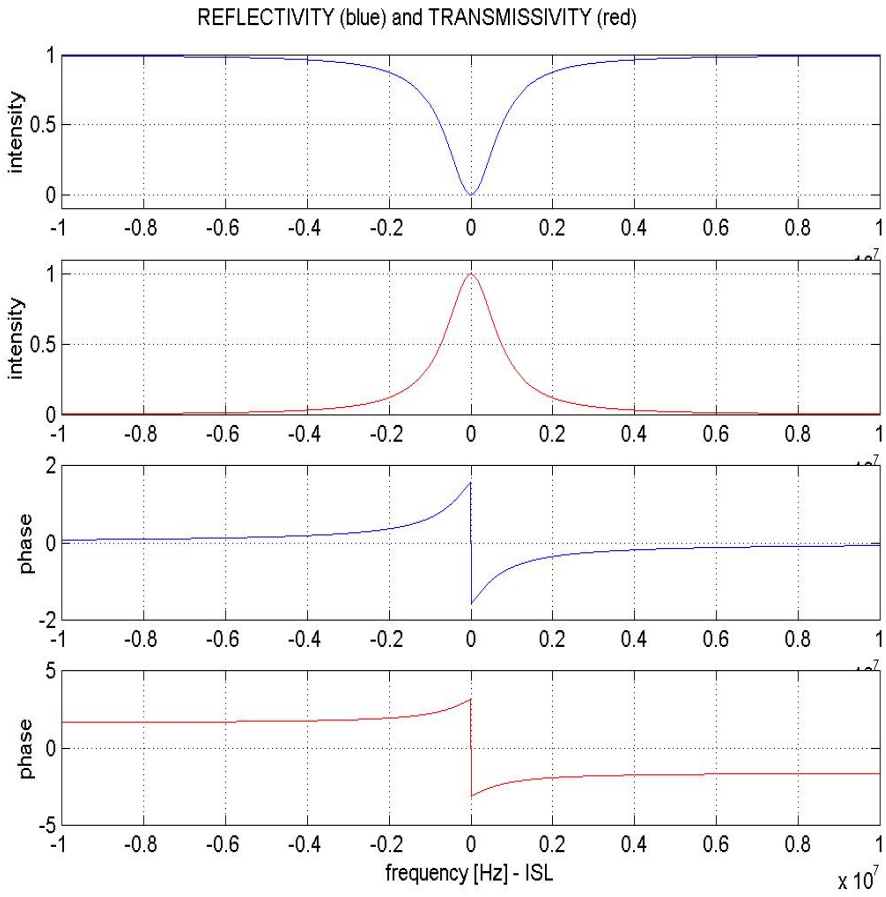

Figure 4–3

Let us now observe that the reflected and transmitted fields shall be given respectively by:

$$E_R(\nu) = r_1 \cdot E_I + it_1 r_2 r_3 \cdot E_{cav} \cdot e^{i2\pi\nu\tau}$$
$$E_T(\nu) = it_2 r_3 \cdot E_{cav} \cdot e^{i2\pi\nu\tau}$$

where $\tau = 1/FSR$ and the field in the cavity shall have the form:

$$E_{cav}(\nu) = \frac{it_1 E_I}{1 - r_1 r_2 r_3 \cdot e^{i2\pi\nu\tau}} = S(\nu) E_I \tag{4-1}$$

where the parameter S(ν) is called storage coefficient of the cavity and is no more than the ratio between the field stocked into the cavity and the field incident on the same. The square of the modulus of S(ν) shall obviously be the ratio between the intensities of stocked and incident light.

This shall yield for the cavity's reflectivity:

$$\Re(\nu) = r_1 - \frac{t_1^2 r_2 r_3 \cdot e^{i2\pi\nu\tau}}{1 - r_1 r_2 r_3 \cdot e^{i2\pi\nu\tau}} \tag{4-2}$$

and transmissivity:

$$\Im(\nu) = \frac{-t_1 t_2 r_2 r_3 \cdot e^{i2\pi\nu\tau}}{1 - r_1 r_2 r_3 \cdot e^{i2\pi\nu\tau}} \tag{4-3}$$

Their intensity and phase profiles are plotted in Figure 4–3.

For each of the terms giving $e^{i2\pi\nu\tau} = 1$ we have a resonance, this means that for all values given by $\nu_{las} = 1/\tau \cdot n = n \cdot FSR$ we shall have a resonance peak. The proper frequency FSR is therefore the distance between different adjacent resonances in the cavity's spectrum. We now wish to determine the width of these resonances. Let us consider a reference linewidth of δν with the caution that it be much smaller than FSR. The stockage parameter this time is:

$$S(\nu) = \frac{it_1}{1 - r_1 r_2 r_3 \cdot e^{\frac{2i\pi\cdot\delta\nu}{FSR}}} \tag{4-4}$$

If we express it in terms of the intensities instead of the fields we shall have:

$$|S(\nu)|^2 = \frac{t_1^2}{(1 - r_1 r_2 r_3)^2 + 4 r_1 r_2 r_3 \sin^2\left(\frac{\pi \cdot \delta\nu}{FSR}\right)} \tag{4-5}$$

and if we approximate the sinus function with its argument and express $S^2(\nu)$ in function of its maximum value we get:

$$|S(\nu)|^2 = S_{Max}^2 \frac{1}{1+\left[2F\frac{\delta\nu}{FSR}\right]^2} \quad (4\text{-}6)$$

where the Finesse *F* is defined as:

$$F = \frac{\pi\sqrt{r_1 r_2 r_3}}{1-r_1 r_2 r_3} \quad (4\text{-}7)$$

in function of the mirror reflectivities; as we have seen it is linked to the number of turns of the light in the cavity before transmission. From Equation (4-8) we also have that the Full Width at Half Maximum of the resonance peak is given by:

$$\delta\nu_{FWHM} = 2f_P = \frac{FSR}{F} \quad (4\text{-}9)$$

which shows how, for high values of the reflectivities (i.e. Finesse=10^6 and FSR=$500\cdot10^6$Hz, cavity length 2L=60cm) we can have cavity linewidths of the order of the 500Hz.

Coupling and pole frequency

Having defined the pole frequency f_P of the resonator and the Free Spectral Range we can rewrite, having defined the coupling ζ_0 obtained from the first order approximation for the complex reflectivity of the cavity (p are the cavity losses, see Equation 4-13) as:

$$\zeta_0 = \frac{r_1-(1-p)r_2 r_3}{1-r_1 r_2 r_3}, \quad (4\text{-}10)$$

both Equation (4-2) and Equation (4-3) as:

$$R(\delta\omega) = \frac{\zeta_0 + i\frac{\delta\omega}{f_P}}{1+i\frac{\delta\omega}{f_P}} \quad (4\text{-}11)$$

and

$$T(\delta\omega) = \frac{\sqrt{1-\zeta_0^2}}{1+\frac{i\cdot\delta\omega}{f_P}} \quad (4\text{-}12)$$

respectively ($\omega=2\pi\nu$, $\delta\omega=2\pi\delta\nu$ is the detuning). It has to be observed that with p in the expression for ζ_0 we indicate the losses of the cavity which are given by the Energy conservation expression:

$$r^2 + t^2 + p = 1 \quad (4\text{-}13)$$

A cavity's coupling can vary between -1 and 1 and is optimal for $\zeta_0=0$. For values of the coupling between -1 and 0, the cavity is over-coupled and the light is more or less

absorbed in the cavity, whereas if ζ_0 is greater than zero then the cavity is said to be under-coupled and the light is partially reflected off the cavity.

If we observe the shape of the expressions for the cavity's transmissivity we see that the FP acts as a frequency low-pass filter with cut-off frequency given by f_P, this explains why optical resonators act as frequency filters, the presence of this cut-off frequency is linked to the storage time.

Waist and Rayleigh distance

Other significant FP parameters are the waist of the cavity, i.e. the waist of the beam with optimal spatial coupling into the reference, and its Rayleigh distance, which is the distance after which the waist of a beam has changed by a factor $\sqrt{2}$. In a stable optical resonator the ratio between the radius of curvature of the end mirror (in our case M_3) and the semi-perimeter (L) of the beam's optical path in the cavity must always be greater than 1, $R \geq L$. As long as this condition is verified we can express the cavity's Rayleigh distance as:

$$z_R = \sqrt{L(R-L)} = \frac{\pi \cdot w_0^2}{\lambda} \tag{4-14}$$

Subsequently the waist shall be equal to:

$$w_0^2 = \sqrt{\frac{z_R \cdot \lambda}{\pi}} \tag{4-15}$$

λ is the laser wavelength. The waist for a triangular cavity like the one shown in Figure 4–1 shall be placed between the two plane entrance and exit mirrors. The adaptation of the beam's waist to the cavity's ensures a good coupling of the light into the reference.

Higher order modes.

The resonance frequency determination seen above was obtained for a TEM_{00} Gaussian beam. But higher order modes TEM_{mn} shall also have their own resonance frequencies. For a triangular cavity the resonance frequencies have been determined by Collins et al.[22][39] both for odd and even m modes. The triangular configuration (much as any cavity with an odd number of mirrors) has a privileged plane. The modes along the principal direction (m even) have the same auto-consistence equation given for the linear configuration which requires that the phase variation be an integer multiple value of 2π:

$$2\pi\nu_{EVEN}\tau - 2(m+n+1)\arccos\sqrt{1-\frac{L}{R}} = 2\pi q \tag{4-16}$$

where L is the semi perimeter of the cavity, R the radius of curvature of the end mirror and q the so called order of the FSR. This gives for the resonance frequency expression for even m modes:

$$\nu_{EVEN} = FSR\left[q + \frac{1}{\pi}(m+n+1)\arccos\sqrt{1-\frac{L}{R}}\right] \quad (4\text{-}17)$$

In the 's' or secondary direction (m odd), instead, the modes' auto-consistence condition changes. The modes with odd m are in fact asymmetric with respect to the optical axis of the cavity's plane. A further π phase lag is necessary to have constructive interference in the reference. The auto-consistency equation becomes:

$$2\pi\nu_{ODD}\tau - 2(m+n+1)\arccos\sqrt{1-\frac{L}{R}} + \pi = 2\pi q \quad (4\text{-}18)$$

which in turn shall give for the resonance frequency:

$$\nu_{ODD} = FSR\left[q + \frac{1}{2} + \frac{1}{\pi}(m+n+1)\arccos\sqrt{1-\frac{L}{R}}\right] \quad (4\text{-}19)$$

The odd n modes are thus shifted a half FSR away from their even counterpart and a triangular cavity shows therefore fewer intrinsically degenerated modes than its linear counterparts.

Reference noise contributions

For Fabry-Perot resonators the main reference noise contributions are linked to thermal deformations of the reference, which require ultimately temperature control at the μK level to have sufficient stability for long term performances. For this reason ULE is preferred thanks to its low linear expansion coefficient ($\alpha=10^{-9}$/K).

In the high frequency range thermal noise can give a significant contribution in these conditions monolithic cavities are to be preferred.

Another contribution shall come from the radiation pressure induced by the laser power built up in the cavity, when the cavity mirrors are suspended. The power in the cavity shall be F/π times the incident Power if we suppose null absorption.

4.1.1 Temperature stabilised FP: COREs and thermal screens

We have seen in the previous paragraph that a thermal stabilisation of a mechanical reference is necessary to obtain adequate long term stabilisation. This doesn't solve the eventual problem of precision but should be sufficient to assure adequate long term stabilities for most space applications.

To stabilise the temperature of the Fabry-Perot we can cool the cavity to cryogenic temperatures typically below 5K. This offers increased temperature stabilities because at this low temperatures for dielectric materials the linear expansion coefficient (α) decreases like T^3 while thermal diffusivity and the ratio κ (heat conductivity) to α increase significantly

with respect to the room temperature conditions. (Seel et al.[23][24]) This not only guarantees lower sensitivity to temperature variations but also better isolation with respect to laser internal heating and greater precision in the temperature stabilisation. Long term stabilities of the order of 0.6Hz at 10^4s have been reported[25], with much better performances of the order of 30mHz @ 1-60s. Unfortunately while cryogenic resonators' performances are excellent even on the long term the energy budget of most space missions could hardly cover the necessary output for this kind of experimental set-up. Furthermore the mean time between failures of cryogenic systems seems to be below the 5 year mark requested for LISA. In the case of space experiments were the aim is to have the longest possible MTBF given the extraordinary costs of each mission such a solution seems risky.

In fact, independent studies at Goddard SFC, University of Florida and Laser Zentrum Hannover, have shown that it is possible to have below the µK temperature variations on a FP resonators using exclusively passive thermal shielding. This is ideal for space mission as it doesn't impact on the energy budget and can, depending on construction also serve as vibration isolation.

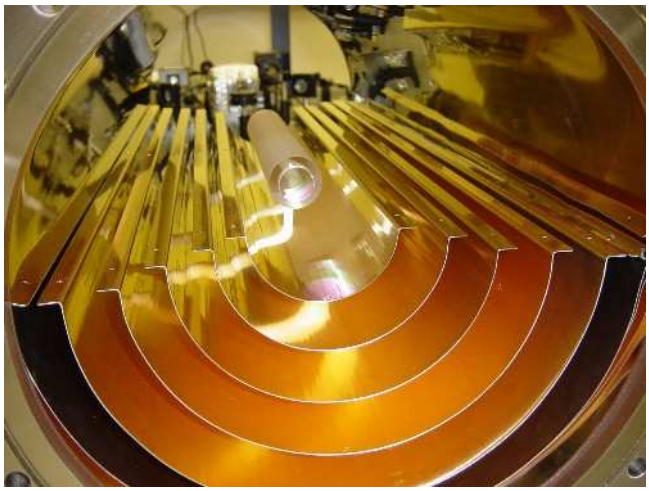

Figure 4–4 Image courtesy of J. Camp, Goddard Space Flight Centre

The solution these teams have been able to produce is a series of concentric and interlocking aluminium gold coated shields to be inserted in the FP vacuum tank. With 5 isolation stages the µK stability on the internal FP is obtained. Since the cost of such a material is hardly negligible studies at University of Florida have been made to obtain the same performances with copper coated screens (Ian Thorpe Private communication L. Mondin LISA Symp. V).An active temperature control might also be a solution to the temperature stabilisation problem. This would be badly adapted to space experiments due to the energy budget limitations. With such a configuration, on the other hand, it might be

possible to gain on the precision of the measure having chosen an absolute reference to control the length of the cavity. A brief overview of techniques to obtain an active length control is presented in Section 4.4.

4.2 Tilt Locking

4.2.1 Single pass

Tilt Locking is a DC locking technique proposed for the first time by Grey in 1999[26].

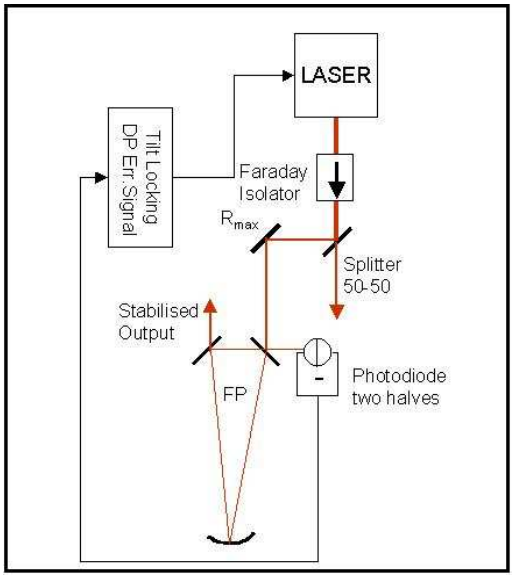

Figures 4–5 and 4-5b

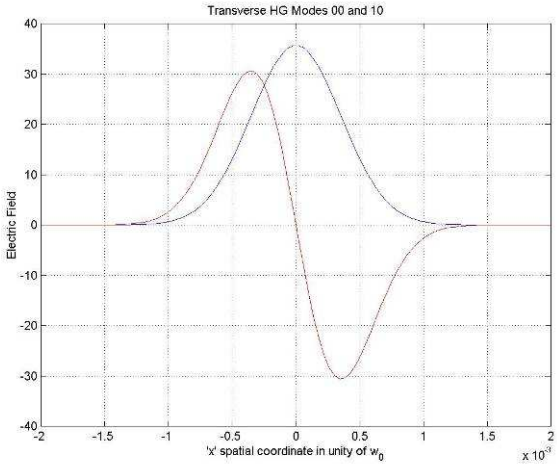

In this technique the property of a cavity of expanding the input field in the bases of the TEM Gaussian Modes is used to create a reference beam which will then interfere with the carrier on a split photo-detector. In particular a small misalignment of the input beam on the Fabry-Perot resonator will generate an odd mode of the first order (i.e. TEM_{10} or TEM_{01} depending on the direction of the misalignment). Errors in the adaptation of the beam size to the cavity's intrinsic waist shall result, instead, in an even mode contribution, these too

could ideally be used to lock the laser frequency as proposed by Shaddock[27] in his thesis work. In the case of Tilt Locking then it is the TEM modes of the first order that are used as reference beams while the TEM_{00} will be the carrier. If the generated TEM of the first order is not degenerated with the TEM_{00}, when the latter is resonant with the Fabry-Perot, the former will be completely (in the ideal case) reflected. The spatial profiles of the two modes in exam in the one-dimensional case are shown in 4-5b and 4-7.The interference of these two modes on the two different halves of a split photodiode will produce, through subtraction of the two contributions, the error signal. This interference is of course influenced by the phase difference between the modes, which in its turn depends from both the type of misalignment introduced and the distance of the detector, as will be shown in the analytical extraction of the error signal. Additionally the carrier will experiment a phase shift of $\pi/2$ around the resonance which will assure the efficiency of the method. The interference on the two different halves will therefore vary with the laser frequency.

As will be shown analytically later, while angular displacements induce phase shifts in the near field condition, shifts will only cause a phase shift in the far field condition. If the photodiode is close to the exit mirror, as is advisable to reduce beam jitter noise effect, we are in the near field condition; it will therefore be the tilt of the beam that shall give an error signal.

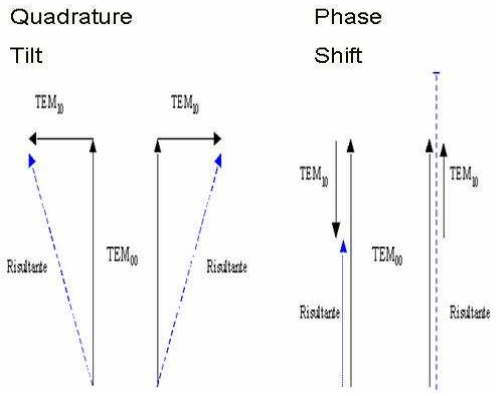

Figure 4–6 Tilt and Shift effects on the two photodiode's halves.

In particular as shown by Figure 4-6 the presence of a shift will result in a variation of the intensity on the photodiode's halves which will not yield an error signal. A tilt shall conversely give a frequency dependent phase variation and thus an error signal. This technique is very attractive for space applications given its lack of active components (EOM and demodulation electronics) and is analogous in this to the more complex, polarisation based, Hänsch-Couillaud[28] and orthogonal mode analysis (Harvey[40]).

Since the error signal is obtained through a misalignment we expect the lock point and the error signal line-shape to be very sensitive to all beam jitter motions. This could indeed be a problem in payloads which are subjected to vibration as is the case in space experiments. To reduce as much as possible the beam jitter noise the solution found by Shaddock et al.[26] was the so called Double Pass Tilt Locking. Before explaining the principle of Double Pass Tilt Locking let us see more in detail how the error signal is obtained for the single pass Tilt Locking.

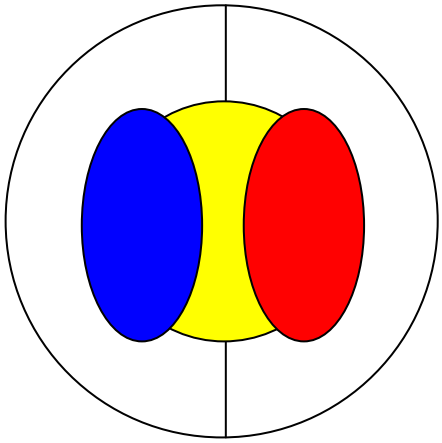

Figure 4–7 Overlap TEM_{00} and TEM_{10}

Error Signal extraction.

In all our calculations a triangular Fabry-Perot cavity with entrance mirror 1, exit mirror 2 and end mirror 3 is used. The low finesse of this cavity is assumed to be 1,000 and its high finesse 30,000, as is the case for the reference used in our laboratories. Let us now choose a reference frame in which the z axis is along the beam's propagation direction, x is parallel and y perpendicular to the optical table. We suppose the laser output a pure TEM_{00} mode, which will be called E_{00}, and will be injected into the FP with an angular displacement (Tilt) of an angle α and a linear displacement on the entrance mirror (Shift)

called *a*. Both of these effects will cause a phase term to appear in the electromagnetic field expression. In particular the tilt, for small values of α, shall give:

$$\Phi_{tilt} = \frac{2\pi\alpha x}{\lambda}, \tag{4-20}$$

whereas in the same conditions the shift will result in:

$$\Phi_{shift} = \frac{2\pi \cdot iax}{\pi w_0^2} + \frac{2\pi}{\lambda}\frac{z^2}{z_R^2}\frac{ax}{\sqrt{z^2 + z_R^2}} \tag{4-21}$$

In these expressions w_0 is the beam's waist and z_R is the Rayleigh parameter. Having considered that:

$$E = E_{00} \cdot e^{i\Phi_{tot}}$$

and having developed in series to the first order, for small values of *a* and α, we have the following expressions of the electromagnetic field, for a tilt:

$$E_{tilt} = E_{00} + i\frac{\pi\alpha \cdot w(z)}{\sqrt{2}\lambda} \cdot E_{10}, \tag{4-22}$$

and for a shift:

$$E_{shiftt} = E_{00} + \left[\frac{i\pi a \cdot w(z)}{\sqrt{2}\lambda R(z)} - \frac{a}{\sqrt{2}w(z)}\right] \cdot E_{10}. \tag{4-23}$$

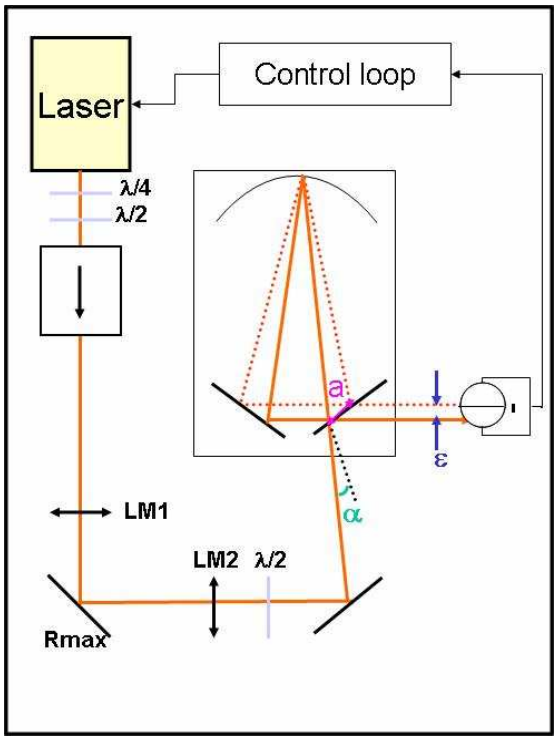

Figure 4–8

In Equations (4-22) and(4-23), *R(z)* is the beam curvature in function of the coordinate *z*, E_{00} and E_{10} are the electromagnetic fields of the TEM modes of the zero and first order respectively. Along the *x* direction, the one of the tilt, the TEM modes can be written as:

$$E_{00} = \frac{2}{\pi}\frac{1}{w(z)^2}\cdot e^{-\frac{x^2}{w_0^2\left(1+z^2/z_R^2\right)}}\cdot e^{\frac{i\pi}{\lambda}\frac{zx^2}{z^2+z_R^2}}\cdot e^{-i\cdot atg\left(\frac{z}{z_R}\right)}\cdot e^{i\omega\cdot t} \tag{4-24}$$

and

$$E_{10} = E_{00}\cdot\frac{\sqrt{2}x}{w(z)}\cdot e^{-i\cdot atg\left(\frac{z}{z_R}\right)} \tag{4-25}$$

respectively, where the term $atg\left(\frac{z}{z_R}\right) = \Phi_{Gouy}$ is known as the Gouy phase shift. Now the reflected field shall have the following form based on the above obtained expressions for the incident field given by Equation (4-24) and Equation (4-25) :

$$E_{Refl} = R(\omega)\cdot E_{00} + A(a,\alpha,z)\cdot R(\omega_{10})\cdot E_{10}, \tag{4-26}$$

where with ω_{10} we indicate 2π the (1,0) mode frequency, of a cavity of semi-perimeter *L* and end mirror radius of curvature *R*, given by:

$$\omega_{10} = \omega\cdot\left(1+a\cos\left(\sqrt{1-\frac{L}{R}}\right)\right) = \omega(1+\beta). \tag{4-27}$$

With $R(\omega)$ and $R(\omega_{10})$ we indicate the complex reflectivity of the reference cavity at the given frequencies. This reflectivity can be written as either:

$$R(\omega) = r_1 - \frac{t_1^2 r_2 r_3 e^{2\pi\omega\tau}}{1 - r_1 r_2 r_3 e^{2\pi\omega\tau}} \tag{4-28}$$

or, equivalently, if we suppose $r_3=1$, having defined the coupling ζ_0 the detuning δω and the linewidth $f_P=FSR/F$ as shown in Section 4.1,

$$R(\delta\omega) = \frac{\zeta_0 + i\frac{\delta\omega}{f_P}}{1 + i\frac{\delta\omega}{f_P}}.$$

The usual conventions are used in Equation (4-28): r_1, r_2 and r_3 are the reflectivities of each the three mirrors, it_i their transmissivity and τ is the inverse of the Free Spectral Range of the cavity. The power incident on the photodiode in function of the *x* coordinate will then be equal to:

$$P(x) = 2 \cdot E_{00}^2 R(\omega)^2 + 2 \cdot E_{10}^2 R(\omega_{10})^2 \frac{1}{2}\left[\frac{i\alpha\pi \cdot w_{inc}}{\lambda} - \frac{a}{w_{inc}}\right]^2 + \\ + \left(\left(E_{00} R(\omega) \cdot E_{10}^* R(\omega_{10})^*\right) \frac{1}{\sqrt{2}} \left[\frac{i\alpha\pi \cdot w_{inc}}{\lambda} - \frac{a}{w_{inc}}\right]^2 e^{-i\Phi_{Gouy}} + c.c. \right) \quad (4\text{-}29)$$

which we can expressed as:

$$P(x) = A(\omega,z) \cdot e^{-2x^2} + B(\omega,z,a,\alpha) \cdot x^2 e^{-2x^2} + C(\omega,z,a,\alpha) \cdot x e^{-2x^2} \quad (4\text{-}30)$$

with:

$$A = \frac{2}{\pi} \frac{1}{w_{inc}} R(\omega)^2$$

$$B = \frac{2\sqrt{2}}{\pi} \frac{1}{w_{inc}^2} \left[\frac{a}{w_{inc}} + \frac{i\alpha\pi \cdot w_{inc}}{\lambda}\right]^2 R(\omega_{10})^2 \quad (4\text{-}31)$$

$$C = \frac{2}{\pi} \frac{1}{w_{inc}^3} \left[\frac{a}{w_{inc}} + \frac{i\alpha\pi \cdot w_{inc}}{\lambda}\right] \cdot \left(R(\omega) R(\omega_{10})^*\right) \cdot e^{i \cdot atg\frac{z}{z_R}} + c.c.$$

In Equation (4-30) we have an expression for the power, were we to look for the current at the photodiode's exit the multiplying term $\frac{\eta q}{h\nu} \frac{1}{Z}$ should be added. In this constant η and Z are respectively the photodiode's quantum efficiency and transimpedance, q is the electron's charge and $h\nu$ is the incident energy of the photons. The intensity profile of the power incident on the photodiode, expressed by Equation (4-30) considering Equations(4-31), is shown at the resonance in Figure 4-9 and has been calculated numerically with the following parameters, α=0.03, a=0.01, in units of w_{inc}, Φ_{Gouy}=0 rad, r_3=1 and r_1=r_2.

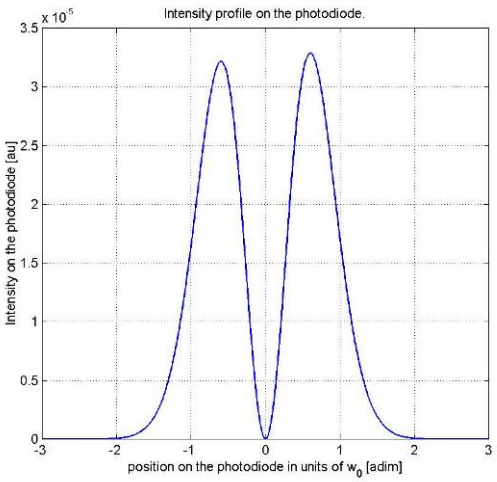

Figure 4–9

The effect of the shift is visible in the lower intensity on the left-hand-side lobe of the detector. The expression in Equation (4-30) must then be spatially integrated on the two photodiodes halves, taking into account the detector's position offset, ε:

$$P_L = \int_{-\infty}^{\varepsilon} P(x)dx$$
$$P_R = \int_{\varepsilon}^{\infty} P(x)dx \qquad (4\text{-}32)$$

and the two halves' subtraction shall give the error signal:

$$ES = -\int_{-\infty}^{\varepsilon} P(x)dx + \int_{\varepsilon}^{\infty} P(x)dx\,. \qquad (4\text{-}33)$$

Now if we substitute in this expression Equation (4-29) the even terms in *x* can't be expressed analytically, as they are of the form $x^{2n}e^{-x^2}$ with *n* integer. Not so for the term given by the interference between the two different modes, which gives the odd component of the power and hence, after subtraction, the error signal. The even terms in *x*, however, cancel completely only for detector offsets equal to zero, but should be taken into account for $\varepsilon \neq 0$ as in the case in exam. Let us decompose the difference of the two integrals given in Equation (4-32) as follows:

$$ES = -\int_{-\infty}^{0} P(x)dx + \int_{0}^{\infty} P(x)dx - 2\int_{0}^{\varepsilon} P(x)dx\,. \qquad (4\text{-}34)$$

Now the two integrals between zero and infinity are known and in particular:

$$\int_{-\infty}^{0} x^{2n}\cdot e^{-2x^2}dx = \int_{0}^{\infty} x^{2n}\cdot e^{-2x^2}dx$$
$$-\int_{0}^{\infty} x\cdot e^{-x^2}dx = \int_{-\infty}^{0} x\cdot e^{-2x^2}dx = \frac{1}{4} \qquad (4\text{-}35)$$

While the Gaussian distribution, which is often called error function or *erf* has no known analytical expression, its numerical values can be calculated. For small values of epsilon ($erf(\varepsilon)\approx\varepsilon$) we obtain for the terms dependent from the detector misalignment:

$$\int_{0}^{\varepsilon} e^{-2x^2} = \frac{1}{2}erf(\varepsilon) \approx \frac{\varepsilon}{2},$$
$$\int_{0}^{\varepsilon} x^2\cdot e^{-2x^2} = \frac{1}{4}erf(\varepsilon) - \frac{1}{4}\varepsilon\cdot e^{-2\varepsilon^2} \approx \frac{\varepsilon^3}{2}, \qquad (4\text{-}36)$$
$$\int_{0}^{\varepsilon} x\cdot e^{-2x^2} = \frac{1}{4}\left(e^{-2\varepsilon^2}-1\right) \approx -\frac{\varepsilon^2}{2}.$$

Where the final expressions in Equations (4-36) are obtained developing in series the exponentials and stopping at the first order. Substituting now the values taken from Equations (4-30), (4-35) and (4-36) into (4-34) we can obtain the following expression for the Error Signal with a detector (ε) and beam (a) offset:

$$ES = -\frac{C(\omega,z,\alpha,a)}{2} - \varepsilon\cdot\frac{A(\omega,z)}{2} + \varepsilon^2\frac{C(\omega,z,\alpha,a)}{2} - \varepsilon^3\frac{B(\omega,z,\alpha,a)}{2}. \tag{4-37}$$

If we consider Φ_{Gouy}=0, stop at the first order in ε, taking into account the expressions in Equation (4-30) and writing the reflectivity as a function of the coupling ζ_0 and the pole frequency of the cavity f_P we can write the error signal analytically as:

$$ES = \frac{2}{\pi}\frac{1}{w_{inc}^3}\left[\begin{array}{l} -\frac{a}{w_{inc}}\left(\frac{\left(\zeta_0^2+\frac{\delta\omega^2}{f_P^2}(1+\beta)\right)\left(1+\frac{\delta\omega^2}{f_P^2}(1+\beta)\right)+\zeta_0\beta^2\frac{\delta\omega^2}{f_P^2}}{\left(1+\frac{\delta\omega^2}{f_P^2}(1+\beta)\right)^2+\beta^2\frac{\delta\omega^2}{f_P^2}}\right)+ \\ +\frac{\alpha\pi\cdot w_{inc}}{\lambda}\left(\frac{(\zeta_0-1)\left(\frac{\delta\omega^2}{f_P^2}(1+\beta)-\zeta_0\right)\cdot\beta\frac{\delta\omega}{f_P}}{\left(1+\frac{\delta\omega^2}{f_P^2}(1+\beta)\right)^2+\beta^2\frac{\delta\omega^2}{f_P^2}}\right) \end{array}\right] + \varepsilon\left(\frac{2}{\pi}\frac{1}{w_{inc}^2}\frac{\zeta_0^2+\frac{\delta\omega^2}{f_P^2}}{1+\frac{\delta\omega^2}{f_P^2}}\right)+\ldots \tag{4-38}$$

$$\cong\frac{2}{\pi}\frac{1}{w_{inc}^3}\left[-\frac{a}{w_{inc}}\left(\zeta_0^2+o\left(\frac{\delta\omega^2}{f_P^2}\right)\right)-\frac{\alpha\pi\cdot w_{inc}}{\lambda}\cdot\left((\zeta_0-1)\zeta_0\cdot\beta\frac{\delta\omega}{f_P}+o\left(\frac{\delta\omega^3}{f_P^3}\right)\right)+\frac{2}{\pi}\frac{1}{w_{inc}^2}\varepsilon\left(\zeta_0^2+o\left(\frac{\delta\omega^2}{f_P^2}\right)\right)\right]$$

where with $\delta\omega$ we indicate the detuning of the laser with respect to the cavity. This formula shows us that the error signal depends under all conditions from the beam misalignment, both linear and angular, and from the detector's alignment.

The Gouy shift phase term has been supposed to be zero, this implies that the previous calculation is only true in the near field condition. As is well known and used to implement auto-alignment loops[32], in the far field condition it is the linear displacement that will give an error signal. In these conditions the angular displacement will conversely be linked to an offset effect. This can be understood if we consider that in the far field condition where $z>>z_R$ the argument of the *atg* function goes towards infinity and hence its value is close to $\pi/2$. But a phase shift of $\pi/2$ does no more than turn the real part into an imaginary part and this results, in Equation (4-38), in the parameters α and a exchanging multiplying constants.

Let us now see what happens to Equation (4-38) for different values of the coupling constant. We shall analyse a perfectly coupled (ζ_0=0), over-coupled (ζ_0=-1) and under-

coupled (ζ_0=1), cavity. Let us remember that under-coupled implies that the electromagnetic field is completely reflected off the cavity, whereas over-coupled means that the field is, this time, completely absorbed by the cavity.

In the perfectly coupled case (ζ_0=0) Equation (4-38) takes on the form:

$$ES = \frac{2}{\pi}\frac{1}{w_{inc}^3}\left[\begin{array}{c} -\frac{a}{w_{inc}}\left(\frac{\left(\frac{\delta\omega^2}{f_P^2}(1+\beta)\right)\left(1+\frac{\delta\omega^2}{f_P^2}(1+\beta)\right)}{\left(1+\frac{\delta\omega^2}{f_P^2}(1+\beta)\right)^2+\beta^2\frac{\delta\omega^2}{f_P^2}}\right)- \\ \frac{\alpha\pi\cdot w_{inc}}{\lambda}\left(\frac{\left(\frac{\delta\omega^2}{f_P^2}(1+\beta)\right)\cdot\beta\frac{\delta\omega}{f_P}}{\left(1+\frac{\delta\omega^2}{f_P^2}(1+\beta)\right)^2+\beta^2\frac{\delta\omega^2}{f_P^2}}\right) \end{array}\right]+\varepsilon\left(\frac{2}{\pi}\frac{1}{w_{inc}^2}\frac{\frac{\delta\omega^2}{f_P^2}}{1+\frac{\delta\omega^2}{f_P^2}}\right)+\ldots \qquad (4\text{-}39)$$

where the terms in a and ε are both even functions of the detuning $\delta\omega$ and it is the term in α that is odd in terms of $\delta\omega$ and as expected gives an error signal. The lock point (*ES=0*) is obtained for $\delta\omega$*=0*.

For the under-coupled situation (ζ_0=1), instead, the error signal shall have the form:

$$ES = \frac{2}{\pi}\frac{1}{w_{inc}^3}\left[-\frac{a}{w_{inc}}\right]+\varepsilon\left(\frac{2}{\pi}\frac{1}{w_{inc}^2}\right)+\ldots \qquad (4\text{-}40)$$

in which, as was to be expected, the carrier is reflected off the cavity, doesn't depend from the cavity-laser detuning $\delta\omega$ and doesn't, therefore, give an error signal.

Finally for the over-coupled situation (ζ_0=-1) the error signal will be:

$$ES = \frac{2}{\pi}\frac{1}{w_{inc}^3}\left[\begin{array}{c} -\frac{a}{w_{inc}}\left(\frac{\left(1+\frac{\delta\omega^2}{f_P^2}(1+\beta)\right)^2-\beta^2\frac{\delta\omega^2}{f_P^2}}{\left(1+\frac{\delta\omega^2}{f_P^2}(1+\beta)\right)^2+\beta^2\frac{\delta\omega^2}{f_P^2}}\right)+ \\ \frac{\alpha\pi\cdot w_{inc}}{\lambda}\left(\frac{-2\left(1+\frac{\delta\omega^2}{f_P^2}(1+\beta)\right)\cdot\beta\frac{\delta\omega}{f_P}}{\left(1+\frac{\delta\omega^2}{f_P^2}(1+\beta)\right)^2+\beta^2\frac{\delta\omega^2}{f_P^2}}\right) \end{array}\right]+\varepsilon\left(\frac{2}{\pi}\frac{1}{w_{inc}^2}\right)+\ldots \qquad (4\text{-}41)$$

in which case the terms in function of a and ε will be responsible for an offset to the lock point: *ES≠0* when $\delta\omega$*=0*.

Signal to Noise Ratio

Let us now try to evaluate the signal to noise ratio for the Tilt Locking single pass. All calculations shall assume that the Gouy phase shift be zero. Let us now use the general expressions for the Error Signal Slope, the Noise and the SNR given by Equations (2-1), (2-) ans (2-3) respectively.

Let us now consider once more Equation (4-38). If we develop in series of Mc Laurin (small values of $f=\delta\omega/f_P$) the expression and stop at the first order we shall obtain for the signal slope:

$$\chi \propto \frac{2}{\pi}\frac{1}{w_{inc}^3}\frac{2\alpha}{\lambda w_{inc}^2}\cdot\zeta_0(1-\zeta_0)\beta\cdot f \tag{4-42}$$

For the noise contribution we have to integrate Equation (4-30) between minus and plus infinity. Taking into account the fact that:

$$\int_{-\infty}^{\infty} e^{-2x^2} = \frac{1}{2}\sqrt{2\pi},$$

$$\int_{-\infty}^{\infty} x^2\cdot e^{-2x^2} = -\frac{1}{2}\sqrt{\frac{\pi}{2}},$$

$$\int_{-\infty}^{\infty} x\cdot e^{-2x^2} = 0,$$

and using the conventions established in Section 2.2 we shall obtain:

$$N = \sqrt{\sqrt{\pi}\left(\frac{\sqrt{2}}{2}A - \frac{1}{2\sqrt{2}}B\right)} \tag{4-43}$$

Once again we develop the expression in series and stopping at the first order in f we get for the noise:

$$N \propto \frac{1}{w_{inc}}\sqrt{\frac{1}{\sqrt{\pi}}}\cdot\zeta_0\sqrt{\sqrt{2}-\frac{\alpha^2\pi^2w^2}{\lambda^2}} \tag{4-44}$$

and subsequently for the SNR:

$$SNR = \sqrt{\frac{\eta}{h\nu}}\cdot E_{00}\cdot\frac{2\alpha}{\lambda}\sqrt[4]{\frac{\pi}{2}}\frac{1-\zeta_0}{\sqrt{\sqrt{2}-\frac{\alpha^2\pi^2w^2}{\lambda^2}}}\beta. \tag{4-45}$$

This parameter is an estimate of the Signal to Noise ratio of the method. It doesn't however give any information concerning the technique's performances on long term stabilisation, which shall be analysed in greater detail in the next paragraph.

Simulation and Lock point stability

In order to have good long term performances a good SNR is not enough. We also need to have a good stability of the locking point position in the face of the main instabilities (offsets) to which the method is subjected to. In the case of Tilt Locking as seen above these instabilities are the beam jitter motions causing the appearance of shifts *a* and detector offsets ε. As seen clearly from the analytical expressions, in the case of a perfect coupling the accuracy of the lock is immune to both shifts and detector's offsets. The general case is however more difficult to treat analytically; it can, however, be treated simply through simulation. The simulation allows us to introduce the Gouy[32][33] phase shift as well as the photodiode dead zone as new parameters in the calculations. The cavity Finesse used in the simulations was of 580. In the simulation we considered a finite sized photo-detector having a radius of roughly $3w_{inc}$. Simulations were also run with a smaller photodiode of only w_{inc} of radius. While the latter modification caused an additional change in the error signal profile, it had no impact on the locking point position. The simulation is a MatLab custom built routine (Appendix C). More on subroutines created to support this program to be found together with the program heading. We can trace the profiles of the error signal line-shapes and appreciate the locking point variations from the graphs or we can define a locking error as:

$$Err = \frac{2f_P \cdot 10^{-2} \cdot ES(0)}{ES\left(\frac{2f_P}{100}\right) - ES\left(\frac{-2f_P}{100}\right)}, \tag{4.46}$$

For increasing variations of the linear displacement or shift we obtain for the line-shapes, in the case ($\zeta_0=0$) of an optimal coupling, the profile shown in Figure (4-10), similarly for detector displacements we have Figure (4-11).

These graphs are better read supported by the numerical values of the locking point offsets calculated for the different parameters. For ease of consultation the computed offset values are shown in three comprehensive tables, one for perfect coupling ($\zeta_0=0$ Table 4-1), a second for a large over-coupling ($\zeta_0=-0.67$ Table 4-2), and the final one for a significant under-coupling ($\zeta_0=0.67$ Table 4-3). All lock point offsets are expressed in units of the reference linewidth ($\delta\nu$), just as the introduced beam displacements are in units of the incident beam waist (w_{inc}). All variations of the locking point position have been calculated for both a zero and 0.01 radians Gouy shift. Similarly the dead zone has been shown to have no effect whatsoever on the locking point.

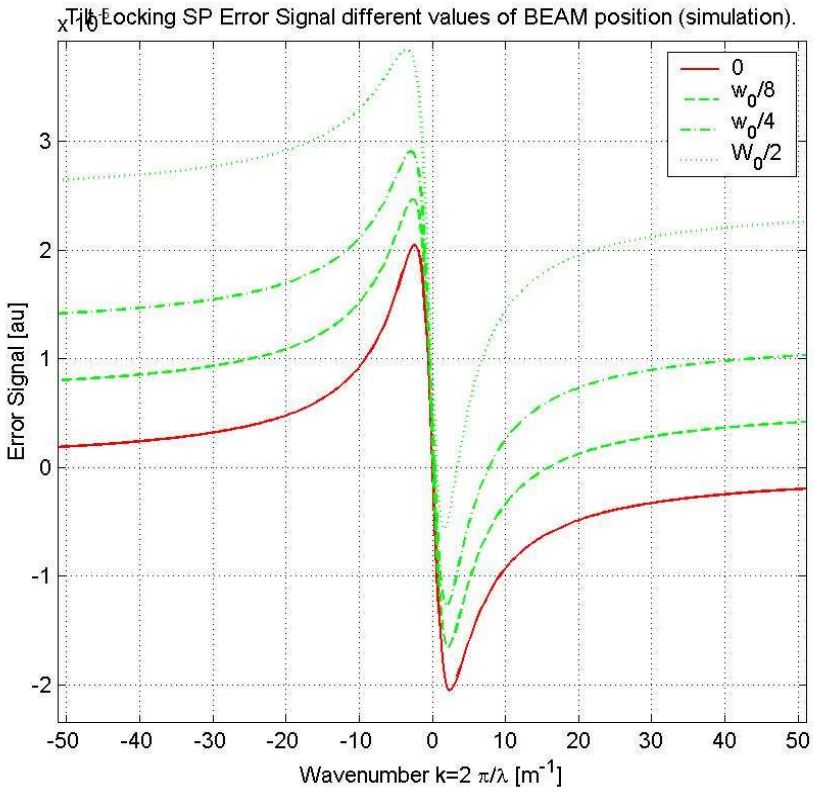

Figure 4–10

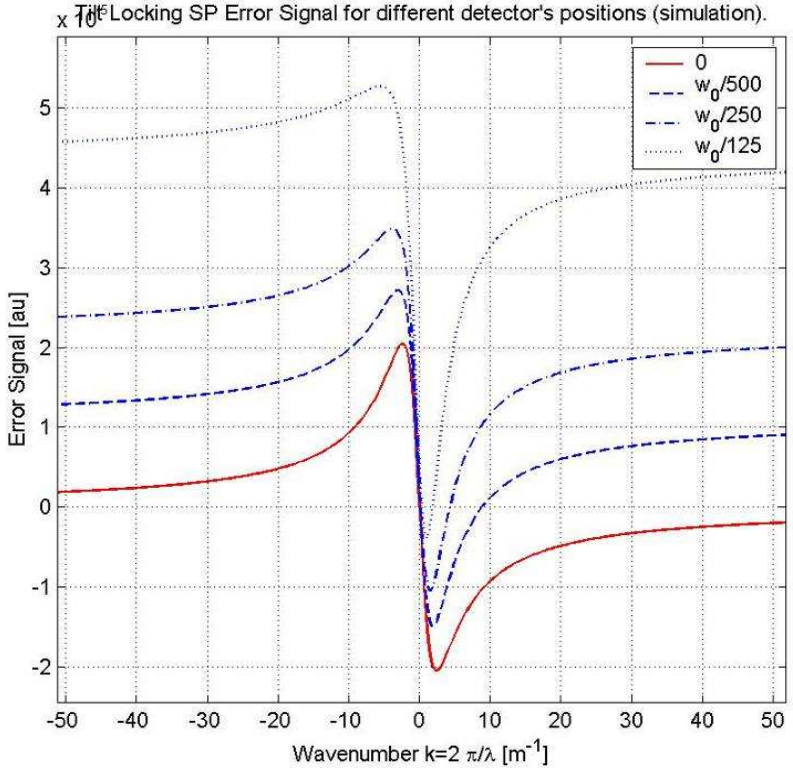

Figure 4–11

ζ_0=0

Tilt α/w_{inc}	Shift a/w_{inc}	Detector Offset ε/w_{inc}	Locking point Error Err/f_P
0.1	**0**	**0**	**$-5\ 10^{-20}$**
0.1	**0.01**	**0**	**$-7\ 10^{-18}$**
0.1	**0**	**0.01**	**$3\ 10^{-16}$**
0.1	**0.01**	**0.01**	**$3\ 10^{-16}$**

Table 4-1

ζ_0=-0.67

Tilt α/w_{inc}	Shift a/w_{inc}	Detector Offset ε/w_{inc}	Locking point Error Err/f_P
0.1	**0**	**0**	**-0.003**
0.1	**0.01**	**0**	**-0.067**
0.1	**0**	**0.01**	**0.093**
0.1	**0.01**	**0.01**	**0.029**

Table 4-2

ζ_0=0.67

Tilt α/w_{inc}	Shift a/w_{inc}	Detector Offset ε/w_{inc}	Locking point Error Err/f_P
0.1	**0**	**0**	**0.003**
0.1	**0.01**	**0**	**0.32**
0.1	**0**	**0.01**	**0.49**
0.1	**0.01**	**0.01**	**0.81**

Table 4-3

From these tables we gather a confirmation of what shown by the analytical calculations insofar as the technique's sensitivity to both shifts and detector offsets is concerned. Firstly the effect on the lock point given by the misalignments is zero in the case of a perfect coupling. It can also be observed that in the case of an over-coupled cavity the lock point offsets caused by a shift have opposite sign from those introduced by a detector misalignment. Hence the resulting much lower than expected value for the offset when both effects are present. Finally, provided the cavity is not heavily under-coupled, we have

shown that we expect the Tilt Locking zero crossing point (locking point) to be insensitive within a tenth of the cavity's linewidth (50Hz for a high Finesse FP) for a strongly over-coupled Fabry-Perot to all optical misalignments. The effects of all beam jitter motions on the Lock should therefore be, for an over-coupled Fabry-Perot negligible. These beam jitters will however influence the robustness of the lock and should be reduced as much as possible. It is with this objective in mind that we can approach the Double Pass configuration.

4.2.2 Double Pass

As we have seen the Tilt locking technique is sensitive to all optical misalignments, it is important to reduce beam jitter noise as much as possible.

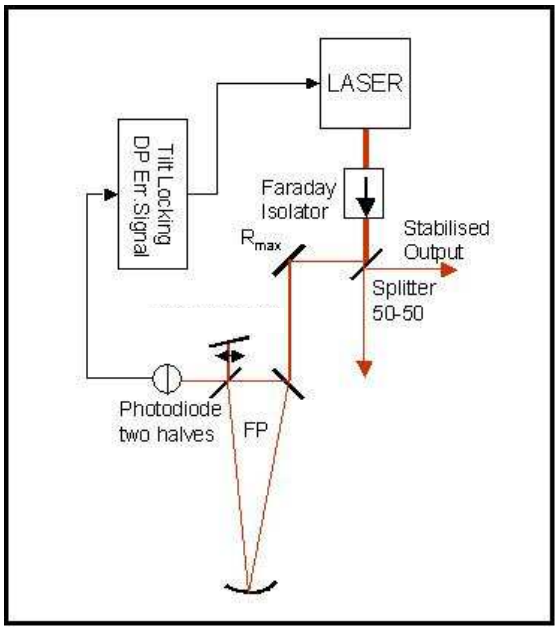

Figure 4–12 Tilt Locking Double Pass configuration with cat's eye.

The obvious solution is to shorten the path between the laser source and the entrance mirror of the FP and reduce the number of optics traversed by the beam, but this is often not practicable once we come to the experimental application. Alternatively a Mode cleaner cavity could be used but this would require a lock on a second reference, thus reproducing the initial problem, and would complicate unnecessarily the experimental system. An elegant solution is obtained by using the Fabry-Perot resonator as a mode cleaner on the first pass and subsequently re-injecting the beam into the cavity with a slight misalignment giving the Tilt. The two beams, being counter-propagating, don't interfere with one another; it is therefore possible to use the reflection off the cavity's second pass entrance mirror to obtain an error signal. The tilt is obtained by misaligning the zero incidence R_{max} mirror that is used to re-inject the beam into the cavity. In this

configuration only the beam jitter of the cavity with respect to the re-injection mirror (and eventually lenses and other optics interposed) and the photo-detector is to be taken into account.

In order to minimise the amount of beam displacement due inevitably to the use of a single re-injection mirror we use a cat's eye configuration with a lens interposed between the mirror and the cavity. This lens will have a double function: on the one side it will allow the creation of a pure Tilt and on the other it will refocus the beam, better matching the second pass of the beam into the reference.

It has to be observed that the beam transmitted by the cavity is perfectly Gaussian thanks to the mode cleaning effect of the Fabry-Perot resonator. In this configuration we no longer have an error signal when the TEM of the first order is resonant with the Fabry-Perot. Additionally for a loss of the lock the beam will be entirely reflected off the cavity at its first pass as was the case for the single pass. The photodiode, placed as it is on the second pass reflection this time, won't have to deal with the whole beam power, at each lock loss.

The main problem with this kind of experimental configuration should be in the delay given by the light's pass into the cavity. As has been shown by Shaddock[27] in his PHD thesis, though, this will limit the lock bandwidth only for frequencies higher than the kHz (bandwidth of the reference) which is outside our frequency band of interest. Of course the fact that the light traverses the cavity twice has to be taken into account in the building of the electronics servo system, the cavity's pole must be compensated twice. Another inconvenient coming from this configuration is the unavoidable backscattered light towards the laser head. This however can be solved by using a Faraday isolator (or an AOM). The Faraday isolator would be problematic, since the presence of a strong magnetic field on board of a magnetically shielded satellite would be unadvisable. The use of an AOM shifter would, however, be a drain on the energetic budget. While the energy budget for the functioning of an AOM could be covered in the case of LISA, thanks to the energy gain given by the lack of the EOM for the Pound-Drever-Hall, this would eliminate the main advantage of the Tilt Locking. Studies at the LZH in Hannover (K. Danzman private communication A. Brillet) have shown that the NPRO Nd:YAG built for LISA can receive up to 4% of its output light back in the laser cavity without showing appreciable variations in the phase and power noise spectra. A configuration without Faraday isolator could, in principle, be conceived to allow a backscattering inferior to 4% of the originally emitted power. Let us now once more calculate the error signal and the signal to noise ratio.

Error signal extraction

We consider our reference to be a triangular Fabry-Perot cavity with entrance mirror 1, exit mirror 2, end mirror 3 and Finesse values equal to those of our reference cavity.

The case of the double pass tilt locking is, as far as the calculation of the analytical form of the error signal is concerned, nearly identical to what we have seen for the single pass configuration. The re-injected beam will be perfectly Gaussian; its form is given by:

$$E_{Trans} = T(\omega)\cdot E_{inc}$$
$$T(\omega) = \frac{t_1 t_2 r_3 \cdot e^{2\pi i\omega\tau}}{1 - r_1 r_2 r_3 \cdot e^{2\pi i\omega\tau}} \qquad (4\text{-}47)$$

with the same conventions used for the definitions of Equation (4-28). To obtain the error signal in this configuration we just have to substitute the first expression in Equation (4-47) in the place of the E_{00} field injected into the Fabry-Perot.

T isn't a function of the spatial coordinate but only of the detuning we can thus multiply the expression of the Error Signal for the single pass for $|T(\delta\omega)|^2$ and thus obtain the double pass Error Signal. The term $|T(\delta\omega)|^2$ is, obviously, real, hence the simplicity of the calculation. In particular we have that:

$$|T(\delta\omega)|^2 = \frac{1-\zeta_0^2}{1+\frac{\delta\omega^2}{f_P^2}} \qquad (4\text{-}48)$$

So that the error signal becomes:

$$ES = \left\{ \frac{2}{\pi}\frac{1}{w_{inc}^3} \left[-\frac{a}{w_{inc}} \left(\frac{\left(\zeta_0^2 + \frac{\delta\omega^2}{f_P^2}(1+\beta)\right)\left(1+\frac{\delta\omega^2}{f_P^2}(1+\beta)\right) + \zeta_0\beta^2\frac{\delta\omega^2}{f_P^2}}{\left(1+\frac{\delta\omega^2}{f_P^2}(1+\beta)\right)^2 + \beta^2\frac{\delta\omega^2}{f_P^2}} \right) + \right.\right.$$
$$\left.\left. + \frac{\alpha\pi\cdot w_{inc}}{\lambda} \left(\frac{(\zeta_0 - 1)\left(\frac{\delta\omega^2}{f_P^2}(1+\beta) - \zeta_0\right)\cdot\beta\frac{\delta\omega}{f_P}}{\left(1+\frac{\delta\omega^2}{f_P^2}(1+\beta)\right)^2 + \beta^2\frac{\delta\omega^2}{f_P^2}} \right) \right] + \right.$$
$$\left. + \varepsilon\left(\frac{2}{\pi}\frac{1}{w_{inc}^2}\frac{\zeta_0^2 + \frac{\delta\omega^2}{f_P^2}}{1+\frac{\delta\omega^2}{f_P^2}} \right) + \ldots \right\} \frac{1-\zeta_0^2}{1+\frac{\delta\omega^2}{f_P^2}} \qquad (4\text{-}49)$$

which doesn't present at first glance any significant difference from the single pass case. In particular for a perfectly coupled cavity ($\zeta_0=0$) the ES remains zero for a null frequency. The error signal expression in this case shall simply be the one Equation (4-39) multiplied by $1/(1+f^2)$. Always with the convention that f is the detuning divided by the cavity's pole. For a completely over-coupled ($\zeta_0=-1$) or under-coupled cavity ($\zeta_0=1$), though, the error signal is, this time, simply zero. This is understandable as a completely over or under-coupled cavity excludes there being any transmitted light, which in turn must and does result in there being a total absence of light and thus of any error signal. Let us now see what happens as far as the Signal to Noise Ratio is concerned in the double pass configuration.

Signal to Noise Ratio

To determine the SNR in this case as well as in the former we have to once more calculate the quantities expressed in Equations (2-1), (2-2) and (2-3) for the Error Signal Slope, the Noise and the SNR respectively. A simple consideration concerning the fact that all terms are multiplied by $T^2(\omega)$ can be used as a shortcut to the final result. In particular the new expression for the Signal Slope and Noise will be:

$$\chi \propto \frac{2\alpha}{\lambda w_{inc}^2} \cdot \zeta_0 \cdot (1-\zeta_0) \cdot \beta \cdot \left(1-\zeta_0^2\right) \cdot f \tag{4-50}$$

where f is still the ratio of the detuning $\delta\omega$ and the pole frequency of the cavity, and

$$N \propto \frac{1}{w_{inc}} \sqrt{\frac{1}{\sqrt{\pi}}} \cdot \zeta_0 \sqrt{\sqrt{2} - \frac{\alpha^2 \pi^2 w^2}{\lambda^2}} \sqrt{1-\zeta_0^2} \tag{4-51}$$

respectively. These last two expressions give for the *SNR*:

$$SNR = \sqrt{\frac{\eta}{h\nu}} \cdot E_{00} \cdot \frac{2\alpha}{\lambda} \sqrt[4]{\frac{\pi}{2}} \frac{1-\zeta_0}{\sqrt{\sqrt{2} - \frac{\alpha^2 \pi^2 w^2}{\lambda^2}}} \beta \sqrt{1-\zeta_0^2} \tag{4-52}$$

which is always smaller or at best equal to the *SNR* obtained for the single pass configuration. The advantage given by the much shorter optical path and the lesser beam-jitter noise, are however more than sufficient to compensate the slight loss in signal to noise ratio accepted in the double pass configuration. Let us concentrate on the locking point stability as obtained through simulation.

Simulation and lock point stability

Much as for the single pass case, the parameter we are interested in is the stability of the lock point, which will directly give us a measure of the exactitude of our frequency technique with respect to the reference.

The main offset contributions as shown by Equation (4-49) are still the shift (*a*), or linear beam misalignment on the cavity, and the detector's offset (ε).

For the double pass a second routine plotting the error signal line-shape and calculating the locking point offset according to Equation (4-46) has been created, always in a MatLab environment. The entered Finesse for the simulated cavity was once again of 580. All our simulation considered a finite sized photo-detector having a radius of roughly $3w_{inc}$. The error signal line-shapes for a perfect coupling this time have the form, in Figure 4–13 and Figure 4–14 for different values of the shift, and for increasing detector misalignments respectively.

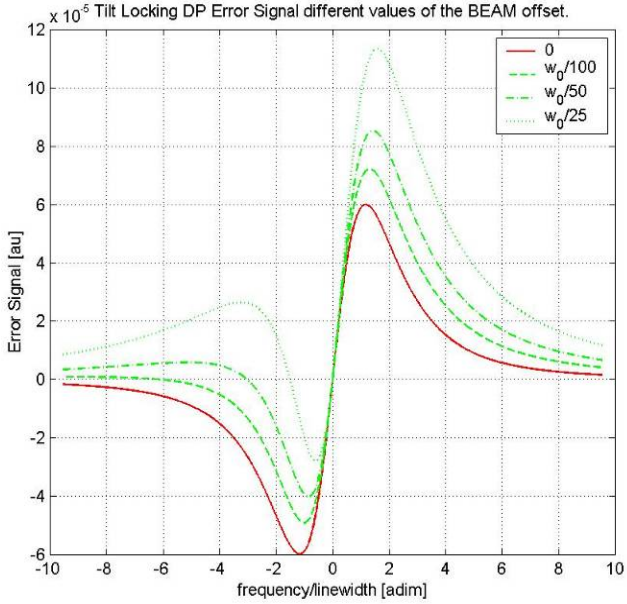

Figure 4–13

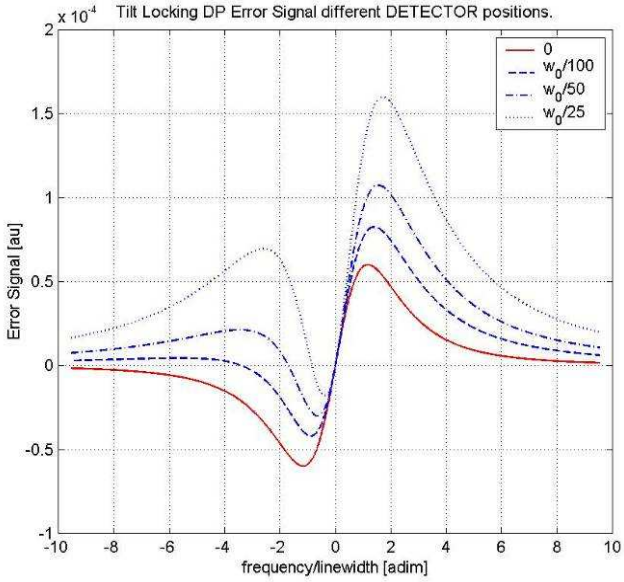

Figure 4–14

The offsets with the same conventions used in Section 4.2.1 are shown in the following tables: Table 4-4 (optimal coupling), Table 4-5 (over-coupled) and Table 4-6 (under-coupled). Once again the Gouy shift and dead zone amplitude have been shown to carry no weight in the locking point offset determination. Much as expected the situation is nearly identical for the offset of the locking point in the double pass and single pass configuration, for equal amounts of the misalignments introduced. As observed for the single pass configuration the tilt locking is once more shown to be, provided the cavity is not heavily under-coupled, insensitive, within the kHz for a high Finesse cavity, to all optical misalignments.

ζ_0=0

Tilt α/w_{inc}	Shift a/w_{inc}	Detector ε/w_{inc}	Offset	Locking point Error Err/f_P
0.1	**0**	**0**		**$-5\ 10^{-20}$**
0.1	**0.01**	**0**		**$-7\ 10^{-18}$**
0.1	**0**	**0.01**		**$2\ 10^{-16}$**
0.1	**0.01**	**0.01**		**$2\ 10^{-16}$**

Table 4-4

ζ_0=-0.67

Tilt α/w_{inc}	Shift a/w_{inc}	Detector ε/w_{inc}	Offset	Locking point Error Err/f_P
0.1	**0**	**0**		**-0.003**
0.1	**0.01**	**0**		**-0.067**
0.1	**0**	**0.01**		**0.092**
0.1	**0.01**	**0.01**		**0.028**

Table 4-5

ζ_0=0.67

Tilt α/w_{inc}	Shift a/w_{inc}	Detector ε/w_{inc}	Offset	Locking point Error Err/f_P
0.1	**0**	**0**		**0.003**
0.1	**0.01**	**0**		**0.31**
0.1	**0**	**0.01**		**0.49**
0.1	**0.01**	**0.01**		**0.81**

Table 4-6

The misalignment we want to reduce is in particular the photo-detector centring error, as seen by the tables above. The use of a large detector coupled by a lens with the cavity's waist should nicely reduce this effect. The lack of active components in view of these conclusions makes tilt locking an extremely attractive technique for space implementation.

The determination of the requirements for a possible application of Tilt locking is presented in Section 6.3.

4.3 Pound-Drever-Hall

4.3.1 Overview

The Pound-Drever-Hall[29] technique is widely used for most lock configuration and is considered somewhat of a state of the art choice for locking a laser to a reference cavity.

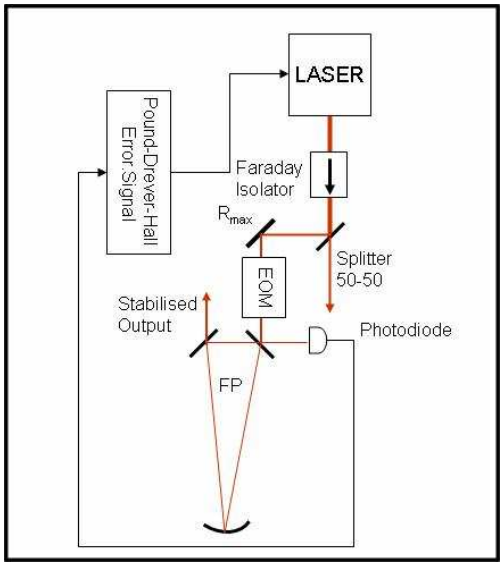

Figure 4–15

Invented by Pound in the micro-wave range, it was applied by Drever and Hall[30][31] to lasers and is now widely used thanks to its first order insensitivity to low frequency laser amplitude noise.

The Pound-Drever-Hall technique uses the interference between the reflected field exiting the cavity and the not-resonant sidebands generated by a phase modulation. The sidebands act as a phase reference for the field before its entrance into the cavity. Since the carrier has passed through the cavity it is possible to measure the detuning between laser and cavity, thanks to the interference between carrier and sidebands.

The main noise sources for this technique are: the laser noise spectral density at the demodulation frequency (hence the normal choice of high frequencies, typically several MHz, for modulation) and the residual amplitude modulation. The former of these effects is significant because on the photodiode we measure the sidebands phase modulation

converted into amplitude modulation. To reduce this effect the modulation frequency as already mentioned is chosen in the area where the laser noise is shot noise limited ($\nu_m \geq 5 \div 10$ *MHz*). The modulation frequency has to be chosen different from the Gaussian transverse modes of the cavity. Hence typically ($5MHz \leq \nu_m \leq FSR$) the modulation frequency is chosen higher than the shot noise limit at 5MHz and lower than the cavity's free spectral range. This second condition is determined by the necessity in the ordinary configuration for the sidebands to serve as phase reference and hence, ideally, for them to be completely reflected off the cavity. For a modulation at the FSR or higher the sidebands can be partially coupled into the cavity.

With respect to amplitude modulation the technique is sensitive to this effect, minimisation of which is obtained through an accurate orientation of the EOM crystal in the experimental apparatus. The technique is insensitive to beam displacements, since an optical misalignment will only influence the quantity of light incident on the photodiode (DC signal), but will not be detectable at the modulation frequency (AC signal). Thus the noise contributions are those at frequencies close to the modulation/demodulation frequency. Let us now see how the error signal is obtained both analytically and through simulation.

Error Signal extraction

Once again we consider the reference as a triangular Fabry-Perot cavity with entrance mirror 1, exit mirror 2 and end mirror 3.

Our perfectly Gaussian field passes through an EOM (electro-optic modulator) which adds sidebands at the modulation frequency. The modulated field has the form:

$$E_M = E_0 \cdot e^{i\omega t} \cdot e^{iB\cdot\sin(\omega_m \cdot t)} \tag{4-54}$$

This expression can be developed using Bessel functions as:

$$\begin{aligned} E_M &\approx E_0 \cdot e^{i\omega\cdot t}\left[J_0(B)+J_1(B)\cdot e^{i(\omega_m)t}+J_{-1}(B)\cdot e^{i(-\omega_m)t}+J_2(B)\cdot e^{i(2\omega_m)t}+J_{-2}(B)\cdot e^{i(-2\omega_m)t}+...\right] \\ &\approx E_0 \cdot e^{i\omega\cdot t}\left[J_0(B)+J_1(B)\cdot\left(e^{i(\omega_m)t}-e^{i(-\omega_m)t}\right)+J_2(B)\cdot\left(e^{i(2\omega_m)t}+e^{i(-2\omega_m)t}\right)+...\right] \end{aligned} \tag{4-55}$$

The modulated field is then partially reflected and partially transmitted by the cavity, the reflected part observed by our photo-detector can be expressed as:

$$E_R \approx E_0 \cdot e^{i\omega\cdot t}\begin{bmatrix} J_0(B)R(\omega)+J_1(B)\cdot\left(R(\omega+\omega_m)e^{i(\omega_m)t}-R(\omega-\omega_m)e^{i(-\omega_m)t}\right)+ \\ J_2(B)\cdot\left(R(\omega+2\omega_m)e^{i(2\omega_m)t}+R(\omega-2\omega_m)e^{i(-2\omega_m)t}\right)+... \end{bmatrix} \tag{4-56}$$

We have for the photocurrent:

$$I=\frac{\eta q}{h\nu Z_{AC}}E_0^2\left[\begin{array}{l} J_0^2(B)R^2(\omega)+J_1^2(B)\cdot\left(R^2(\omega+\omega_m)+R^2(\omega-\omega_m)\right) \\ +J_2^2(B)\cdot\left(R^2(\omega+2\omega_m)+R^2(\omega-2\omega_m)\right)+ \\ \left(J_0(B)J_1(B)\cdot\left(R(\omega)R^*(\omega+\omega_m)e^{i(-\omega_m)t}-R(\omega)R^*(\omega-\omega_m)e^{i(\omega_m)t}+c.c\right)\right. \\ \left.+J_1(B)J_2(B)\cdot\left(\begin{array}{l}R(\omega+\omega_m)R^*(\omega+2\omega_m)e^{i(-\omega_m)t}+\\ R(\omega-\omega_m)R^*(\omega-2\omega_m)e^{i(\omega_m)t}+c.c\end{array}\right)+\ldots\right) \end{array}\right]+\ldots \quad (4\text{-}57)$$

Were in the above formula we have explicitly written only contributions up to the first harmonic in ω_m as these are the contributions we shall extract through synchronous demodulation. The error signal is obtained through a demodulation at the modulator driving frequency, depending on the demodulation phase we can have:

$$Phase = I\cdot\frac{e^{i\omega_m\cdot t}-e^{-i\omega_m\cdot t}}{2i} \quad (4\text{-}58)$$

for a zero phase difference between the modulation and demodulation phase,

$$Quadrature = I\cdot\frac{e^{i\omega_m\cdot t}+e^{-i\omega_m\cdot t}}{2}. \quad (4\text{-}59)$$

for a $\pi/2$ phase lag or a linear combination of the two for an arbitrary phase. After demodulation only the component at the modulator driving frequency shall give a continuous signal hence the insensitivity of the technique to noises not close to ω_m.

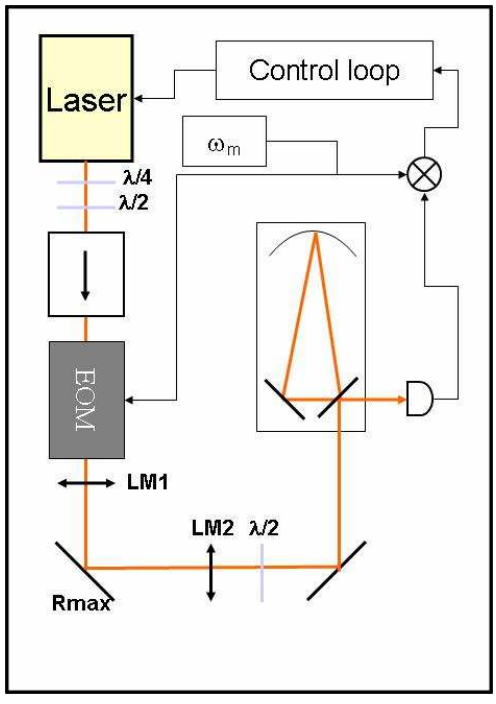

Figure 4–16

Substituting the expression for *I* given by Equation (4-57), into Equation (4-58) and Equation (4-59), leaving out the multiplying constants, stopping at the first harmonics, we obtain respectively:

$$Ph = \frac{E_0^2 J_0(B) J_1(B)}{2i}\left[\left(R(\omega)R^*(\omega+\omega_m)+R(\omega)R^*(\omega-\omega_m)-c.c\right)+...\right] \tag{4-60}$$

and

$$Q = \frac{E_0^2 J_0(B) J_1(B)}{2}\left[\left(R(\omega)R^*(\omega+\omega_m)-R(\omega)R^*(\omega-\omega_m)+c.c\right)+...\right] \tag{4-61}$$

The traditional error signal is obtained for the in phase demodulation, we shall analyse analytically only this signal in detail. With the same conventions used in section 4.2: *f* is the detuning of the laser with respect to the cavity, in units of the reference's linewidth (f_P), and the coupling is given by ζ_0 and varies between -1 and 1:

$$Ph = E_0^2 J_0(B) J_1(B)\frac{1}{\left(1+\frac{\omega_m^2}{f_P^2}\right)}\frac{\omega_m^2}{f_P^2}(\zeta_0-1)\left[1+2\zeta_0+\frac{\omega_m^2}{f_P^2}\right]\cdot f \tag{4-62}$$

Before using the above expression to obtain the Signal to Noise Ratio let us observe that in the above calculations the amplitude modulation would appear as an imaginary contribution in the term $B=A+iB_m$. This was not taken into account in the calculation of the above expression. If we take into account amplitude modulation we have that the in-phase signal shall have the form:

$$Ph_{AM} = \frac{E_0^2}{2i}\begin{bmatrix}\left(J_0(A)J_1(A)\left(1-\frac{B_m^2}{2}\right)\right)\cdot\left(R(\omega)R^*(\omega+\omega_m)+R(\omega)R^*(\omega-\omega_m)-c.c\right)\\ +iB_m\left(J_1^2(A)-\frac{J_0^2(A)}{2}\right)\cdot\left(R(\omega)R^*(\omega+\omega_m)+R(\omega)R^*(\omega-\omega_m)+c.c\right)\end{bmatrix} \tag{4-63}$$

which we shall analyse in detail through simulation.

Signal to Noise Ratio

As we have already done in the case of the tilt locking we can consider the signal to be given by the slope of the error signal considered approximated with a line.

The Noise will still be given by the shot noise of the photons incident on the photodiode:

$$N = \sqrt{P|_{DC}}\cdot\sqrt{\frac{\eta}{h\nu}}\cdot q\frac{Z_{AC}}{Z_{DC}} \tag{4-64}$$

This time we take into account the fact that most of the photon noise will be contributed by the DC terms of the incident power hence the introduction of the term Z_{AC}/Z_{DC}.

The signal using Equation (4-62), is of the form:

$$\chi \propto E_0^2 J_0(B) J_1(B) \frac{1}{\left(1+\frac{\omega_m^2}{f_P^2}\right)} \frac{\omega_m^2}{f_P^2} (\zeta_0 - 1) \left[1 + 2\zeta_0 + \frac{\omega_m^2}{f_P^2}\right] \cdot f \tag{4-65}$$

The noise shall give:

$$N = E_0 \left[J_0(B) \zeta_0 \sqrt{\frac{1-\zeta_0^2}{1-2\zeta_0^2}} + J_1(B) \frac{2\left[\zeta_0^2 + \frac{\omega_m^4}{f_P^4} + \frac{\omega_m^2}{f_P^2}\left(1+\zeta_0^2\right)\right]}{1+\frac{\omega_m^4}{f_P^4}+\frac{\omega_m^2}{f_P^2}} \right] \tag{4-66}$$

The SNR following Equation (2-3), using the two above written equations and considering the Noise principal term in $J_0(B)$ (correct as long as $\zeta_0 \neq 0$) will be proportional to:

$$SNR \propto \sqrt{\frac{\eta}{h\nu}} \cdot E_0 J_1(B) \cdot \frac{1}{\left(1+\frac{\omega_m^2}{f_P^2}\right)} \frac{\omega_m^2}{f_P^2} \frac{(\zeta_0 - 1)}{\zeta_0} \sqrt{\frac{1-2\zeta_0^2}{1-\zeta_0^2}} \left[1 + 2\zeta_0 + \frac{\omega_m^2}{f_P^2}\right] \tag{4-67}$$

If we compare the latter value to that we obtain for the Tilt Locking for our experimental parameters, we shall have that Tilt Locking signal over noise signal shall be equal to 96.7% of the Pound-Drever-Hall. From a purely SNR the Tilt Locking is as performing as the Pound-Drever-Hall technique.

Simulation and lock point stability

As for the Tilt Locking we want to establish the technique's locking point sensitivity to its main cause of locking offset.

In the case of the Pound-Drever-Hall misalignments of the beam only produces a reduction of the incident power, conversely an amplitude modulation at the modulation frequency shall result in an offset. Since the interference of the sidebands and the carrier gives precisely an amplitude modulation at the modulation frequency any spurious effect of this type will result in a phase term in the signal. Tilt Locking being a DC detection technique is insensitive to any such modulation.

A MatLab simulation routine capable of tracing the Error Signal line-shape and compute the Error to the locking point according to Equation (4-46) has been built. We have run the program for a modulation frequency of 6.25MHz on a perfectly coupled cavity with a Finesse of 580.The line-shape variations in function of the Amplitude Modulation depth are shown in Figure 4–17. As for the locking point offsets, for different values of the coupling ζ_0 they assume the values in Table 4-7, which show that as long as the cavity is perfectly coupled the effect given by amplitude modulation is negligible. Once the cavity is over-coupled we have an offset of 6% of the cavity's linewidth which is nearly constant for

increasing values of the amplitude modulation depth. Not so for the under-coupled case in which the increasing values of the modulation amplitude depth are responsible for growing offsets reaching over 16% of the cavity's linewidth. The offsets caused by amplitude modulation in the Pound-Drever-Hall technique are of the same order (close to 10%) of those caused by misalignments compatible with a Tilt Locking experimental assembly (1% of waist) if the cavity is not heavily under-coupled.

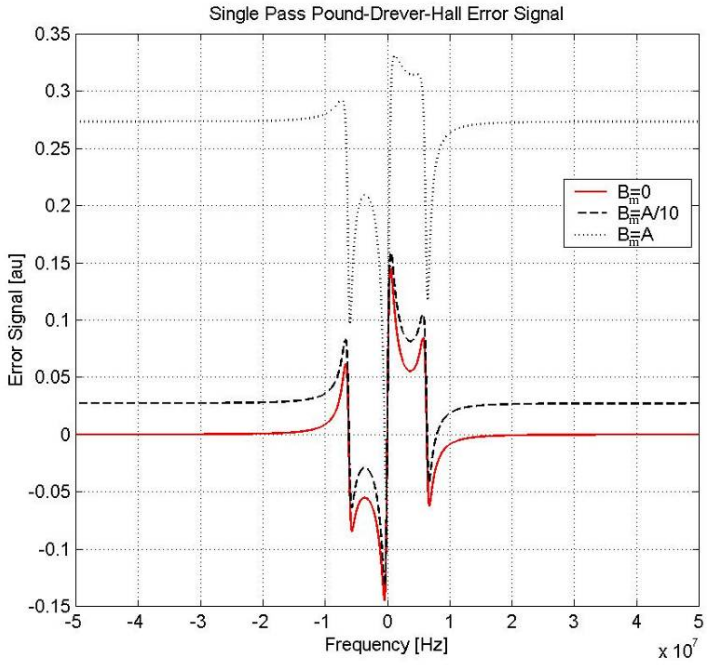

Figure 4–17

Coupling ζ_0	Phase Modulation depth Re(B)=A	Amplitude Modulation depth Im(B)=B_m	Offset in units of f_P
0	**0.3**	**0**	**0**
-0.67	**0.3**	**0**	**0**
0.67	**0.3**	**0**	**0**
0	**0.3**	**0.03**	**$-2\ 10^{-18}$**
-0.67	**0.3**	**0.03**	**-0.06**
0.67	**0.3**	**0.03**	**0.015**
0	**0.3**	**0.3**	**$-2\ 10^{-17}$**
-0.67	**0.3**	**0.3**	**-0.063**
0.67	**0.3**	**0.3**	**0.158**

Table 4-7

4.4 Cavity length control techniques (atomic reference)

We have seen that it is possible to stabilise a laser so that it will follow accurately the reference chosen cavity or molecule. But in the former case the long term stability of the reference might not be sufficient. Specifically, as shown experimentally further, we see that the length variations of an U.L.E cavity can still be sufficiently large to cause frequency derives of the order of the MHz. An active control of the cavity length could be extremely beneficial to ensure precision as well as stability. Given, as we shall see in the following chapters, the important energetic output to implement the possible techniques of active control, a passive monitoring of the cavity FSR might also be of interest.

4.4.1 Double Modulation

This technique has been extensively used by the Japanese team of TAMA300[34] and has given precisions of the order of 10^{-17}m/√Hz on the interferometer arm's length measurement.

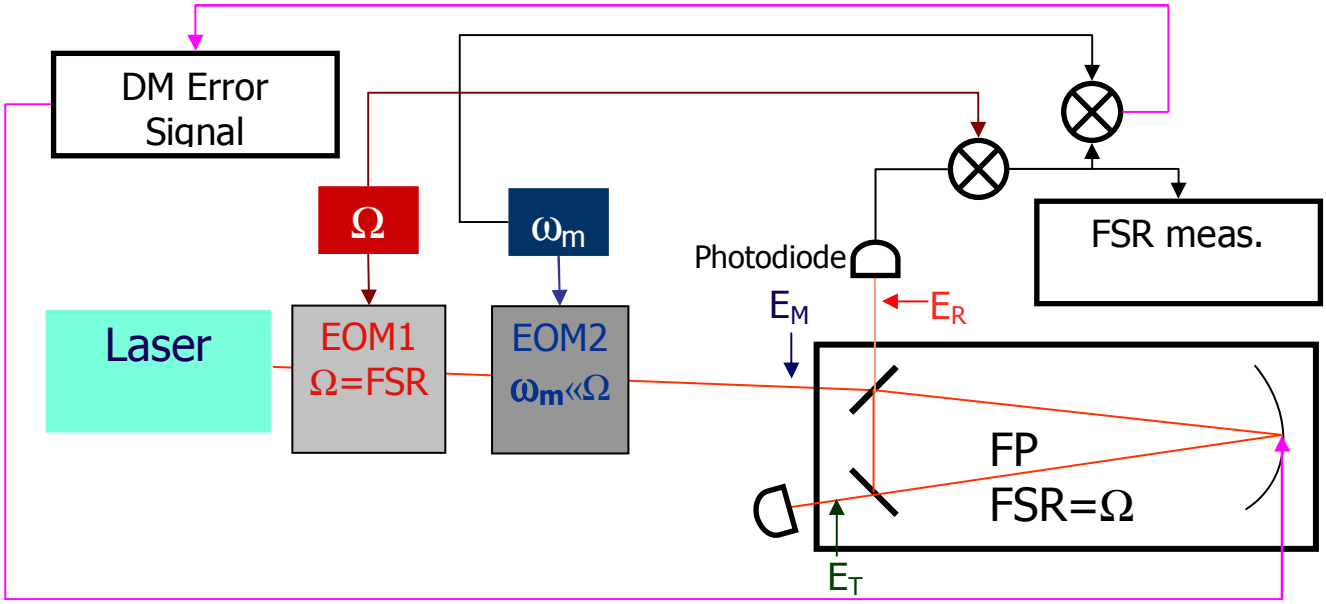

Figure 4–18

The laser beam emitted by the laser is modulated twice: once at a frequency Ω equal to the cavity's FSR and a second time at a lower frequency. This second modulation can be chosen to be within the Fabry-Perot's bandwidth if we wish to work on the transmission signal of the resonators. To obtain the measure of the FSR we then have to demodulate the signal incident on the photodiode first at Ω and then subsequently either in phase or in quadrature at ω_m. Technically we could use the modulated signal also to obtain a Pound-Drever-Hall if we started with the ω_m demodulation. In this configuration the laser would be

locked on the cavity and the cavity length to the generator producing the signal at Ω. The lock between the laser and the resonator could also be obtained with Tilt Locking, placing no extra energy demands. Let us now see how the error signal is obtained, as well as the SNR. We also have to demonstrate that the measure of the FSR is independent on the laser-cavity detuning (δω) and that the demodulated signal at ω_m is insensitive to the FSR variations (cavity-Ω detuning δΩ) to assure the possibility of creating a double lock.

Error Signals extraction

Let us first of all see the form of the double modulated field and which sidebands have been created by the two independent subsequent EOMs. As can be seen in Figure 4–19 the modulation at Ω (modulation depth A) shall create two sidebands distant FSR from the carrier frequency, while the ω_m modulation (modulation depth B) will be responsible for bands at ω_m from all the main components. The modulated field shall have the form, after the expansion stopped to the first harmonic of the modulation terms:

$$E_M = E_0 \cdot e^{i\omega t}\begin{bmatrix} J_0(A)J_0(B)+J_1(A)J_0(B)\left(e^{i\Omega\cdot t}-e^{-i\Omega\cdot t}\right)+J_0(A)J_1(B)\left(e^{i\omega_m\cdot t}-e^{-i\omega_m\cdot t}\right)+ \\ J_1(A)J_1(B)\left(e^{i(\Omega+\omega_m)t}-e^{-i(\Omega-\omega_m)t}+e^{i(\Omega-\omega_m)t}-e^{-i(\Omega+\omega_m)t}\right) \end{bmatrix} \quad (4\text{-}68)$$

Multiplying each term for the complex reflectivity or transmissivity at its given frequency we have the expressions for the reflected or transmitted field respectively. The error signal is for the case of a reflection signal given by:

$$ES_{Ph_q} \propto E_R^* E_R \cdot \frac{e^{i\Omega\cdot t}+e^{-i\Omega\cdot t}}{2}\cdot\frac{e^{i\omega_m\cdot t}-e^{-i\omega_m\cdot t}}{2i}$$

in phase for ω_m and

$$ES_{Q_q} \propto E_R^* E_R \cdot \frac{e^{i\Omega\cdot t}+e^{-i\Omega\cdot t}}{2}\cdot\frac{e^{i\omega_m\cdot t}+e^{-i\omega_m\cdot t}}{2}$$

in quadrature for ω_m.

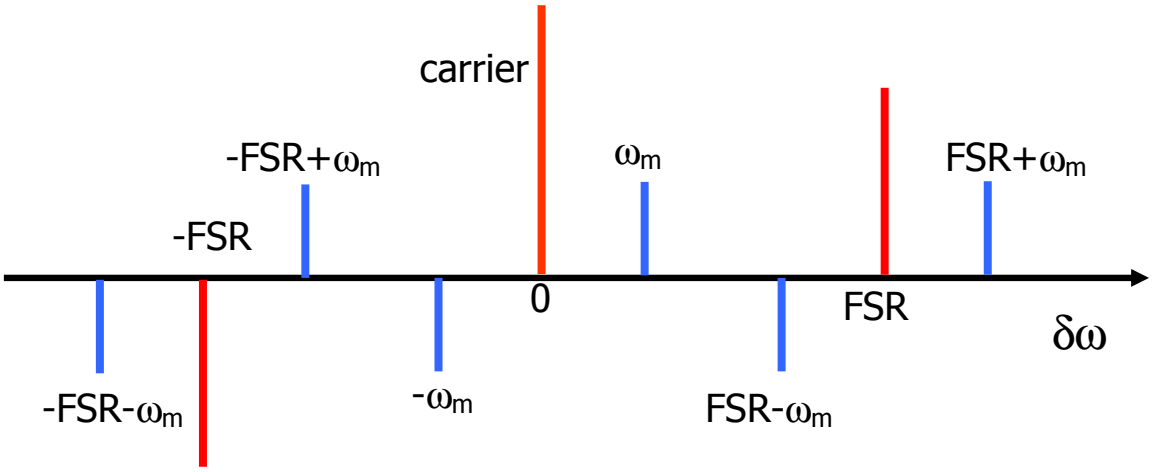

Figure 4–19

Given the unwieldy character of the formulas included in these calculations I shall simply write the end result in the phase case which is:

$$Ph_q \propto \frac{1}{4i}\begin{bmatrix} J_0^2(A)J_0(B)J_1(B)\cdot\begin{pmatrix} R(\omega)R^*(\omega+\Omega+\omega_m)+R(\omega)R^*(\omega-\Omega-\omega_m)- \\ R(\omega)R^*(\omega+\Omega-\omega_m)-R(\omega)R^*(\omega-\Omega+\omega_m)-c.c \end{pmatrix}+ \\ J_0(A)J_1(A)J_0(B)J_1(B)\cdot\begin{pmatrix} -R(\omega+\omega_m)R^*(\omega+\Omega)+R(\omega+\omega_m)R^*(\omega-\Omega)- \\ R(\omega-\omega_m)R^*(\omega+\Omega)+R(\omega-\omega_m)R^*(\omega-\Omega)-c.c \end{pmatrix} \end{bmatrix} \quad (4\text{-}69)$$

and which through a development to the first order in δΩ (Ω-FSR detuning) shall yield the final expression:

$$ES_{Phq} \propto \frac{f_P^2}{\omega_m^2+f_P^2}(1-\zeta_0)\begin{bmatrix} J_0^2(A)J_0(B)J_1(B)\cdot\zeta_0\dfrac{2\omega_m^2}{\omega_m^2+f_P^2}+ \\ J_1^2(A)J_0(B)J_1(B)\cdot\left(\zeta_0+\dfrac{\omega_m^2}{f_P^2}\right) \end{bmatrix}\cdot\frac{\delta\Omega}{f_P} \quad (4\text{-}70)$$

Proceeding similarly for the quadrature signal, we shall have instead:

$$ES_{Qq} \propto \frac{2f_P^2}{\omega_m^2+f_P^2}\begin{bmatrix} J_0^2(A)J_0(B)J_1(B)\cdot\zeta_0\dfrac{\omega_m}{f_P}\left(1-\dfrac{\zeta_0\cdot f_P^2}{\omega_m^2+f_P^2}-\dfrac{\omega_m^3}{\omega_m^2+f_P^2}\right)+ \\ J_1^2(A)J_0(B)J_1(B)\cdot\dfrac{\omega_m}{f_P}(\zeta_0-1)^2 \end{bmatrix}\cdot\frac{\delta\Omega}{f_P} \quad (4\text{-}71)$$

Both the above expression are calculated for detunings of the FSR with respect to the modulation frequency Ω in units of the cavity's line-width. The error signal for the lock of the laser to the cavity, assured through the demodulated signal at ω_m, will have the customary form:

$$ES_{Ph_{cav}} \propto E_R^* E_R \cdot \frac{e^{i\omega_m\cdot t}-e^{-i\omega_m\cdot t}}{2i}$$

and thus shall be:

$$ES_{Phcav} \propto \frac{1}{2i}\begin{bmatrix} J_0^2(A)J_0(B)J_1(B)\cdot\left(R(\omega)R^*(\omega+\omega_m)+R(\omega)R^*(\omega-\omega_m)-c.c\right)+ \\ J_1^2(A)J_0(B)J_1(B)\cdot\begin{pmatrix} R(\omega+\Omega)R^*(\omega+\Omega+\omega_m)+R(\omega+\Omega)R^*(\omega+\Omega-\omega_m) \\ -R(\omega-\Omega)R^*(\omega-\Omega+\omega_m)-R(\omega-\Omega)R^*(\omega-\Omega-\omega_m) \\ -c.c \end{pmatrix} \end{bmatrix} \quad (4\text{-}72)$$

which, as long as we leave out the second smaller term in $J_1^2(A)J_0(B)J_1(B)$, is exactly the standard phase demodulated Pound-Drever-Hall signal, with an adjunctive $J_0^2(A)$ multiplying our expression. We can thus show analytically that in this configuration it is

possible to obtain a lock of a laser to a reference cavity while at the same time controlling the reference length. Let us now analyse in detail the SNR before showing how the simulation built for these error signals validates the lock insensitivity to the other detuning (FSR-Ω and laser-cavity respectively).

Signal to Noise Ratio

The signal to noise ratio is once more calculated according to the expressions given in Section 2.2, and for the case of laser to cavity lock is indeed at first order exactly the one given for the Pound-Drever-Hall single Pass signal as long we multiply by $J_0^2(A)$. For the cavity-modulation frequency lock, we have already seen the expression of the error signal at first order in function of the detuning. There remains to be calculated the Noise contribution which shall yield if we rename the quantity ω_m/f_P as *f:*

$$N \propto \sqrt{\left[J_0^2(A)J_0^2(B)+2J_0^2(B)J_1^2(A)\right]\cdot\zeta_0^2+2\left[J_0^2(A)J_1^2(B)+2J_1^2(B)J_1^2(A)\right]\cdot\frac{\zeta_0^2+f^2}{1+f^2}} \qquad (4\text{-}73)$$

for the noise contribution. And thus for the in phase (easier to use as it doesn't require a dephaser) case in ω_m we have the following expression for the signal to noise, considering only the biggest contributions in terms of the Bessel *J* functions:

$$SNR \propto (1-\zeta_0)J_0(A)J_1(B)\cdot\frac{1+2f^2}{1+f^2} \qquad (4\text{-}74)$$

with the same conventions used above. From now on we shall only analyse the in phase signal, but all conclusions concerning the cavity-modulation lock are just as valid for the quadrature signal.

Simulation and double lock

Once again we use the MatLab environment to create a routine tracing the error signal line-shapes of the DM error signals. For the cavity-modulation frequency lock it is possible to demonstrate that the laser-cavity detuning doesn't effect the error signal. For a cavity Finesse of 1,500, a ω_m=100kHz and an optimal coupling we have that the error signal, in this case on reflection, doesn't change when we move $f_P/4$ out of resonance as can be seen for the phase in Figure 4–20 and for the quadrature in Figure 4–21. The same result can be obtained in the case of the transmission signal as long as we choose a modulation frequency ω_m smaller than the cavity's cut-off frequency f_P.

Thus we have an error signal that can be used to lock a cavity FSR to a chosen reference producing a stable modulation frequency, be it an atom (e.g. Ultra Stable Oscillator) or a molecule. The Pound-Drever-Hall signal's being independent from the length variation of the cavity is a well known fact. This cavity length control technique requiring a double

modulation and demodulation one at a very high frequency since typically a FSR is of the order of 10^8 to 10^9Hz, is however difficult to image applied in space.

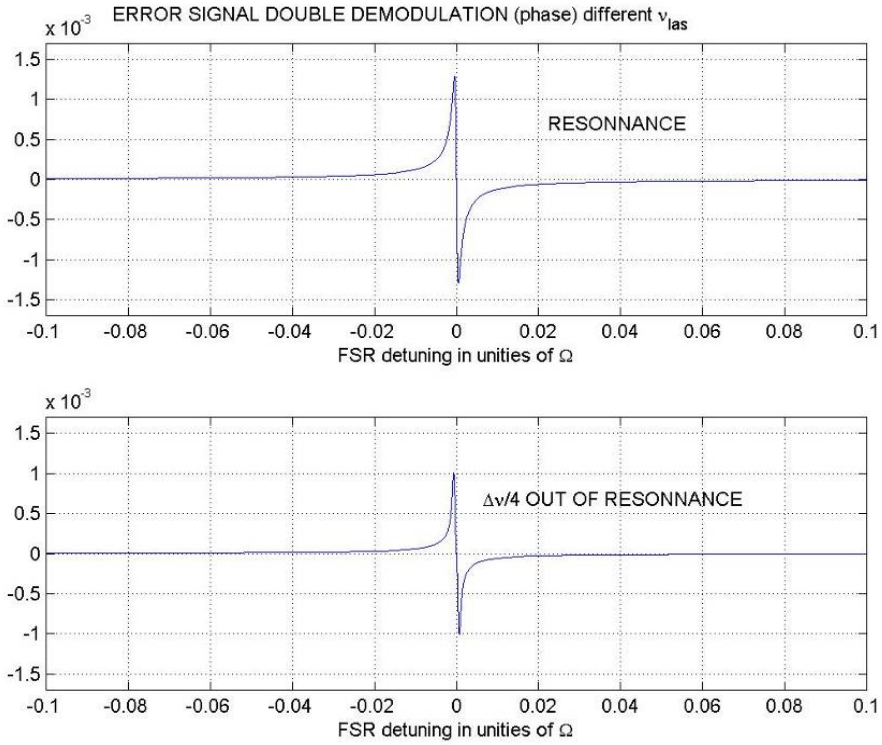

Figure 4–20

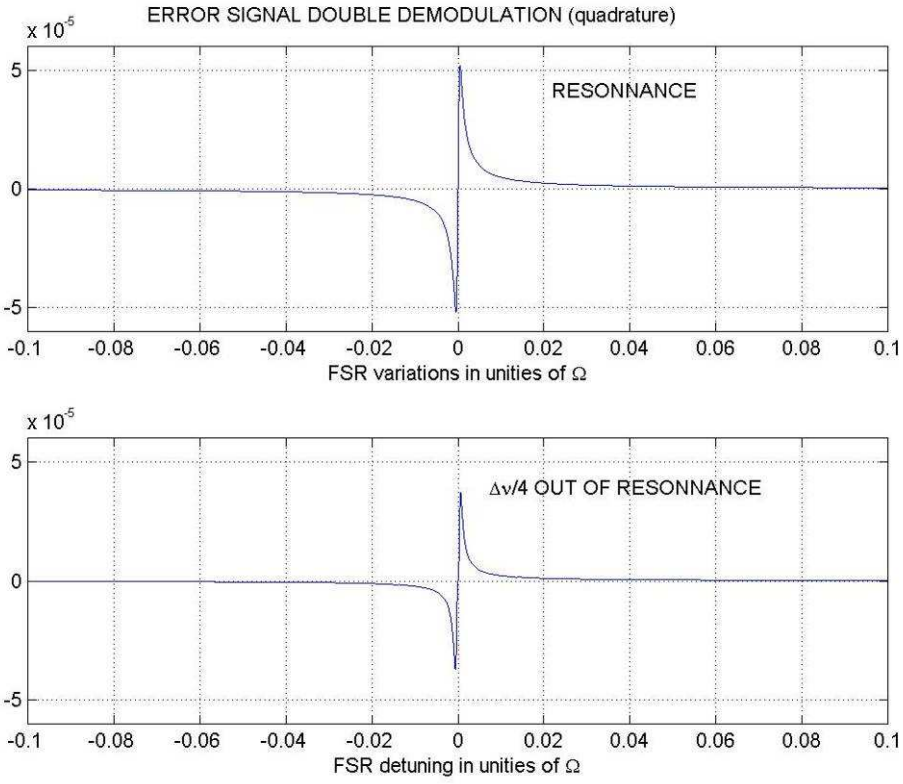

Figure 4–21

4.4.2 Determination of the FSR of a FP Oscillator

While a double demodulation is necessary to implement a lock of the cavity length to the modulation frequency a simple measure of the FSR of the Fabry-Perot can actually be obtained with a single demodulation and no more sophisticated instrumentation than an oscilloscope. We introduce the two modulations at both the FSR and the lower ω_m frequencies. Demodulating just the once at Ω we can obtain by monitoring the amplitude of the signal at ω_m an accurate estimate of the FSR actual value. If we are in a condition were it is possible (as is the case for the Virgo interferometer) to cause a drift of the FSR of the cavity in exam, and we do so, then the right-hand minimum in the profile of the signal intensity shall be an estimate of the FSR value.

The data used for the fit in Figure 4–22 were obtained courtesy of F. Bondu (Virgo collaboration) and were fitted to the theoretical profile with a MatLab routine developed in collaboration with M. Taubman of PNNL. This routine allowed us to also estimate the quantity of Amplitude Modulation present on all three EOMs on the Virgo laser source up to that point in the optical path.

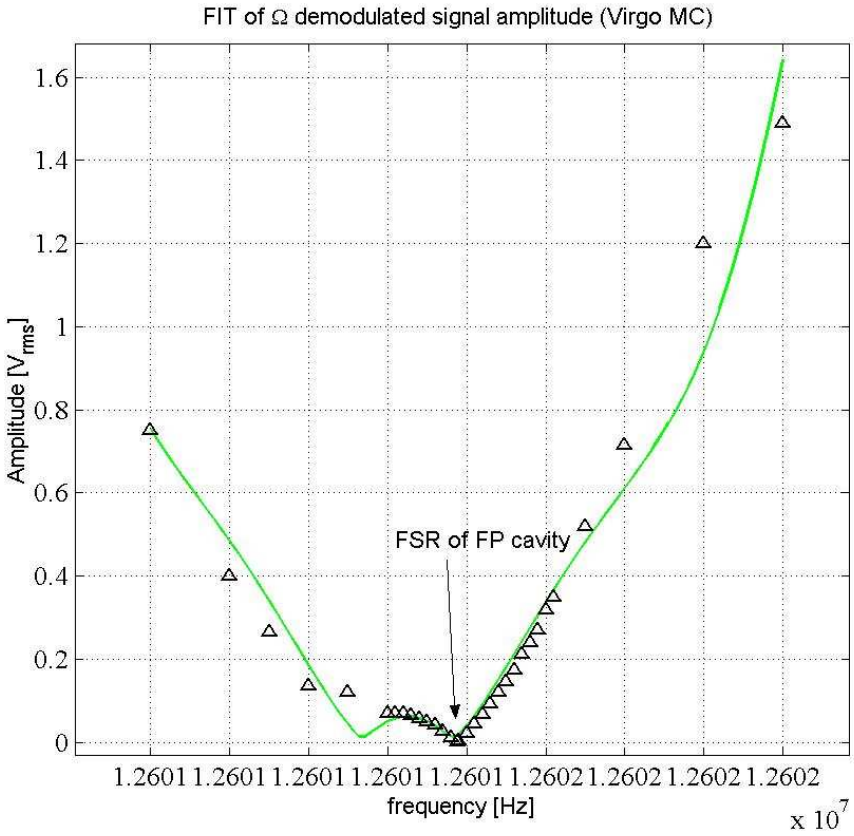

Figure 4–22

4.4.3 FSR Lock (NICE OHMS)

A simplification of the DM cavity control technique was suggested and used by the Hall[29] group at JILA. In this configuration that has been called FSR-Lock the two modulations are introduced through a single EOM, the FSR modulation signal being in its turn modulated at ω_m. The main advantage is however in the demodulation chain since a single demodulation at ω_m in quadrature suffices to obtain an error signal measuring the detuning between the cavity's FSR and the modulation at Ω. Let us now see how we obtain the error signal, before calculating the expression for the SNR and showing numerically that the lock technique is not dependent from the laser-cavity detuning.

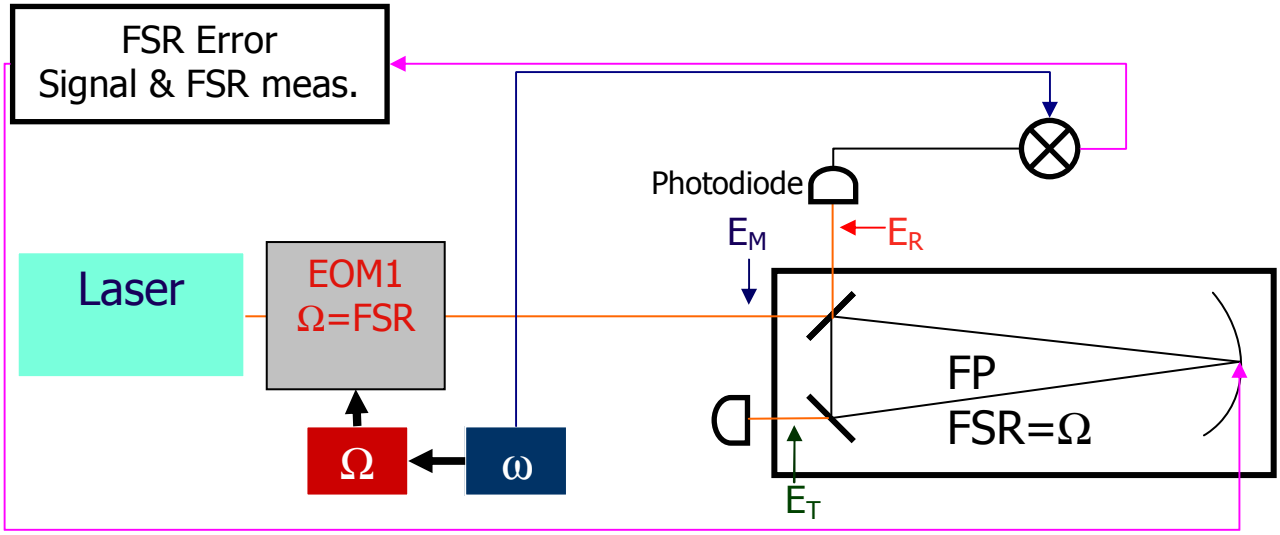

Figure 4–23

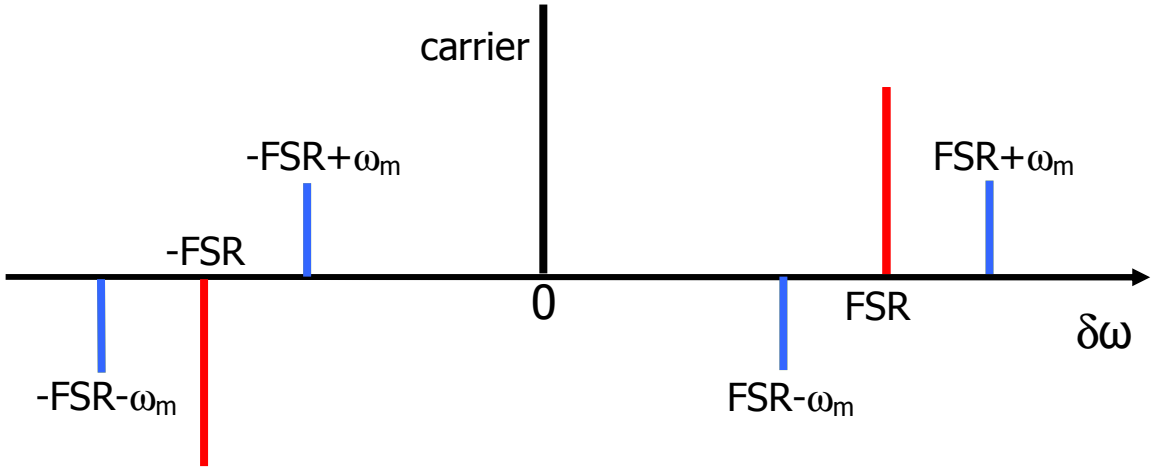

Figure 4–24

Error Signals extraction

Let us determine the form of the modulated field in this modulation configuration. If we compare this modulation schematic, Figure 4–24, with the one shown in Figure 4–19 we can spot the lack of modulation sidebands on the carrier field. The two sidebands at Ω (modulation depth A) shall show the effect of their driving signal's modulation at ω_m (modulation depth B). The modulated field shall have the form, this time, after the expansion stopped to the first harmonic of the modulation terms:

$$E_M = E_0 \cdot e^{i\omega t}\begin{bmatrix} J_0(A)+J_1(A)J_0(B)\left(e^{i\Omega\cdot t}-e^{-i\Omega\cdot t}\right)+ \\ J_1(A)J_1(B)\left(e^{i(\Omega+\omega_m)t}+e^{-i(\Omega-\omega_m)t}-e^{i(\Omega-\omega_m)t}-e^{-i(\Omega+\omega_m)t}\right)\end{bmatrix} \tag{4-75}$$

The reflected field can be calculated in the customary fashion, as can the transmitted field. The error signal will be given, for the case of a signal on the reflection port of the cavity, by:

$$ES_{Q_R} \propto E_R^* E_R \cdot \frac{e^{i\omega_m\cdot t}+e^{-i\omega_m\cdot t}}{2},$$

which gives in function of the reflectivities:

$$ES_{Q_R} \propto \frac{1}{2}\left[J_1^2(A)J_0(B)J_1(B)\cdot\left(\begin{array}{l} R(\omega+\Omega)R^*(\omega+\Omega+\omega_m)-R(\omega+\Omega)R^*(\omega+\Omega-\omega_m)- \\ R(\omega-\Omega)R^*(\omega-\Omega+\omega_m)+R(\omega-\Omega)R^*(\omega-\Omega-\omega_m) \\ +c.c \end{array}\right)\right] \tag{4-76}$$

in its turn after a development to the first order in δΩ (FSR-Ω detuning) yielding the final expression:

$$ES_{Q_R} \propto J_1^2(A)J_0(B)J_1(B)\cdot\frac{4\omega_m^2}{\omega_m^2+f_P^2}\left[\zeta_0^2\cdot\left(1-\frac{2\omega_m^2}{\omega_m^2+f_P^2}\right)+1-\frac{2f_P^2}{\omega_m^2+f_P^2}\zeta_0\right]\cdot\frac{\delta\Omega}{f_P} \tag{4-77}$$

Where, as seen for the DM, the expression is the ES for detunings of the FSR with respect to the modulation frequency Ω, in units of the cavity's line-width.

The error signal, for the lock of the laser to the cavity, won't be assured by the demodulation at ω_m as was the case for the previous locking technique. But the lock between laser and Fabry-Perot can still be assured through Tilt Locking or indeed Pound-Drever-Hall provided we introduce a second modulation on a separate EOM, which effectively brings us back to the DM configuration. The laser might also be locked onto a molecular resonance. In this configuration the cavity would be effectively locked onto a molecular resonance hence acquiring the latter's long term stability. This configuration (NICE-OHMS[35][15]) is nearly exclusively used for very low absorption molecules such as

acetylene (C_2H_2) and mono-deuterated acetylene (C_2HD) which require such important absorption paths that they must be inserted into a cavity to obtain a significant signal. On the other hand this configuration allows the spectroscopic analysis of narrow (kHz) overtone transitions which are eminently attractive for laser frequency locks. The insertion of a strongly absorbing molecule such as Iodine in an optical resonator will only result in an augmentation of the losses in the Fabry-Perot with a subsequent deterioration of the cavity Finesse. This is the main reason for our choice of not using this configuration with our Iodine cells. Having shown analytically that it is indeed possible to control a reference cavity's length in a simpler configuration than the one chosen by the TAMA300 team, at the price of losing the Pound-Drever-Hall lock of the laser on the Fabry-Perot, let us see what happens to the SNR.

Signal to Noise Ratio

Once more we refer to the expressions in Section 2.2 for the starting point of the SNR calculation. For the error signal of the cavity length control we have already extracted the approximated form at the first order of the detuning. There remains to be calculated once again the Noise which shall give, if we rename the quantity ω_m/f_P as f :

$$N \propto \sqrt{\left[J_0^2(A)J_0^2(B)+2J_0^2(B)J_1^2(A)\right]\cdot\zeta_0^2+4J_1^2(B)J_1^2(A)\cdot\frac{\zeta_0^2+f^2}{1+f^2}} \tag{4-78}$$

And thus for the signal to noise, considering only the biggest contributions in terms of the Bessel J functions, we get:

$$SNR \propto J_1^2(A)J_1(B)\cdot\frac{4f^2}{1+f^2}\left(\zeta_0\cdot\left(1-\frac{2f^2}{1+f^2}\right)+\frac{1}{\zeta_0}-\frac{2}{1+f^2}\right) \tag{4-79}$$

with the same conventions used above.

This SNR is always smaller than the one obtained for the DM; this technique results less efficient than its more complicated counterpart.

Simulation and double lock

The numerical simulation is as always built using MatLab. As done for the DM technique we want to ascertain the cavity-modulation frequency lock independence from the laser detuning. We take once more a cavity with a Finesse of 1,500, a modulation frequency ω_m=100kHz and an optimal coupling. The error signal doesn't change when we move $f_P/4$ out of resonance as can be seen in Figure 4–25. We have run our routine for values of the amplitude modulation within 10% of the phase modulation depth without obtaining a substantial change of the error signal line-shape, or indeed any coupling between cavity-modulation and cavity-laser detuning. Thus we can conclude that much as its DM

counterpart the FSR Lock technique is well adapted to measuring and locking a reference to a given modulation frequency.

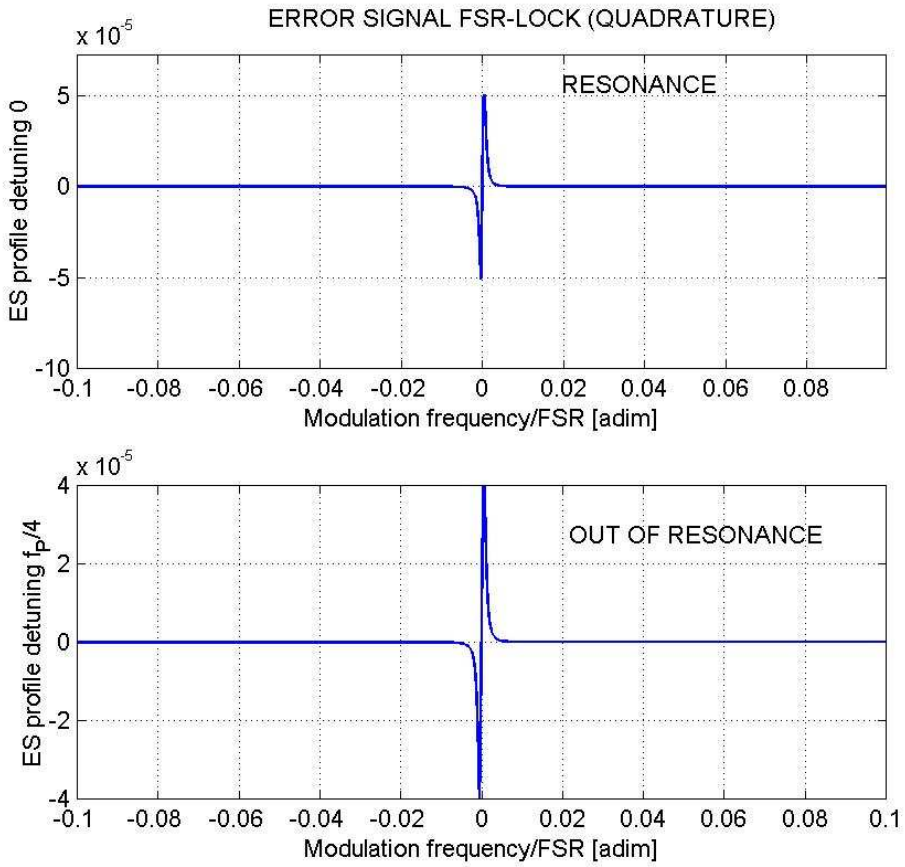

Figure 4–25

4.4.4 USO Lock

In this section we shall see how the above techniques could be implemented to give a reliable and long-term-stable laser source. The thermal deformations of an optical reference can be monitored if we can produce a modulation frequency with stability characteristics better than those desired for the reference. This can be done quite easily with a quartz, a synthesiser, an Ultra Stable Oscillator (USO) or a Caesium clock. The latter enjoys relative frequency stabilities as good as 10^{-14} / $\sqrt{Hz}$ even in commercial products. Hence the proposed technique of the USO-Lock control scheme detailed in Figure 4–26. In this configuration we couple an FSR Lock (since we are aiming for the greatest simplicity for what is a fairly energy consuming and complicated technique) with a Double Pass Tilt Locking. The FSR Lock uses an RF modulation and subsequent demodulation. It is therefore insensitive to all beam misalignments and can work depending on the chosen modulation frequency *f* either on the reflection or the

transmission port (the case shown in Figure 4–26) of the Fabry-Perot resonator. Similarly since Tilt Locking is a DC technique it shall be insensitive to the signals at the modulation frequency and will thus yield an independent FSR measurement of the Laser-cavity detuning. Once the laser is locked to the narrow linewidth of the FP it is then possible to correct the thermal drifts of the cavity bettering the long term performances of the system significantly. In the ideal case, electronic Gain greater than 10^{10} for frequencies below the mHz, we would have created a reference no more than some kHz large with an exactitude equal to that of the USO as long as the sum of the electronics noises was below the mV. Experimental tests of this configuration should be able to confirm the performances of this suggested technique. The laser frequency variations, as shown in Section 4.4.3, do not influence the USO-cavity lock, also once the laser is locked to the cavity these fluctuations go towards zero.

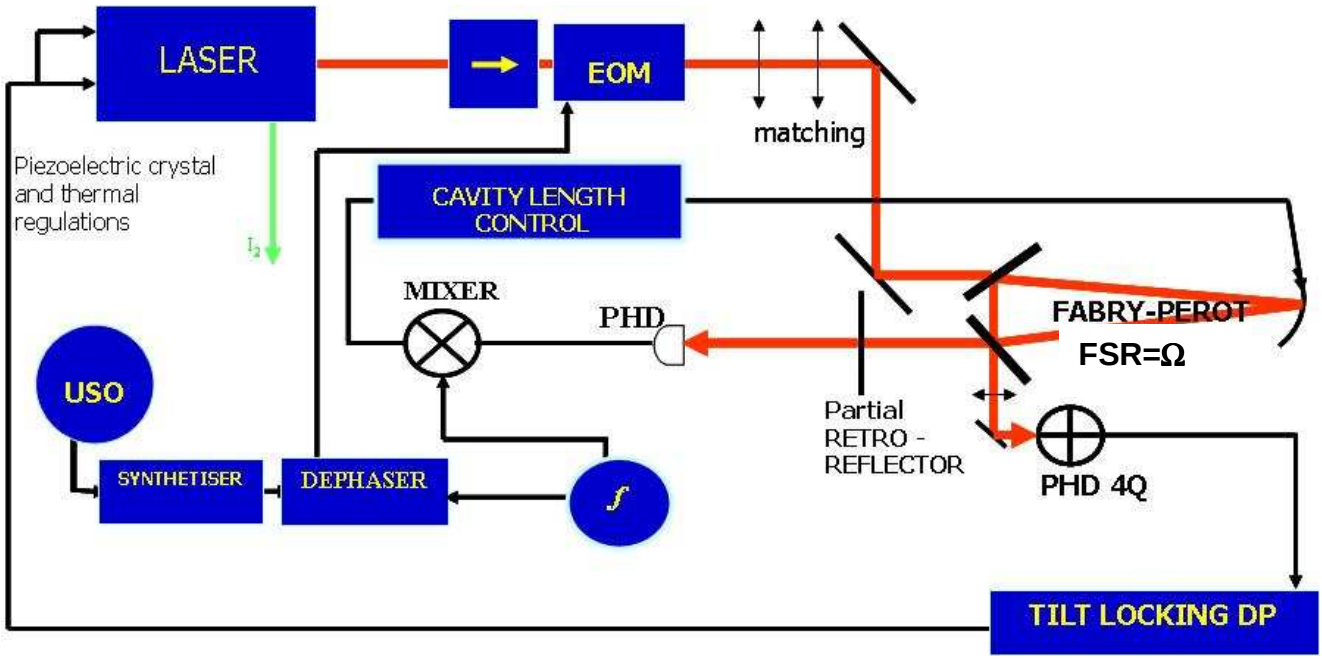

Figure 4–26

4.5 Choosing appropriate techniques

Concerning the lock on resonators the following experimental tests seem to be necessary to chose appropriate laser and cavity stabilisation techniques. The performances of Tilt Locking have to be tested experimentally, against the Pound-Drever lock and against Iodine to confirm the findings obtained with theoretical calculations and simulation.

If a FP cavity is chosen as reference for any practical reason a long term length stabilisation of this cavity has to be implemented either by thermal isolation or an active control. The actual deformations and equivalent frequency variations of a ULE cavity under

vacuum for over 10 years will be measured to determine the isolation (active feed-backs) necessary to stabilise the reference frequency within LISA specifications.

5 Iodine: experimental work

In order to test the performance of our Iodine locked laser we have to compare the created frequency reference with an identical one. With a single experiment, in fact, only an in-loop measurement is possible. This is but a measurement of the efficiency of the servo loop in the correction of the frequency fluctuation. To validate the performance of the laser a beat note with another locked laser of comparable or better stability is necessary. Since Iodine is the suggested metrological reference in the neighbourhood of the doubled YAG laser frequency we have put into place two identical iodine assemblies. After choosing the best transition we have proceeded to analyse its linewidth parameters and have validated the performances of the locked lasers, through a measure of the beat note.

5.1 Experimental lay-out

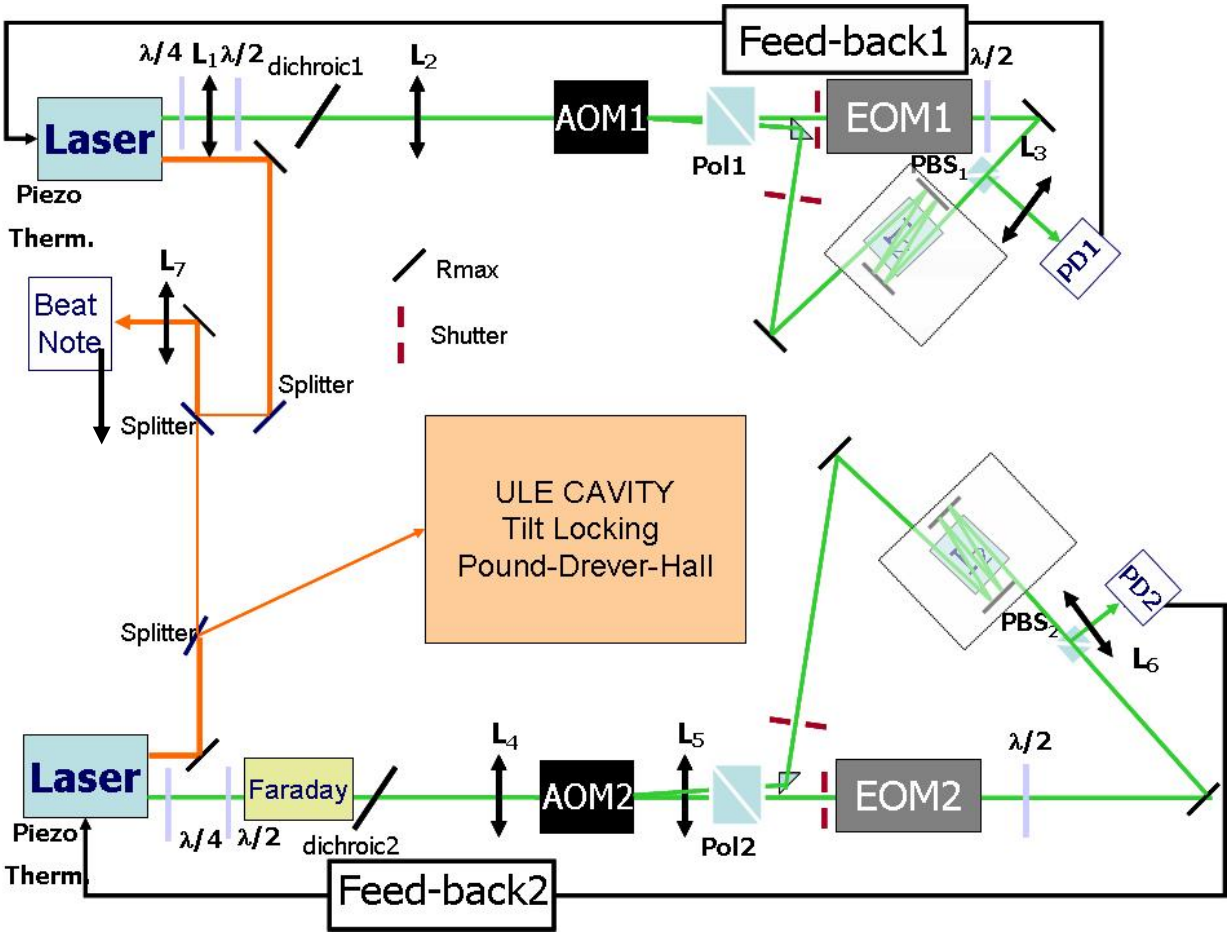

Figure 5–1

In Figure 5–1 we have shown the full experimental schematics of our Iodine set-up including the IR beat note. Let us now analyse in detail the different components of our optical standards set-up.

Lasers and optics

The laser beam is provided by two identical Prometheus20, doubled Nd:YAG laser produced by Innolight, with an IR output of 1W and a green output of 20mW. The frequency doubling is obtained through a single pass in a periodically poled KTP crystal kept at a temperature of 31.5℃ and 32.8℃ for lase r 1 (from hereon P1) and 2 (P2) respectively, for which the green output is maximal. The green and IR beams are separated by two dichroic splitters within the laser head with a transmissivity for the IR close to 1 and high reflectivity in the green region of the spectrum. A third dichroic splitter external to the laser is placed by us on each experiment to reject all IR remaining light intensity from the green beam. Their measured transmissivities and reflectivities are: R_1=0.995 @1064nm and T_1=0.95 @532nm, R_2=0.997 @1064nm and T_2=0.97 @532nm for Experiment1 and 2 respectively (E1, E2). The presence of these splitters is a help in isolating the laser from IR back-reflections which can cause a peak of 43dB$_{QNL}$@130Hz in the power spectrum of the laser, as observed experimentally.

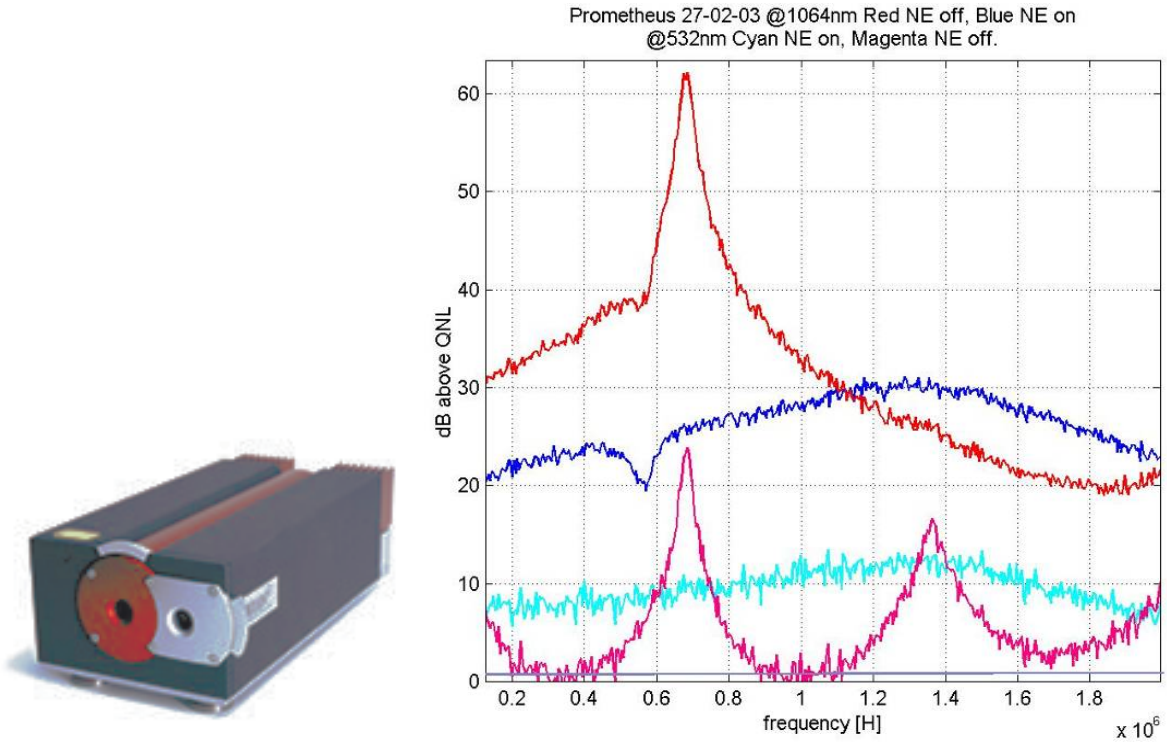

Figure 5–2

The Prometheus laser allows for feed-back on the piezoelectric crystal regulating the length of the laser cavity (cut-off @100kHz), the thermal control of the laser (cut-off @1Hz)

and doubling (1K/V controlled internally) crystals and the current of the injection diodes (cut-off @5kHz, controlled internally, Noise Eater circuit). The linewidth of this type of laser is, as claimed by the builder, 1kHz @ 0.1s. The laser has an integrated power control loop (the Noise Eater) which reduces the intensity noise of some 10dB at low frequencies. This regulation effectively corrects the noise peak at the laser relaxation frequency (close to 700kHz) but adds noise above 1.1MHz as can be seen in Figure 5–2. The beam is Gaussian with an M coefficient lower than 1.1. This value declared by the constructor is in good accord with what we have measured, using a beam scanner for the waists at different positions from the laser head and fitting the obtained data with a custom routine. Our beam scanner is a narrow slit in a rotating cylinder containing a calorimeter and works in the IR domain. We suppose the green beam to have the same spatial characteristics as comforted by doubling crystals theoretical behaviour. The beam waists are for P1: w_H=190µm and w_V=230µm (80mm and 70mm behind the laser head) and for P2: w_H=200µm and w_V=130µm (70mm and 70mm behind the laser head). It has to be noted that a measure of the waists after the first arrival of the lasers into our labs showed waists in the horizontal and vertical direction which were identical in size: for laser 1 of 230µm (67mm behind the laser head) and for laser 2 of 190µm (12mm behind the laser head). The beams became elliptical probably due to a misalignment within the laser heads produced by unknown causes. Since the green spot showed several parasitic beams, at that time, we at first suspected a misalignment of the doubling crystal and acted accordingly. The laser head was opened and the doubling assembly realigned. While this corrected the problem of the loss of power on the green central beam it didn't influence the shape of the IR and green outputs of the beam, which has been, ever since, elliptical. The beam profiles remain Gaussian along all axes. Their profile has been measured at different times showing reproducibility within 5% (experimental errors).

The emitted beams are focalised through a doublet of converging lenses in each experiment to position the imaged waist close to the centre of the beam's path within the gas. The focal lengths for the lenses forming the doublets are L_1=50mm and L_2=257mm for experiment 1 (E1) and L_4=1030mm and L_5=500mm for experiment 2 (E2). The image waists are placed at a distance of 1.33m (1.4m) and measure 1457µm (1365µm) in the horizontal (vertical) direction respectively for E1. In experiment 2 the waist size is smaller of 771µm (1098µm) at a distance of 1.91m (1.78m) in the horizontal and vertical direction respectively. The two arms of the triangular ring containing the gas cell are asymmetric to

compensate for the passing of the pump in the EOM which has a refractive index n_{EOM}=1.7, thus the probe arm is longer by some 22mm than its saturating counterpart.
Polarisation measurements showed for P1 an intensity along the p (in the plane of propagation but perpendicular to the beam) direction 5 times lower than along the s (perpendicular to the plane of propagation) direction, for P2 we measure I_S/I_P=9/2, instead. The polarisation along the beam path is controlled by polarizers, quarter-wave (QWP) and half-wave (HWP) plates. The laser output is first passed through a combination of a QWP and a HWP which acts as a polarisation adjustment (residual rejected polarisation state is lower than 8% of original) but with no loss of power, then is passed through either a Farady isolator (transmissivity=0.92, isolation=27.5dB) and a polarizer or a simple polarizer for experiment E1. The polarizers are given by a double Brewster plate system with AR coatings, they transmit >75% and isolate to $8 \cdot 10^{-3}$, which is an order of magnitude worse than expected for transmission. Defective coatings cannot explain this observed transmission which is also not linked to local defaults of the surface as displacing the beam on the plate surfaces doesn't change the measured values. The Brewster angle error on the mount of the plates can account for the observed transmission loss if coupled with inferior coatings.

P^{tot}=5.7mW for test	Glan pol. 1	Glan pol. 2	Pol. Brewster 1	Pol. Brewster 2
P_t^{max} [V]	98.72%	98.72%	77.15%	75.58%
P_t^{min} [mV]	($8\ 10^{-4}$) 0.08%	($8\ 10^{-4}$) 0.08%	0.85%	0.83%
Isolation	99.92%	99.92%	99.2%	99.2%

Table 5-1

These polarizers serve a double function. First of all, they isolate the laser from all pump beam returns towards the laser head. They also insure that the laser beam injected into the Electro-Optic Modulator is in the s polarisation state, as specified by the constructor for optimal performances (reduction of Amplitude Modulation, though this can also be regulated in our case simply by the turning the cylindrical housing of the EOM crystals) of

the same, after its pass through the Acousto-Optic Modulator. The AOM, after micrometric alignment (which is responsible for the power of emitted beams) with the incident beam, creates an adjunctive -1 order beam which shall have, in our setup, a frequency shift equal to minus the driving frequency. Thus for E1 we have a frequency shifted beam, the intensity (and potentially alignment) of which is regulated by the modulating signal amplitude, of -80Mhz and on E2 of -160MHz. These second beams are used as probe beams whereas the 0 order, not frequency shifted, is used as pump. The AOM are calibrated to work close to the 532nm domain and were produced by A&A. On E1 we have an AA.ST.80-A1-VIS model with a TeO_2 crystal an aperture of 1mm and a central frequency of 80MHz, on E2 we have AA.ST.150-A0.5-VIS (central frequency 150MHz, and aperture 0.5mm). The AOM are driven by an Adret Electronique 730A Synthesiser for the 160MHz on E1 and by a 80MHz not thermalised quartz for E2, their stability, measured with our frequencymeter, is presented in Figure 5–4 and Figure 5–3 respectively.

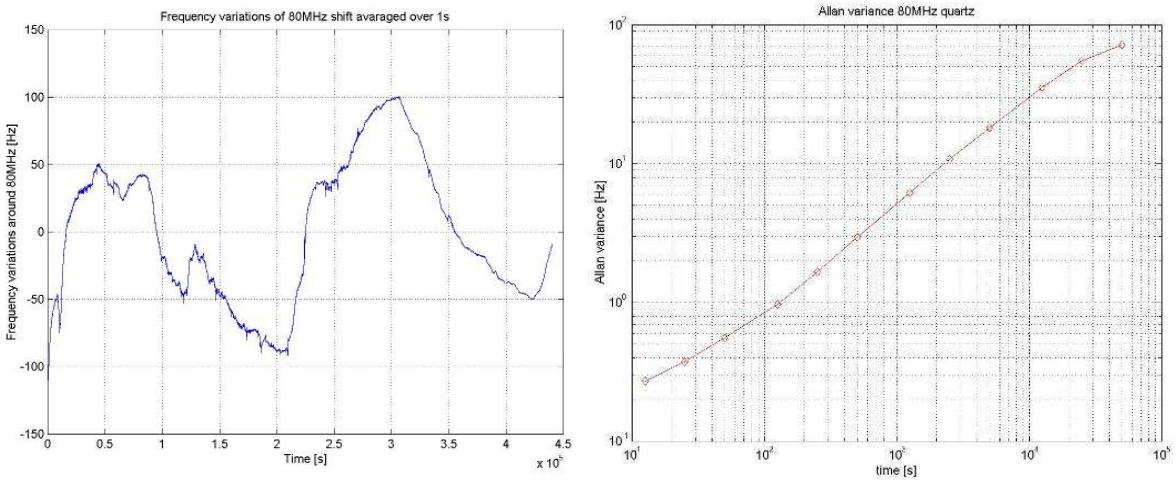

Figure 5–3

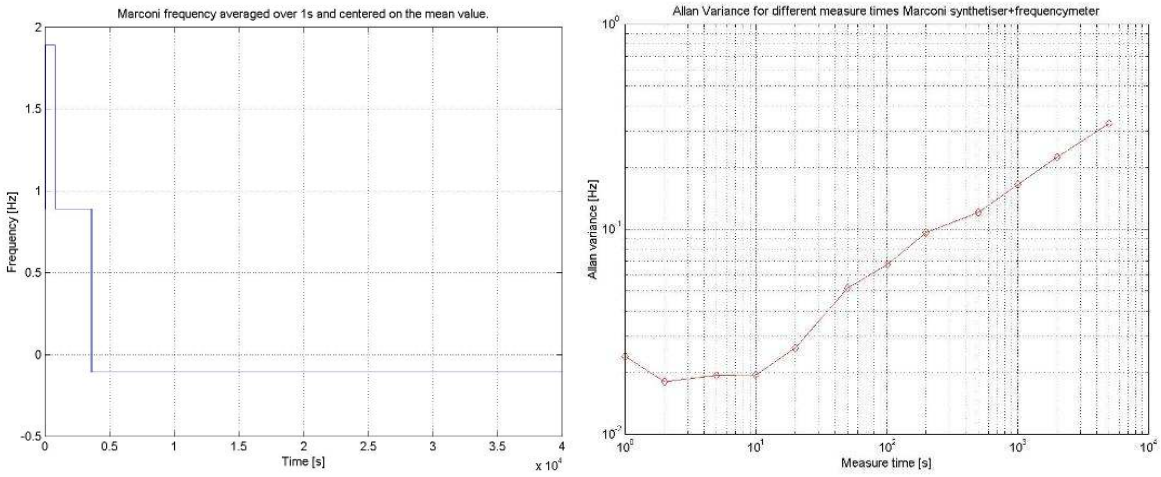

Figure 5–4

The quartz signal is passed through a low noise amplifier and an attenuator which allows for a regulation of the 'modulation depth'. The synthesiser signal can be set to emit signals between -21 and 21 dB of amplitude. The measured beam intensities are for the saturating beams I_{Sat1}=5.7mW and I_{Sat2}=6.1mW, for the probe beams instead we have I_{Probe1}=50μW and I_{Probe2}=48μW. The pump (saturating) beams are then passed through the Electro-Optic Modulators (LM0202PHAS, LINOS, half wave voltage 160V) which create a phase modulation at a frequency of 82.3kHz for E1 and 91.7kHz for E2. These frequencies are variable but in our last experimental configuration are always lower than 100kHz. The introduced amplitude modulation, which has been reduced by turning the EOM crystal, in the best configuration, is always lower than $16\mu V_{RMS}/\sqrt{Hz}$. The EOM are driven by a Philips PM5134 and a TTi TG120 sinusoidal generator, for E1 and E2 respectively. Their signals are amplified by a LC resonating circuit using the 82pF EO crystal capacitance and having a Q of 1. The beam exiting the EOM is passed through a zero order HWP which turns its s polarisation into a p. This is useful firstly to ensure that the saturating beam doesn't arrive on the detection photodiode and secondarily to ensure that is has the polarisation state that will be rejected by the polarizers positioned after the AOM and which will therefore isolate the laser from the returning intense saturating beam. The laser is isolated from the probe beam return because the latter is frequency shifted. To separate the pump from the probe we use a Glan polarizer. These polarising beam-splitters deviate slightly both beams and in particular eject the s polarisation state beams with a 30° angle but also assure much better performances than standard polarising beam splitters. Ideally isolating to 10^{-5} they have measured isolation of $5 \cdot 10^{-4}$ (Table 5-1). They are positioned before the delay line start on the pump beam path in order to reject its s polarisation component before the first nearly 0 angle reflection of the saturating beam. This should ideally reduce the back scattering of the modulated pump (responsible for offsets on the error signal), also the detection splitter must be placed after the probe has traversed the gas cell. The alignment of the Glan polarizers must be extremely accurate as otherwise given the presence in our polarizer of only one exit window we shall have the appearance of fringes on the probe beam sent towards the photodiode. To ensure that there were no contributions on the photodiode due to back-reflection of the pump beam we positioned a second Brewster polarizer on the detection beam. This having been shown to have no positive effect, but entraining the loss of 25% of the power, we subsequently removed this component.

Molecular reference: Iodine cell, support, cooling system and isolation

The iodine gas is held in two 10cm long glass cells with AR treated plane windows, which reflect less than 1% (instead of the customary 4% but much more than the 0.1 afforded by most AR coatings) of the incident light backwards at each pass. In order to have a better contrast we have lengthened the beam optical path in the gas cell by using a multi-pass configuration with a delay line. We first set up a delay line with 7 passes in the gas cell, subsequently due to the amount of backscattering per pass and the presence of overlap of the different beams we decided to reduce the number of passes to five. The total path in Iodine is of (510±2)mm. The temperature of the cell is regulated through a water cooled Thermoelectric (Peltier) element. The current applied to the Peltier device is given by two continuous generators whose output is regulated by a transistor driven divider. The current used is regulated through a feed-back loop which measures the temperature of the copper block close to the point of contact with the gas cell and corrects the variations.

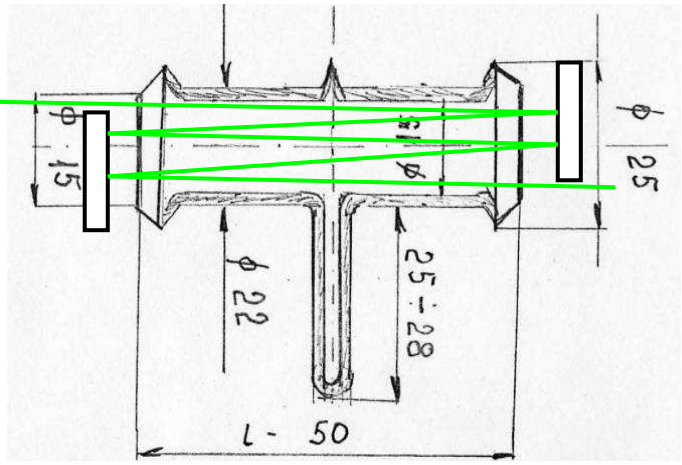

Figure 5–5

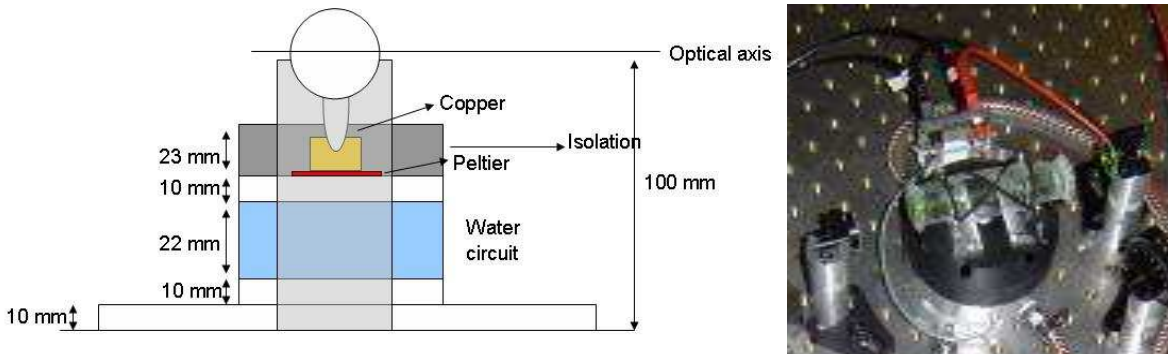

Figure 5–6

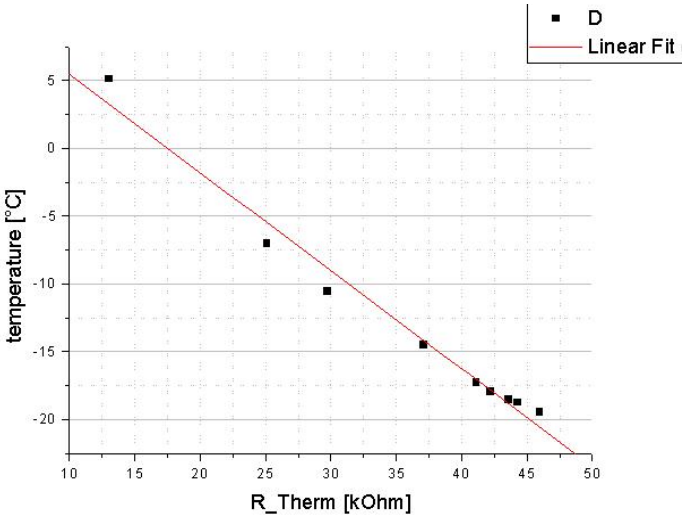

Figure 5–7

The temperature is measured by an NCTS, a very sensitive temperature dependent impedance, whose values vary typically (as shown in Figure 5–7) from 5kΩ for room temperature to some 45kΩ for -20℃, in a bridge configuration (see Figure 5–9). We calibrated our thermal control regulation (the blue variable impedance in Figure 5–9) in order to have a correspondence between the regulation and the chosen temperature obtained as shown in Figure 5–8 for both cell1 and cell2.

It is also possible by measuring the error signal (V_S) of the regulation electronics to obtain the values of the temperature of the cold points and to measure their variations. Let us now consider the bridge configuration shown in Figure 5–9.

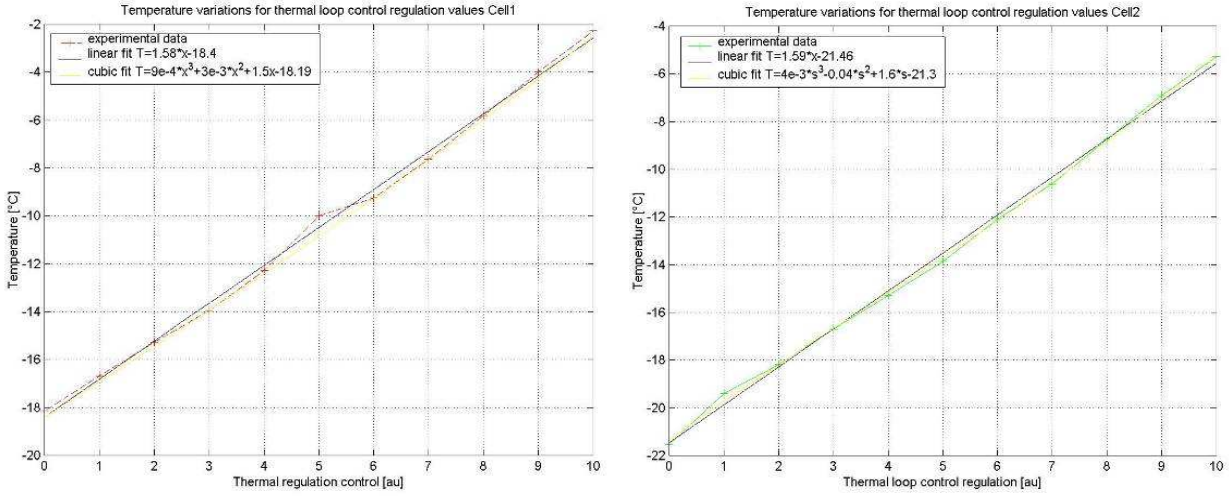

Figure 5–8

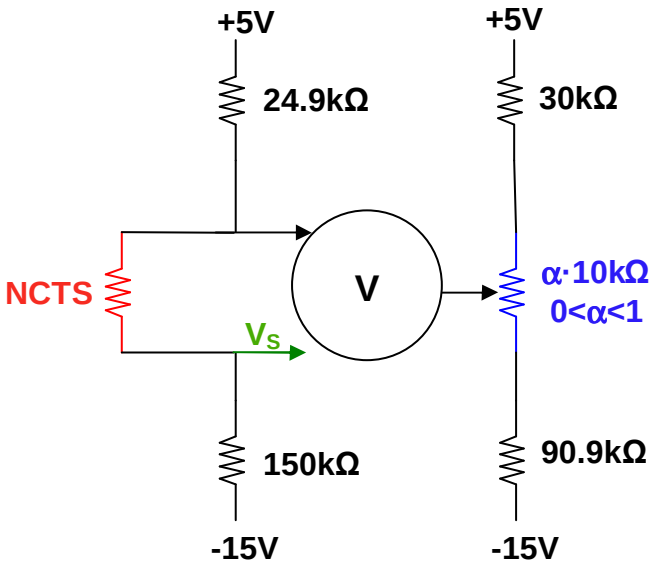

:

Figure 5–9

The value of the NCTS impedance at the equilibrium, if we express all impedances in kΩ, shall be given by:

$$\frac{R_{NCTS}+150}{R_{NCTS}+150+24.9}=\frac{10\cdot\alpha+90.9}{90.9+30+10} \tag{5-1}$$

The impedance variations monitored by the error signal variations V_S shall be obtained multiplying by the conversion constant given by deriving the expression:

$$V_S=\frac{20V\cdot 150}{(150+24.9+R_{NCTS})}+C \tag{5-2}$$

where once again all impedances, including R_{NCTS}, are in kΩ, and thus:

$$\frac{dV_S}{dR_{NCTS}}=\frac{-20V\cdot 150k\Omega}{(150+24.9+R_{NCTS})^2}=-71mV/k\Omega\,@\,30k\Omega\,. \tag{5-3}$$

We have seen that for a 30kΩ value of the impedance of the NCTS (which corresponds to a temperature close to -10℃, in its turns a regula tion of the E1 potentiometer of 5 and for E2 of 7) the conversion constant between the temperature variations and the error signal variations (taking into account that from Figure 5–7 we have K_{NCTS}=-0.8℃/k Ω) is

$$\frac{dT}{dV_S}=11.3°C/V\,@-10°C\,.$$

As seen in Section 3 the temperature of the cell cold point influences both the transition linewidth and weakly its intrinsic frequency. From Section 0 we determine that a temperature stability of 10^{-3}℃ is necessary to assure frequency stability and a ccuracy of the order of the Hz, but for a frequency stability of 10Hz a temperature controller regulating

to 0.01℃ (variations of the error signal below the mV) is sufficient. The servo loop assuring this temperature stabilisation suffers mainly from the long response time of the Cell-Peltier-support which is greater than 500s. In view of this it is obvious that the unity gain of the servo-loop must be placed close to the mHz, faster temperature shifts are not corrected. This also limits the gain which we can have at frequencies close to the unity gain. Thus the temperature of the cooling water must also be stabilised to avoid excessive variations (especially at frequencies close to the unity gain) that the servo loop won't be able to compensate. To obtain this we first used the water coming from a 4l temperature stabilised commercial cooling system bringing the water to a lowest temperature of 9℃. This system has an all-or-nothing Freon cooler with a hydraulic temperature sensor and an incorporated vane pump. Its residual temperature variations of 4℃ are too large to be corrected by the cold point servo loops resulting in variations of the temperature of the degree Celsius. To solve this problem we first tried to force the cooler to be on in permanence by adding a home-made heating system on the return water, this unfortunately left variations of the order of the 1℃ on the water and of the order of 0.1℃ on the cold point temperatures. We subsequently took a large 20l reservoir, cooled it to temperatures around 16℃ by using the ancient coole r and a home made copper coil, and used an aquarium pump to have the water circulating.

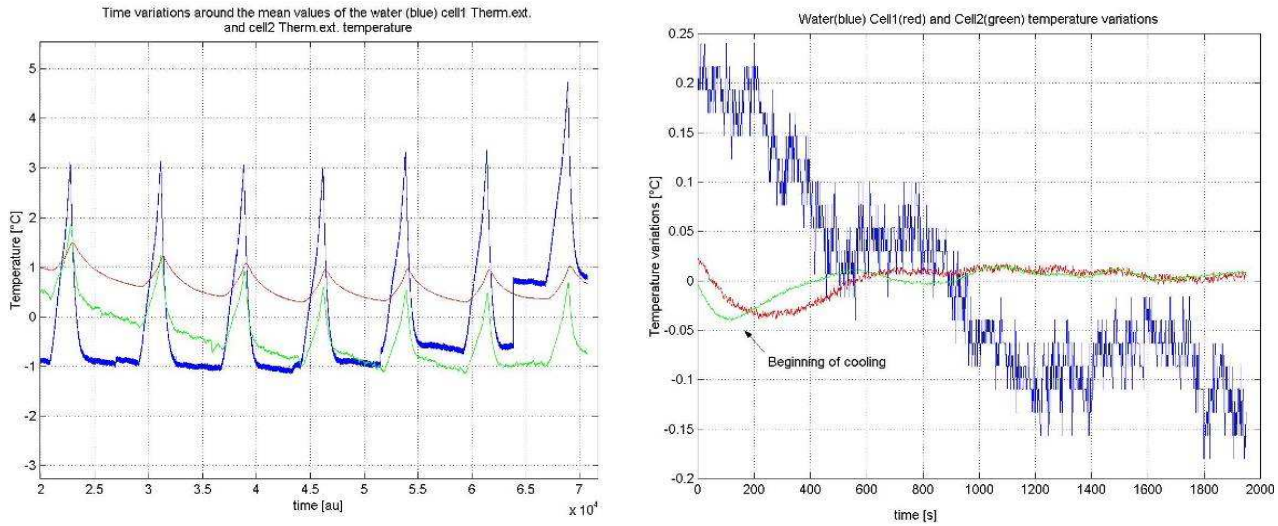

Figure 5–10

As shown in Figure 5–10 with this configuration we reach water temperature stability close to 0.5℃, which in turn translates, once transitory effects no longer influence the system, into a cold point stability of 0.01℃ as requested. Improvements of the cooling system would require a better thermal contact between the Peltier cooled copper piece and the gas cell, this would reduce the time constant of the system and allow us to have greater

loop gains at higher frequencies. 0.1mK temperature stabilities are reported by Braxmeier (Private Communication L.Mondin LISA Symp.V) using a copper lining around the whole of the gas cell. The fact that our cell touches the copper in one point is troubling because this causes both gradients of temperature in the cell and the mentioned delays in the response of the system. To reduce this problem we have added thermal shielding for the whole cell and support system. These plastic lined foam boxes have been clamped to the table and afford us a passive thermal isolation of the cell and support (extending even to the delay line mirrors) which can be estimated to be no lower than 6.0dB.

Photodetectors

For these experiments we have used two identical Silica photo-detectors (PD) accorded at 100kHz (Q=1) with a continuous impedance of 100kΩ and a transimpedance of 200MΩ. The quantum efficiency of this particular Silicium PIN is η=0.38 @532nm. The dark currents have been measured. It is always much lower than the photon noise Power Spectral Noise Density, for our chosen laser power in the case of PD2 (see Figure 5–11). Not so for PD1 where we have a 200mV electronic dark offset coming from the detector. This effect is however negligible in the face of the much larger size of the error signal (tens of Volts) especially since the offset value monitored over long time stretches has been shown to be constant.

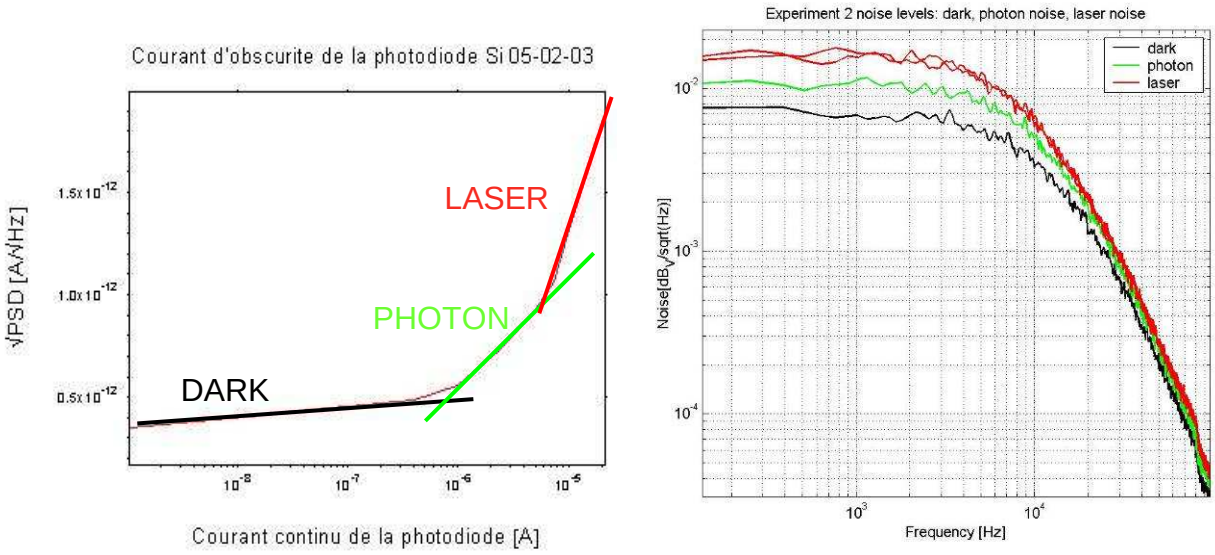

Figure 5–11

Lock in and servo loops

The electronics were conceived and built by J.P. Coulon.

The two iodine control loops are identical. The demodulation on the iodine system is taken care of either through a digital SR830 lock-in Amplifier (DS error signals) or through a

home built mixer and amplifier (ES signals). The demodulation phase reference signal is given by the modulation generator TTL signal, opportunely dephased through the phase regulation of the SR830, to give the desired error signal. The two different signals (ES and DS) have the same amplitude, are both filtered at 1ms and then one of them is injected into a series of integrator. This series counts a single integrator and then, in series, a cascade of three more integrator. This set up gives a 1/frequency Gain at frequencies between 3.5kHz and 300Hz and a 1/frequency to the fourth for the frequencies below the unity gain of the cascaded integrators (300Hz). The pole introduced by the 1ms time constant low pass filter (6dB/OCT) is compensated through a 1ms time constant (RC combination) on the first integrator. The resulting integrated signal is then fed back, for frequency above 0.1Hz to the laser cavity piezoelectric and for frequencies below 0.1Hz, after another more integration, to the temperature controller of the laser crystal. The out of loop error signal is used to monitor eventual variations in the frequency, not corrected by the feed back loop.

VCO and lock on beat note

In order to make the analysis of the iodine transition simpler we decided to build a frequency to Voltage Converter. This shall transform a frequency variation into a voltage variation. The scope of this element created and conceived by J.P.Coulon was to enable us to lock one laser on the other by using the IR beat note between the two which effectively measures their frequency variations with respect to one another. Our particular VCO allows us to have Allan variances as low as the Hz and shows also in its central zone (around 20MHz) a nearly perfectly linear behaviour in the correspondence between frequency and voltage, as shown in Figure 5–12. With these performances we can make precision measures of the linewidth of the molecular transition.

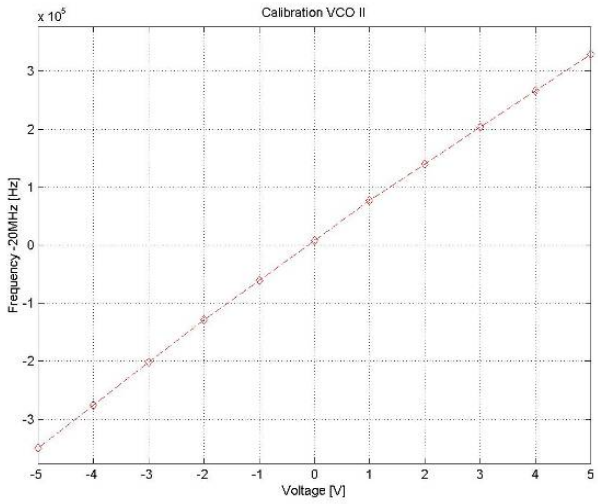

Figure 5–12

Measurement and data acquiring instrumentation

To measure the beat note between the lasers we not only need the photodiode tuned at 20MHz but also an instrument capable of measuring the frequency of the beat note. This is, in our case, a Hewlett Packard frequencymeter, model HP53131A. This instrument allows us to measure the frequency of a signal with a precision of the mHz, an accuracy of the mHz and a stability of 10^{-14} thanks to its oven stabilised clock. While better Caesium clock powered versions of the same measurer exist, this was sufficient for our application where the precision needed for the measurement was equal or inferior to that of the frequencymeter. This instrument is capable of measuring the instantaneous frequency of a signal, its mean value over a user inputted number of acquisition, its variance and standard deviation. The gate time of the instrument can be chosen by the user between 0.1, 1 and 10s. It is capable of measuring frequencies up to 150MHz on its two front face entries, and up to 1GHz on its end face panel. The two front face entries can be used to measure frequency differences between two signals, or phase measurements. The HP53131A also has a 10MHz reference source, coming from the clock, that can be used for tests and which enjoys the latter stability. The instrument can be controlled remotely through a GPIB cable. Ready made software is capable of interfacing with Excel on a windows platform PC. LabView VI can be found on the internet (NI site) to save the data coming from the instrument.

To measure voltages and by extension temperatures we use a Keithley DMM199 multimeter, which also has a GPIB connection. This instrument can measure up to 8 values of a chosen physical quantity on its end face BNC channels. Drivers and LabView VI are also available for this instrument. The Keithley multimeter can read Voltages (precision of the μV), currents (nA) and impedances (mΩ), but only one quantity at a time, hence the necessity of the read out of the temperature sensors to come to the instrument from a bridge read-out. The measurements on this instrument are instantaneous thus for noisy signals, filtering (typically with a time constant of 1-10ms) is required. The measurements are taken in series one after the other and stocked into a buffer before being transferred to the PC.

For most measurements we had to read at the same time the frequency coming from the frequencymeter and the Voltages coming from the Keithley multimeter. In order to synchronize the two acquisitions a LabView routine was created by C. Baudouin to acquire all signals at intervals given by the PC clock. This routine creates two ASCII text files, one

containing the time of the PC clock and the frequency, the other grouping all chosen channels of the Keithley multimeter.

Data analysis

The text files created through the LabView routine are then treated with a series of MatLab routines created by myself as a comprehensive and user friendly data analysis system. It is possible to calculate and trace beat note variations, temperatures, frequency equivalent temperature variations, residual frequency variations coming from the error signals. We can trace the curve, with or without additional filtering, the FFT, the histogram (including the fit of the distribution), the Allan variance in function of the integration time. We can also compute the correlation and coherence between two parameters. We can fit the data profile to a lorentzian or Gaussian profile. For more on the data analysis programs please refer to Appendix C.

5.2 Sub-Doppler Iodine molecular spectroscopy

First of all we need to find an adequate molecular transition for the lock of our iodine systems. Two parameters are of interest for the choice of the transition: the linewidth of the transition (which influences the strength of the same, the narrower the less intense) and the isolation of the transition from other transitions. This second parameter is of interest because if we have a narrow doublet it is easy for the system to be locked on the wrong component introducing an a priori error in the precision difficult to identify. The first thing to do then is to identify likely isolated transitions and to determine their linewidth as a function of experimental parameters such as modulation frequency, temperature of the cell's cold point, saturating intensity and modulation depth. As shown in Section 3 molecular linewidth can change significantly (10^4Hz/K) with the pressure but the central position of the reference will be independent (10^2Hz/K typically, 50 Hz/K for our chosen I_2 transition at the temperatures of interest) at first order from the thermodynamic parameters of the gas. Following the indications of the BIPM we have chosen to use the suggested frequency standard which is the a_{10} component of the R56 (32-0) molecular roto-vibrational band. This band corresponds to a transition with a ΔJ=+1 and a vibration level variations between the excited level 32 and the fundamental. Other components, of this same band, which have the necessary isolated character and narrowness, for laser locking, are the a_1 and a_{15} lines. These too were tested to determine their linewidth. Linewidth had to be estimated, both to give a first estimate of the conversion constant of the voltage variations in Hz and for all broadening effects to be identified. Linewidth while an important parameter was not the only parameter we had to consider to optimise our experiment. We

also had to determine the error signal dependence on the intensity of the saturating beam (saturation), the demodulation phase, the modulation frequency and depth (modulation broadening) and the cell cold point temperature (pressure broadening) to choose the best value for all these experimental parameters.

Determination of the experimental linewidth

We can try to obtain an estimate of the linewidth by using a VCO on the beat note photodiode to lock laser 2 on laser 1. While the latter shall be locked to the transition we wish to analyse, the VCO-locked laser shall then be dithered in frequency around 20MHz (frequency shift of laser 2 from laser 1). Since the frequency difference between experiment 1 and experiment 2 is 20MHz, on the IR photodiode, when both systems are on the same Iodine transition, in this way we shall be dithering the green laser frequency around the centre of the transition.

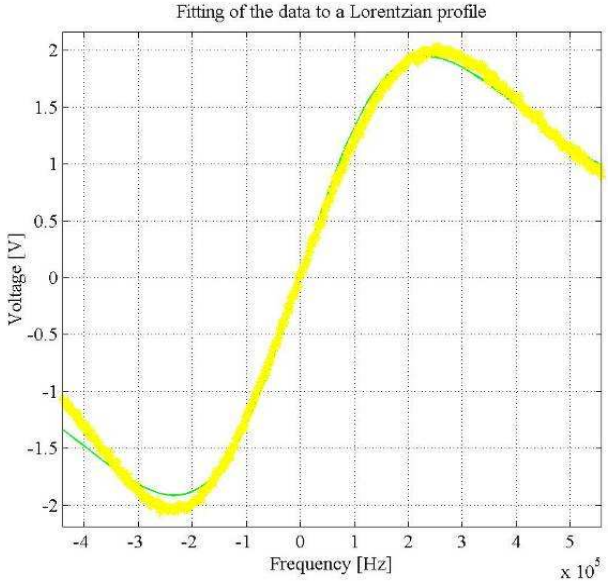

Figure 5–13

By determining with the frequencymeter the value of the frequency offset for the smallest and greatest values of the corresponding error signal we can calibrate the Voltage as a function of the frequency and also give an estimate of the linewidth. This first estimate gives a value of (630±80)kHz. To attain better precision we can trace the profile of the error signal as a function of the frequencymeter measured frequency by acquiring both data streams coming from the frequency measurement and from the multi-meter, measuring the voltage of the Iodine error signal. If the profile of the saturated absorption peak is supposed to be perfectly lorentzian, by fitting the experimental data to the derivative of the Lorentzian function we have a first estimate of the linewidth. The fit has been accomplished through a custom built MATLAB routine. In Figure 5–13 we see an

example of the routine applied to experimental data (yellow stars) taken with a temperature -4.6℃ and a modulation frequency of 53 2kHz. The lorentzian derivative fit is represented by the green continuous line. This estimate yields a value for the broadened linewidth of γ=(700±50)kHz, for the a_{10} transition with a temperature approaching -5℃.

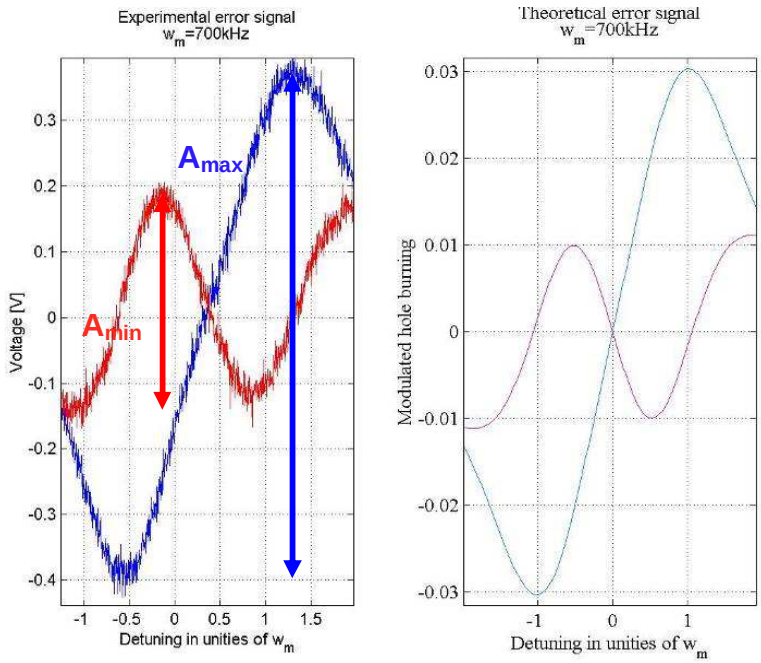

Figure 5–14

This in the case were the modulation frequency ω_m is smaller than the linewidth. If this condition is not satisfied then the error signal has a width equal to $2\cdot\omega_m$. This estimate is however accurate only within a few tens of kHz typically which is why we want to have an independent and more precise fashion of measuring the linewidth. To determine the linewidth of the transition in exam for a set of thermodynamic and optical parameters we can start with the observation that the amplitude relationship between the ratio of the amplitude of the signal in 'quadrature' (A_{min}), and its amplitude in phase (A_{max}) is proportional to the ratio of the modulation frequency (ω_m) over the broadened linewidth (γ). The term quadrature is a bit of a misnomer, in fact the quadric profile shown in Figure 5–14 is not obtained for a phase lag of $\pi/2$ but rather for a value close to the latter. This observation ensures that if we take different measurements of A_{min} over A_{max} for varying ω_m we shall be able to fit the angular coefficient of the slope which is none other than the inverse of the linewidth (γ). This procedure is accomplished thanks to a series of programs developed by M. Taubman during his visit in our laboratory in the fall of 2002. These programs were modified to calculate also the theoretical linewidth for experimental parameters entered by the user. Then the values of A_{min} over A_{max} are computed for corresponding ω_m and the expected γ is calculated. A series of results obtained for the a_{10}

transition at a cold point temperature of -3℃ and a modulation frequency of 500kHz is shown below in Figure 5–15. The experimental points are in red, the green stars indicate the theoretical points and the cyan line is the fit of the experimental points. The value of the linewidth is presented in the MATLAB command window and for the case in exam was of (710±20)kHz. The computed theoretical value γ_{theory}=725kHz supposing a saturation coefficient of S=2 and a modulation broadening of M=1.5 is consistent with the experimental measurement. Having determined the experimental linewidth within a few tens of Hz we can also try to obtain a dependence of the same from all experimental parameters.

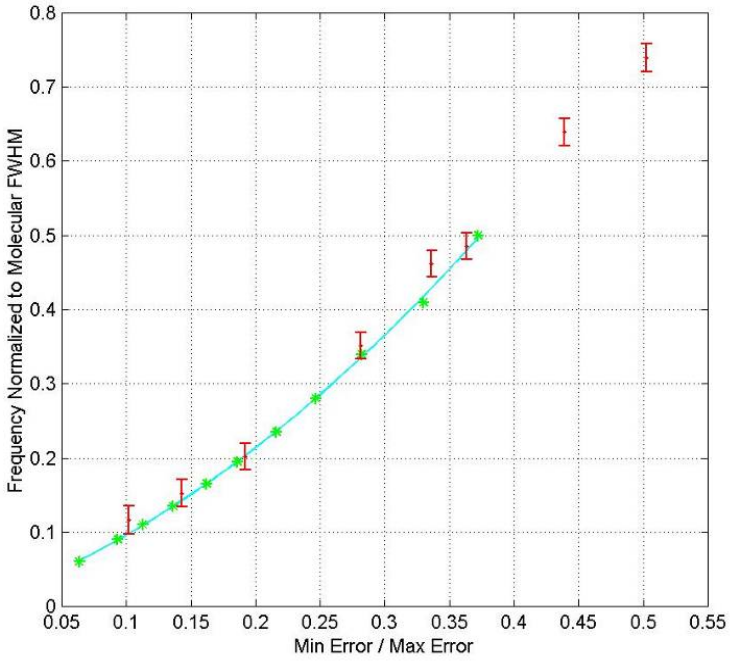

Figure 5–15

Error signal vs. experimental parameters

Let us now see for the transition a_{10} the behaviour of the error signal with respect to the different parameters. The behaviour of the other transitions is similar with respect to all parameters. With respect to the phase we know how the error signal varies from theory. In particular for the case of the in phase signal and close to quadrature signal which gives the quartic we have the profiles shown in Figure 5–16a, experimental curves. Theory predict as shown by Figure 5–16b that variations of the phase, between $\pi/20$ and $\pi/4$, give no appreciable change in the error signal slope, this is verified experimentally. If we now consider the variations of the error signal slope as a function of the modulation frequency we have that the behaviour is shown in Figure 5–17. This shows that for smaller values of the modulating frequency we have narrower error signals and hence greater values of the

ES slope. Only values above 300kHz were investigated, the modulating frequency of our system was then accorded around 300kHz which made a measure at lower frequencies misleading. Subsequent measures at lower frequencies showed that the error signal slope was at its largest for frequencies close to the 100kHz mark, the linewidths in Figure 5–17b are measured on the IR beam, therefore, they have to be multiplied by a factor of 2 when dealing with the green light.

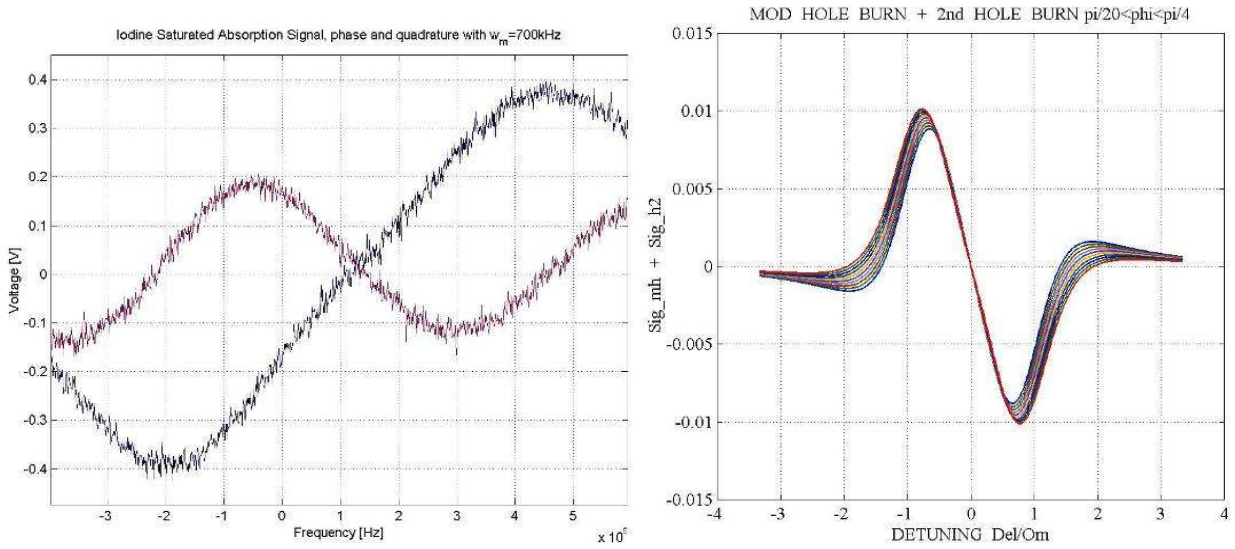

Figure 5–16

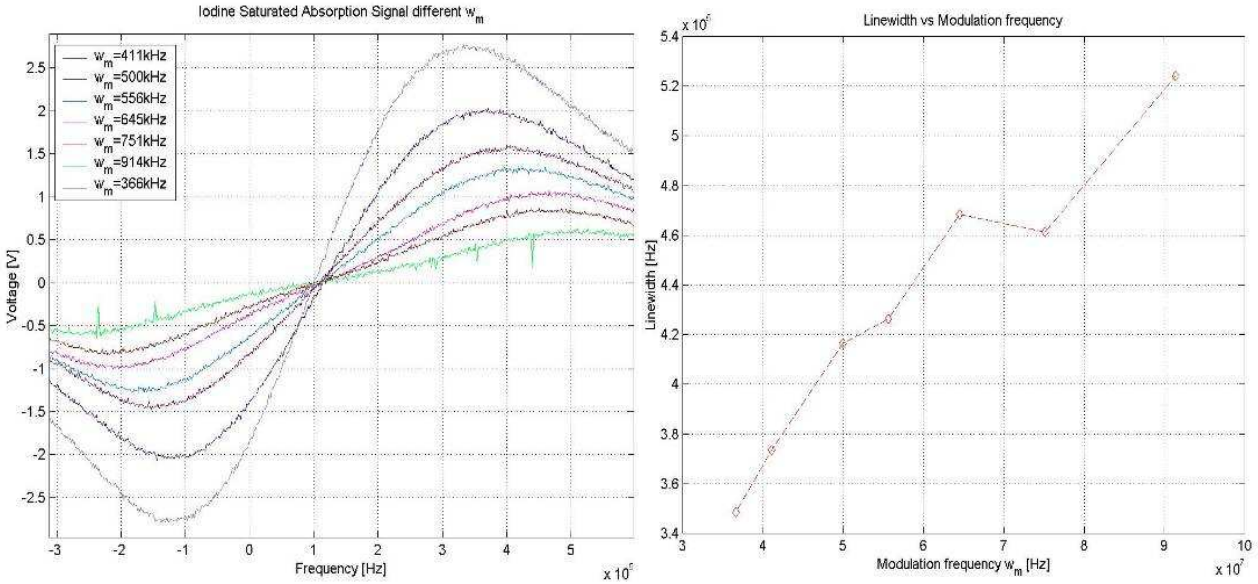

Figure 5–17

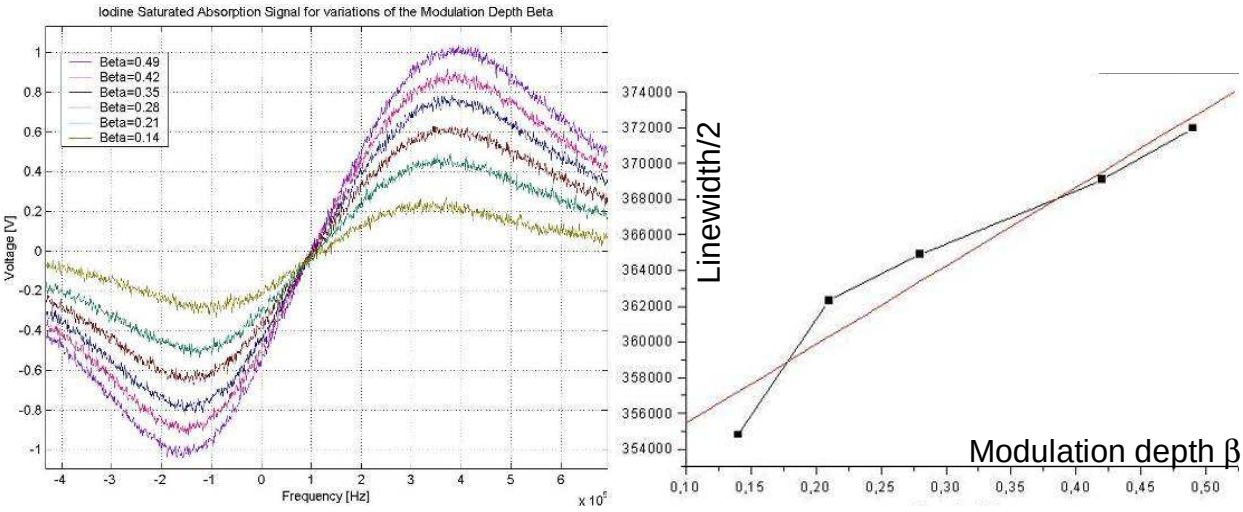

Figure 5–18

We can then study the dependence of the linewidth from the modulation depth, as done in Figure 5–18. This time, though, the linewidth can be calculated using the fit of the amplitude as function of different modulation frequencies. It has to be remembered that the half wave voltage for our EOM is 160V. Hence the modulation depth shall be given by the applied voltage to the EOM crystal divided by 160V. We see that for higher values of the modulation depth than 0.1 the linewidth augments almost linearly with this parameter. Below the value of 0.1 for the modulation depth we have however a serious loss in the signal amplitude this offsets the gain in the linewidth narrowness. The slope has its optimum value for β close to 0.3.

Similarly we proceed to determine the best value of the saturating beam power. Once again the linewidth is determined from the fit rather than from the simple frequencymeter estimate. The power is measured on the DC output of the photodiode and independently with a calorimeter. This time the linewidth is close to constant for values of the saturating beam power lower than 3.5mW (Figure 5–19) which gives us an estimate of the saturation intensity. For values of the pump power greater than this value we can expect to see a broadening of the transition.

After having determined the best value of the saturation intensity we still have to test the dependence of the linewidth on the temperature. This is well know from the theory, as we have seen in Section 3, but an experimental measure to confirm the prediction is still necessary. Once again we have computed the linewidth using the fitting routine. As seen from Figure 5–20a, the linewidth decreases with the temperature but the peak to peak amplitude also gets lower with the temperature. The end result is shown in Figure 5–20b, were we see that for temperatures close to -15℃ th e error signal slope decreases with the temperature. This indicates that working at a very low temperature, decreasing the signal

as it does, due to the reduction of absorption (lower contrast) is not the optimal choice. Furthermore we have seen that for temperatures much lower than -8℃ the mean time between failures of our Peltier devices is of a few months, though this might also be due to sector instabilities we have observed. Also, for the very low temperatures the condensation of water becomes a problem especially in conjunction with the electronics of the cell supports. We have thus decided to sacrifice on the narrowness of the linewidth in favour of security, better working conditions for the Peltier and greater peak to peak amplitude of the error signal. We have, therefore, decided to work between -7 and -2℃. To solve the water condensation problems in conjunction with the use of the thermoelectric devices we also have sealed the support of the cell containing the Peltier with candle wax and silicone. Having optimised the slope of the error signal we now wish to see which stability we can reach with our two iodine systems.

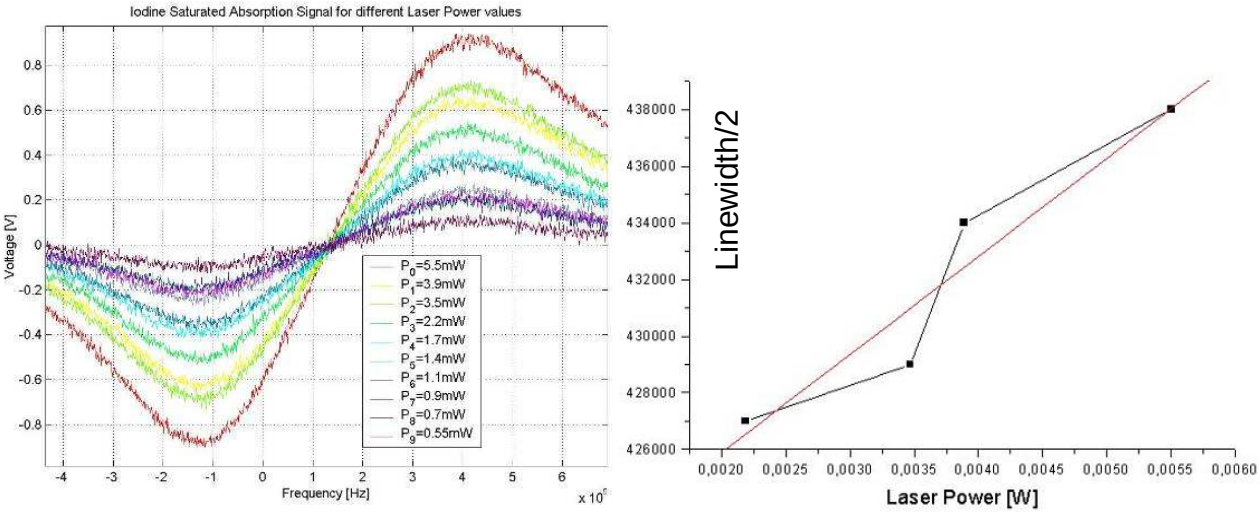

Figure 5–19

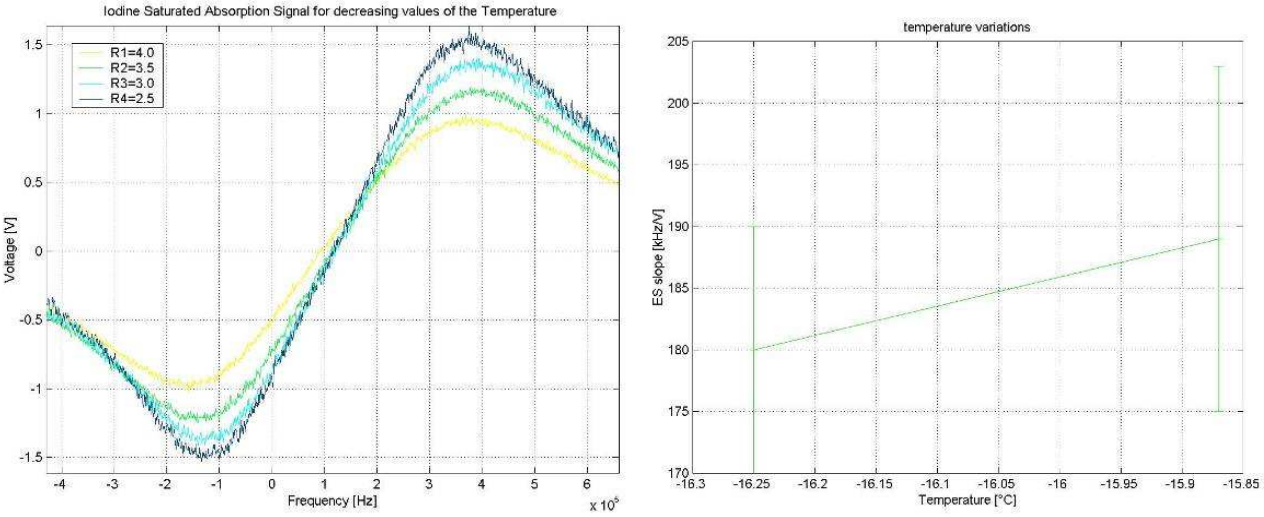

Figure 5–20

5.3 Iodine Lock stability

As seen in Sections 1 and 2 we need to evaluate three different parameters in order to validate the stability performances of a laser system. In order to evaluate all stability parameters of the Iodine locked laser we measure the beat note of the IR components of the locked lasers. This means that our green noise will be a factor of 2 greater than the measured variations. On the other hand, both Iodine systems will contribute to the measured variations. We can suppose that the experiments noise contributions add in quadrature, being unrelated, and that they are of equal amplitude on the beat note. This brings us to divide the observed signal by a factor of $\sqrt{2}$. Hence the real frequency variation for a single system is given by the measured beat note variation multiplied by a factor of $\sqrt{2}$.

Reproducibility

The beat note frequency varies after the last modifications of the feedback servo between 19.998 and 20.001 MHz. If we consider all measurements of the frequency taken on each different day for the month of September of 2004, a statistic counting more than 10^6 data points, taken at different times of day, with or without temperature isolation, we have that the mean value of the frequency is 19.9994 MHz with a standard deviation error of 840Hz. if we go further back into the past and consider all measurements of the frequency taken in the last two months, in which the experimental conditions have not changed, it has to be taken into account that a month ago the obtained frequency stabilities for the Iodine systems were much inferior to those enjoyed nowadays, then the mean value is 20.001MHz with a standard deviation this time of 4kHz. Going further back the issue of temperature variations, due to different regulations of the temperature controllers and different experimental conditions, has to be taken into account. For the temperature shifts we can correct the old values by applying the theoretical temperature shift to bring the measurements temperatures to the actual values of -7℃ for E1 and -2℃ for E2. This way we are still neglecting the effects of the modulation broadening and of the modulation frequency. In the last seven months though the modulation frequency has always been below 100kHz and the modulation depth has not been changed for more than 0.01. As seen above these variations can be neglected. Once we have rescaled for the temperature shifts we can, therefore, simply take the mean value of the measurements to give an estimate for reproducibility. We take the mean value of each day's acquisition rescale it for the temperature, take its standard deviation as incertitude of the measurement and get the graph in function of the time (Figure 5–21). From Figure 5–21 we get a mean value of

19.9998MHz and a standard deviation of 2kHz. The reproducibility of our locked Iodine system is, for now, limited to the kHz.

Precision (Offsets)

When dealing with 'exactitude' (once again we use the word with the caveat that it be not interpreted in the metrological sense) we have to establish the nature and amplitude of all known offsets in the error signal and feed-back electronics. This because all offsets will cause us to be frequency shifted by an amount $\Delta\nu = off \cdot \chi$ (where with χ we indicate the ES slope in Hz/V) from the expected frequency. To estimate the precision of our optical standard we would thus have to measure all offsets on the error signal and if possible reduce or eliminate them.

The most significant offset comes, for our experiment 1, from the dark current offset in photodiode 1. While constant and thus not worrying in the face of a simple frequency stability request, this 200mV dark, purely electronic, offset is still a problem for the precision of the measure. Given the most recent slope measurements for experiment 1 which give a value of χ_1=-30kHz/V we can estimate the frequency offset on laser 1 to be of the order of -6kHz. Smaller contributions from other offset causes may also be present but are at present drowned in this electronic limitation.

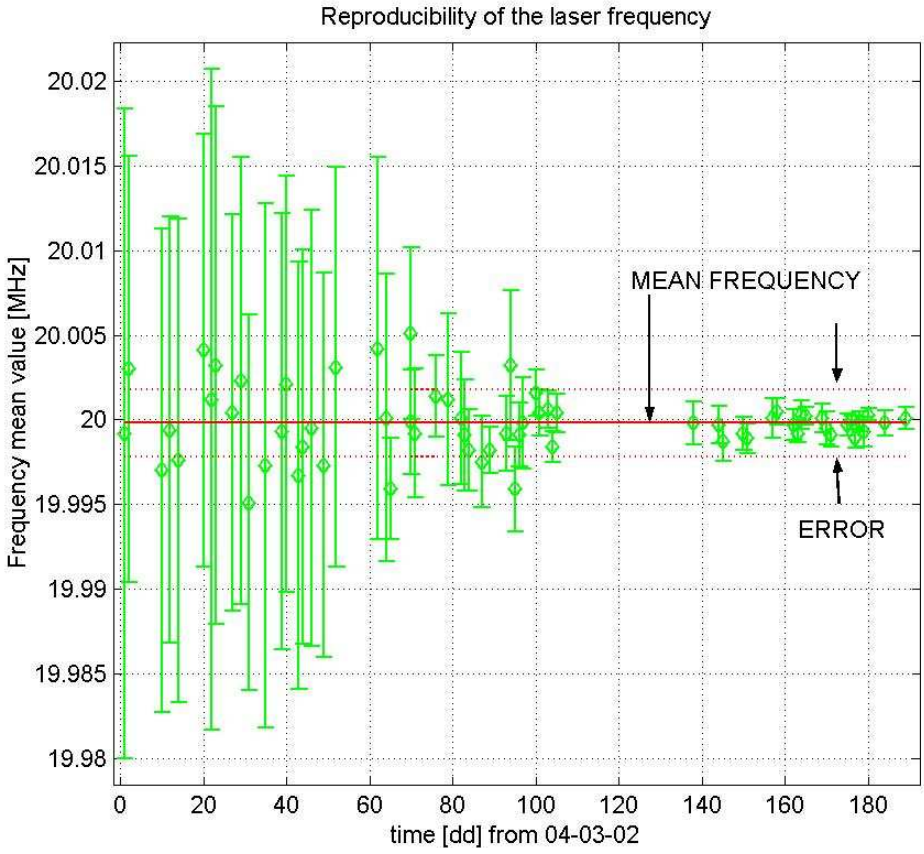

Figure 5–21

For experiment 2 instead the offset is not due to simple dark current offsets. While its origin is electronic its link with the Noise Eater circuit of laser 2 is difficult to explain. The offset is in fact below 40mV and is given by the dark current of the photodiode unless the NE is turned on, it then takes a value closer to -170mV. Working without the NE on experiment 2 is not advisable as this laser is intrinsically noisy; we have therefore decided to tolerate the offset introduced. The explanation for this experimental observation is not evident. Laser 2 is well isolated from all light backscattering we have, in fact, placed Faraday isolators both on the green and IR beams. There is no signal at the modulation frequency on either of the correction channels sent to the laser (piezo and thermal controls) that could modulate the laser power. The only effect we have observed producing an offset is the amplitude modulation in the EOM and is due to pump backscattering towards the photodiode in the s polarisation state. This effect, which has been reduced by rotation of the EOM holder, is however not linked with the observed offset or with the laser NE circuit and cannot explain the observed phenomenon. The only possible interpretation would be for the signal to be due to electromagnetic pick-up which is however unlikely given the low values of the RF modulation frequencies (below 100kHz). Taking as offset value the observed value we can compute the equivalent frequency shift. This is, given the value of $\chi_2 = -35$ kHz/V, equal to a frequency offset of 5.95kHz.

Precision is not the main requirement we are working on. We limited our activity on this parameter to the simple determination of the main offset causes and, having verified that the error on the frequency remains well below the 100MHz mark taken as specification, we didn't try to better the exact frequency incertitude for the moment.

Stability (Allan variance)

We finally come to the stability measurement; this is given by the variations of the frequency on a chosen time-scale which we shall call integration time. The variations can be measured either directly to get a time curve of the variations (from which we can get the Allan variance) or as a spectral noise density. In order to understand the residual variations of the frequency (shown in blue in Figure 5-22) we also systematically acquired the error signals of the temperature controllers, the out of loop and in loop Iodine error signals and the room temperature. We have also occasionally acquired the measurements of the continuous signal coming from the photodiode to measure eventual variations of the laser power, as well as the temperature of the outside of the iodine cell and the correction signals sent to the piezoelectric crystal and thermal control of the laser. Unfortunately none of these parameters, but for the out of loop error signals (in red and green for E1 and E2

respectively in Figure 5-22), show any correlation (either by calculating the correlation coefficient or the coherence) with the frequency variations. Since the in loop error signals are not correlated with the residual variations we can safely exclude lack of gain as the possible cause of the observed frequency oscillations which have a period of 0.5 to 2.5ks. In Figure 5-22 we used the signal coming from the home-made mixer (ES) in the feed-back loop and observed the error signal also on the lock-in-amplifier (DS). The situation is unchanged if we lock on DS, Figure 5-23, where the black curve, as in Figure 5-22, is the sum (with sign) of the two out of loop (ES) signals. The possible causes for this oscillation will be explained in the next Section; for now let us simply observe that the out of loop error signal, once we have determined the conversion constants and the eventual time delay between the variation and its measure, describes efficiently the observed variations. While it would be advisable to correct the observed variations we can ideally simply subtract the measured frequency offsets and have the effective value of the frequency variations. This has been done and we have been able to get rid of the large (for the best measures of the order of 600-1000Hz) mHz oscillation to get to see temperature caused variations (in Figure 5-23 the curve in magenta). We can now plot the Allan variance for the frequency variations as shown in Figure 5-24b, while Figure 5-24a shows the histogram before correction. For low values of the integration time the Allan variance is satisfactorily in the neighbourhood of 10^{1}s. This remains true for integration times up to 200s, after which the imperfect correction of the fluctuations brings the Allan variance to the order of 10^{2}Hz. For integration times much greater than the 1000s presented above the Allan variance becomes, once again, better as the effect of the 1ks oscillation becomes negligible.

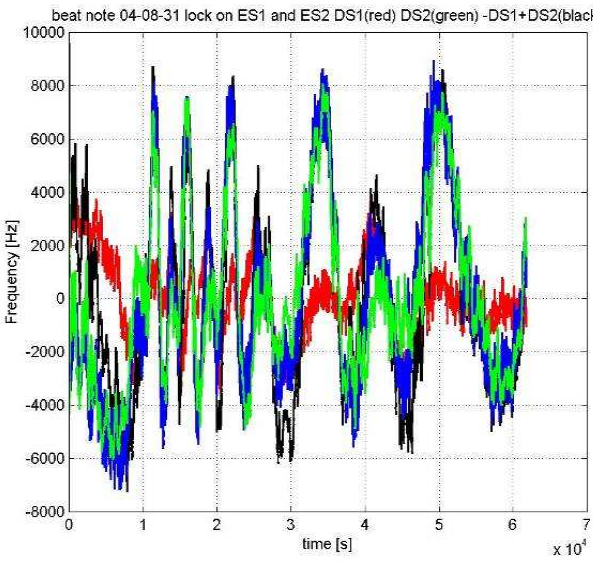

Figure 5–22

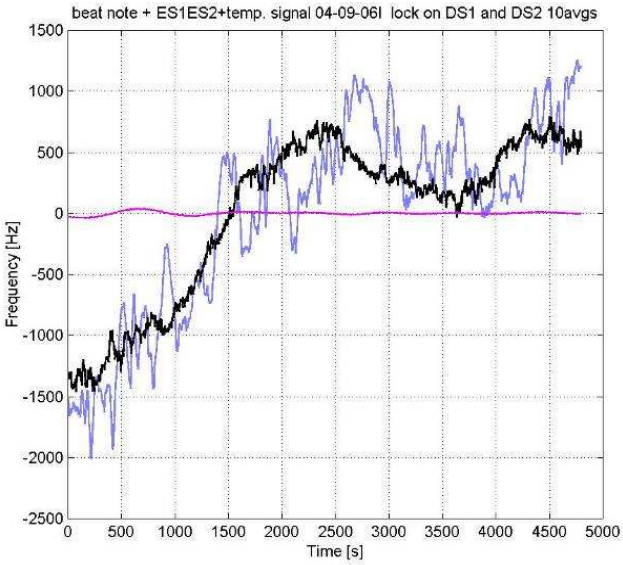

Figure 5–23

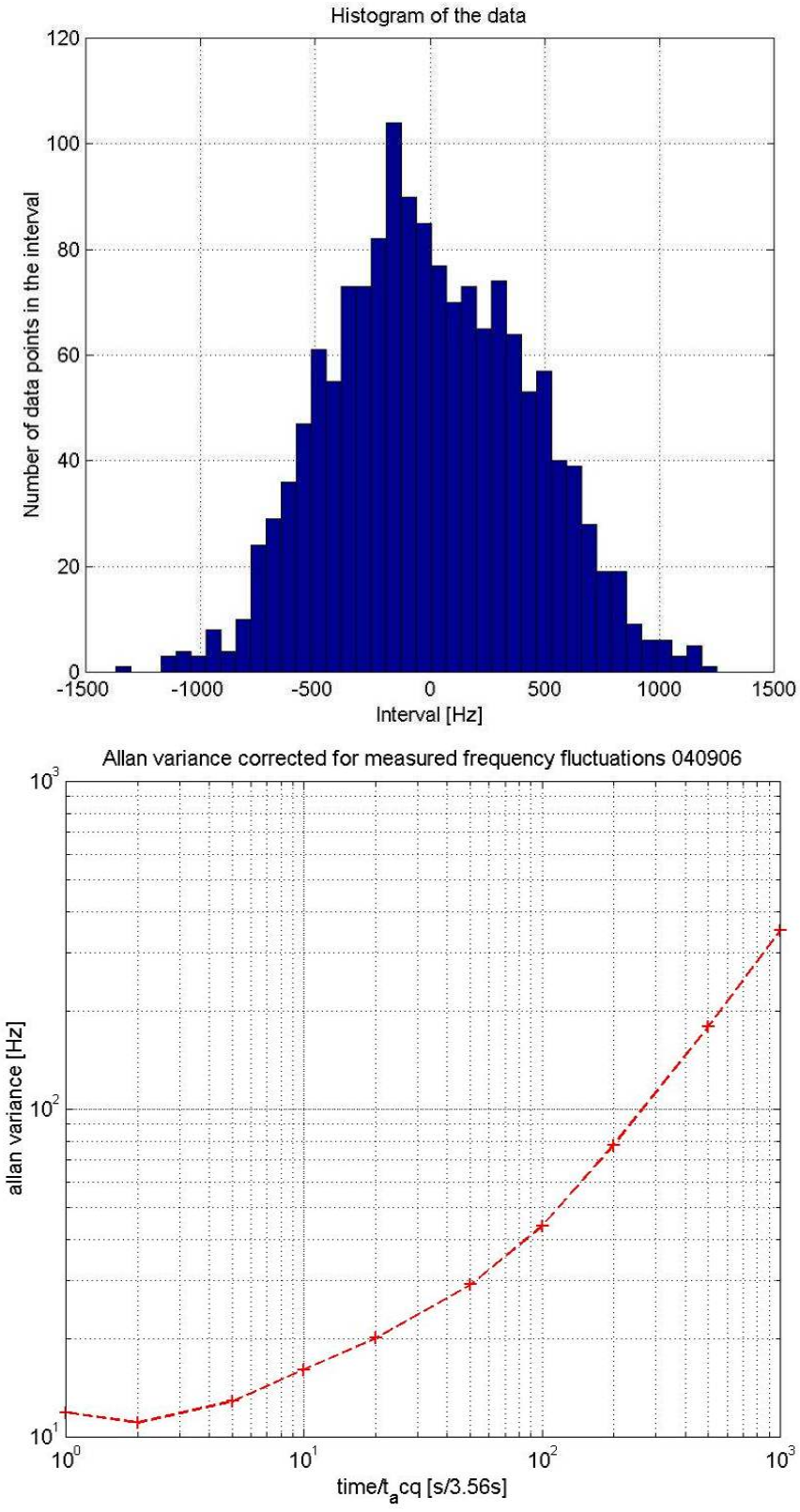
Histogram of the data
Number of data points in the interval
Interval [Hz]
120
100
80
60
40
20
0
-1500
-1000
-500
0
500
1000
1500
Allan variance corrected for measured frequency fluctuations 040906
allan variance [Hz]
time/t_acq [s/3.56s]
10^3
10^2
10^1
10^0
10^1
10^2
10^3

Figure 5–24

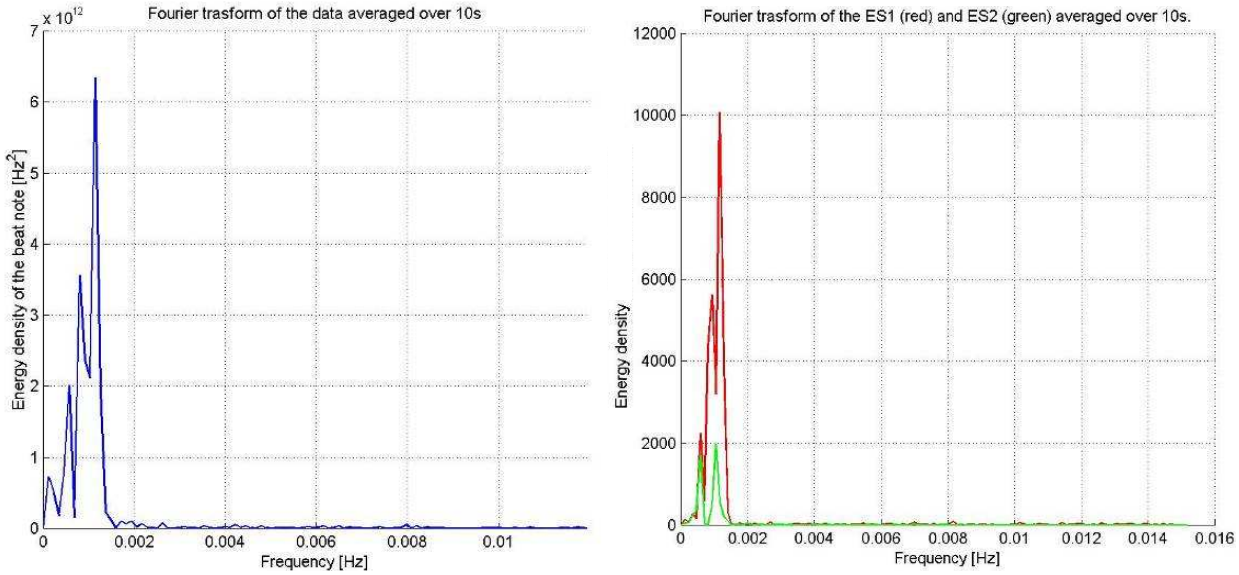

Figure 5–25

Studying the FFT of the time signal shows a peak at a frequency typically close to the mHz in good accord with what we observe in the time domain. Even more significant, if we take the out-of-loop error signals the two have peaks close to the same frequencies in the frequency domain, as shown in Figure 5-25. There remains now to analyse the main error contributions we have been able to identify and to try and explain the oscillation of the locked lasers and why they should be measured always on the out-of-loop mixer independently of the chosen error signal (ES or DS) we use to obtain the lock.

Residual noise contributions

We now have to determine the noise contributions responsible for our limits in terms of stability, precision and reproducibility. As we have seen precision is mainly limited by electronic offsets, to which is added for experiment 2 the possible contribution coming from amplitude modulation and the effect coming from the ‘pick-up’ of the modulation in the NE. As explained this is hardly problematic for specifications of precision of the order of those required for LISA. Reproducibility is mainly limited by the temperature and frequency stability of the experimental set-up. The bettering of the stability, as seen from Figure 5–21 in the last part of the graph, also engenders a better reproducibility of the experiment. This means that we need a better understanding of the effect causing the frequency shifts on the Iodine systems and the reason behind the measurement we can take of it through the out of loop error signals. These error signals always have correlation coefficients higher than 0.75 (going up to 0.98) with the beat note variations, but are unfortunately not linked to a single mixer. We could have supposed, had that been the case, that a defective mixer

was introducing the observed noise on the beat note. This hypothesis, however, is invalidated by the perfect symmetry of the observed situation for different mixers. We also tried to lock on a home built mixer and observe the variations with the second mixer the test was repeated using the two lock-in amplifiers. Both tests have shown that the problem is not linked with a type of mixer. We could suppose that the problem be due to either a mass loop in the feed back loop or an error on both mixers. The mass loop hypothesis has been studied and, while in the case of small signals injected in the integration we had a loss of gain due to this phenomenon, is not able to explain the observed effect. Now if we suppose that there be a phase error on the demodulation reference of the mixer, given the fact that the Modulation Transfer never has a purely zero error signal, we might be introducing a phase related offset to the error signal. Changing the phase for the locked system has shown frequency variations of the order of the kHz for phase shifts of the order of the 10° in the case where the amplitude modulation was minimal. This effect is unfortunately nearly an order of magnitude greater than the maximum phase shift we can expect to have for our experimental apparatus.

Temperature changes of the cold point could also be responsible for frequency variations over long periods of time. However, as seen from Figure 5-23, the frequency variations corresponding to the temperature shift (magenta curve) are of the order of 10Hz and therefore an order of magnitude lower than the observed oscillation. Another effect which might produce a variable offset would be a variation of the AOM driving frequencies. But as seen in Section 5.1 the variations of the 80MHz quartz frequency (the noisier of the two AOM generators) are still of the order of the 10^{1}Hz (@1mHz) which is an order of magnitude smaller than the observed effect. We could then suppose that the small misalignment given by the AOM frequency variation be responsible for the greater frequency variations than foreseeable considering just the direct frequency variation. This is however not in accord with the experimental observation that a shift of ¼ of their waist for the beams entering the delay line containing the cell is not sufficient to cause a sensible frequency variation. The expected misalignment due to the typical quartz frequency shift is of less than 0.13 times the waist. This last phenomenon is still not important enough to explain the observed frequency variations, which are still under study. Once the mHz frequency shift shall be corrected to once again better the performances of our optical standard we will have to either change or stabilise thermally (e.g. inserting it into an oven) the 80MHz quartz oscillator and bring the temperature stabilities of the cell cold point regulation to the mK.

Photon noise limit

Finally let us now determine the photon noise limits for our experimental set-ups taking into account the values of the probe beam powers (50 and 48 μW for E1 and E2 respectively) incident on the photo-detectors, since these determine the upper limit for our expected frequency stability. We can observe that for a given frequency ν the energy of each photon shall be according to the well known expression:

$E = h\nu$ =3.7 10^{-19} @532nm (5-4)

We can thus obtain the number of photons per unit of time (s) from the measure of the power incident on the photodiode:

$$n(phot/s) = \frac{P}{h\nu} \quad (5\text{-}5)$$

and hence considering the fact that photons have a Poissonian statistic we get for the photon noise (B) that it shall be $B = \sqrt{n}$ in terms of photon number. This implies that if we convert this photon number noise we shall have a corresponding photocurrent noise of:

$$\Delta I = \eta \cdot e \cdot \frac{B}{Z_{DC}} \quad (5\text{-}6)$$

this can be converted in a Voltage noise if we know the value of the AC channel of the photodiode trans-impedance (Z_{AC}) and since we have measured the slope of the error signal we can get the frequency equivalent noise in Hz/√Hz. For the case in exam we have that the photon noise in terms of equivalent frequency noise shall be given by $\Delta\nu_1$=7.5Hz/√Hz and $\Delta\nu_2$=6.9Hz/√Hz.

These values are only slightly lower than the temperature shifts (10Hz/√Hz typically) and than the observed best stability value obtained of 11Hz @ 20s.

6 Fabry-Perot resonator: experimental work

Concerning the lock of FP resonators we want both to test the long term performances of Tilt Locking with respect to Pound-Drever-Hall and then the cavity lock with respect to the molecular reference.

To validate the long term performances of the Tilt Locking technique we had to monitor both the variations of the error signal out of loop and the effects of the optical misalignments on the locked laser. Since we were using the Tilt Locking Double Pass configuration we decided to use the Pound-Drever-Hall in the same experimental configuration to ensure symmetry between the two techniques. For an analytical analysis of the DP Pound-Drever-Hall please refer to Appendix B.

The determination of the cavity lock performances was more difficult due to the lack of any thermal screening on the reference. This, however, allowed us to measure the linear expansion coefficient of the ULE used to build our Fabry-Perot as well as determine the necessary upper stability limits for the thermal isolation of the FP.

6.1 Experimental lay-out

In order to compare the two techniques and the cavity lock with respect to the Iodine reference (this is the only way to determine the long term variations of the cavity frequency) we set-up the experimental configuration shown in Figure 6–1.

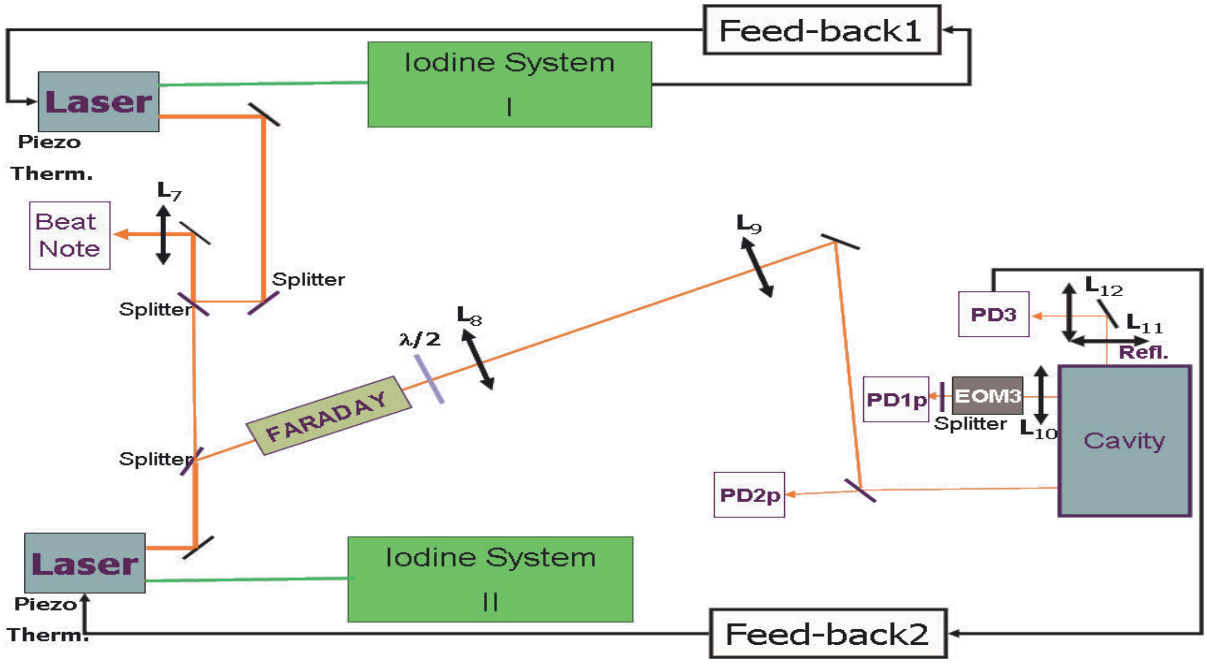

Figure 6–1

Laser1 is locked on an iodine transition (either a_{10} for the high Finesse of the FP, or a_{15} for the low). Laser2 is instead locked using part of its IR component on a FP resonator in a vacuum tank in which we made a 10^{-8}mbar vacuum. This provides some thermal isolation and also acoustic isolation for the mechanical reference. On this cavity we put into place both a double pass Tilt locking and double pass Pound-Drever-Hall at the same time, so that we can always lock the laser on one of the two error signals and monitor the one outside the loop. Let us now analyse in detail the experimental configuration.

Laser and Optics

The laser sources are once again the two Innolight NPRO doubled Nd:YAG lasers, emitting 1W of IR (1064nm) and 20mW of green (532nm) power, described in Section 5.1. The iodine locked laser1 (E1) has also been described extensively above in Section 5.1 and has remained unchanged for this second set of tests. The IR beam coming from laser2 is divided for this set of experiments in two equal power beams with a 50-50 splitter. Half of the beam power is sent on towards the beat note set-up while the other half is used to interrogate the cavity. On this second beam we place a Faraday isolator to avoid all back scatterings typical of the double pass configuration (refer to Section 4.2.2 for a comprehensive analysis of this experimental set-up). This element assures a transmission of 96% and an isolation of 36dB. This is followed by a half wave plate which is used to adjust the polarisation state of the beam in order to ensure that we are using at each time only the polarisation chosen (p for the low finesse and s for the high finesse of the FP). The initial 200μm in the horizontal direction and 130μm in the vertical of the waist are matched (to 261μm) by the doublet given by L_8=300mm (400mm from the waist) and L_9=514mm (1682mm from L_8) to the cavity's waist (289μm) close to the middle of the plane mirrors. The matching is of 95% on the first pass, adding a cylindrical lens L_{13}=305mm in the y direction we should bring the coupling to 98%. Matching can be estimated using:

$$\tau = \frac{4}{\left(\frac{1}{x}+x\right)^2 + x\left(\frac{z}{z_R}\right)^2}, \qquad (6\text{-}1)$$

where x is the ratio between the cavity and the beam waist ($x=w_{cav}/w_{beam}$), z is the position offset of the waist with respect to the centre of the plane mirrors and z_R is the Rayleigh distance. The alignment is given by two mirrors one having a reflectivity of

R=0.985 and the other a splitter with R=0.72. The adaptation (matching and alignment) can also be estimated experimentally by observing the relative transmission of the TEM_{00} mode with respect to the total transmitted light. Our measure was obtained experimentally with this latter technique and at (94±3)% is in good accord with the theoretical expected value of (95±2)%. The transmitted beam is then passed through a lens positioned so that its focal planes are coincident with the waist of the cavity on the one side and on the other with the re-injection splitter (cat's eye configuration). This lens of focal length L_{10}=150mm is mounted on two micrometric translation plates. These ensure micrometric alignment in the z (along the beam direction, to ensure that the cat's eye configuration is effectively reached) and the x direction (perpendicular to the beam but still in the propagation plane). By changing the regulation of the lens along the x axis we can produce a pure tilt of the beam, the lens also serves the function of re-matching the second pass beam to the cavity thus avoiding adaptation losses. After the lens we have an EOM with a modulating frequency of 6.25MHz and a splitter R=0.84 followed by a photodiode monitoring the transmission of the first pass. The transmission of the second pass is monitored behind the splitter in the injection and shows a coupling of (91±2)% for the second pass in the cavity. It has to be observed that the presence of the EOM on the re-injection causes a double modulation to be introduced on the beam; the effect of this double modulation has been studied in Appendix B. The reflection of the beam second pass into the cavity is picked up by an R_{max}=0.98 reflectivity mirror and sent towards the quadrant photodiode which shall create the error signal. An adjunctive doublet of lenses focusing the beam on the photodiode is also necessary. This doublet conjugates the cavity 289μm waist with the 1mm of radius photodiode (near field condition) with L_{11}=80mm (410mm from the cavity waist) and L_{12}=158mm (252mm from L_{11}), the imaged waist measures 811μm.

Mechanical reference

The FP we have used is a ten year old, football shaped, Corning ULE cavity with three mirror. The age of this FP is significant to ensure that commonly known abrupt mechanical changes and oscillations due to the creep effects in the cavity and the degassing be, ideally, negligible. The football shape was chosen when the cavity was created as the best one to avoid the mechanical resonances below 10 kHz (studied with finite element analysis) of the cavity spacer thus reducing the thermal noise in this range. ULE, as can be seen from Figure 6–2, enjoys linear expansions

coefficients, having the form with temperature $\alpha=\alpha_0$ $(T-T_0)$, of the order of 10^{-9}/K for temperatures within some degrees of the best operating temperature T_0 which, in the case of our Corning ULE, is theoretically close to 30℃. This cavity has been always kept in vacuum, but before starting our experiments we evacuated the vacuum tank of all degassed elements bringing the residual pressure to below 10^{-8}mbar. To ensure that pressure variations were not acting on the mirrors invalidating our measurement of the temperature induced drifts we also took two acquisitions with the pumping system turned on. No significant variations in the behaviour of the reference were seen.

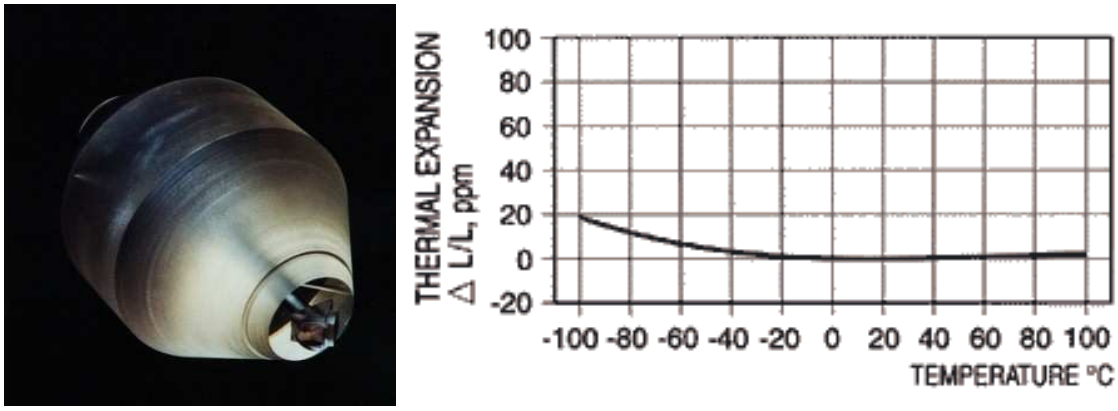

Figure 6–2

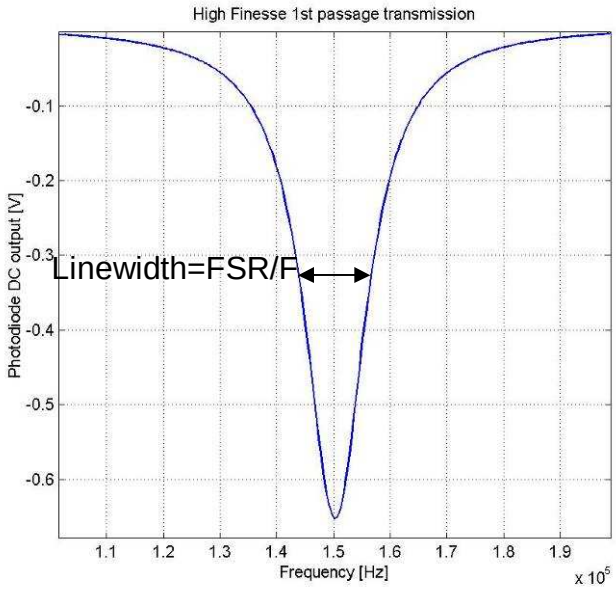

Figure 6–3

This cavity is triangular with a length of 300mm and an end mirror having a radius of curvature of 0.5m. The waist of the cavity calculated referring to Equation 4-15 is thus

equal to 289µm and the Rayleigh distance (calculated according to 4-14) gives instead 246.6mm, the cavity's Free Spectral Range is of 480MHz. The cavity's Finesse as measured in F. Bondu's thesis (Bondu private communication) is for the p polarisation state equal to 1000 and for the s polarisation of 30000. The independent measure we have taken of the half width at half maximum of the transmission peaks compared to the known value of the FSR gives the following acceptable, within the experimental uncertainties, values of F_P=998±50 and F_S=29832±600. The transmission profiles have been acquired on the SRS780 a multi-function, low frequency, FFT spectral analyser which can also function as a digital oscilloscope. The output of this instrument in the SRS file format has been transformed into ASCII thanks to the ABSPHASE routine created by H. Heitmann.

Photo-detectors

For these tests we have used two photodiodes to acquire the locks, two others to monitor the transmissivities of the cavity on each pass and finally one to monitor the beat note between the two laser systems. The photodiode used to obtain the lock on the Iodine system has already been described in more detail in Section 5.1. The two photodiodes monitoring the 1st and 2nd pass transmissions are two Si photodiodes having large dark current caused offsets of the order of the 100mV.

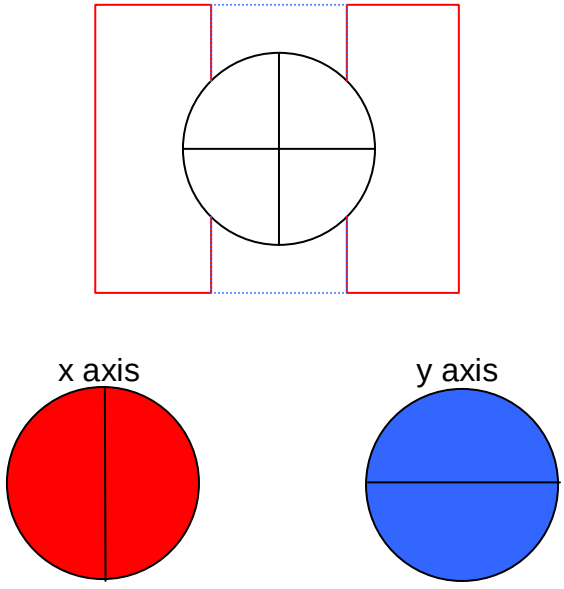

Figure 6–4

The lock on the cavity is obtained either through a PDH lock or through a Tilt Locking configuration. In both cases the photodiode (Hamamatsu G6849-01) used is a quadrant photodiode adapted for detection @ 6.25MHz (the modulation frequency

used for the PDH lock). The quadrant photodiode's elements are joined two by two creating effectively two separated split photodiode configurations one along the x axis the other along the y axis. The split photodiode elements, thus created, can be either summed and then demodulated thus giving the PDH error signal or subtracted yielding the Tilt Locking error signals. In this configuration where the detector as well as the whole of the optical path are common to the two experiments we can best test the performances and long term stability of the Tilt locking technique. The photodiode is an InGaAs with a quantum efficiency of η=0.4 @1064nm. Its active area is of 3.14mm^2 and the dead zone between the different elements is 30µm wide. The dark current is below 1nA. The beat note photodiode has also an InGaAs detection element with a quantum efficiency close to η=0.4 @1064nm. Its active area has a radius of 1mm, and the electronics is accorded for detection in the neighbourhood of 20MHz. This frequency has been chosen because the frequency difference between the high Finesse transmission, of the cavity, and the a_{10} component of the R56(32-0) molecular band, we are using to lock the Iodine system, varies between 20 and 30MHz. At the same time a low Finesse transmission peak is some 5 to 15MHz apart from the a_{15} component of the same molecular band. Also the beat note between the two lasers when they are locked on the same iodine transition is also in the neighbourhood of 20MHz. Here too the dark current is much lower than the photon noise for the chosen values of the incident power:

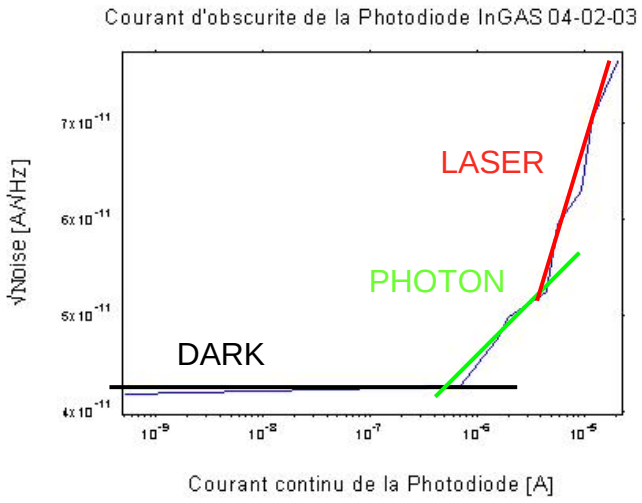

Figure 6–5

Electronics and servo-loops

Iodine:

A description for the iodine feed-back loop is to be found in Section 5.1.

Pound-Drever-Hall:

Another home made mixer and feed-back loop for the demodulation and lock on the Pound-Drever-Hall error signal was built in our electronic laboratory in Nice. The demodulation phase was given by the TTL signal of the modulation generator but the phase lag was obtained by an appropriately constructed dephasor. Ideally the phase lag could be regulated with an appropriate length of cable (delay), but since we wish to be able to fine tune the phase the above mentioned solution has been chosen. A dephaser takes a sinusoidal signal and shifts its phase with the variation of an adjustable impedance. The error signal is then fed back to the laser after integration, in the case of the piezoelectric feed-back we have a series of 4 integrators giving a gain behaviour as $1/f^4$ whereas on the thermal regulation of the laser crystal we have an extra integration making the gain increase as $1/f^5$. The thermal correction becomes dominant at frequencies lower than 0.1Hz. The piezo correction is in 1/f for frequencies higher than 300Hz and has unity gain at 5kHz. At 300Hz we have the knee given by the effect of the three in series integrators bringing the gain to $1/f^4$. While there is no electronic filtering as is the case for the Iodine experiments still a filtering at either 17kHz or 500kHz, depending on the Finesse of the FP, is introduced by the cavity, which as has been seen in Section 4.1 is equivalent to a low pass filter and must be compensated appropriately. Furthermore since we are using a double pass configuration the pole given by the FP must be compensated twice. A switch allows us to lock either on the high or on the low Finesse (changing the time constant of the first integrator of the feed back loop).

Tilt Locking:

While the integration and feed-back loop is identical to that of the Pound-Drever-Hall system the error signal extraction is this time much easier to obtain. The error signal is simply given by the subtraction of the two lobes of the photodiode and doesn't require demodulation, or amplification.

Instrumentation, data gathering and analysis

Once again the acquisition of significant parameters is made through the frequencymeter HP53131A and the Keithley DM199 multimeter (used as Voltmeter) interfaced with the PC thanks to the GPIB card and LabView. The parameters we

wish to measure this time are the error signals coming from both the in-loop and the out of loop error signals (be they either Tilt Locking or Pound-Drever-Hall), the temperature of the vacuum chamber (which with a retard we shall measure will be followed by the cavity's) and room temperature. The last two parameters are measured with PT100 sensors inserted in a bridge configuration. To measure the different transmission parameters as well as the offsets due to misalignments we used a Hameg oscilloscope, a Fluke Voltmeter and the already mentioned SRS780. The oscilloscope has a read-out error which is typically 0.1 of the chosen scale plus the classical 3% measurement error of this type of instrument. The Fluke Voltmeter has an error which is of 3 on the least significant digit. Finally the SRS780 has an average error of 3%.

6.2 Construction of an ultra-stable FP

In order to better test the performances of the Tilt locking technique we would need to build an experimental set-up with excellent properties of mechanical stability. This would have ideally to be a monolithic assembly grouping the Fabry-Perot, the re-injection mirror and the detector.

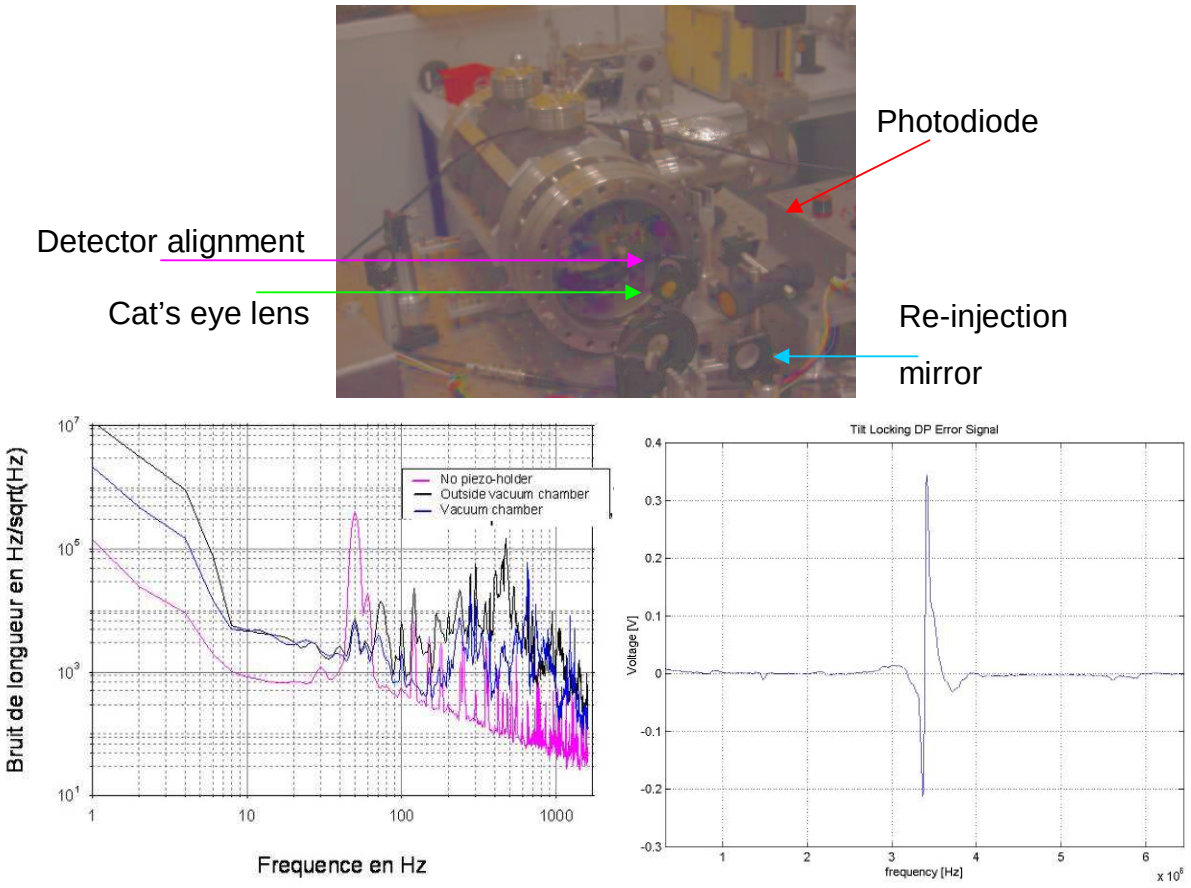

Figure 6–6

To further our research project we decided to commission, with the sponsoring of the CNES, the realisation of a silicate bound cavity to the society SESO of Aix. This cavity was to be a high Finesse (50000) reference consisting of a silicate bound ULE spacer and dihedron with silica mirrors. The necessity of such a reference was comforted by the theoretical observation that Tilt Locking is sensitive to optical misalignment as well as by the first set of experimental tests we realised on a mechanical reference (which is shown together with its length spectral noise density and the obtained Double Pass Tilt Locking error signal in Figure 6–6) not having the characteristics of stability necessary. The length spectral noise of the reference converted in Hz, on a Pound-Drever-Hall system (with Tilt Locking our typical lock was less than a minute long) was of the order of 10^2-10^3Hz. For Tilt locking, in particular, the alignment of the photodiode was not sufficiently precise to allow a proper alignment of the detector, hence the asymmetric aspect of the error signal in Figure 6–6. With these results to guide us we decided to use for the first tests an old ULE cavity and to study and construct a monolithic silicate bound optical assembly.

6.2.1 Cavity parameters determination

Let us now see how we determine the optical parameters for the construction of the ultra-stable reference. We decided on a simple geometry with a cylindrical spacer and a support holding up the dihedron, on which the plane mirrors are bound, the injection prisms and the detectors. The end mirror, dihedron and the detector support will be bound to the spacer. The triangular geometry is preferred for the greater ease with which it allows us to use the Tilt Locking configuration as the exit prism with a simple semi-reflective coating will be usable as re-injection mirror. Also in this configuration the error signal and the transmitted beam are not along the same direction and thus we do not need a splitter, nor shall we have power loss due to the presence of such a component. Having chosen the geometry of the assembly we now have to determine the optical parameters for the cavity. The first constraint we shall fix is dimensions. Since we wish to have a reference which is to be ideally well adapted to space experiments we shall try and keep its length contained, between 100 and 200mm. Having made this choice we now have to start considering the appropriate value of the end mirror curvature in order to have a cavity and also to avoid modal degeneration.

Fundamental parameters definition, astigmatism.

Let us now refer to Figure 6–7 to determine the relationships between the different parameter in the cavity. The main elements we want to determine are the angle between the plane mirrors (α) and the length of the spacer as a function of the semi-perimeter given by the beam path in the reference. The relationships between these parameters are presented in Equation (6-2):

$$L - \frac{d}{2} = \sqrt{L'^2 + \left(\frac{d}{2}\right)^2}$$

$$L' = \sqrt{\left(L - \frac{d}{2}\right)^2 - \left(\frac{d}{2}\right)^2} \qquad (6\text{-}2)$$

$$\alpha = arcsen \frac{L'}{L - \frac{d}{2}}$$

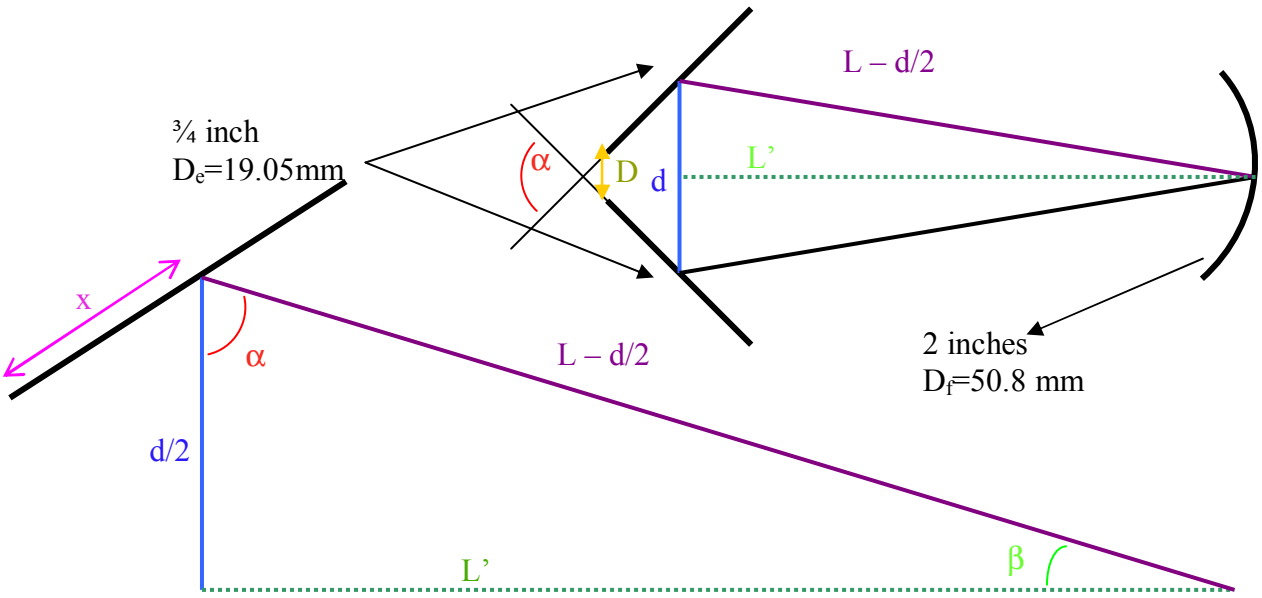

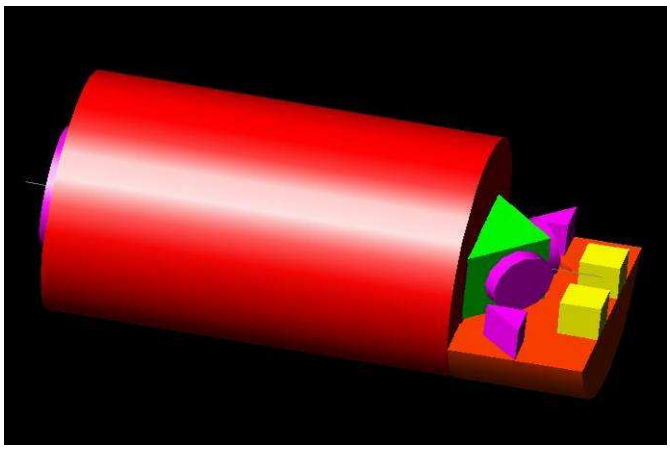

Figure 6–7

where d is the distance between the centres of the two plane mirrors and L is the semi-perimeter of the beam in cavity, or the length of the equivalent linear cavity. We have limited L' between 100 and 200mm, to work in space-mission conditions (light, small equipment); d shall be small enough not to produce a significant astigmatism with such a short cavity. Astigmatism is given by the tangent of β and we wish for it to be of the order of the percent:

$$\tan(\beta) = \frac{d}{2 \cdot L'} \approx 0.01 \qquad (6\text{-}3)$$

At the same we also want to be able to place at least ¾ of an inch mirrors on the dihedron (D>0) which for α supposed to be close to π/2 means that we shall have $d \geq \frac{D_e}{\sqrt{2}} = 13.49\,\text{mm}$. Since we wish for D to be more than 1 mm wide in order to avoid cutting the mirrors extremes in order to fit in their thickness we shall choose d=15mm. With this value of the distance (the choice of a small value of d is advisable for a tilt locking configuration, where we don't have a lens conjugating the waist with the detector, to reduce the Gouy phase shift) we have that the astigmatism shall be of 5%, for a chosen L'=147mm±0.1mm, as seen below.

Dihedron: determination of α(L, R), degeneracy.

The angle of the incident beam on the entrance mirror (when the beam traverses the cavity) shall always be equal to α (dihedron angle) but its position on the mirror shall

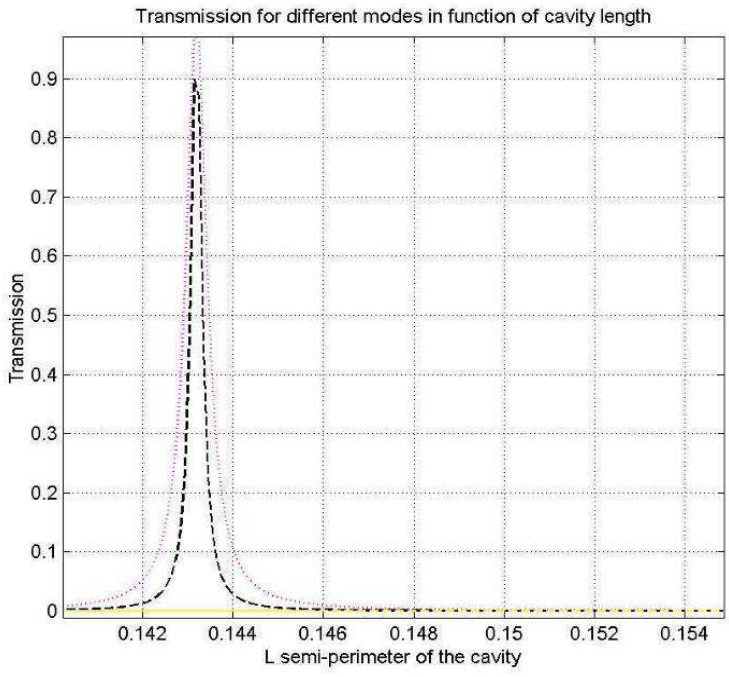

Figure 6–8

vary with respect to the centre of the mirror. This introduces a *geometric* constraint on the error of α depending from the dihedron characteristics. A second constraint on α shall come from the choice of the L and R parameters, this we shall call *degeneration* constraint. We shall determine the degeneration limit and then dimension the constraints on the dihedron mechanics before concluding which values of the uncertainty $\Delta\alpha$ shall satisfy the geometric limit on α. Since a mirror substrate with a curvature radius R=1.4995 was already polished at SESO's we decided to make use of it and choose the best length of the cavity, within our chosen interval, for the modal degeneration. We have seen in Section 4.1 the expression for a triangular cavity different modes frequency we now want to determine for which values of L we shall have an overlap of higher order modes with the $TEM_{00,}$ which is to say for which L values we shall have $\omega_{00}=\omega_{mn}$. We calculate, to keep into account the effect given by the Finesse (F), the transmission peaks of the cavity, as a function of L for a given R, with a newly created MATLAB routine. For each mode the symbol ν_{mn} shall indicate this time the frequency with respect to the TEM_{00} one calculated according to Equations (4-17) and (4-19), which shall yield this time for odd and even modes respectively:

$$\begin{aligned} \nu_{ODD} &= FSR\left[q + \frac{1}{2} + \frac{1}{\pi}(m+n)\arccos\sqrt{1-\frac{L}{R}} \right] \\ \nu_{EVEN} &= FSR\left[q + \frac{1}{\pi}(m+n)\arccos\sqrt{1-\frac{L}{R}} \right] \end{aligned} \tag{6-4}$$

Given that with FSR we indicate once again the Free Spectral Range, depending from L, the transmission peaks shall have the form:

$$T\left(\nu_{mn}^{o(e)}\right) = \frac{1}{\left(1+\left(\frac{2F}{\pi}\sin\left(\pi\nu_{mn}^{o(e)}\,{}^{1}\!/_{FSR}\right)\right)^{2}\right)} \tag{6-5}$$

If we now trace the placement of the transmission peaks as a function of L, their positioning will represent the values of L interested by the degeneracy. If we group all these transmissions peaks we shall have the type of graph shown in Figure 6–8, which shows the typical curve for the area of interest. As seen above for L close to 150mm±2mm we have no degeneracy with the modes of interest. This gives us a measure of L' which shall be 147.3mm±0.1mm, from Equations (6-2), where the error on L' is given by the spacer length uncertainty which is assumed to be 0.1mm since

this is close to the best expected precision in the working of ULE. These constraint on the semi-perimeter and length (of the spacer) can be translated into a limit on the value of the error of α (α=1.5188rad). From Equation (6-2)c we shall have for the error on α that:

$$\frac{\Delta\alpha}{\sin\alpha} = \frac{\Delta L}{L} + \frac{\Delta L'}{L'} \tag{6-6}$$

and if we substitute the numerical values in the expression above we shall have that $\Delta\alpha$ must be smaller than 13mrad to avoid modal degeneration.

Mirrors: coating size, determination of α(d,x), thickness of the mirrors, spacer parallelism

Let us now determine the necessary size of the coatings of the plane mirrors. In Figure 6–9 x indicates the beam displacement on the surface of the mirror and the angle 2γ is the supplementary to α ($2\gamma=\pi-\alpha$), when the dihedron holes to ensure the pass of the beam are exactly aligned. In the realised ULE bloc instead there was a displacement of 0.4mm which considering also the error of placement of the mirrors (±1mm) brought alone the minimum value of the coating to 2mm. But the mirror coating size (κ) must also be sufficiently large to ensure the passage of the beam without creating diffraction effects which means that the free area must be at least of $5\cdot w_0$ which in our case, considering that for our cavity of L=150mm (hence FSR=1GHz) and R=1.4995, the Rayleigh parameter z_R=456mm and the cavity waist w_0=393μm, is equal to nearly κ=2mm.

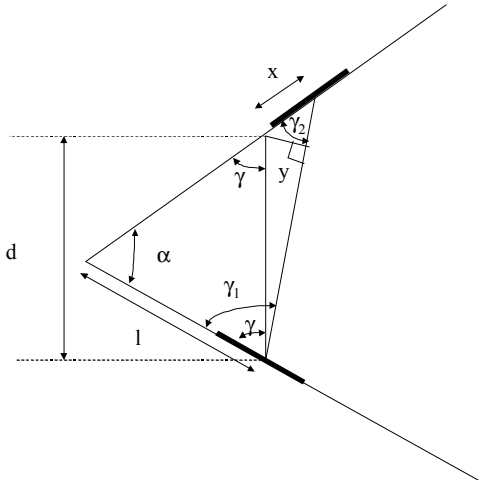

Figure 6–9

If we now consider the displacement given by the thickness of the mirror we shall have, as seen in Figure 6–10, that this parameter ξ shall only depend from the

incident angle and the thickness of the mirror p. In particular $\xi=p\cdot\tan(\gamma)$ which for p of the order of 6.35 (a standard mirror thickness) will yield a value of the displacement on the mirror's surface of ξ=2mm which shall force us to have a coating at least κ=4mm wide to be sure to compensate for this effect.

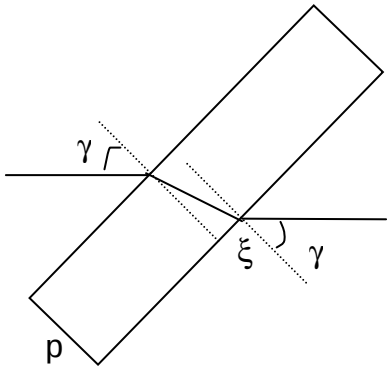

Figure 6–10

Let us now consider the displacement of the beam on the mirror surface due to a possible error in the value of the angle α. The position variation coming from this effect shall have the form:

$$\Delta x = \left|\frac{1}{2\cdot\sin\frac{\alpha}{2}}\right|\Delta d + \left|\frac{\cos\frac{\alpha}{2}\cdot d}{4\cdot\sin^2\frac{\alpha}{2}}\right|\Delta\alpha \qquad (6\text{-}7)$$

which for an error in the distance d, which coherently with what shown in Figure 6–9 will be of $y=d\cdot\sin(\gamma_1-\gamma)$ and which is typically for the case in exam of 6μm, and an error in α of 13mrad, as seen above, shall yield a displacement error on the surface of the mirrors of Δx=0.6mm. For the total size of the coating we shall thus request that κ have a size of nearly 5mm.

The spacer two contact surfaces must also satisfy a requirement of parallelism to avoid introducing too important a displacement on the surfaces of the mirrors. The displacement on the mirror due to the presence of a parallelism error δ shall be simply given by:

$$\Delta x = R\cdot\delta, \qquad (6\text{-}8)$$

where with R we, again, indicate the radius of curvature of the end mirror. For our numerical values we shall have that if the error of parallelism is of the order of 2mrad the displacement shall be close to 3mm, whereas if δ=0.2mrad, as measured for the

SESO spacer, then the adjunctive coated surface must be of only κ'=0.44mm. Adding this requirement we shall have that the total size of the coating must be κ=5.5mm, we shall ask, therefore, that it be at least κ=6mm in order to ensure the planarity of the coating surface. Ideally a larger coating would simplify alignment and allow us to relax the specifications on the dihedron and the spacer parameters.

Mirrors: reflectivity

The mirror's reflectivities shall be determined by the necessity of reaching a Finisse of 50000 on the s polarisation state. Also for the two plane mirrors we shall have that their values have to be identical in order to have optimal coupling of the cavity. The end mirror should have a reflectivity of a true R_{max} and we shall suppose from hereon that it shall have a reflectivity of 1. Since Finesse is given by, as seen in Section 4.1,

$$F = \frac{\pi\sqrt{r_1 r_2 r_3}}{1 - r_1 r_2 r_3}, \qquad (6\text{-}9)$$

where we have supposed r_3=1 and imposed r_1=r_2, we shall have that (r_3>)r_1=r_2=0.9998 in amplitude, between 43° and 45° for the s polarisation. We wish for the coupling to remain between -0.1 and 0.1. This ensures that the Tilt Locking central frequency changes are limited to 0.01Hz for optimal alignment and to below 100Hz for photodiode displacements of the order of 10% of the beam's waist. This condition shall bring us to an amplitude reflectivity difference between the plane mirrors having a maximum value of Δr=50ppm.

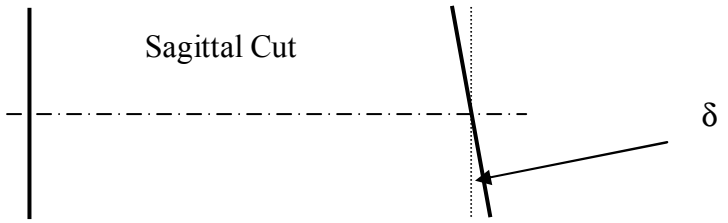

Figure 6–11

Spacer and dihedron: internal dimensions

We now have to determine the size of the internal parts of the dihedron and spacer which must be large enough to account for the beam displacements considered above.

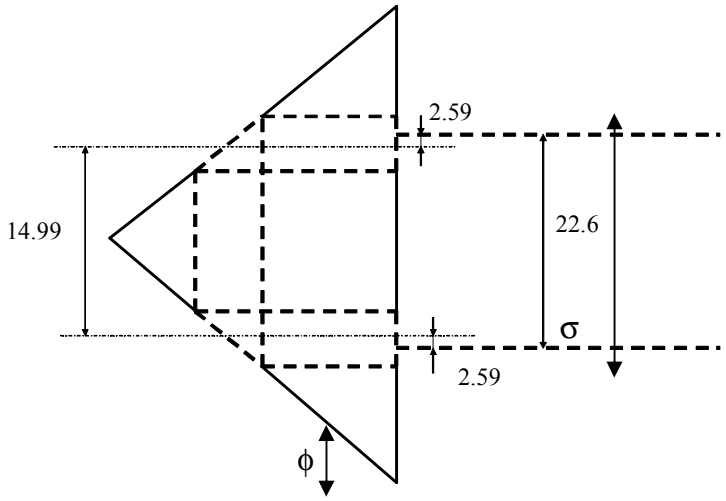

Figure 6–12

The contact faces of the plane mirrors must have holes of dimensions at least equal to the size of the needed free coating plus the 2mm needed for the centring of the mirrors, which means that its dimension ϕ must be at least greater than 7.6mm, which means that along the dihedron surface the hole must have dimension greater than $7.6\text{mm}\cdot\sqrt{2}=10.75\text{mm}$. The spacer must have an internal diameter greater than $d+\phi$ which means that σ must in its turn be: $\sigma>22.59$. If we consider the initial plans for the dihedron and the spacer, shown in Figure 6–12, we see that the spacer internal cavity must be enlarged by some 5.18mm in order to satisfy this parameter.

Test and results

This cavity has unfortunately been completed with a delay of well over a year due to unforeseeable delays. The completed assembly has arrived in our laboratories in September 2004. The first tests have shown a cavity transmission of only $4\ 10^{-4}$ (reflectivity is 0.9996) which coupled with the low value of the high Finesse (200) makes us suspect a low reflectivity of the end mirror. This is comforted by the coater's measurement of the planarity of the end mirror surface; while at $\lambda/10$ over all the mirror surface showed high values of the local rugosity. Having already tested the performances of the Tilt locking technique on the Virgo pre-stab cavity, as explained

in Section 6.1, and since the cavity will require long substitution processes to be usable, we decided to forbear from further testing, for the moment.

6.3 Long term performances of the Tilt Locking

We now wish to progress in our analysis of Tilt locking moving onto a long term validation of the same. Measurements with two lasers locked on a single cavity with the Tilt locking technique have given excellent results, Allan variances of the order of the Hz as reported by Slagmolen et al.[36], but this was @ 0.1Hz. We wish to validate the stability at longer time-scales (mHz and below) and to try a comparison with the Pound-Drever-Hall technique. This is particularly interesting to validate the technique's possible application in a LISA like space experiment, which would greatly benefit from the technique absence of active components. Let us, first of all, determine which properties a FP resonator would require for Tilt Locking to be compatible with LISA. As shown in Section 4.2 Tilt locking is not sensitive to misalignments as long as the cavity is perfectly coupled. This however doesn't hold true in the case where the entrance and exit mirrors of the cavity don't have equal reflectivities. Supposing the misalignments to be of the order of the μm which is compatible with a monolithic assembly (be it silicate bound or optically contacted), we can proceed to estimate the maximum reflectivity difference tolerable for the application of Tilt locking in LISA. For a cavity with a FSR of 1GHz, Finesse 10^5 (10^4) and waist 400μm, a photodiode with a diameter of 1mm and a dead area of 40μm we have that the superior limit for the parameter $r_2 \cdot r_3 - r_1$ is of 50ppm, which can be realised in LMA in Lyon (F. Cleva private Communication L.Mondin). If this condition is verified our model predicts locking point frequency shifts of 0.8Hz (8Hz), which are compatible with the LISA specifications. This frequency offset value is obtained for the worst case scenario where we have 1μm of detector offset and no beam offset. If we consider a cavity with re-injection prism in the presence of which the beam and detector offsets shall have the same sign the presence of both effects leads to a partial cancellation of the offset as shown in Section 4.2. It also has to be observed that for a given beam offset, a value of the Gouy shift can always be chosen that shall allow us to obtain an odd error signal line-shape. In fact, the quadrature odd signal is given by the presence of a tilt only in the near field configuration, in the far field it shall be given by the shift. Analogously the even error signal component deforming the line-shape shall be due to the tilt (shift) in the far (near field)

configuration respectively. We can pass from one configuration to the other by displacing the lenses L_{11} and L_{12} shown in Figure 6–1. Comforted by this observation let us now consider the experimental comparison with PDH.

6.3.1 Comparison with the Pound-Drever-Hall

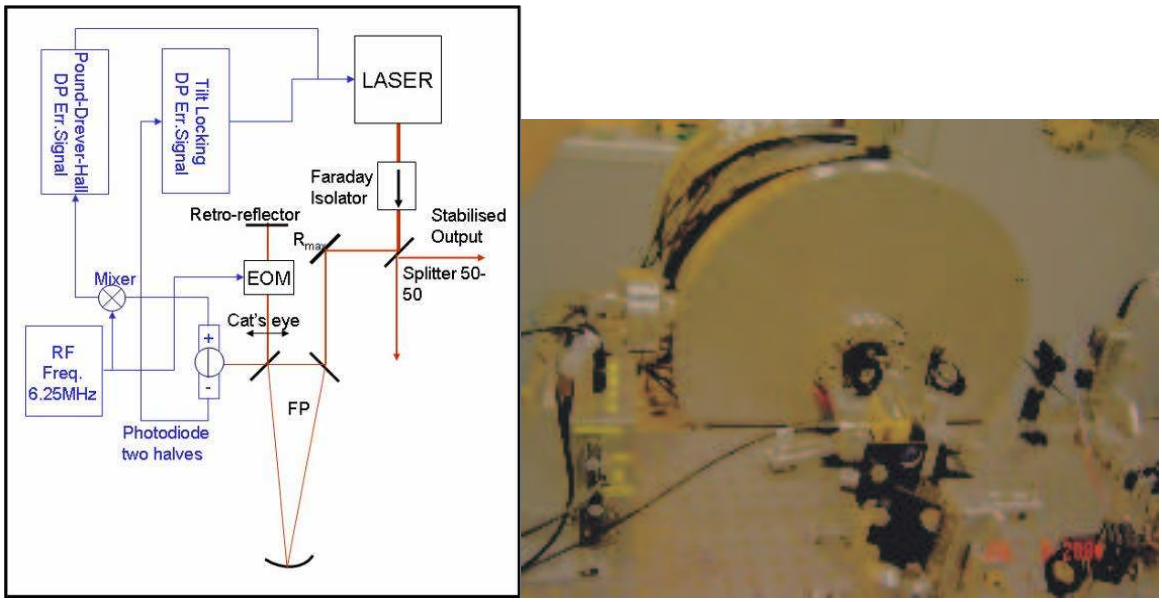

Figure 6–13

After having demonstrated, analytically and through simulation, analogous locking point stability for the Tilt Locking and Pound-Drever-Hall techniques with dependence from alignment and modulation amplitude, respectively the main causes of offset (Section 4) we now want to compare the performances of the techniques experimentally. The experimental configuration is shown in Figure 6–1. The FP in its vacuum tank was positioned on a separate table while the laser and all components needed for the lock where on the large marble holding the rest of the experimental set-up, as can be seen from Figure 6–13. This ensured that μm displacements of the cat's eye lens or of the re-injection mirror resulted in beam displacements of the order of w_0 (waist in the cavity 289μm) over 8 on the mirror surface. Similarly these displacements will result in detector misalignments of the same sign and order of magnitude but smaller in unities of the waist since the conjugated waist on the photodiode shall be larger than the cavity's (close to 800μm). We observed the two error signal profiles when the Tilt Locking was close to the best alignment and obtained the graph in Figure 6–14. While the Tilt Locking error signal (in red) line-shape was slightly asymmetric as shown by its crossing with the Pound-Drever-Hall (PDH, in blue) on the left hand side of the graph, we can observe that the zero

crossing point is coincident for the two curves. Furthermore once the error signals were amplified to obtain the same peak to peak amplitude, as shown below in Figure 6–14, their slopes had the same value close to the zero crossing point (1kHz/V).

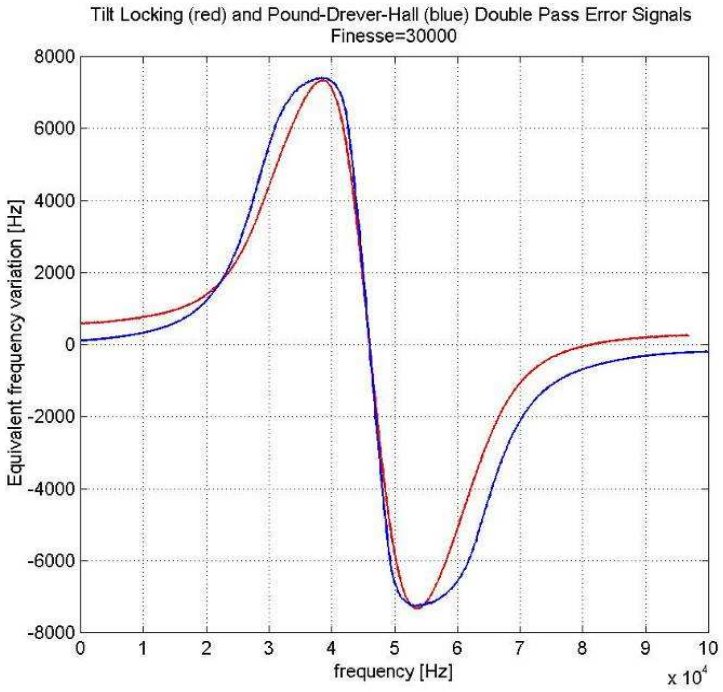

Figure 6–14

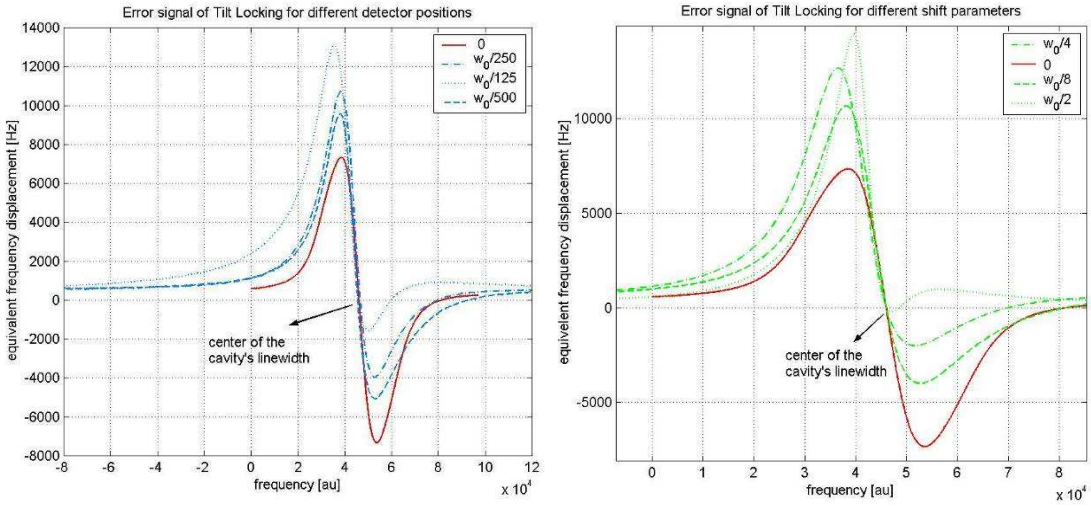

Figure 6–15

We then proceeded to evaluate the error signals line-shape changes for different values of the beam and detector shifts (Figure 6-15) in order to be able to determine the influence of the deformations on the profile. It can be seen that analogous deformations are obtained for smaller values of the detector shift with comparison with the beam's. This is consistent with what calculated analytically and with the simulation since the detector contribution is larger. The beam contribution is too small

with comparison to the expected value (1/3 of the detector offset). This can however be explained if we take into account that a beam offset shall also introduce a detector offset. This latter shall have, in our experimental configuration, the same sign as the beam offset, and thus as predicted by both the model and the analytical calculations the two effects shall have competing behaviours. The resulting frequency shift and profile distortion shall be reduced to values compatible with the measured ones.

Optical misalignments offset

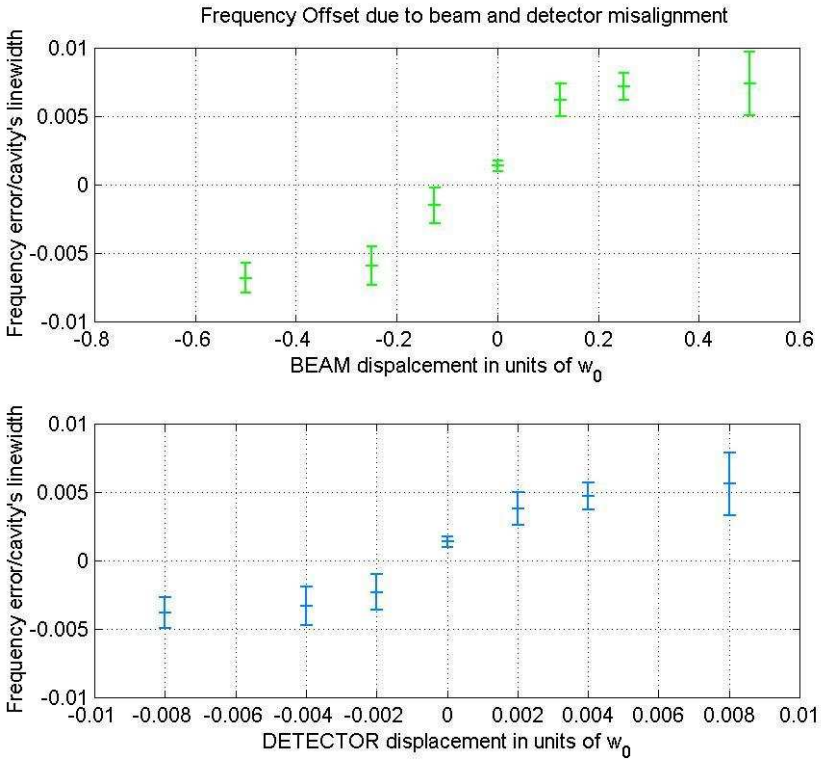

Figure 6–16

To measure more exactly the offsets values especially on the mHz scale we then locked laser 2 on the PDH error signal and observed the residual Tilt locking error signal. For the experimental configuration, please refer to Figure 6–13. The 190mW laser beam was perfectly aligned and mode matched to the cavity. The beam transmitted by the cavity was then re-injected and both refocused and tilted by the lens in a cat's eye configuration. Prior to re-injection the beam is also passed through the EOM enacting a phase modulation at 6.25MHz, the reflected signal is then observed the split photodiode. The sum of the two halves' contribution is then demodulated at the EOM driving frequency and produces the PDH error signal whereas their difference gives the Tilt locking signal. In this configuration we can change the photodiode position and the tilt and shift of the beam on the cavity to

monitor the offset on the lock position of the tilt locking error signal. We observed over a time of 1.2ks the Tilt Locking error signal to monitor both offset and offset variations from the expected null signal for different values of beam and detector displacements. The resulting equivalent frequency errors in units of the cavity's linewidth are shown in Figure 6–16. As seen for the unlocked state the frequency variations are of the same order for values of the beam offset three times bigger than the detector offset. This confirms that the detector positioning is critical for the Tilt locking technique. There remain two things to be explained in the behaviour of the frequency offset presented in Figure 6–16: the saturation effect seen for the higher values of the position offsets and the smallness of the effect caused by the beam displacement. The first effect is due to the finite nature of the detector in particular to its small size ($1mm^2$) compared to the incident beam waist ($800\mu m$). The reduced effect of a beam misalignment is as seen above due to the competition between the beam and the induced detector offset effects. The experiments have been realised for both polarisation states (low and high Finesse) but the long term validation was only done for the low Finesse as there was less chance of a spurious lock loss during the measure.

6.4 Allan variance Iodine vs. Fabry-Perot

Having validated Tilt Locking experimentally with respect to Pound-Drever-Hall we now have to determine the performances of our lock on the mechanical reference with respect to the molecular reference. As seen in the description of the experiment (Section 6.1) we lock one laser on the molecular transition and the second laser is locked with either Pound-Drever-Hall or Tilt-Locking to the high or low finesse of the Fabry-Perot cavity. The frequency variations between the two lasers are observed on the beat note detector (a photograph of the beat note experiment is to be found in Figure 6–17).

The comparison must of necessity be made with both Tilt locking and Pound-Drever-Hall to ascertain that no unexpected phenomenon, or beam jitter motion, degrades the performances of Tilt Locking (though as shown by Slagmolen[36] Tilt locking can reach the 3Hz stability @ 0.1Hz) on the long term. We thus repeat the measure with both techniques. With this kind of measurement we can only hope, in our actual configuration, to determine the stability of the mechanical reference. Since we don't have any form of thermal isolation (apart for the vacuum tank) protecting our cavity

from temperature fluctuation, we fully expect to measure exclusively the deformations of our Fabry-Perot with the long term comparison. This, however, is on its own a significant test as it shall allow us to determine the necessary temperature stability for the Fabry-Perot not to undergo frequency shifts at the Hz level. Furthermore, we shall be able to measure with a better than 5℃ acc uracy the working point for our cavity ULE.

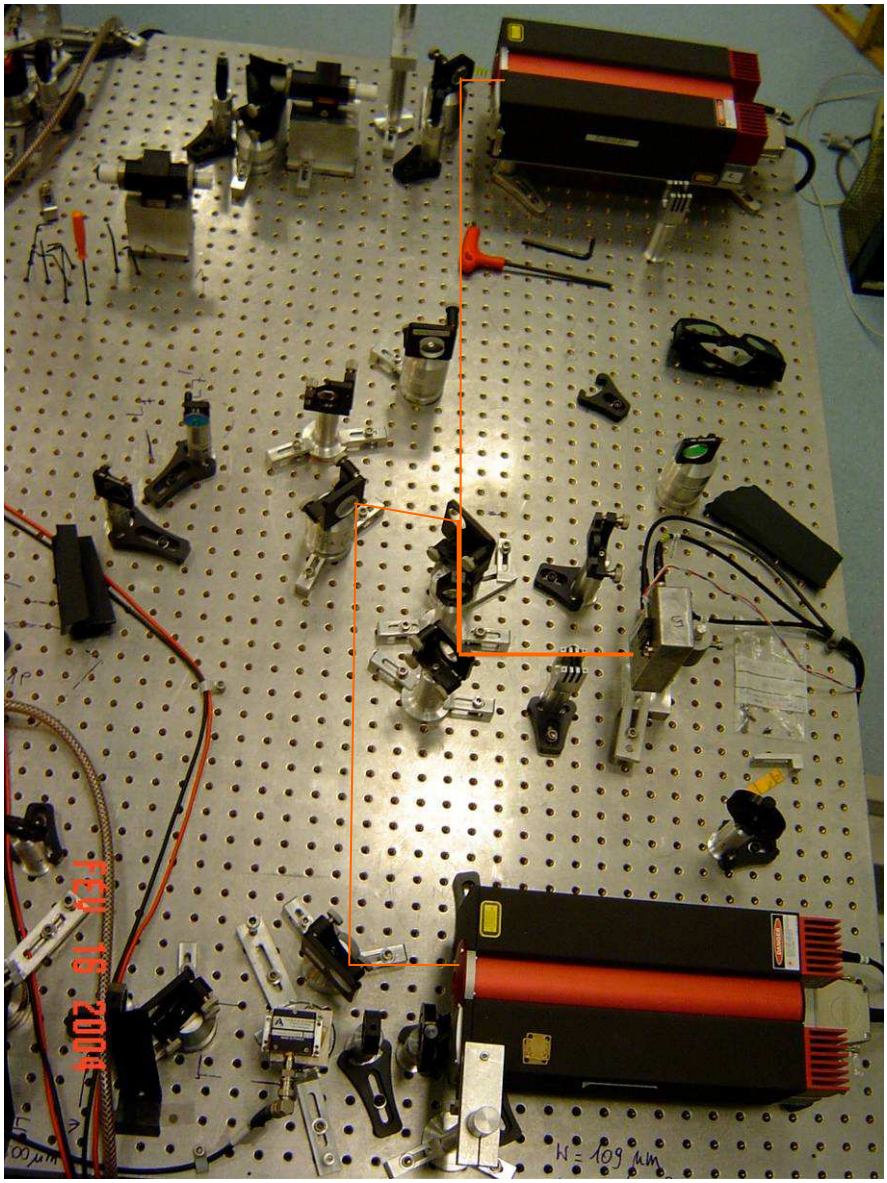

Figure 6–17

6.4.1 Pound-Drever-Hall

We decided to test the performance of our Pound-Drever-Hall system with respect to the Iodine locked laser first. This because we fully expected to only measure the cavity frequency shift using this technique. We locked the laser 1 on the Iodine transition (either a_{10} or a_{15}) and laser 2 on our FP reference cavity (high and low

Finesse respectively). We acquired both the frequency of the beat note (which we can assume to be a measure of the frequency variations due to the thermal dilatation/compression of the cavity) and the temperature of the tank containing our cavity. The 10^{-8}mbar vacuum ensures that there is a large time constant between the cavity and the exterior of the tank, where we measure the temperature with a PT_{100} and a NCTS. Both sensors are in good thermal contact with the cavity and isolated, thanks to a system of isolating foam coated with aluminium paper, from the room temperature changes. The temperature measurement obtained is therefore the actual vacuum tank temperature. It was shown (Figure 6–18) that the beat note frequency shifts (blue curve) follow with a 13000±2000s delay the temperature shifts (black curve) converted with the theoretical estimate of the linear expansion coefficient into frequency shifts).

These time delays were calculated thanks to the routine 'fitdel' (see Appendix C). It can also be shown that the coherence, a function of the frequency with values between 0 and 1 which indicates how well an input (I) correspond to a given output (O) for each frequency, between the frequency shifts and the cavity temperature variations goes towards its maximum value of 1 for frequencies below the mHz (Figure 6–19). The coherence is more precisely defined as:

$$C_{IO} = \frac{\left|\overline{FFT(I) \cdot FFT(O)}\right|^2}{P_{II} \cdot P_{OO}} \qquad \text{(6-10)}$$

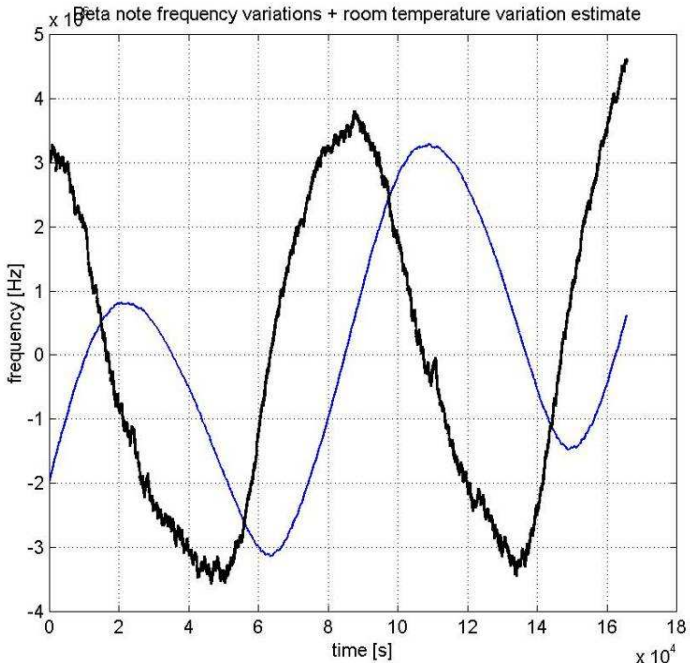

Figure 6–18

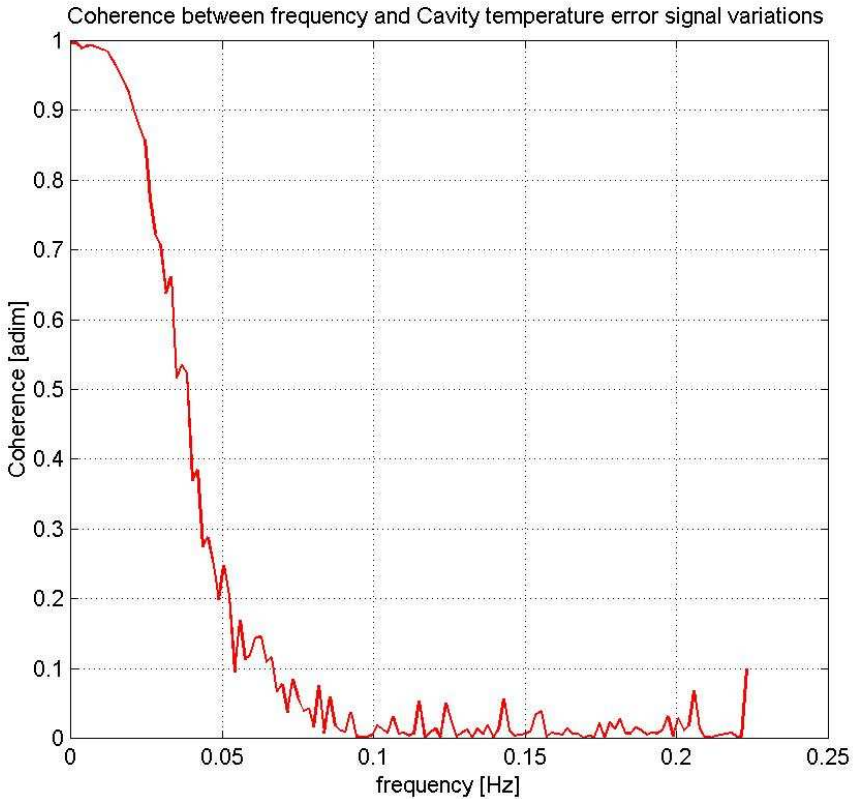

Figure 6–19

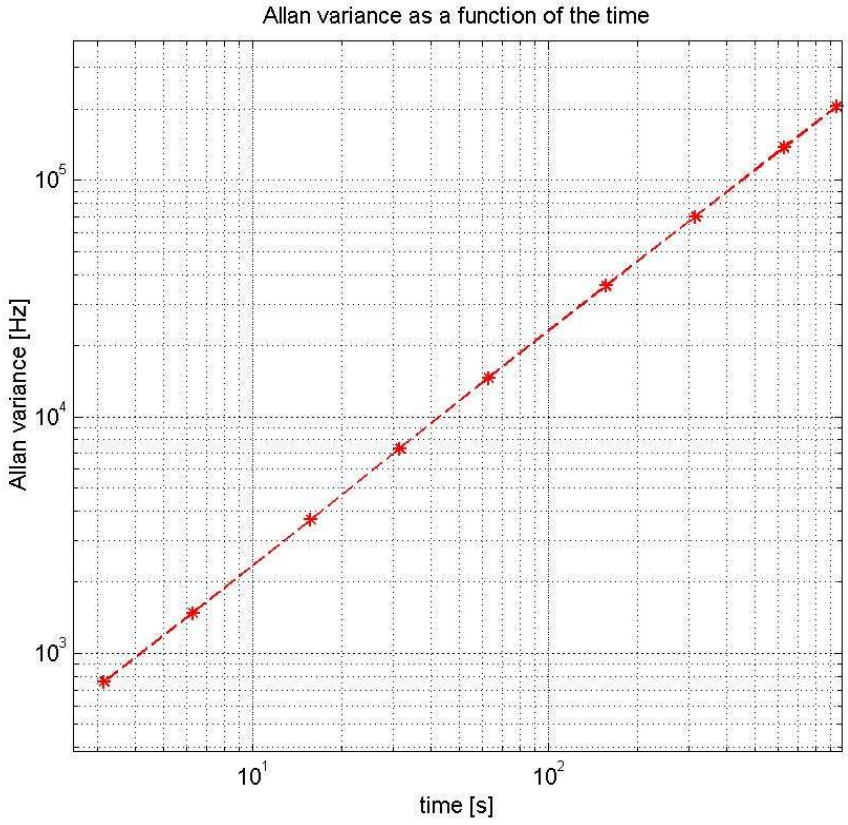

Figure 6–20

where the quantity $\overline{FFT(I)\cdot FFT(O)} = P_{IO}$ is often called cross spectral density, and with P_{II} and P_{OO} we indicate the power spectral densities of the Input and Output respectively. The coherence can be calculated only for frequencies below the sampling frequency ($1/T_{acq}$), also the FFT lines must be calculated for a number of points much lower than the number of acquisitions. From the time measurements shown in Figure 6–18, we also can trace the Allan variance of the frequency as was done in Figure 6–20. The measured shifts of the beat note frequency are limited by the cavity sensitivity to temperature variations. For the instant (and for as long as the cavity shall not be thermally isolated, or length controlled) we shall only be capable of determining an upper limit for the actual technique frequency variations (see Figure 6–20). The shown measurements were taken on the 04-10-05. We were able to obtain reproducibility for the central frequency of the beat note on a given transition with an error below 6MHz. The statistic for the high Finesse was of 3 data points and for the low Finesse of 6. There was no possible verification that we were locked on the same order for the cavity, indeed more than once the necessary manual thermal regulation when looking for the beat note with the corresponding Iodine transition spanned more than one FSR.

6.4.2 Tilt Locking

For the Tilt locking technique we have, as a matter of course, analogous results to those obtained with the Pound-Drever-Hall, this was to be expected since we shall be still limited by the cavity temperature caused frequency drifts. The possible effects coming from misalignments, as seen in Section 6.3.1, are well below the MHz effects provoked by temperature variations even for the low Finesse (linewidth 480kHz) of the reference. The delay between the temperature and the frequency shift is in this case too of the order of 10^4s, in particular we obtain (always using the routine fitdel, modified) that the delay shall be τ=(15000±2000)s which is compatible with the observed values given for the Pound-Drever-Hall lock.

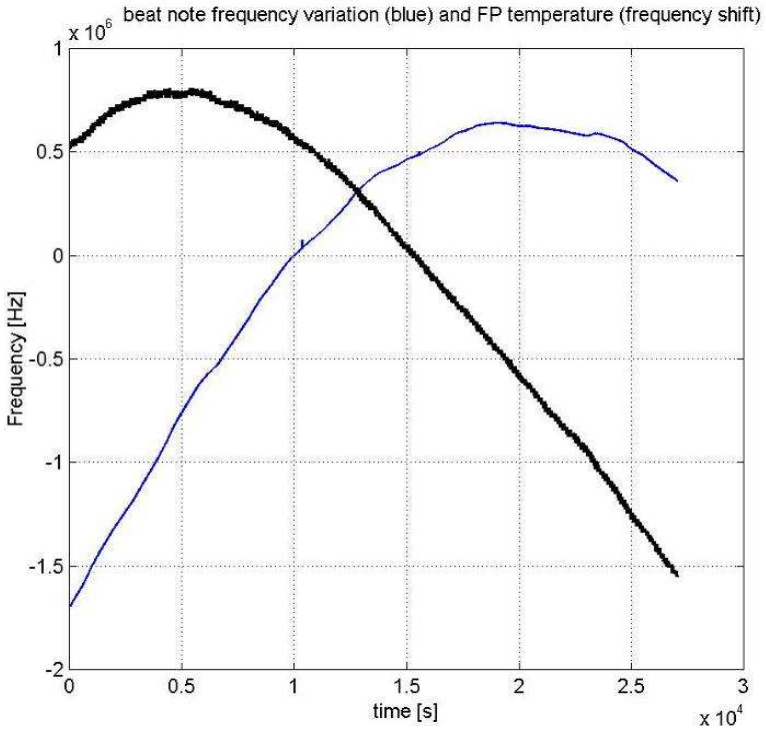

Figure 6–21

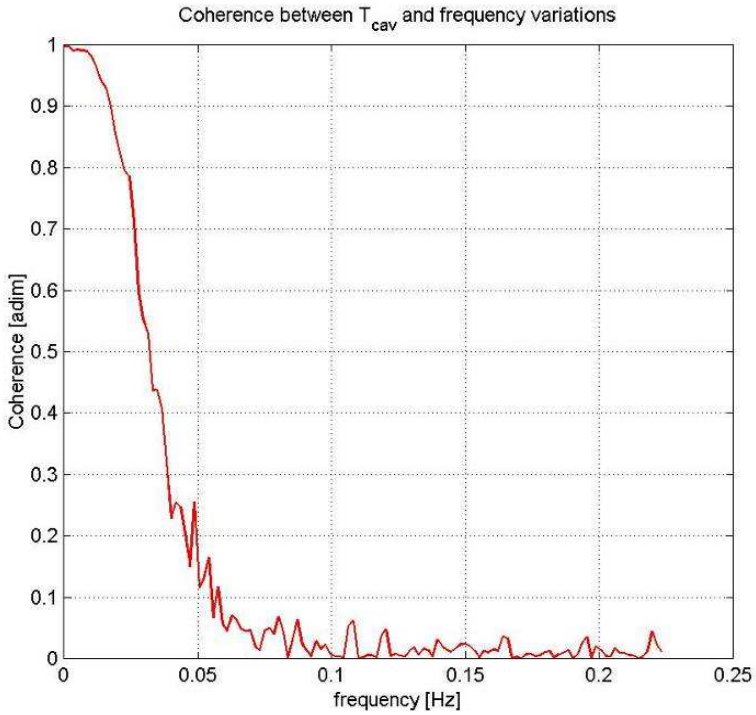

Figure 6–22

The time curve for the Tilt Locking is shown in Figure 6–21. We can once again trace the profile of the calculated (according to Equation (6-11)) coherence. This time too we shall have that the coherence shall go towards 1 for frequencies below the mHz, as shown in Figure 6–22. If we trace the Allan variance, Figure 6–23, we obtain similar values for longer time stretches but higher ones for the short integration times.

This can be explained as for times below the 10s we can expect the main cause of frequency variation to be linked with the Iodine locked laser rather than with the thermal drifts of the cavity (whose period is much larger) or with the Tilt Locking technique. At the time when the Tilt locking measures were taken, 04-06-29, the performances of the Iodine locked lasers were, as can be seen from Section 5.3, significantly inferior to those we have reached nowadays. We can therefore fix an upper limit to the Tilt locking possible effect on the lock of a laser compared to the Pound-Drever-Hall and that is the MHz. We could ideally think of a way to better the sensibility of our measurement. This would require the knowledge of the ULE working temperature, which is the temperature that shall yield the lowest linear expansion coefficient for our ULE cavity. The determination of our working temperature would allow us to reduce the temperature induced shifts even before subtraction of the measured shifts.

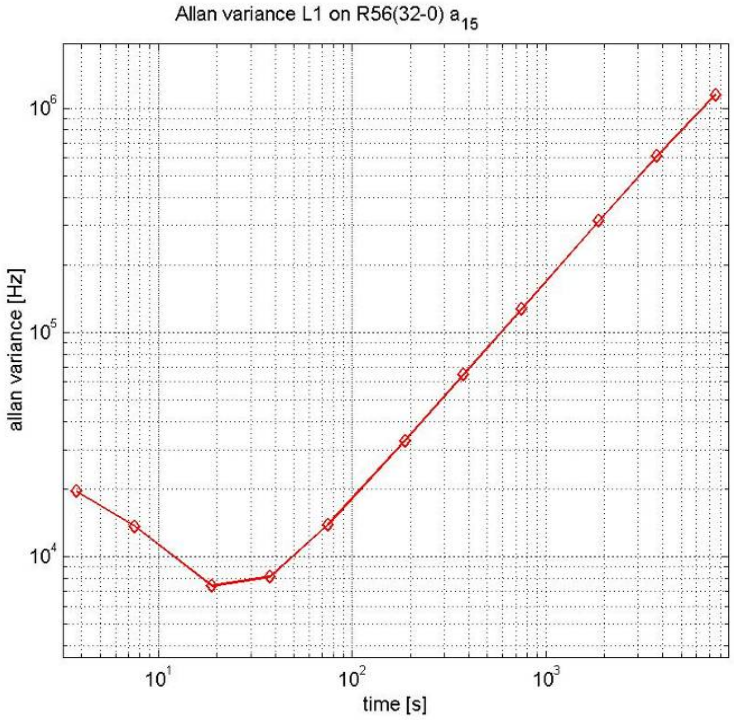

Figure 6–23

Even with this knowledge the temperature variations remain too large to descend below the MHz level in the precision of our qualification. The Tilt Locking showed a reproducibility of the beat note central frequency of some 8MHz with a statistics of 2 measures for the high finesse and 5 for the low finesse. Significantly there was no difference in the measures taken with or without air conditioning on. We initially thought that the acoustic noise might perturb Tilt Locking especially on the high

Finesse, this phenomenon was seen on our previous cavity. The only effect linked to this difference was the bigger temperature excursion due to the lack of air conditioning. Measures taken with the pumping system on and off also allowed us to determine that the drifts are exclusively of thermal origin, and not linked to residual pressure in the tank. The lack of a larger statistic for the different experimental conditions was not as worrying as might be thought given the fact that even after a few months the same frequency values were found and analogous drifts were observed.

6.4.3 Frequency Drifts in a cavity (measurement of α_{lin})

In order to measure the linear expansion coefficient we decided to heat the vacuum tank with a thermal coil capable of bringing the whole cavity and tank assembly to a temperature of 100℃ over the course of 1 day of he ating. For our measurement we were rather interested in small temperature shifts, so that we used a DC power supply with a variable output. In particular between the start of the heating and the corresponding frequency measure of the beat note (Figure 6–24) we wait for about 1h. The beat note was averaged over 1000 measurements, having a duration each of 1s, to obtain a corresponding frequency value. The measurement was repeated twice to ensure that the frequency had stopped drifting. A subsequent 1000 measure yielded a standard deviation (thanks to the HP53131A mathematical mode function) which we took as experimental error of our measurement. Having measured the beat note frequency in function of the different temperature values we then proceeded to consider that over 1000s the variation of the frequency are to be considered as depending on the cavity locked laser exclusively, the frequency shifts were therefore converted in their totally into length variations of the reference. The fact that the frequency becomes lower for increasing values of the temperature can be understood if we consider that the length expansion of the cavity shall introduce a reduction of the FSR. If we now consider these length variations and we determine their angular coefficient for each point as the mean of the angular coefficient of the lines on the right and on the left hand side of the given point, we shall have an estimate of the linear expansion coefficient of our ULE as a function of temperature, as shown in Figure 6–25. The optimum value obtained for a temperature of (26.7±1)℃ is of $3 \cdot 10^{-9} K^{-1}$ which means that we shall require a temperature stability of

the μK to obtain frequency shifts of the order of the Hz due to the thermal drifts of the cavity.

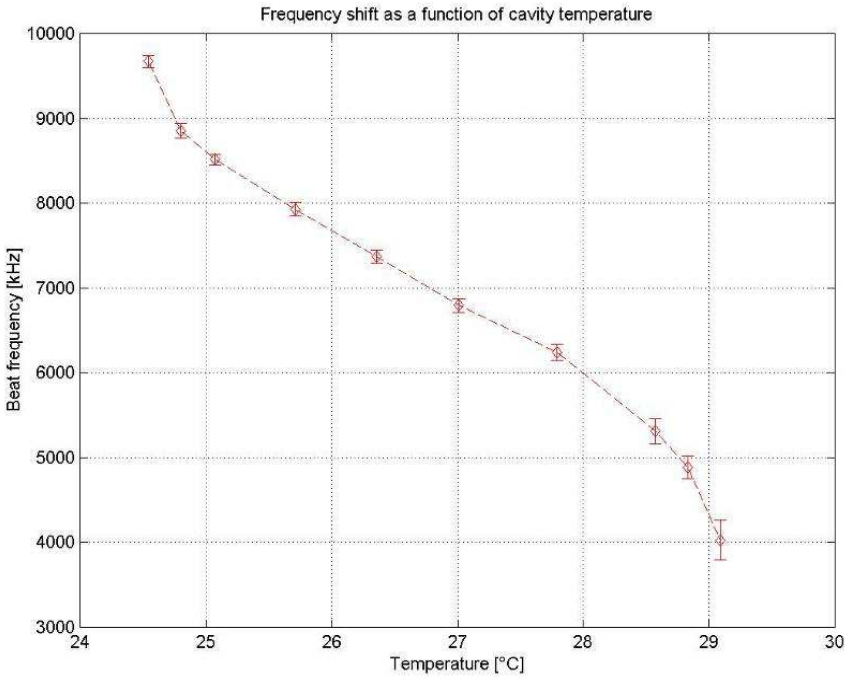

Figure 6–24

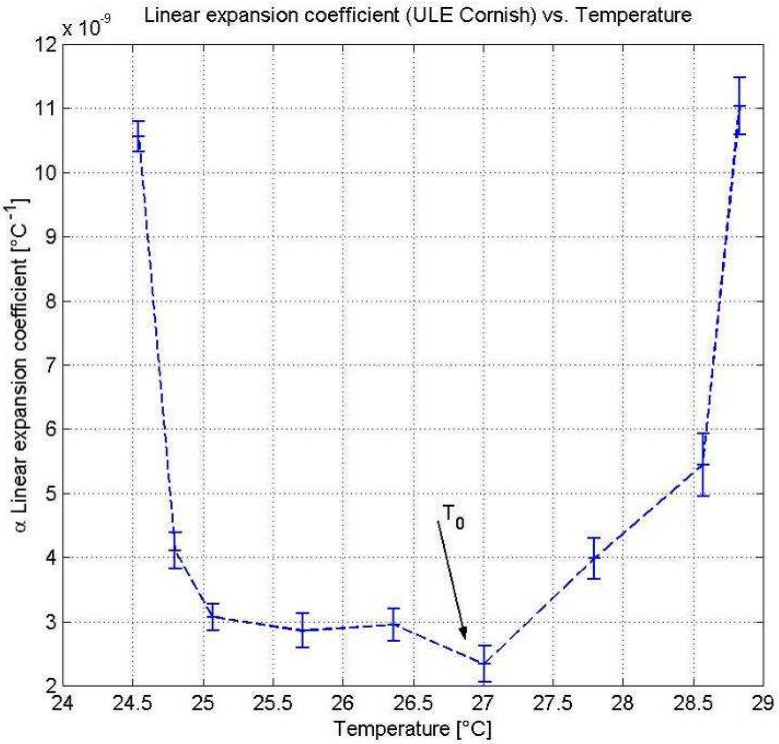

Figure 6–25

Photon noise limit

Finally let us now determine as done for the Iodine experiments the intrinsic limit of our measurement, that is to say let us calculate the photon noise limit for our experimental FP set-up. The calculation is perfectly identical to the one shown for the Iodine case with the single difference that the term determining the energy of the single photon shall this time have (while the analytic expression is unchanged) a different numerical value ($E = h\nu$ =1.87 10^{-19} @1064nm). The calculation shall yield a photon noise limit of 64.7Hz.

Alternative Tilt Locking configuration

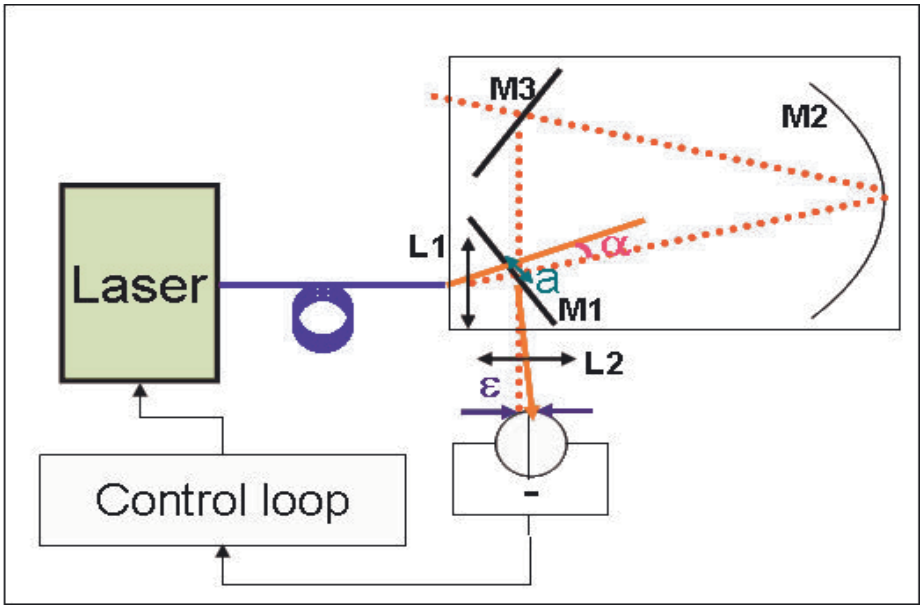

Figure 6–26

We have seen (Section 4.2.2) that one drawback of the double Pass tilt locking is the limitation of the bandwidth due to the storage time of the light by the cavity. A possible alternative configuration to the Double Pass Tilt locking would require the use of a fiber long enough (10m M.Dubreil private communication) to ensure a good mode cleaning effect without this limitation. The remaining beam jitter would be due to the focalisation lens at the exit of the fiber, since all beam jitters before the entrance of the beam into the fiber would translate in a simple variation of coupled power.

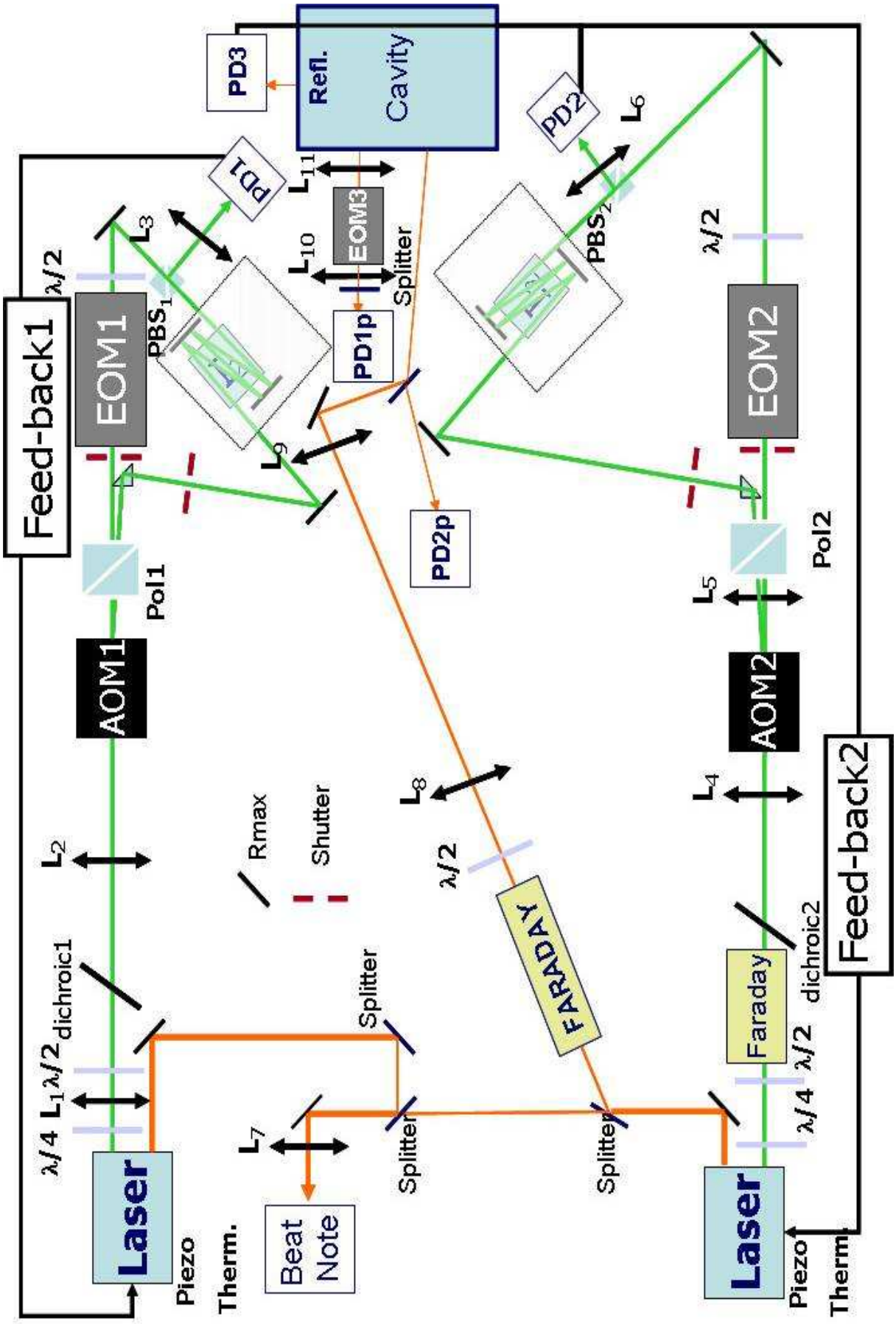
Feed-back1
EOM1
AOM1
Pol1
λ/2
λ/4
L1
dichroic1
L2
Laser
Piezo
Therm.
L3
PBS1
PD1
L10
EOM3
L11
PD3
Refl.
Cavity
PD1p
Splitter
L9
PD2p
L8
λ/2
Rmax
Shutter
FARADAY
L7
Beat Note
Splitter
Splitter
PD2
L6
PBS2
λ/2
EOM2
Pol2
L5
AOM2
L4
Faraday
λ/2
λ/4
dichroic2
Feed-back2
Laser
Piezo
Therm.

Figure 6–27

7 Conclusions and further work

To conclude we have shown through analytical calculation, simulation and experiments that the Tilt Locking technique is insensitive enough to beam displacements (for reflectivity values of the input and output mirrors no more than 50ppm apart) to potentially reach the LISA frequency stability goal. There is a dependence of its lock point on the alignment of the photodiode, but when the alignment is better than the μm (monolithic assembly) we have performances equivalent to those of the Pound-Drever-Hall technique. This has been tested against an iodine locked system. The performances of the latter tests were unsatisfactory for a validation with a precision equal to the LISA requirements. It was however possible to determine through these tests both the required temperature stability (μK) and the operating temperature of our ULE cavity (27℃) with a precision of 1℃, as opposed to the 5℃ uncertainty given by the constructor. Tilt locking has been shown as an extremely attractive technique for space implementation due to its lack of active components and its good performances in the presence of important beam shifts. All of this provided that the detector stable position is assured. The performances of a stable ULE cavity with no acoustic, seismic or thermal isolations were shown to be largely insufficient for LISA and for most of our tests. In the future when the SESO cavity reflectivity shall be corrected, we might be able, using thermal screens guaranteeing temperature stabilities of the μK, to actually validate our PDH and Tilt locking frequency locked lasers with respect to the iodine. This shall allow for a determination of stability, reproducibility and also for a measure of the absolute frequency variations.

Our iodine systems have reached LISA specifications for the higher frequencies of the LISA band, we still have a noise source at 1mHz, of electronic origin, which we haven't been able to completely cancel up to now. The cancellation of the measured mHz noise while reproducible and sufficient to reach overall frequency stability at the 10^2Hz level is unsatisfactory. Further studies to understand the nature of the problem and correct it are underway.

Appendices

A. Laser Interferometer Space Antenna

Gravitational Waves

The existence of Gravitational Waves is a direct consequence of Einstein's Theory of General Relativity formulated in 1916.[37] This theory is based on the both the Theory of Special Relativity and the Principle of Equivalence. The latter is but a generalisation of the fact that, as can be observed, bodies of different materials behave in an identical fashion under the action of gravity. Thus we can separate gravity from the bodies generating it and begin to consider it simply as an intrinsic property of the space-time.

If gravity is a property of the space time then it can be identified as a metric, thus for a stationary gravitational field with a spherical symmetry, such as the Solar System if the planets are seen as test masses perturbing the central field given by the Sun, we have:

$$ds^2 = A(r)\cdot dt^2 - B(r)\cdot\left(dr^2 + r^2\cdot\sin^2\vartheta\cdot d\varphi^2 + r^2\cdot d\vartheta^2\right). \qquad \text{(A-1)}$$

Now if this metric is close to the flat space-time metric, A and B are functions only of $\frac{GM_\Theta}{rc^2}$ and we can thus rewrite the above equation as:

$$ds^2 = \left(1 - 2\alpha\frac{GM_\Theta}{rc^2} + 2\beta\left(\frac{GM_\Theta}{rc^2}\right)^2 + \ldots\right)\cdot dt^2 - \left(1 + 2\gamma\frac{GM_\Theta}{rc^2} + \ldots\right)\cdot\left(dr^2 + r^2\cdot\sin^2\vartheta\cdot d\varphi^2 + r^2\cdot d\vartheta^2\right) \qquad \text{(A-2)}$$

In this last expression the coefficients α, β, and γ are called post-Newtonian parameter and are given for a chosen theory of gravitation. In the case of General Relativity these parameters take the values $\alpha = \beta = \gamma = 1$, which are in good accord with their measured values in the Solar System and also for (PSR1913+16) the double Taylor and Hulse[38] pulsar (precision of these measurement 10^{-4} for α et 10^{-3} for β and γ.) Unfortunately the measured values are also consistent with other theories of gravitation for which the Post-Newtonian parameters are different from unity only for strongly gravitating bodies. This is one of the main reasons why LISA, which is built

to observe the low frequency ranges of the GW spectrum, hence for example the coalescence of two massive black holes, would be extremely interesting from an experimental point of view.

Let's now see how we can obtain from Einstein's field equations the equations for the Gravitational Waves. We have that matter is linked to the metric, as gravity, a property of mass, has been identified with the metric of the space-time expressed by

$$G^{\mu\nu} = 8\pi T^{\mu\nu} \tag{A-3}$$

where $G^{\mu\nu}$ is the tensor representing the curvature of the space-time and $T^{\mu\nu}$ expresses the distribution of the mass-energy. For the law of conservation of the mass-energy we know that must verified:

$$\nabla_\mu T^{\mu\nu} = 0\,. \tag{A-4}$$

And in these conditions the only solution for Equation (A-3) is:

$$G^{\mu\nu} = \Lambda g^{\mu\nu} + \left(R^{\mu\nu} - \frac{1}{2} g^{\mu\nu} R^{\mu}_{\mu}\right), \tag{A-5}$$

where Λ is the cosmological constant and $R^{\mu\nu}$ is Ricci's tensor which describes the curvature of the space-time. For weak gravitational fields we can simply use a metric which is given by a small perturbation of Minkowskji's metric which is to say :

$$g_{\mu\nu} = \eta_{\mu\nu} + h_{\mu\nu}\,, \tag{A-6}$$

with $\eta_{\mu\nu}$=diag(-1,1,1,1) and $|h_{\mu\nu}| << 1$.

In this limit Einstein's equation will have the form of a Wave equation:

$$\left(\nabla^2 - \frac{1}{c^2}\frac{\partial^2}{\partial t^2}\right)\cdot h_{\mu\nu} = 0\,, \tag{A-7}$$

And once this is solved for a transverse and null trace gauge we shall obtain:

$$h_{\mu\nu} = \begin{pmatrix} 0 & 0 & 0 & 0 \\ 0 & a & b & 0 \\ 0 & b & -a & 0 \\ 0 & 0 & 0 & 0 \end{pmatrix} = a\cdot\hat{h}_{+} + b\cdot\hat{h}_{\times}\,. \tag{A-8}$$

With $\hat{h}_{+}$ and $\hat{h}_{\times}$ we indicate the conventional two polarisation states of a Gravitational Wave propagating along the direction perpendicular to the deformations. The effect of the passage of a GW is a variation of the distance between two free-falling bodies, in the direction perpendicular to the propagation, but not a measurable acceleration on the test masses themselves. The passage of a GW has a tidal effect as can be seen in Figures A-1 and A-2. But these deformations are extremely small, of the

order of an atomic diameter for distances of the order of the AU[1]; a measure of such an effect is riddled with enormous technical difficulties.

Gravitational Waves are expressed by the equation of the waves, they are transverse waves and like light they propagate at a speed of *c*. We can, now, decide to further develop the analogy with the electromagnetic case by looking for the multi-poles terms of the emission. This approximation as is the case for light is only acceptable for sources having dimensions much smaller than the distance observer-emitter, which is always verified for astrophysical objects. In the gravitational case, as in the electromagnetic, the monopole term is zero as mass and charge respectively are conserved. But whereas for electromagnetic radiation the dipole moment is not null this is not true for the gravitational case where the conservation of momentum renders this term too equal to zero. Given that the gravitational equivalent of the 'magnetic dipole' is null too for the conservation of angular momentum the first non zero term is the quadrupole one which has the form:

$$I_{\mu\nu} = \int \left(x_\mu x_\nu - \frac{1}{3}\delta_{\mu\nu} r^2 \right) \rho(\vec{r}) dV \,, \qquad \text{(A-9)}$$

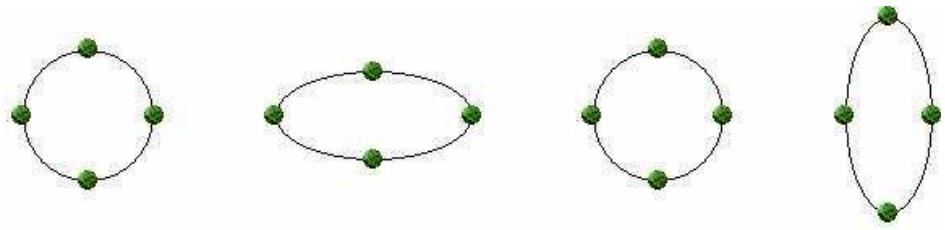

Figure A–1 Polarisation + of a GW

Figure A–2 Polarisation × of a GW

[1] 1 Astronomic Unity is the mean distance between the Sun and the Earth and is 150 10^6 km.

From this expression we can derive the form of the deviation from the flat space-time metric which will be:

$$h_{\mu\nu} = \frac{2G}{rc^4}\ddot{I}_{\mu\nu}\Big|_{t-\frac{r}{c}} . \qquad \text{(A-10)}$$

From these considerations it is therefore obvious that gravitational radiation is several orders of magnitude weaker than its electromagnetic counterpart, which is indeed to be expected since Coulomb's force is 10^{39} times stronger than gravitational attraction. For example if we try to produce gravitational waves in a laboratory setting by taking two 10^3 kg masses separated by a 2 m long rigid bar setting it in rotation with a frequency of 1KHz we have an emitted GW with an amplitude of the order of the10^{-39}. Whereas if we had to produce an electromagnetic wave with charges of 10^3 C separated by 2m and a frequency of the kHz we would have amplitudes of the order of 10^2. From this observation we can also realise that only events implicating enormous masses, of the order of the mass of the sun, which is to say astrophysical high energy events, can actually be capable of producing signals sufficiently intense for detection.

While indirect evidence of the existence of Gravitational Waves was obtained by Taylor and Hulse's study of the already mentioned double pulsar PSR1913+16 no direct detection of these phenomenon has been possible up to now.

Detectors

As we have seen detecting a gravitational wave is no easy task given the extremely small nature of the observed phenomenon. We now want to see which kind of antenna is the best suited to attempt a direct detection of Gravitational Waves.

There are two main types of GW detectors: *Bar antennas*[45] and *Interferometers*[46].

As gravitational waves are a tidal effect a detector works the better the more sensitive it is to acceleration variations in the volume it occupies. For a bar detector we can imagine it as an harmonic oscillator (such as a spring) that at the passage of a GW, having a frequency within its bandwidth, typically of the order the Hz, resonates at its own frequency. For an interferometer the test masses relative distances vary at the passage of the GW.

Let us now see more in detail the workings of a triangular shaped interferometric detector such as LISA.

For the purposes of this thesis we shall consider LISA as a three armed Michelson interferometer (equal to three correlated inclined Michelson interferometers), even if other data analysis techniques, using Time Delay Interferometry, yield better results for the antenna sensitivity, as can be seen in Figure A-4.

Taking into account Figure A–3 let us now calculate the time flight of a photon along two of the antenna arms, which make up one of the inclined Michelsons. For arms 1 and 2 for example in the presence of a GW moving along the axis perpendicular to the interferometer's plane we have:

$$0=ds^2=g_{\mu\nu}dx^\mu dx^\nu=(\eta_{\mu\nu}+h_{\mu\nu})dx^\mu dx^\nu=-c^2dt^2+\left(1+h_{11}e^{i\cdot(2\pi\nu t-\vec{k}\vec{x})}\right) \quad \text{(A-11)}$$

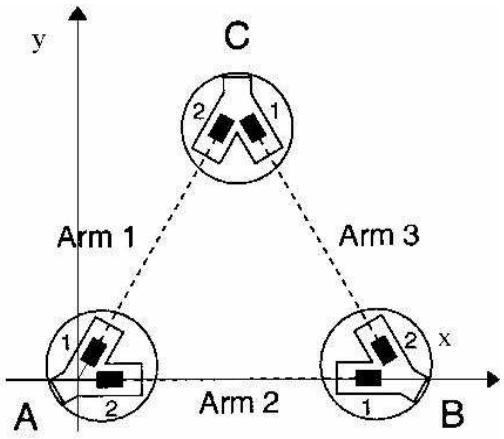

Figure A–3 From LISA: a mission report 1998

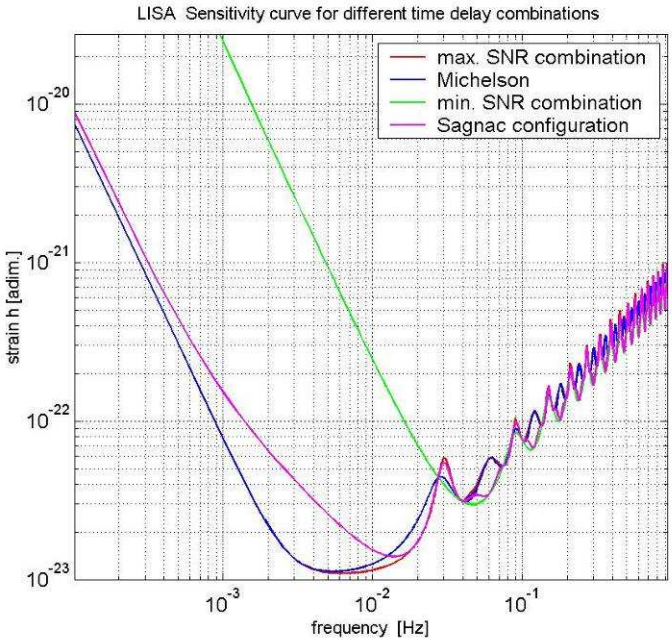

Figure A–4 R. Nayak private communication

Now the forward flight time for a photon along arm 2 can be obtained from Equation A-11 by integrating the time and developing in McLaurin's series (Taylor first order), we get:

$$\int_0^{t0} dt \cong \frac{1}{c}\int_0^L \left(1+\frac{1}{2}h_{11}\cdot e^{i\cdot(2\pi\nu t-\bar{k}\bar{x})}\right)dx\,. \tag{A-12}$$

For the backward flight in a completely analogous fashion we shall this time obtain:

$$\int_{t0}^{ttot} dt \cong -\frac{1}{c}\int_L^0 \left(1+\frac{1}{2}\cdot h_{11}\cdot e^{i\cdot(2\pi\nu t-\bar{k}\bar{x})}\right)dx\,. \tag{A-13}$$

where the forward time is t=x/c and the backwards time is instead t=(2L-x)/c. If we now calculate the total flight time of the photon we have:

$$T_{Tot\_2} \cong \frac{2L}{c}+\frac{1}{2c}\int_0^L \left(1+\frac{1}{2}h_{11}\cdot e^{i\cdot(2\pi\nu t-\bar{k}\bar{x})}\right)dx-\frac{1}{2c}\int_L^0 \left(1+\frac{1}{2}\cdot h_{11}\cdot e^{i\cdot(2\pi\nu t-\bar{k}\bar{x})}\right)dx\,. \tag{A-14}$$

If we proceed in the same fashion for the flight time along arm 1 we now have for the forward flight:

$$\int_0^{t0} dt \cong \frac{1}{c}\left[\int_0^{L\cdot\cos\frac{\pi}{3}} \left(1+\frac{1}{2}h_{11}\cdot e^{i\cdot(2\pi\nu t-\bar{k}\bar{x})}\right)^2\cdot dx+\int_0^{L\cdot\sin\frac{\pi}{3}} \left(1+\frac{1}{2}h_{22}\cdot e^{i\cdot(2\pi\nu t-\bar{k}\bar{x})}\right)^2\cdot dx\right]^{\frac{1}{2}}, \tag{A-15}$$

the backward flight:

$$\int_{t0}^{ttot} dt \cong \frac{1}{c}\left[\int_{L\cdot\sin\frac{\pi}{3}}^0 \left(1+\frac{1}{2}h_{11}\cdot e^{i\cdot(2\pi\nu t-\bar{k}\bar{x})}\right)^2\cdot dx+\int_{L\cdot\sin(\frac{\pi}{3}}^0 \left(1+\frac{1}{2}h_{22}\cdot e^{i\cdot(2\pi\nu t-\bar{k}\bar{x})}\right)^2\cdot dx\right]^{\frac{1}{2}} \tag{A-16}$$

and the total flight time:

$$T_{tot\_1} \cong \left[\begin{array}{l}\left(\dfrac{2L}{c}\cdot\sin\dfrac{\pi}{3}+\dfrac{L\dfrac{\pi}{3}}{c}\cdot\displaystyle\int_0^{L\cdot\cos\frac{\pi}{3}}\left(1+\frac{1}{2}h_{11}\cdot e^{i\cdot(2\pi\nu t-\bar{k}\bar{x})}\right)^2\cdot dx\right)^2+ \\ \left(\dfrac{2L}{c}\cdot\cos\dfrac{\pi}{3}+\dfrac{L\dfrac{\pi}{3}}{c}\cdot\displaystyle\int_0^{L\cdot\sin\frac{\pi}{3}}\left(1+\frac{1}{2}h_{22}\cdot e^{i\cdot(2\pi\nu t-\bar{k}\bar{x})}\right)^2\cdot dx\right)\end{array}\right]^{\frac{1}{2}}. \tag{A-17}$$

which depends on the amplitude of any passing Gravitational Wave. Let us now consider the phase difference of the recombined light due to the optical path changes in the case of a sinusoidal GW, propagating along the z axis, with frequency:

$2\pi\cdot\nu_{grav}=\Omega_{GW}$

and amplitude:

$h_{11}=-h_{22}=h\,.$

Now if the period of the GW is much bigger then the flight time of the photon ($\Omega_{GW} \cdot T_{tot} << 1$) we can consider the amplitude of the GW as a constant on the whole of the arm length and integration of Equations (A-14) and (A-17) will yield respectively:

$$T_{tot\_1} = \frac{2L}{c} + \frac{2L}{c} \cdot h \tag{A-18}$$

and

$$T_{tot\_2} = \frac{2L}{c}\left[1 + \frac{h^2}{4} + h \cdot \left(\cos^2\frac{\pi}{3} - \sin^2\frac{\pi}{3}\right)\right]^{\frac{1}{2}}. \tag{A-19}$$

So the distance strain is traduced into a difference of flight time which is given by:

$$\Delta T \cong \frac{2L}{c}\left[1 + \frac{h}{2} - \sqrt{1 + \frac{h^2}{4} + h \cdot \left(\cos^2\frac{\pi}{3} - \sin^2\frac{\pi}{3}\right)}\right], \tag{A-20}$$

which is at the first order equal to:

$$\Delta T \approx \frac{2L}{c}\left[h \cdot \cos^2\frac{\pi}{3} + \frac{h^2}{8} + \ldots\right]. \tag{A-21}$$

Considering only the first order terms we have for the phase difference due to the passage of the gravitational wave:

$$\Delta\Phi = \frac{L \cdot \cos^2\frac{\pi}{3}}{c} \cdot \frac{2c\pi}{\lambda_{grav}} \cdot h \tag{A-22}$$

Where the amplitude h is not constant over the arm length (A-14) and (A-17) have to be integrated by using the ‘retarded potentials’ as done in the electromagnetic case. To conclude it is obvious from Equation A-22 that the arm length of the detector depends strictly from the frequency range it is built for.

While the idea of implementing an interferometer to detect GW in space may seem simple it requires a complex melding of high technology solutions to be made possible. The problem as a whole is however much more complex than the few aspects presented and doesn’t constitute the scope of this thesis, for a broader overview please refer to LISA System and technology report[1].

The antenna

LISA shall be a constellation in the shape of an equilateral triangle with a distance between spacecrafts of $5 \cdot 10^6$ km. The centre of the constellation shall follow behind the Earth’s in its orbit around the sun with a 20° angle of delay. The orbit of the

centre of the constellation shall therefore be heliocentric and its distance from the sun will be equal to 1A.U.

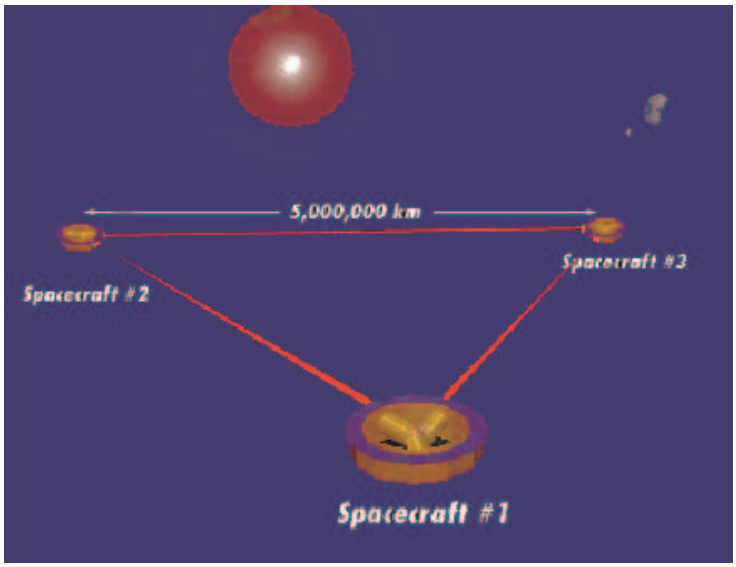

Figure A–5 From Laser Interferometer Space Antenna Home Page

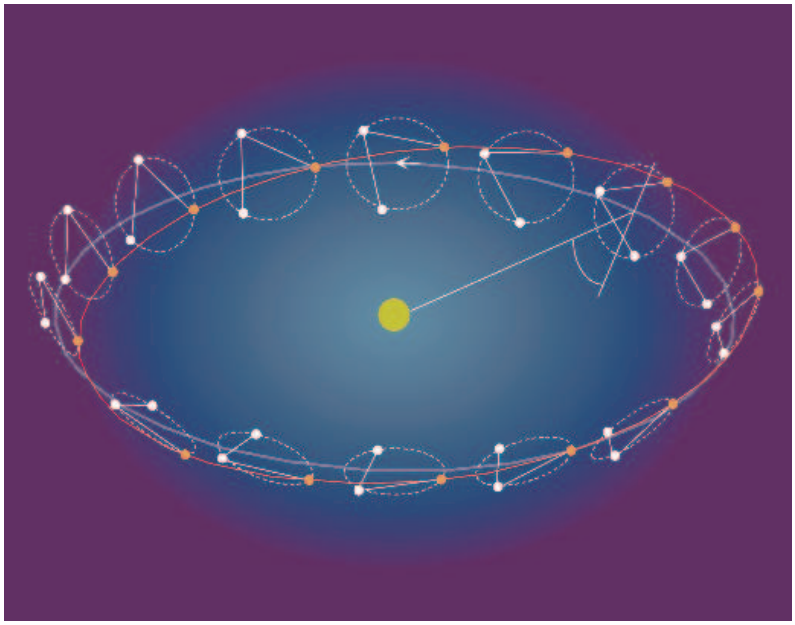

Figure A–6 From Laser Interferometer Space Antenna Home Page

The plane of the antenna shall have an angle of 60° from the ecliptic, as can be seen in Figure A–6. This choice for the formation has been made as it affords each satellite a closed orbit during the integration time of one year. Also, while the constellation rotates along its barycentre, the distance between the satellites can be considered constant within 10% of the arm length. The thermal effects due to variations of the sun's emission and exposure will cause temperature gradients but these will be limited to frequencies lower than 10^{-4}Hz thanks to the payload materials

(ULE and carbon epoxy) as well as to the thermal shielding. The rotation of the constellation will be useful as it shall allow for directionality in the detection with a single antenna. The principle is aperture synthesis, the well known observation technique typically used by terrestrial fixed radio-antennas. The three arms will be useful for redundancy to confirm obtained data as well as to measure polarisation. As explained above the arm length is directly linked with the frequency domain of the detectable Gravitational Waves. LISA is chosen to allow the observation of low frequency signals, 10^{-4}-1Hz. This frequency range is of great interest both because it is not observable on earth due to seismic and Newtonian (terrestrial gravity gradient) noise but also because in this spectral band most strongly gravitating bodies emit.
LISA will thus be complementary to Earth based detectors and will also allow the scientific community to test General Relativity in further detail than has ever been accomplished.

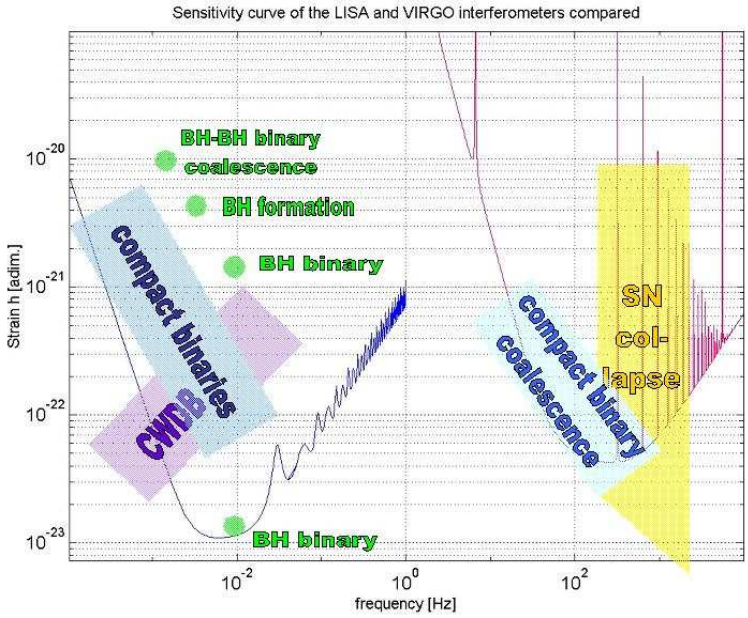

Figure A–7

All LISA satellites will have two Nd:YAG lasers on board each pointing, after alignment will be completed, towards one of the other spacecrafts. This 'redundancy' given by the three arms will also assure that the eventual malfunctioning of one laser will not be enough to invalidate the whole mission. On board lasers will, as already mentioned, use the Neodymium doped $Y_3Al_5O_{12}$ (YAG) matrix which emits radiation at a wavelength of 1064nm. Its long time between failures, weak thermal dissipation, solidity and intrinsic frequency stability make YAG lasers ideal for a space mission.

These Non Planar Ring Oscillators with a 1 to 2 W of emitted power enjoy a typical intrinsic unstabilised linewidth of 1kHz @1s.

Each second laser on the spacecrafts will be phase locked to the other (which will be called master laser) in order to ensure that the light along two adjacent arms will be coming from the 'same' source, without the use of a beam splitter which would halve the available power.

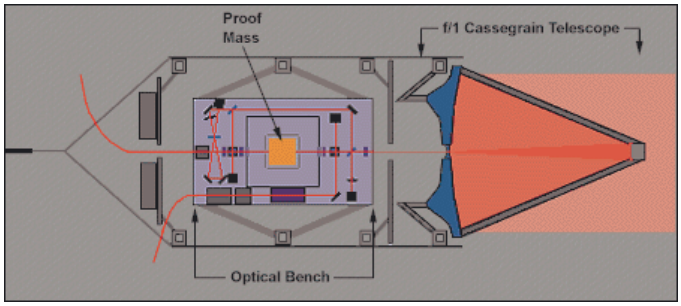

Figure A–8 From Laser Interferometer Space Antenna Home Page

While LISA will be able to function as a three armed Michelson Interferometer, traditional interferometry won't be able to meet our requirements in this type experience. A typical laser beam (with a waist w_0 of the order of the mm and hence a divergence of $\theta=\frac{\lambda}{w_0}$ =0.001rad) after travelling for 5 millions km would cover an area of 10^5km of radius and would therefore have insufficient power to be reflected back to the source. Each of the laser beams is enlarged by Cassegrain telescope of focal f/1 and aperture 30cm to produce a bigger waist and thus narrower beam. Even so the beam will cover typically an area with a radius of the order of 10km. The optical equivalent of the RF 'Satellite tracking' technique will have to be employed. Instead of using a mirror to reflect the light, at the end of the arm, the onboard laser will be phase locked to the incoming beam thus allowing a return beam at full power. It has to be observed that the telescope serves a second function allowing for the capture and focalisation on the test bench of as much of the incoming light as possible.

The return beam once arrived on the original spacecraft is bounced off the test mass and then mixed with a fraction of the outgoing light to obtain an interference pattern on a sensitive photodiode. If this procedure is repeated along all arms by taking the subtraction of adjacent arm's signals we shall obtain a measure of the length variations (this is the signal provoked by the GW), while their sum will yield a measurement of the frequency noise of the laser. As test masses, 40mm sided cubes of a platinum and gold alloy with high reflectivity but low electric and magnetic

susceptibility are chosen. These are shielded from radiation pressure and other perturbation by a vacuum chamber and by the satellites. The satellites are in their turn kept centred on the masses thanks to the action of Newton thrusters to prevent collisions between them and the free falling mass.

The satellites should be launched with a single Ariane type vector, solar panels will help them reach their orbital positions. The antenna should operate for five years with a one year integration time. LISA launch is for now planned for the year 2012.

Figure A–9 From Laser Interferometer Space Antenna Home Page

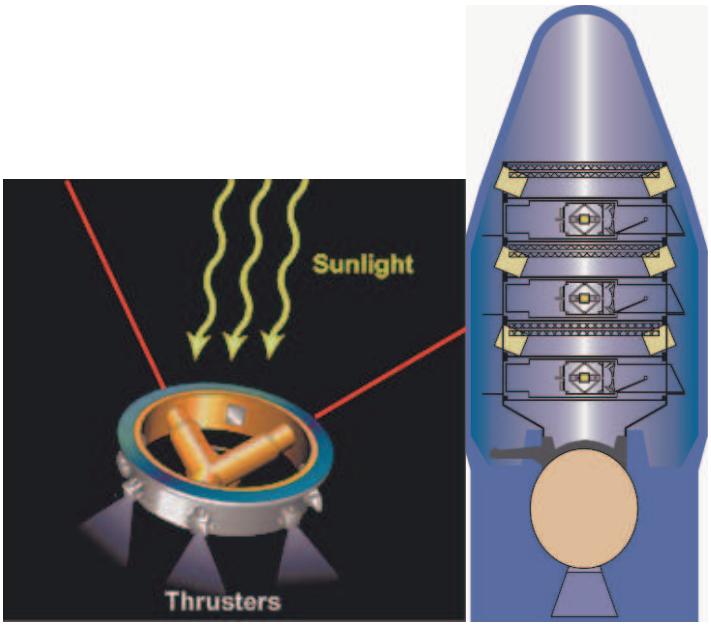

Figure A–10 From Laser Interferometer Space Antenna Home Page

Laser Stability

Let us calculate the power and frequency stabilisation necessary for the laser source. The test mass is illuminated by two counter-propagating beams, the return beam and a portion of the local beam (which shall serve as phase reference) if these two beams

don't have null amplitude noise this shall translate into an acceleration noise. To have a sensitivity of the order of the pm @ 30mHz the acceleration noise must be lower than a=10^{-16} m/s^2 at this frequency. This in turn corresponds to a power stability given by:

$$\delta P = mca \tag{A-23}$$

with m the mirror's mass (1.3kg), of the order of $\delta P = 4 \cdot 10^{-8} W/\sqrt{Hz}$ which for a mean incident power on the mirror of 100μW shall yield:

$$\frac{\Delta P}{P} = 3 \cdot 10^{-4} \ / \sqrt{Hz} \ .$$

This kind of stability has been obtained for higher frequencies than those of interest for LISA (10kHz) and is studied at LZH in Hannover by implementing a control of the pump diodes' current of the laser.

Frequency stability is determined by considering the arm lengths' asymmetries. If the two arms had exactly the same length then laser frequency noise would give the same contribution along the two arms and would cancel out in the phase subtraction that yields the gravitational signal[2]. As there exist no orbit that could maintain the satellite's distances equal and unchanged, frequency stabilisation becomes a vital necessity for LISA. Let us now consider the two phases due to the light's travel along the arms L_1 and L_2, they shall be respectively:

$$\varphi_1 = \frac{2\pi L_1 \nu}{c}$$

$$\varphi_2 = \frac{2\pi L_2 \nu}{c}$$

Now for a GW the phase lag shall have the form:

$$\Delta\varphi_{GW} = \frac{2\pi(L_1 + L_2)h}{\lambda} \tag{A-24}$$

whereas for a laser frequency fluctuation it shall be:

$$\Delta\varphi_{LN} = \frac{4\pi(L_1 - L_2)\Delta\nu}{c} \tag{A-25}$$

In order to have a detection of a GW we have to request that the laser induced phase lag be smaller or equal to the one introduced by the GW. Thus acceptable frequency variations are given by:

$$\frac{\Delta\nu}{\nu} = \frac{(L_1 + L_2)}{(L_1 - L_2)}\frac{h}{2} \tag{A-26}$$

which for wavelengths of 1.064µm and *h* of the order of 10^{-21} on the whole band shall yield:

$$\frac{\Delta\nu}{\nu} = 2\cdot 10^{-19} \quad /\sqrt{Hz}$$

for arm length variations of the order of 10^{8}m which is the typical expected asymmetry in the case of the LISA arms. Now this condition on the laser frequency stability cannot be satisfied with today's technology. Luckily time delay interferometry can help in the relaxing of this specification. Combining adequately the different data streams it is possible to cancel partially laser noise (this can also be seen as measuring the asymmetry of the interferometer arms). While there is no conclusive value for the requested frequency stabilisation limit the LISA specification has been set by the "LISA System and Technology Report[1]" to:

$$\Delta\nu = 10\,Hz/\sqrt{Hz}$$

This is not a definitive specification as Time Delay Interferometry studies are still underway to relax the requirements on the laser frequency stabilisation. Additionally to this request on the frequency stability it is also necessary that the lasers on different satellites be no more than 100MHz apart in frequency in order for the regeneration of the return beam to work properly. In view of these specifications, both for LISA and the other experiments, we decided to start some studies on Iodine locked lasers and on the possible lock techniques to be used in conjunction with a mechanical reference.

Sources

LISA is as we have seen an antenna dedicated to the direct detection of low frequency GWs. In our galaxy the main sources in the LISA frequency domain are binary systems. Outside our galaxy the formation, accretion and merging of massive black holes should be detectable. Gravitational background radiation (the gravitational equivalent of the CMBR[1]) the signature GW dating from the first few seconds of the Universe's life might also be observable with LISA.

[1] Cosmic Microwave Background Radiation

Galactic binary systems [1]

Compact binary systems should, according to nowadays theories of gravitation, emit detectable signals within LISA bandwidth. These binary systems are formed by of compact objects, such as white dwarves, black holes, pulsars and neutron stars, orbiting closely together.

Neutron star binaries can emit in LISA frequency range; to evaluate the number of expected signals from such sources one has to estimate the number of pulsars in the galaxy and their formation rate. These two parameters depend entirely on the chosen models and vary typically, for the binary pulsar population N between 10^3 and $3{\cdot}10^6$ and for the formation rate τ between 10^{-5} y^{-1} and $3{\cdot}10^{-4}$ y^{-1}. Since pulsars are a subclass of neutron stars, this estimate gives a lower bound to the expected binary NS emission in the LISA frequency band.

Binary system composed of a neutron star and black hole, once more depending on the chosen model, have a population between 10% and 100% of the neutron stars binaries.

Figure A–11 From Laser Interferometer Space Antenna Home Page

Binaries of two back holes should also be observable. While the number of these systems in the galaxy is estimated to be lower than 10, if we consider all such systems, detectable with LISA, within the Virgo cluster (counting more than 2500 galaxies at some 17Mpc of distance from us) their number is close to 50-70% of that of NS binaries.

Close white dwarf binaries should also give a signal within the LISA bandwidth, in the lower extremity of the spectra below 3mH. While there are no more than 10 known such systems in our galaxy their total number might very well be of the order of 10^6.

Given that CWDB from neighbouring galaxies should also be detectable, it is not unlikely that the antenna sensitivity, at the lower frequencies, should be limited by their background confused noise rather than by technical noise contribution.
Binary stars of regular stars will give a low frequency signal which will most likely be completely covered by the CWDB background.
Last but not least in this quick overview of compact systems emitting in the LISA bandwidth are cataclysmic binaries, where one of the stars has filled its Roche lobe and has started transferring its gas to its companion. Only 6 such systems have been observed for which distance, inferior to 100pc, and intensity of emission are sufficient to give an estimated signal observable with LISA.

Super-massive Black Holes

Black hole formation and accretion are the most scientifically relevant sources in the LISA domain, since, as has already been explained, they involve strongly gravitating bodies. Massive black holes in the centre of a dense galactic nucleus can reach masses of the order of 10^6 $M_\odot$ which is the required value for detection with LISA. Now these BH will emit GW during their formation if we suppose that they originate from merging of pre-existent black holes. If for any massive black hole ten merging are supposed to be necessary then LISA expected event ratio would be of 1-5 y^{-1}.
Even more influential contribution to LISA observations will be given by the MBH coalescences to form super-massive black holes. A MBH-MBH merger would have the characteristic chirp form which has been extensively studied by Damour[42][47] amongst others. The expected number of signal is of 1 per year.

Figure A–12 From Laser Interferometer Space Antenna Home Page

Another signal which should be visible with LISA is the cannibalism of a massive or super-massive black hole of stellar mass compact objects. These compact bodies can't give a direct contribution to the accretion disc around the MBH as neighbouring stars but will follow complex orbits around the black hole before being accreted. These events are particularly useful both to test General Relativity and to give an estimate of MBH population, with the provision that there be 10^4 stars for each MBH a rate of one event per year is estimated.

Cosmological background

As is the case for the electromagnetic cosmological background radiation we can expect to be able to detect traces of the gravitational waves emission produced during the first instants of life of the Universe. This gravitational background radiation would however be even more interesting then its electromagnetic counter part. Gravity decoupled at the Planck timescale and could allow us to gather measurements of the Universe during the inflation era, well before the last photon scattering which constitutes the earliest moment in the life of our Universe we can hope to observe with electromagnetic radiation. Also the observation of gravitational radiation coming from these eras could provide essential information on dark matter, baryon production and cosmological structure formation. These primordial GW[43] could have been caused by different phenomena, such as perturbations of the metrics during the inflation era or density fluctuations due to strings. Their actual spectra should be a red-shifted version of their original emission. We are supposing that the GW emission at this epoch were not of a thermal character. The spectra of primordial GW is usually expressed through the energy density in units of frequency to Universe critical density, ρ_c, ratio :

$$\Omega_{GW}(\nu) = \frac{\nu}{\rho_c}\frac{d\rho_{GW}}{d\nu} \qquad \text{(A-27)}$$

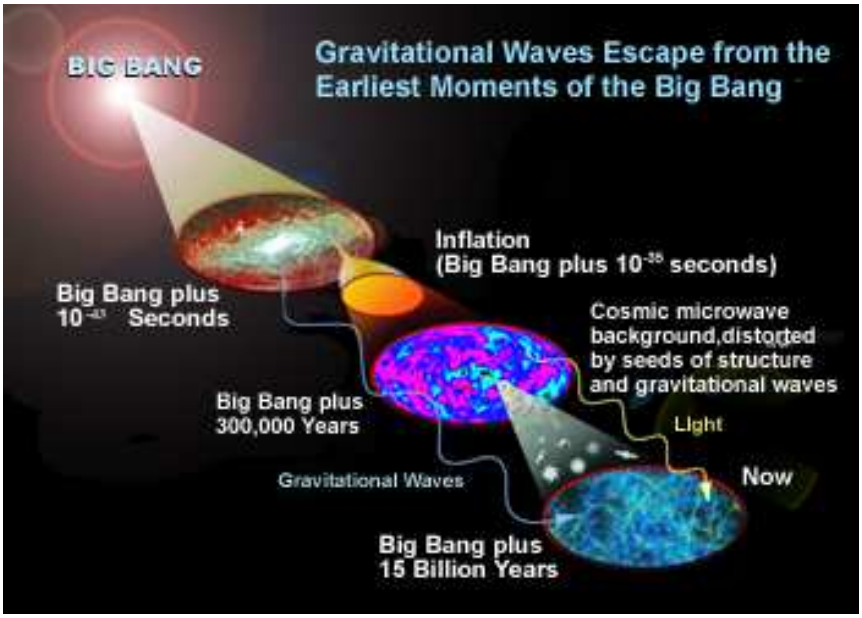

Figure A–13 From Laser Interferometer Space Antenna Home Page

Since background radiation will consist of incoherent radiation coming from any direction for all frequencies the description of the phenomenon shall have to be a statistical one.

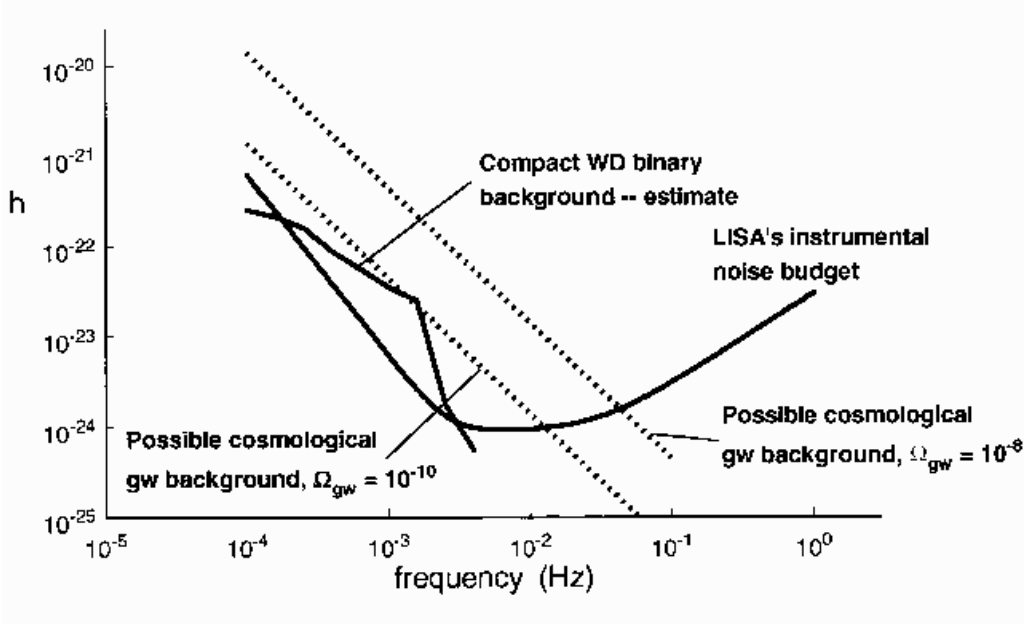

Figure A–14

The RMS amplitude of all GW fluctuations in a $\Delta\nu$ band around ν shall be given by:

$$h_{RMS}(\nu,\Delta\nu)=10^{-15}\left[\Omega_{GW}(\nu)\right]^{\frac{1}{2}}\left(\frac{1mHz}{\nu}\right)\left(\frac{H_0}{75km\cdot s^{-1}\cdot Mpc^{-1}}\right) \tag{A-28}$$

where H_0 is the actual value of the Hubble constant. If nowadays energy density is rescaled to LISA frequencies, plausible values of the gravitational strain are assumed

and H_0 is assumed to be $75 km \cdot s^{-1} \cdot Mpc^{-1}$ then for Ω_{GW} between 10^{-8} and 10^{-10} we have that the emissions should be detectable within the antenna's detection band, as shown by the curves for h_{RMS} as a function of the frequency shown in Figure A-14 with respect to LISA sensitivity curve. In the case of a detection LISA directionality should also help in the mapping process of the anisotropies of the gravitational background radiation.[44]

B. Double Pass Pound-Drever-Hall

As was done for the Tilt Locking technique we can think of using the Fabry-Perot on the first pass as a mode cleaner cavity. In our experimental set-up this configuration was used to assure analogous performances to the Tilt Locking DP for the Pound-Drever-Hall experiment.

This configuration can be used in the case where the mode cleaning effect of a cavity is necessary but the building of a second Fabry-Perot and its accompanying electronics is unadvisable. Actually this configuration could also be used with a modulation at the input of the first pass for modulation frequencies smaller than the linewidth of the FP. Detection on the transmission of the cavity would then be necessary. Since Pound-Drever-Hall is not a beam jitter sensitive technique the advantages of its implementation in a Double Pass configuration are slight.

This technique much as its tilt locking based counterpart suffers on its response time due to the time delay on the servo loop due to the first pass delay. It too, like DP Tilt Locking, shall be limited in unity Gain of the servo loop at 5kHz, for a Fabry-Perot of 30cm of semi-perimeter and Finesse 100,000. The problem of the beam's return towards the laser is once again to be considered, with the further problem given by the modulation present on the backscattered beam, which might cause an amplitude modulation of the laser itself.

In view of these observations double pass Pound-Drever-Hall should be avoided in experimental set-ups where a good isolation of the backscattered light cannot be assured, in particular it is not well adapted for LISA.

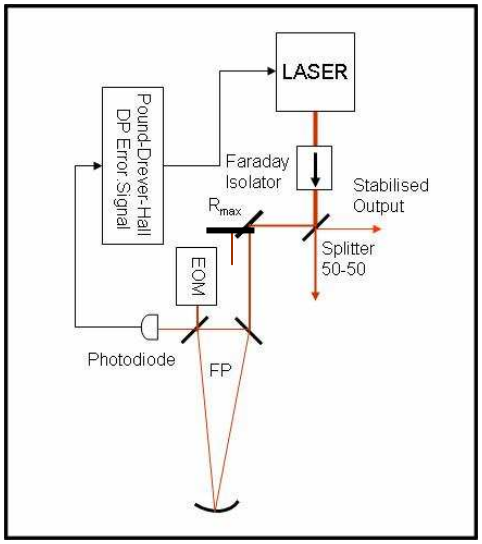

Figure B-1

Error Signal extraction

Pound-Drever-Hall in the double pass into the cavity configuration also requires a double modulation of the re-injected beam. This double modulation seems a phenomenon best avoided since it will transfer some of the energy in our beam on higher order harmonics, also amplitude modulation shall be acquired on both passes. Let us see how this observation translates into formulas.

The transmitted field after the first pass into the cavity shall have the well known form:

$$E_T = T(\omega)E_0 \cdot e^{i\omega t}$$

After passing in the modulator the first time the field becomes:

$$E_M = T(\omega)E_0 \cdot e^{i\omega t} \cdot e^{iB\cdot\sin(\omega_m \cdot t)}$$

and the second pass gives finally:

$$E_{2M} = T(\omega)E_0 \cdot e^{i\omega t} \cdot e^{iB\cdot\sin(\omega_m \cdot t)} \cdot e^{iB\cdot\sin(\omega_m \cdot t)} \quad \text{(B-1)}$$

where B is once again the complex modulation depth, ω_m is the modulation frequency and $T(\omega)$ is the cavity's complex transmissivity defined in Equation (4-48).

We can develop the expression by using the spherical Bessel J functions. We obtain:

$$E_M \approx T(\omega)\cdot E_0 \cdot e^{i\omega t}\left[J_0^2(B)+J_1^2(B)\cdot\left(e^{i2\omega_m t}+e^{-i2\omega_m t}\right)+2J_0(B)J_1(B)\cdot\left(e^{i\omega_m t}-e^{-i\omega_m t}\right)+\ldots\right] \quad \text{(B-2)}$$

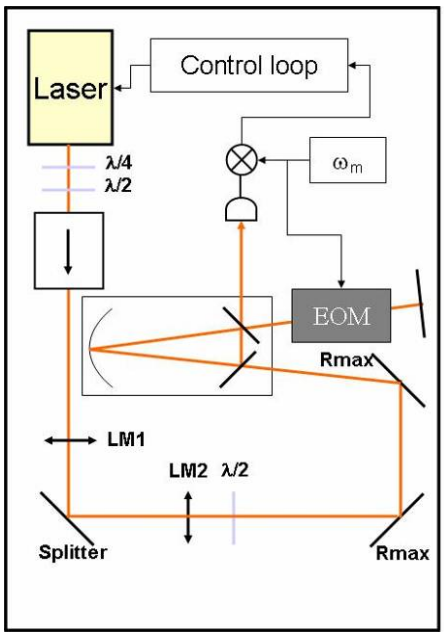

Figure B-2

Taking this expression we can write the form of the reflected field and hence calculate the photodiode's current:

$$I=\frac{\eta q}{h\nu Z_{AC}}\left|T(\omega)\right|^2 E_0^2\left[\begin{array}{l} J_0^4(B)R^2(\omega)+J_1^4(B)\cdot\left(R^2(\omega+\omega_m)+R^2(\omega-\omega_m)\right)^2+ \\ 4J_0^2(B)J_1^4(B)\cdot\left(\begin{array}{l}R^2(\omega+\omega_m)\\+R^2(\omega-\omega_m)\end{array}\right)+ \\ 2J_0^3(B)J_1(B)\cdot\left(\begin{array}{l}R(\omega)R^*(\omega+\omega_m)e^{-i\omega_m t}-R(\omega)R^*(\omega-\omega_m)e^{i\omega_m t}\\+c.c\end{array}\right)+\ldots \end{array}\right] \quad \text{(B-3)}$$

Now this must once again be demodulated synchronously. We have the choice of a phase or quadrature demodulation, as seen for the single pass we choose the phase signal.

The resulting Error signal is this time given by:

$$Ph_{2P}=\left|T(\omega)\right|^2\frac{2E_0^2J_0^3(B)J_1(B)}{2i}\left[\left(R(\omega)R^*(\omega+\omega_m)+R(\omega)R^*(\omega-\omega_m)-c.c\right)+\ldots\right] \quad \text{(B-4)}$$

which can in turn be approximated, at first order for the normalised detuning $f=\delta\omega/f_P$, as:

$$Ph_{2P}=E_0^2J_0^3(B)J_1(B)\frac{2}{\left(1+\frac{\omega_m^2}{f_P^2}\right)^2}\frac{\omega_m^2}{f_P^2}\left(1-\zeta_0^2\right)\left(\zeta_0-1\right)\left[1+2\zeta_0+\frac{\omega_m^2}{f_P^2}\right]\cdot f \quad \text{(B-5)}$$

Signal to Noise Ratio

Let us now calculate once more the value of the signal to noise ratio. The expression of the signal is very similar to the one obtained in Equation (4-56), but for the term coming from the transmission and the exponents of the J functions, this latter being an effect due to the double modulation. Similarly if we only consider the main terms of the noise (i.e. those in J_0 only, since J_1 is significantly smaller than J_0, especially when elevated to the fourth) the noise contribution is nearly unchanged from Equation (4-66). We can thus obtain for the SNR the expression:

$$SNR\propto\sqrt{\frac{\eta}{h\nu}}\cdot E_0J_0(B)J_1(B)\cdot\frac{1}{\left(1+\frac{\omega_m^2}{f_P^2}\right)^2}\frac{\omega_m^2}{f_P^2}\frac{\left(\zeta_0-1\right)}{\zeta_0}\sqrt{\left(1-2\zeta_0^2\right)\left(1-\zeta_0^2\right)}\left[1+2\zeta_0+\frac{\omega_m^2}{f_P^2}\right] \quad \text{(B-6)}$$

This SNR is generally smaller than the one obtained in the case of the single pass Pound-Drever-Hall which further supports the arguments against the use of this

technique, unless there be a driving pressure given by a faulty laser profile. This type of problem could however be corrected with the use of a sufficient length of fiber.

Simulation and Lock point stability

Let us now analyse the lock point variations due to the presence of an amplitude modulation component in the modulation. As done for all techniques in this chapter the simulation of the error signal profile was created as a MatLab custom routine. We have run the program for a modulation frequency of 6.25MHz on a cavity with a Finesse of 580 obtaining the profile variations shown in Figure B-3 for an optimal coupling of the cavity.

Similarly the stability of the locking point was evaluated according to Equation (4-46). The locking point offset, for different values of the coupling ζ_0 assumes the values in Table B-1.

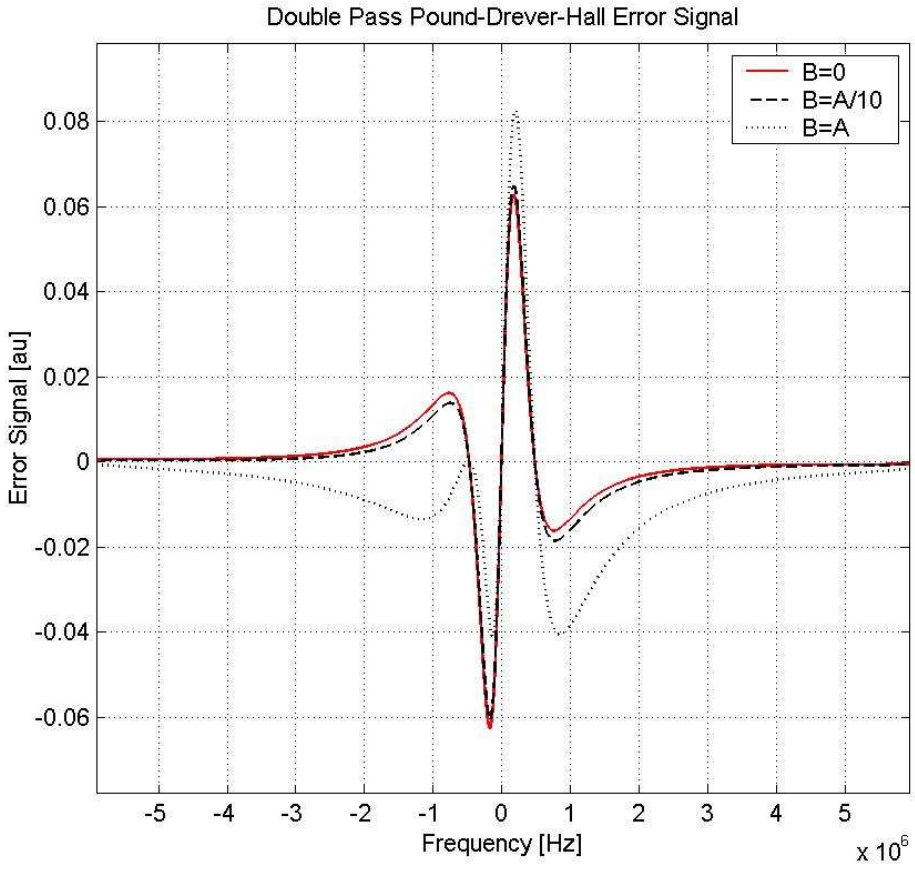

Figure B-3

Which shows that the Pound-Drever-Hall double Pass technique is sensitive to amplitude modulation as far as the locking point is concerned, as expected, as long as the cavity is not perfectly coupled. In this case too we see that the under-coupled

case is more sensitive to the amplitude modulation, as obvious since a greater share of the amplitude modulated beam falls on the detector, with values of the offset reaching 26% of the cavity's linewidth. Obviously the double pass doesn't influence the insensitivity of the technique to all beam misalignments as these give no effect at the modulation frequency.

Coupling ζ_0	Phase Modulation depth Re(B)=A	Amplitude Modulation depth Im(B)=B	Offset in units of f_P
0	**0.3**	**0**	**0**
-0.67	**0.3**	**0**	**0**
0.67	**0.3**	**0**	**0**
0	**0.3**	**0.03**	**$-4\ 10^{-18}$**
-0.67	**0.3**	**0.03**	**-0.01**
0.67	**0.3**	**0.03**	**0.025**
0	**0.3**	**0.3**	**$-4\ 10^{-17}$**
-0.67	**0.3**	**0.3**	**-0.105**
0.67	**0.3**	**0.3**	**0.263**

Table B-1

C. Programs and simulations

All the below presented routines were written for MATLAB. Only the headings of the programs are presented below.

Data analysis

```
ACQTIME('file.ext') gives as outputs the linearised time vector
(timevector.txt) and the time between acquisitions acqtime which is the
mean value of the time differences between two consecutives time
measurement points.
%Nice 04-06-11
%LM
%Version Beta 1

ADJUST(FNAME,K) takes the first column of fname and adds to its elements
smaller than x(1,1) the value K. Program to correct PC counter resetting.
%Nice 04-08-31
%LM
%Version: beta1

ALLAN(fname,t_acq,n) where n must be an integer divisor of the numer of
taken acquisitions. This program computes the Allan variance of a series of
data acquired with the Labview interface of the HP53131A counter. Allan
variance calculated over times intervals of n seconds. N.B. The number of
acquisitions MUST be EVEN! The return result time is the time of measure.
This routine has been modified to work with the two column files coming
from Labview. To find the time between acquisitions use ACQTIME(fname).
%Nice 29-06-04
%LM
%%VERSION: Beta6

COHERENCE(fname,t_acq,i,j) where fname is the name with path and extension
fo the data file to be analised, t_acq is the time between two subsequent
acquisitions (calculated by ACQTIME)i and j are the indexes of the columns
in the data file whose coherence I want to measure. This function uses the
cohere MATLAB inbuilt function to calculate the coherence of two data
streams coming from the same file. 256 fft lines are used as in the
standard COHERE case.
A Hanning window is used to create the correlations and cross-correlations.
Graph is plotted.
%Nice 04-06-30
%LM
%VERSION: BETA1

CROSSCORR('H','K','L') plot the cross-correlation coefficients of the
counter file h the Keithley file k, and the temperature file l. The
crosscorrelations are given in the same order as used in the CrossCorr.doc
file. MUST have created sums file.
%Nice 04-09-01
%LM
%Version Beta1.

CUTCOUNT(fname,I,J) where I is the first data point we keep and J the last,
takes a data file FILENAME of dimension #N and turn it into a new data file
of dimension j-i. This works for the counter two data columns files only.
```

```
%Nice 04-01-30
%LM
%Version: Beta 1

CUTKEITH(fname,I,J) where I is the first data point we keep and J the last,
takes a data file FILENAME of dimension #N and turn it into a new data file
of dimension j-i. This works for the Keithley 8 data columns files only.
%Nice 04-01-30
%LM
%Version: beta1

ESTHERM('fname.ext',R_p1,R,p2)
This function should get the Error Signal values from a data file for the
cells' cold points and returns the temperature equivalent frequency and
pressure variations in a data file with temperature in [°C] equivalent
frequency variations in Hz and Pression in [mTorr]. Data file is called
Tempdata.txt.
%Nice 04-04-28
%LM
%VERSION Beta2

ESTHERMAMB('fname.ext',i,j)
'fname' is the file with path and extension, whereas i is the index of the
data column representing the room temperature data and j that for the
cavity. This function should get the Error Signal values from a data file
for the cavity and the room temperature and return the equivalent
temperatures in a data file with temperature in [°C].
The data file is called Tempdata-amb.txt.
%Nice 04-06-09
%LM
%VERSION alpha2 (To be tested)

FOURIER(fname) calculates the cross-correlation function, time graphs, fft
in units of sqrt(Hz) and transfer functions graphs (real and imaginary
parts) as well as the coherence of datas in fname, with those in a chosen
counter file (N.B. this file name is entered IN the program!) as well as
the auto and cross-correlation coefficients.
%Nice 09-02-04
%LM
%VERSION: Beta5

GAUSSFIT(fname,t) fits the  distribution of the datas in fname avaraged
over
t on a gaussian. This is a script file for using CURVEFIT (M.Taubman) to
fit the distribution of the data taken with the HP53131A counter on a
gaussian. Variable is 'x' which is the frequency intervals of the
distribution, and the fitted parameters are M mean value and s standard
deviation. Uses GAUSSIAN.
%Nice12-09-03
%LM
%VERSION:Beta1

GAUSSIAN(x,m,s) is the function used to fit the data of a histogram
on a Gaussian distribution. x is a variable in this case the frequency or
variation thereof; M is the mean value and s the standard deviation which I
want to calculate.
%Nice 11-09-03
%LM
%VERSION:beta1

GETCOLUMN('fname',i) saves the chosen set of data saved in fname in a new
```

```
file named column.txt
%Nice 01-10-03
%LM
%VERSION: Beta1


GRAPHALL(fname) is a function getting a set of datas in a file fname from
the HP53131A Counter or the Keithley multimeter and plotting their
behavior. This function should trace the graph directly.
%Nice 26-02-04
%LM
%VERSION: Beta2.

GRAPHFFTB(fname,t_acq,n,i) is a function getting a set of data (the ith
column) in a file fname from a Labview file and plotting their FFT behavior
after averaging them over a given number of acquisitions n entered by the
user. The time between acquisitions t_acq has to be entered into the
program by the user it can be calculated by the function ACQTIME which will
also generate the timevector file with the rescaled time vector. This
function traces the Fourier Transformation directly. Most of this routine
works on the same principle used by GRAPHTIME2,HISTO etc.
%Nice 21-09-03
%LM
%VERSION: Beta2.
%See also: ACQTIME, GRAPHTIME, GRAPHTIME2, HISTO.

GRAPHGLIS(h,fname,t,i,Conv) is a function getting a set of data in a file
fname and plotting their behavior after averaging them over a given time t
entered by the user. This function should trace the graph directly. It
works for any given column of data in the chosen file. Said column is
chosen by index i in the command line. The mean values are calculated with
a moving start point. The time vector must be entered through the filename
'h'. Use ACQTIME. The eventual Conversion factor must also be entered.
%Nice 26-02-04
%LM
%VERSION: Beta2.

GRAPHTEMP(fname) is a function getting a set of data in a file fname from
the HP53131A Counter or the Keithley multimeter and plotting their
behavior. This
function should trace the graph directly with the Keithley data converted
into temperature. N.B. The counter file name is entered directly into the
program!!!!
%Nice 04-02-04
%LM
%VERSION: Beta1.

GRAPHTEMP2(fname,V_dc1,V_dc2) is a function like GRAPHTEMP but treats the
data sets coming from the cells' transmitted light. V_dc1 and V_dc2 are the
values the transmitted light has outside the transition and must be entered
by hand. This yields no water temperature information. N.B. The counter
file name is entered directly into the program!
%Nice 04-02-24
%LM
%VERSION: Beta1.

GRAPHTIME(fname,t) is a function getting the frequency data in a file fname
from the HP53131A Counter and plotting their behaviour after averaging them
over a given time t entered by the user. This function traces the graph
directly.
%Nice 03-09-10
```

```
%LM
%VERSION: Beta2.

HISTO(fname,t,N) should draw the histogram of a series of data points from
the file fname. These data points are averaged over the time interval t
before the histogram is made. The histogram will have N columns where N is
the size of the data vector. The width of the histogram should be linked
directly to the std of the distribution.
%Nice 03-09-10
%LM
%VERSION:Beta2.

HISTOALLAN(fname,t,N) draws the histogram of a series of data variations
from the file fname. These data points are averaged over the time interval
t before the histogram is made. The histogram will have N columns where N
is the size of the data vector.
%Nice 04-04-28
%LM
%VERSION:Beta2.

IODEPARAM(T_1,T_2,I_1,I_2) calculates the linewidth and frequency
variations of the a_10 line of the R56(32-0) band of molecular Iodine in
function of laser pump power and temperature in each cell respectively.
%Nice 28-01-04
%LM
%Version: Beta1.

SMOOTH(fname,i) corrects the data points in fname column I which are more
than sigma away from the Mean value of the set. The correction is
implemented on a three point basis. Each point is evaluated by the rapport
to the mean value of its two neighbours. If its value is farther apart than
either sigma or 200kHz then the point is changed to the mean value of its
two neighbours.
%Nice 04-09-09
%LM
%VERSION: Alpha3 (To finish testing)

SUMCREATE(FNAME,I,J,K1,K2)
sumcreate takes two data columns from file fname, column i and j sums them
as k1*x(:,i)+k2*x(:,j) and writes the results into the file sums2.txt. To
determine k1 and k2 suggested use of FITDEL or FITDATA2 (Utilities).
%Ventimiglia 04-08-27
%LM
%Version Beta1

TEMPCONV(fname) where fname (insert the name of the file including path and
extension) is the input file to convert. This program takes the file output
from the LABVIEW program Keithley+counter and converts the keithley
temperature error signals into the temperature values measured by the
PT_100 (Water temperature) and the two NCTS: Therm_1 and Therm_2, Iodine
cells 1 and 2 respectively.
%LM
%Nice 04-01-12
%VERSION: Beta3

TRACER('h','k',i,c,Conv) traces the i-th column of the file named 'k' or
'h' with respect to the time axis defined by the first column of the
counter file 'h'. i is zero for the second column of the 'h' file (i.e. the
beat note) and then varies between 1 and n for all the Keithley's columns.
c is the colour index of the graph:
0 -> blue
```

```
1 -> red
2 -> green
3 -> magenta
4 -> cyan
5 -> yellow
6 -> black
Conv is the conversion constant in Hz/V for the given error signal or
whatsoever
%Ventimiglia 04-08-26
%LM
%Version: Beta3.
```

Demodulation @2f

```
PDUE(f,w)
Signal in phase demodulated at twice the frequency modulation f. w is the
detuning. Uses REFL(Utilities).
%Nice 03-02-06
%LM
%Version:Beta2.


QDUE(f,w)
Signal in quadrature demodulated at twice the frequency modulation f. w is
the detuning. Uses REFL(Utilities).
%Nice 03-02-06
%LM
%Version:Beta1.
```

DM

```
DM(f,W,w)
W is the modulation at w=ISL and w<<W is the second modulation frequency. f
is the VIRGO third modulation can be put f=0. This routine computes the
value of the demodulated error signal after a demodulation at w in phase.
Uses REFL and TRANS (Utilities).
%Nice 01-11-05
%LM
%Version: Beta2


DMP2(f,W,w)
W is the modulation at w=ISL and w<<W is the second modulation frequency. f
is the VIRGO third modulation can be put f=0. This routine computes the
value of the demodulated error signal after a demodulation at the ISL
frequency in quadrature and a demodulation at w in phase.
Uses REFL and TRANS (Utilities).
%Nice 01-11-14
%LM
%Version: Beta2


DMP2t(f,W,w)
W is the modulation at w=ISL and w<<W is the second modulation frequency. f
is the VIRGO third modulation can be put f=0. This routine computes the
value of the demodulated error signal after a demodulation at the ISL
frequency in quadrature and a demodulation at w in phase. Error signal is
obtained on transmission.
Uses REFL and TRANS (Utilities).
%Nice 01-11-14
```

%LM
%Version: Beta2

DMQ(f,W,w)
W is the modulation at w=ISL and w<<W is the second modulation frequency. f is the VIRGO third modulation can be put f=0. This routine computes the value of the demodulated error signal after a demodulation at w in quadrature.
Uses **REFL** and **TRANS** (**Utilities**).
%Nice 01-11-05
%LM
%Version: Beta2

DMQ2(f,W,w)
W is the modulation at w=ISL and w<<W is the second modulation frequency. f is the VIRGO third modulation can be put f=0. This routine computes the value of the demodulated error signal after a demodulation at the ISL frequency in quadrature and at w in phase.
Uses **REFL** and **TRANS** (**Utilities**).
%Nice 01-11-05
%LM
%Version Beta1

DMQ2t(f,W,w)
W is the modulation at w=ISL and w<<W is the second modulation frequency. f is the VIRGO third modulation can be put f=0. This routine computes the value of the demodulated error signal after a demodulation at the ISL frequency in quadrature and at w in phase. The error signal is obtained on the transmission.
Uses **REFL** and **TRANS** (**Utilities**).
%Nice 01-11-05
%LM
%Version Beta1

Fitting

ACC(w,W,D,E,F,G)
The function **ACC** = acc(w,W,D,E,F,G) is the function used to fit the data in cavity FSR determination experiments. "w" and "W" are vectors, while the fitting parameters are scalars. "w" is the laser frequency, "W" is the FSR, "D", "E", "F" are the amplitude modulation depths and "G" is the amplitude of the curve AKA a function proportional to the laser power.
Uses **CURVEFIT** and ERRFUN (M. Taubman.)
%Morbegno 02-01-04
%LM
%Version: beta2

ACCORD2(w,W,D,E,F) is the function used to fit the data in cavity ISL determination experiments. "w" and "W" are vectors, while the fitting parameters are scalars. w laser frequency, W = n*ISL, x and f modulation frequencies cavity Finesse 1500 as for Virgo MC. Modulation frequencies and modulation width are given by the experimenter(Bondu)
%Morbegno 02-01-03
%LM
%Version: beta2

LORENTZ(gamma,w, K) is the function used to fit the data in the MT transfer Iodine experiment "w" (detuning) is a vector while the fitting parameter gamma (linewidth) and K (area of the curve) are scalars.
%Nice 03-03-09
%LM
%Version: Beta3

LORFIT(fname)
Script file for using CURVEFIT with the Lorentz function. This script returns the values of the parameters of the derivative of a Lorentzian fit on the data. Said parameters are:
GAMMA Linewidth
K Area of the curve
LORFIT('complete path of the file chosen',w_0 Offset on the frequency axis, x_0 Offset on the Voltage axis).
Beware the piezo file chosen for the automatic conversion of the data is entered in the program to change edit!
Uses **CURVEFIT** and **ERRFUN** (M. Taubman.)
%Last Modified NICE 03-10-15
%LM
%Version: Beta 1

FSR Lock

DEMQ1(f,W,w)
This routine computes the FSR lock error signal obtained through a demodulation at the low modulation frequency f. W is the modulation frequency at FSR. W is the detuning.
Uses **REFL** and **TRANS** (**Utilities**).
%Nice 01-12-22
%LM
%Version Beta1

DEMQT1(f,W,w)
This routine computes the FSR lock error signal obtained through a demodulation at the low modulation frequency f. W is the modulation frequency at FSR. W is the detuning. Signal obtained on the transmission.
Uses **REFL** and **TRANS** (**Utilities**).
%Nice 01-12-22
%LM
%Version Beta1

Gaussian modes

HERMAN(o,s)
Subroutine used to create a symbolic Hermite function of order o and variable s.
%Nice 20-05-03
%LM
%Version Beta1

HG(n,m,x,y) where the n and m define the order in the horizontal and vertical direction and x and y are the spatial coordinates in the horizontal and vertical directions. Distances are to be entered in meters! Waist is equal to 500 microns. This value can be changed inside the program. Function of Hermite Gauss. Uses subroutine **HERMAN**.
%Nice 22-05-03
%Last modified 20-06-03
%LM
%Version Beta3

PLOTHG(n,m) where n and m are the orders of the HG function in the horizontal and vertical directions respectively. Plotting of the Hermite Gauss mode TEM_nm. The spatial units are in meters and the waist is the one chosen in the subroutine **HG**(500microns).
Routine uses **HERMAN** and **HG**.
To obtain representation of typical cavity modes in the case of superposed modes (degeneracy), type 'hold on' in the MATLAB command window after the first usage of the routine. You will obtain something like this:

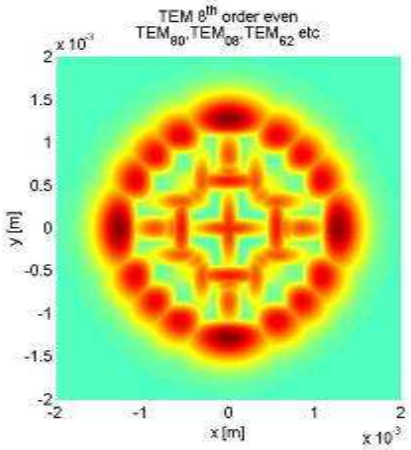

if you have all correct modes.
Uses subroutines **HERMAN** and **HG**.
%Nice 23-05-03
%LM
%Version: Beta3

HGX(n,x,waist) where the n defines the order in the horizontal direction, x is the spatial coordinate and waist is the cavity or beam waist.
%Distances to be entered in meters! This is the mono-dimensional Hermite Gauss function of order n in the x direction. Uses subroutine **HERMAN**.
%Nice 22-05-03
%LM
%Version: Beta2

Pound-Drever-Hall

%**PDHAM**(Wm,epsilon,A,B) where Wm is the modulation frequency A the modulation depth, B the amplitude modulation depth and epsilon the reflectivity difference between the entrance and exit mirrors. We calculate the PDH single pass error signal; the signal is demodulated in phase. Also calculates locking point error.
Uses REFL and TRANS.

%Ventimiglia 06-10-03
%LM
%VERSION Beta1

PDH2AM(Wm,epsilon,A,B) where Wm is the modulation frequency A the modulation depth, B the amplitude modulation depth and epsilon the reflectivity difference between the entrance and exit mirrors. We calculate the PDH double pass error signal with double modulation; the signal is demodulated in phase. Also calculates locking point error.
Uses **REFL** and **TRANS**.
%Ventimiglia 04-10-03
%LM
%VERSION Beta3

Tilt Locking

PROFILE(THETA,DELTA)

This routine computes the intensity profile on the photodiode in function of the coordinate x of the tilt (theta) and the shift (delta). All distance units are in waist dimension units. Waist is 500e-6m in this program. Waist is 500e-6m in this program, FSR=5e8Hz. All distances are in units of the waist dimension.
%Nice 04-08-04
%LM
%Version: Beta1

TILTALL(off1,A,alpha,z,d0) plots as a function of the wave-vector k the TL Double Pass error signal (integrated by summing), as a function of detector's offset (off1), beam offset (A), tilt (alpha), detector distance from the waist of the cavity (z) (Gouy shift) and d0 dead zone. All distances are in units of the waist dimension. Waist is 500e-6m in this program, FSR=5e8Hz.Also calculates locking point error.
Uses subroutines: HERMAN, HGX, HGINT0, HGINT1, REFL and TRANS. See also PROFILE, TSPALL.

%Ventimiglia 04-09-03
%LM
%VERSION: Beta5

TSPALL(off1,A,alpha,z,d0) plots as a fnction of the wave-vector k the TL Single Pass error signal (integrated by summing), as a function of detector's offset (off1), beam offset (A), tilt (alpha), detector distance from the waist of the cavity (z) (Gouy shift) and d0 dead zone. All distances are in units of the waist dimension. Waist is 500e-6m in this program, FSR=5e8Hz.Also calculates locking point error.
Uses subroutines: HERMAN, HGX, HGINT0, HGINT1, REFL and TRANS. See also PROFILE, TILTALL.
%Ventimiglia 04-09-08
%LM
%VERSION: Beta3

Utilitities

CONVERT(fname, Volt, timescale) where you have to enter the exact emplacement and name of the data file to convert, the Voltage on the piezo ramp for a given time-range. This function should convert the time axis into a frequency axis. System works only for Innolight Prometheus Laser. For a different Laser the piezo-frequency conversion has to be changed.
%LM
%Nice 03-02-13
%Version : Beta1

CUT(fname,I,J) where I is the first data point we want to keep and J the last. This routine takes a data file FILENAME of dimension #N and turn it into a new data file of dimension j-i.
%Nice 03-09-23
%LM
%Version: Beta 1

DERIVE(fname,x)
It works as long as you write the function you want to derive as a function of t! Example derive('sin(t)',x). It gives the derivative of a function fname calculated in the points given by vector x.
%Ventimiglia 02-12-15
%LM
%Version: BETA1

FINESSE(r_1,r_2,r_3)

This routine calculates the Finesse of cavity.
%Nice 01-05-16
%LM
%Version : beta1

FITDATA('h','k',i,j) finds the coefficients k1 and k2 that minimise the difference k1*k(i)+k2*k(j)-h(:,2)=A(t) where t is the vector h(:,1) and we are using the counter and Keithley data files. This function should write the k1*k(i)+k2*k(j) data stream in corr.txt
%Nice 04-09-13
%LM
%Version: BETA1

FITDATA2('h','k',i,j) finds the coefficients k1 and k2 that minimise the difference k1*k(i)+k2*k(j)+k3-h(:,2)=A(t) where t is the vector h(:,1) and we are using the counter and Keithley data files. This function writes the nu-(k1*k(i)+k2*k(j)+k3) data stream in corr2.txt
%Nice 04-09-15
%LM
%Version: BETA3

FITDEL('h','k',i,j,tol,step) finds the coefficients k1 and k2 and the delay tau
that minimise the difference k1*k(i)(t)+k2*k(j)(t)+k3-h(:,2)(t-tau)=A(t) with tolerance TOL, where t is the vector h(:,1) and we are using the counter and Keithley data files. Step is the width of steps between the 10 possible tests of tau. This function should write the nu(t-tau)-(k1*k(i)(t)+k2*k(j)(t)+k3) data stream in corrdel.txt
N.B. Works only if there have been no bad (loss of frequency data) delocks.
%Ventimiglia 04-09-21
%LM
%Version: Beta2

MODFREQ(R,L,n,m) , R radius of curvature of the FP end mirror, L semiperimeter of the cavity n and m order of the mode horizontal and vertical respectively.
This function calculates the frequencies of the modes in a given FP resonator. All distancies must be entered in METERS!
%Nice 26-06-03
%LM
%Version: Beta1

OMEGA(L,R,F), this function of the parameters: L semi-perimeter of the FP oscillator, R radius of curvature of the end mirror and F finesse give an idea on the placement of the different TEM_{nm} modes for a laser incident on a triangular FP cavity. The TEM_{00} is be placed on the 1 mark, and again 1 FSR away.
Distances to be entered in METERS!
%Nice 26-06-03 retouched 19-04-04
%LM
%Version: Beta5

PRESSION(R) where R is in OHMS and the pressure is given in mbar.
This function get the value of the pressure in the gas cell given the impedance read out of a PT100 temperature sensor.
%Last modified 03-07-17
%Nice LM
%Version: Beta1

REFL(r-1,r-2,r-3,w)

Calculates the reflection of a cavity with entrance mirror 1 exit mirror 2 and
end mirror 3 for different value of detuning laser cavity w. The reflectivities are the field's.
%Nice 02-01-06
%LM
%Version: Beta2

ResIR(W_0,f,Z_1) where w_0 in MICRONS is the original beam's waist, f is focal length of the lens in METERS and z_1 is the distance between the lens and the original waist, in METERS. This function calculates the position and width of a Gaussian beam's waist after a lens of focal length f placed at a distance z_1
From the original's beam waist w_0.
BEWARE lambda is 1064nm!!!!
%Nice 03-12-11
%LM
%VERSION: Beta2

TRANS(r-1,r-2,r-3,w)
Calculates the transmission of a cavity with entrance mirror 1 exit mirror 2 and
end mirror 3 for different value of detuning laser cavity w. The reflectivities are the field's.
%Nice 02-01-09
%LM
%Version: Beta2

TRANS10(R,F), where R is the radius of curvature of the FP end mirror and F cavity's Finesse. This is the simulation of the modes transmissions in function of the cavity's length. All quantities to be entered in METERS!!! Up to the order ten code coloured:
%Nice 19-06-03
%LM
%Version: Beta2

WAIST(w_1,w_2,z_1,z_2) is a function calculating the waist of a laser beam. This function calculates the position and size of a Gaussian beam's waist given two measures of the beams size at a distance Delta=z_2-z_1 from the other. To be turned into a routine that works for a number N of beam measurement and calculates automatically M.
ALL QUANTITIES IN UNITS OF MICRONS 10^-6m!!
%Nice 03-12-11
%LM
%Version: BETA1

D. Nouveau chapitre de la these (Conduite du projet de recherche)

I. Contexte et enjeux du projet

Les raisons du projet.

Les ondes gravitationnelles sont une déformation de l'espace-temps prévue comme conséquence directe de la théorie de la Relativité Générale formulée par Einstein en 1916. Leur existence a été montrée de façon indirecte par Taylor et Hulse en 1974.

La détection directe des Ondes Gravitationnelles n'a jusqu'à présent jamais été réalisée. Cette observation a un grand intérêt scientifique car elle permettrait de valider la théorie de la Relativité Générale ainsi que d'écouter l'Univers ai lieu de l'observer comme on a fait jusqu'ici en Astronomie. La détection des OG nous amènerait à mieux connaître des corps célestes comme les trous noir, ou peut-être à découvrir des nouveaux objets tout court.

Pour répondre à ce défi scientifique plusieurs antennes, pour la détection des OG, telles que LIGO, VIRGO, TAMA, GEO, Auriga ont été conçues, développées et réalisées sur Terre. Ces détecteurs peuvent être classés en deux catégories principales : les barres (détecteurs mécaniques) et les interféromètres (détecteurs optiques).
Pour cette deuxième classe de détecteurs, des sources laser stabilisées en fréquence sont indispensables, mais peuvent aussi être utiles pour donner une lecture optique des signaux provenant des antennes à barre.

Actuellement un seul projet de ce type dans l'espace est en examen pour un lancement dans la prochaine décennie et le laser source sera un laser stabilisé à long terme (stabilité relative de l'ordre de 10^{-14} entre 10-1000 secondes).

Ce laser requiert des performances identiques à celles utilisées en métrologie des fréquences et des longueurs.

Ceci présente des défis technologiques importants, notamment pour des lasers qui doivent fonctionner dans l'espace (projets LISA et DARWIN) et sont donc sensés être robustes et fiables.

Les autres applications, qu'on peut mentionner pour ce type de Laser sont la sismologie, la géodésie, les expériences de vol en formation (DARWIN), la spectroscopie etc…

L'équipe

Mon laboratoire d'accueil, l'UMR 6162 du CNRS, intitulée depuis Janvier 2004 «Artemis,» est impliquée dans la construction, l'intégration et la mise au point de l'antenne franco-italienne pour la détection des OG, VIRGO (Pise, Italie).

Mise à part l'activité sur VIRGO, l'équipe a aussi plusieurs contrats de R&D, dont les expériences sont réalisées sur le site de Nice à l'Observatoire de la Cote d'Azur.

Un contrat important pour la recherche appliquée sur les lasers stabilisés à long terme a été financé par le CNES dans les dernières années. C'est dans le cadre de ce projet que s'inscrit mon travail de thèse.

J'ai démarré l'activité expérimentale avec mon équipe actuelle dans le cadre de mon stage de fin d'étude pour l'obtention du Diplôme de « Laurea » (équivalent Maîtrise + DEA) auprès de l'Università degli Studi di Firenze (Italie).

Ce stage de fin d'étude a été réalisé au moyen d'une bourse Erasmus et en collaboration avec l'équipe VIRGO, dont font partie mon laboratoire actuel et celui de mon ancien directeur de stage à Florence.

Le choix du stage a été motivé par mon intérêt pour l'optique, l'astronomie et la gravitation, disciplines qui sont toutes reliées au projet sur lequel j'ai travaillé dans les dernières années.

Pendant mon stage, le CNES vu les résultats expérimentaux obtenus au cours de celui-ci, a décidé de financer une bourse de thèse et un contrat de CDD Ingénieur, ainsi que de confier à l'équipe un forfait dédié à l'achat de matériel pour que l'activité expérimentale puisse continuer.

Financement du projet de recherche

En terme de personnel et de crédits pour l'achat de matériel, les moyens suivants ont été prévus :

Organisme	Personnel (temps plein)	Personnel (temps partiel)	2001 (k€)	2002 (k€)	2003 (k€)	2004 (k€)
CNES	2 à 3	-	20	30	40	TBD
OCA (ARTEMIS)	-	5	-	-	-	-

Les montants indiqués pour les années 2001 à 2003 n'incluent pas le salaires des deux personnes qui ont été embauchées (un ingénieur CDD et moi-même, bourse de thèse cofinancée CNES -Région PACA).

Seulement une partie des financements prévus pour 2001 et 2002 ont été livrés, à cause des difficultés économiques du CNES. Les sommes susmentionnées ont été rapportées en 2003. Finalement le financement pour 2004 n'a pas encore été décidé.

Un cahier de charges avait ainsi été établi :

- -création d'une référence laser à long terme sur une molécule
  - -choix de la molécule,
  - -éventuel doublage en fréquence du laser Nd :YAG,
  - -choix de la technique pour le verrouillage sur molécule ;
- -validation de la référence à long terme par comparaison avec un système identique ;
- -validation des performances de la technique nouvelle dite du « Double Pass Tilt Locking »

-transfert technologique vers une entreprise de la région PACA (la société SESO créatrice de systèmes optiques de précision pour le spatial) pour la construction d'une référence mécanique monolithique qui sera remise à l'OCA pour les tests et les études à suivre ;
-choix et étude sur les techniques de verrouillage sur référence moléculaire
-validation de la référence mécanique par rapport à la molécule.

II . Déroulement, gestion et coût du projet

Préparation

La recherche dans les articles publiées dans les revues scientifiques d'intérêt et la réalisation d'une bibliographie m'ont permis de connaître, de comprendre et de modéliser le comportement des différentes techniques de verrouillage en fréquence du laser.

En même temps, j'ai procédé à la recherche et à l'achat du matériel nécessaire pour démarrer les expériences pratiques en laboratoire.

J'ai ainsi étudié et participé à la conception optique et mécanique d'une cavité de Fabry-Perot de test primaire, et de la référence monolithique qui sera réalisée par SESO.

Les études théoriques et les recherches bibliographiques m'ayant permis de choisir les meilleures techniques et références j'ai donc démarré les études expérimentales.

Expériences

La mise en place des expériences pratiques a demandé une collaboration assez étroite à la fois avec l'atelier de mécanique et celui d'électronique.

Les délais de livraison et le manque initial de moyens ont parfois ralenti le montage des manipulations expérimentales. Heureusement des solutions temporaires ont permis de continuer les études prévues.

Un laser verrouillé sur l'Iode a été comparé à un système identique comme demandé par le cahier de charge. Ses performances sont satisfaisantes même si elles ne rejoignent pas encore celles prévues pour LISA sur toute la bande de fréquence souhaitée.

La technique du « Double Pass Tilt Locking » a été mise en place et étudiée. La stabilité de la référence mécanique utilisée n'étant pas suffisante, et l'ensemble en réalisation chez SESO ayant cumulé un retard important, mes collègues et moi même avons pu démarrer des tests sur une cavité réalisée pour VIRGO. Ces tests ont montré que la technique n'étant sensible qu'au déplacements du détecteur, elle est bien adaptée à l'utilisation dans l'espace. Autrement dit, nos travaux ont validé notre hypothèse de travail, et répondu au cahier de charges.

Gestion et coût du projet

Pour la réalisation du projet, ma formation a demandé un encadrement par deux chercheurs à temps partiel sur une période qui peut être estimée à 10-15 mois, le coût monétaire étant proche de 35k€

De même, deux mécaniciens et un ingénieur électronicien ont travaillé à temps partiel sur cette expérience, représentant ainsi un coût de 40k€

Le montant de ma bourse versée par le CNES et la Région PACA est proche de 58k€ sur les trois ans.

L'ingénieur d'études qui a travaillé avec moi a reçu un salaire brut d'environs 70k€ sur les trois ans.

Le matériel acheté pour la réalisation des expériences en laboratoire :

- 2 laser Nd :YAG doublé en fréquence 50k€
- 1 fréquencemètre 9k€
- 2 détections synchrones 7k€
- 2 cuves à Iode 7k€
- électroniques diverses 8k€
- optique diverses 14k€
- mécanique diverses (OCA) 35k€

Les missions et la participation aux congrès ont demandé une somme proche de 4k€.

Le tableau ci-dessous récapitule le coût global consolidé du projet, sur trois ans.

Les salaires des membres de l'équipe permanent prenant part au projet ont été versés entièrement par leur employeur, cet à dire le CNRS.

Le CNES comme prévu dans les accords initiaux s'est chargé des salaires des deux ingénieurs qui ont travaillé sur le projet et de ma bourse de thèse.

Les contributions adjonctives (pour un total de près-ce que 90k€) qui avaient été prévues par le CNES nous ont permis l'achat d'une grosse partie du nouveau matériel de laboratoire nécessaire pour les tests. Notamment ils ont permis l'achat de deux nouvelles sources lasers.

Les composants mécaniques ont été fournis pour une bonne partie par l'atelier de mécanique de l'Observatoire, seulement la construction de certains composants critiques a été faite à l'extérieur. Les pièces réalisés par Méca2000 et autres ont été achetées avec des financements CNES ou CNRS.

Les expériences électroniques ont été réalisées par l'ingénieur électronicien de l'équipe avec des composants achetés avec des crédits CNRS ou CNES, selon les cas.

Les missions ont été prises en charge par le CNRS ou par VIRGO.

Le coût total de la thèse peut être estimé à environs 330K€.

Le CNRS a contribué aux salaires du personnel permanent et à la gestion normale de l'équipe, y compris une partie du matériel de laboratoire.

L'Observatoire a aussi supporté une partie des coûts de la mise en ouvre de l'expérience.

Le CNES a payé les salaires du personnel non permanent embauché pour la mise en ouvre de cet étude.
Des 90k€ promis, la presque totalité a été versé au laboratoire, les dépenses extraordinaires qui ont été faites par le groupe, en optique, électronique et mécanique, estimables à 89k€, ont été couvertes par ce montant.

Sources Désignation	CNRS	CNES-PACA INSU	OCA-VIRGO	Montant [k€]
Salaires DR1+DR2	√			35
Bourse thèse		√		58
Salaires Ing. Mec.+El.	√			40
Salaires Ing. CDD		√		70
Lasers+Optiques	√	√		71
Mécaniques	√	√	√	35
Electroniques	√	√		17
Missions-Congrès	√		√	4
TOTAL				330

III. Compétences professionnelles et personnelles acquises

- **Les savoirs scientifiques** :
  - Mesurer les quantités physiques
  - Utiliser les instruments de laboratoire de pointe
    - Acquérir, stocker, analyser des données expérimentales
    - Interfacer instrumentation avec l'ordinateur
  - Utiliser, modéliser les sources lasers
  - Comprendre et appliquer l'optique Gaussienne

- Déterminer et calculer les spécifications et les paramètres d'une cavité optique
- Définir le projet d'une cavité optique
- Spectroscopie sous-Doppler d'une molécule : analyser la structure d'un atome-molécule
- Métrologie : Mesurer avec une précision extrême les grandeurs physiques fondamentales
- Verrouiller un laser en fréquence
- Travailler en laboratoire optique : salle grise et blanche
- Utiliser les outils informatiques spécifiques du secteur (ex. Paraxia, traceur de faisceau optique)
- Créer et mettre au point de logiciels sous MatLab pour la modélisation et le traitement des données
- Comprendre et utiliser les principes de l'analyse de Fourier
- Définition de procédures (R&D)

- **Les savoir être**
  - Rigueur et diplomatie
  - S'exprimer en publique
  - S'exprimer en français, en anglais, en allemand

- **Les savoir-faire profesionnalisants**
  - Gestion de projet (recherche, R&D)
  - Gestion des achats
  - Veille :
    - Documentaire
    - Technologique
  - Travailler en équipe, notamment dans des équipes interculturelles
  - Assurer les transversalités
  - Interfaçage avec les ateliers mécanique et électronique
  - Organiser les réunions de travail
  - Publication et communication scientifiques

Mon travail de thèse m'a aussi appris, d'un point de vue humain, à résoudre des problèmes apparemment insurmontables avec les moyens à disposition.

Sur un plan plus personnel la thèse m'a permis de poursuivre plusieurs de mes intérêts scientifiques et de bricoleuse, grâce surtout au travail en laboratoire.

IV. Retombées de la these

Dans le cadre de mon projet de thèse, il y a eu un transfert de technologie d'une équipe du projet VIRGO vers une entreprise industrielle (SESO) de la Région PACA, qui aura certainement des implications positives pour ce constructeur de systèmes optiques. Cette technologie sera certainement dans les années à venir utilisée dans les bancs optiques des futures expériences spatiales.

Mon équipe est parvenue à construire une « référence laser stable à long terme », dès à présent, est assez proche des spécifications demandées. Des

nouvelles techniques de verrouillage en fréquence on été également introduites et testées.

Les lasers stabilisés en fréquence pourront être utilisés non pas seulement pour la détection des OG mais aussi appliqués dans les domaines de la sismologie, l'étude du champ gravitationnel terrestre, la mesure de précision de composants optiques ou mécanique, etc.

Les techniques de spectroscopie qui ont été mises en place sont celles usuellement utilisées pour la caractérisation et l'étude des atomes et des molécules dans les laboratoires de chimie.

Pour ma part, j'ai appris à me situer et à gérer un projet de recherche. Et cela me permettra sûrement d'assumer des responsabilités au sein d'une équipe projet.

Les compétences acquises dans la réalisation de ma thèse me préparent à l'insertion dans plusieurs domaines de recherche, comme les vols en formation dans l'espace, la sismologie, la spectroscopie, etc.
Dans le futur, j'aimerais bien pouvoir continuer l'activité de recherche avec un post-doctorat ou bien démarrer par un emploi en R&D sur les lasers et les systèmes optiques dans une industrie optique.

BIBLIOGRAPHY

[1] LISA System and Technology Study Report, *ESA-SCI* (2000) **11**

[2] Easterbrook *et al. Phys.Rev.D*, **62** (2000) 042002

[3] Brillet *Application de l'absorption saturée à la realisation d'étalons de fréquence optique*, **Thèse Paris XI** (1976) I.6

[4] Camy *et al. Optics Communications*, **41** (1982) 5

[5] Burck *et al. IEEE Journal Quantum Electronics*, **37** (2001) 6

[6] J.H. Shirley *Optics Letters*, **7** (1982) 11

[7] Brookman *Detections d'Ondes Gravitationnelles avec LISA*, **Report OCA** (2000)

[8] Eickhoff *et al. IEEE Trans. on Instr. and Meas.,* **44** (1995) 2 *Pag.155-158*

[9] Ye *et al. IEEE Trans. on Instr. and Meas.,* **48** (1999) 2 *Pag.544-548*

[10] Picard *et al. Applied Optics*, **42** (2003) 6 *Pag.1019-1028*

[11] Hall *et al. Appl. Phys. Letters*, **39** (1981) 9 *Pag.680-682*

[12] Nakagawa *et al. Optics Communications*, **107** (1994) *Pag.369-372*

[13] Edwards *et al. Optics Letters*, **29** *Pag.566-568*

[14] Dubé *et al. J.Opt.Soc.Am.B,* **13** (1996) 9 *Pag.2041-2053*

[15] Ma *et al. J.Opt.Soc.Am.B,* **16** (1999) 12 *Pag.2255-2268*

[16] Ye *et al. Optics Letters,* **21** (1996) 13 *Pag.1000-1002*

[17] Fritschel *et al. Applied Optics,* **31** (1992) 12 *Pag.1910-1912*

[18] Inbar *et al. Applied Physics B,* **68** (1999) *Pag.99-105*

[19] Orlov *et al. Sov.Tech.Phys.Lett.* **12** (1986) 3 *Pag.120-121*

[20] Wallmeroth *et al. Optics Letters,* **15** (1990) 14 *Pag.812-813*

[21] Inbar *et al. J.Opt.Soc.Am.B,* **13** (1996) 7 *Pag.1598-1604*

[22] Barsuglia et al. **VIRGO-NOT-LAS-1390-XXX** (1998)

[23] Seel *et al. Proc. V Symp. Frequency Standards and Metrology* (1996)

[24] Seel *et al. Phys. Rev. Lett.* **78** (1997) 25 *Pag.4741-4744*

[25] Storz *et al. Optics Letters* **23** (1998) 13

[26] Shaddock *et al. Optics Letters,* **24** (1999) 1499-1501

[27] Shaddock *Advanced interferometry for GW Detection,* ***Thesis ANU*** (2000)

[28] Hänsch *et al. Opt.Comm.,* **35** (1980) 441

[29] Houssin *et al. Optics Letters,* **13** (1988) 10

[30] Drever *et al. Appl. Phys. B,* **31** (1983) 97

[31] Black **LIGO-T980045-00-D** (1998)

[32] Gouy *et al. C.R.Acad.Sci.Paris,* **110** (1890) 1251

[33] Feng *et al. Optics Letters*, **26** (2001) 8 *Pag.485-487*

[34] Araya *et al. Applied optics,* **38** (1999) 13 *Pag.2848-2856*

[35] Ye *et al. IEEE Trans. Instr. Meas.,* **46** (1997) 2 *Pag.178-182*

[36] Slagmolen *et al. IEEE J.Quant.Elec.* **38** (2002) 11 *Pag.1521-1528*

[37] Einstein *Ann.Phys.Lpz.* **49** (1916) *769*

[38] Hulse & Taylor *Astroph.J. Letters* **195** (1975), L51

[39] Collins *Applied Optics* **11** (1964) 1263

[40] Harvey and White *Optics Comm.* **221** (2003) 163-171

[41] Auto-alignment (F. Cleva Private Communication)

[42] D'Amour *Nucl.Phys.* **B568** (2000) 93-119

[43] Hogan *Second International LISA Symposium on Gravitational Waves* (1998) ed. W. Folkner.

[44] Cornish *Class.Quant.Grav.* **18** (2001) 4277-4292

[45] Weber *Phys.Rev.Lett.* **22** (1969) 1320

[46] Saulson *Fundamentals of interferometric gravitational wave detectors* (1994) World Scientific.

[47] Buonanno *et al*. *Phys.Rev.D* **62** (2000) 064015

[48] Vinet *Physique Modèles et simulations numeriques des antennas gravitationnelles optiques* **DEA HRAG UNSA** (2000)

[49] Hils and Hall *Ultra Stable Cavity-stabilised Lasers with Subhertz Linewidth* **Frequency standards and metrology** (1989) *Pag.162-173*